Durham E-Theses

Diffuse Interface Modelling of Wetting on Complex Structured Surfaces

OKTASENDRA, FANDI

How to cite:

Use policy

Diffuse Interface Modelling of Wetting on Complex Structured Surfaces

Fandi Oktasendra

A thesis submitted for the degree of
Doctor of Philosophy

Durham University

Department of Physics
Durham University
United Kingdom

· March 2024 ·

Diffuse Interface Modelling of Wetting on Complex Structured Surfaces

Fandi Oktasendra

Abstract

Wetting on solid surfaces textured with geometries from simple to highly complex structures is of interest from fundamental physics perspective and for potential applications. From the physics point of view, interesting phenomena can be observed, such as hemiwicking, when perfectly wetting liquids propagate through the corrugation of these structured surfaces, and wetting transition, when liquids initially in a suspended state (Cassie-Baxter state) transition to a collapsed state (Wenzel state). In addition, on a microscopic scale where the wettability is dictated by the intermolecular interactions, distinct wetting phenomena can be observed, such as liquid filling and emptying. From the application perspective, wetting on structured surfaces is key to a broad range of technological and industrial applications, from coating and microfluidic to liquid hydrocarbon recovery.

In this thesis, we employ dynamical and quasi-static numerical methods based on diffuse interface model for studying wetting phenomena on structured surfaces. First, we use the Lattice Boltzmann method, which is powerful for studying liquid dynamics. Second, we employ the phase-field energy minimisation method by incorporating distance-dependent solid-liquid interactions to obtain the equilibrium state of the system. Third, we develop a new method based on the phase-field model in the energy minimisation framework, the frozen fluid method, for constructing highly complex geometry structures.

We develop a fully analytical model to predict the propagation coefficients for liquids hemiwicking through square and face-centre/hexagonal arrays of micropillars. This is done by balancing the capillary driving force and a viscous resistive force and solving the Navier-Stokes equation for representative channels. The theoretical predictions for the square array case exhibit excellent agreement with the simulation results for a wide range of geometries and improved accuracy compared to previously proposed models. Furthermore, we demonstrate the applicability of the hydraulic-electric circuit analogy approach in approximating the equivalent channel for face-centred/hexagonal arrays of micropillars.

In the study of liquid filling and emptying on grooved surfaces, we consider short-range and long-range liquid-solid interactions, with the latter including purely attractive and repulsive interactions and those with short-range attraction and long-range repulsion. Comparing the filling and emptying transitions for complete, partial, and pseudo-partial wetting states, we find that the filling and emptying transitions are reversible for the complete wetting case, while significant hysteresis is observed for the partial and pseudo-partial cases. In agreement with previous studies, we show that the critical pressure for the filling transition follows the Kelvin equation for the complete and partial wetting cases. For the pseudo-partial wetting case, we find that the filling transition can display a number of distinct morphological pathways.

Finally, we validate the frozen fluid method through several benchmarking tests, demonstrating its applicability across various solid geometries, including those with flat, curved, and corner features. Subsequently, we utilize the method to investigate the critical pressure of a liquid on superhydrophobic surfaces textured with cylindrical and truncated cone pillars, and mesh geometry. By analyzing the impact of texture parameters, we can optimize superhydrophobic surfaces to enhance their wetting stability.

CONTENTS

ACKNOWLEDGMENTS

Declaration

The work presented in this thesis has been developed by the author under the supervision of Prof Halim Kusumaatmaja of the Department of Physics at Durham University. All text and figures are the work of the author unless otherwise stated. No part of this thesis has been presented for any other degree or qualification.

CONTRIBUTIONS

The work presented in this thesis has been developed by the author under the supervision of Prof Halim Kusumaatmaja of the Department of Physics at Durham University. The original simulation methodologies in Part III and IV were developed by Dr Jack Panter of the University of East Anglia (previously at Durham University). The author has also benefited from Dr Samuel Avis for his assistance and discussion in developing the simulation methodologies in Part II and IV.

The work presented in Part II and III is a collaborative work between our group and the group at ExxonMobil Technology and Engineering Company, USA. In Part II, the collaborators proposed and developed the original theoretical model as well as conducted experimental work, while the author performed the numerical confirmation of the theory and expanded the theoretical model. In Part III, the author benefited from fruitful discussions with the collaborators.

The SEM image in Fig. 9.15(a) is the work done by Dr.-Ing. Hutomo Suryo Wasisto (Infineon Technologies AG) and used with permission.

Publications

The following published works form the majority of Part II and III.

- B. Natarajan, A. Jaishankar, M. King, **F. Oktasendra**, S. J. Avis, A. R. Konicek, G. Wadsworth, A. Jusufi, H. Kusumaatmaja, and M. S. Yeganeh, "Predicting hemiwicking dynamics on textured substrates", *Langmuir* **37**(**1**), 188-195 (2020)

- **F. Oktasendra**, A. Jusufi, A. R. Konicek, M. S. Yeganeh, J. R. Panter, and H. Kusumaatmaja, "Phase field simulation of liquid filling on grooved surfaces for complete, partial, and pseudo-partial wetting cases", *Journal of Chemical Physics* **158**(**20**), 204501 (2023)

Part I

Introduction

CHAPTER 1

Motivation

Nature stores numerous amazing features of surfaces which exhibit intriguing phenomena when in contact with liquid such as water. After millions of years of evolution, organisms have evolved specific surface structures and chemistry that allow them to adapt to their surroundings. For example, the leaves of the Lotus (*Nelumbo nucifera L.*) plant exhibit water-repellent properties, which keep the leaves dry when rainwater falls onto them. The water droplets that fall on the leaves form spherical beads and roll off while collecting and removing dust and other contaminants from the surface. This self-cleaning property of Lotus leaves is known as the "Lotus effect" [1, 2]. A closer look at the leaf reveals that the leaf has a multi-scale rough structure covered with cuticular wax crystals, as shown in Fig. 1.1 (a). This structure has inspired many attempts to reproduce similar surfaces to get this superhydrophobic (i.e. repellent to water) effect.

Furthermore, some natural surfaces were discovered to be repellant to not only water but also oil (superamphiphobic) or even to all types of liquids (superomniphobic) [3]. The Springtails, for example, live in a humid environment and have a strong ability to avoid being wet by either water or other liquids with low surface tension (e.g. more oils) [4]. The cuticle of a springtail has a re-entrant micro/nanostructure composed of the densely-distributed hexagon or rhombus nanoarrays [5], as shown in Fig. 1.1 (c). This structure can keep an air layer in place to prevent wetting by aqueous or oil-based liquids, which is why it is repellent [5]. Because of their unique hierarchical surface structures, several plants and animals have extraordinary water transport properties. Spider silk, for example, with periodic spindle-knots and joints, can transport water (with velocity $\sim 30 \, \mu\mathrm{ms}^{-1}$) [6], and cactus spine can transport water (with velocity $\sim 12 \, \mu\mathrm{ms}^{-1}$) due to gradient grooves on the surface [7, 8, 9]. Recently,

one type of insect-trap plant, *Sarracenia*, has been found to have ultrafast water transport properties (with a velocity of about three orders magnitudes faster than that on cactus spine) due to its unique hierarchical surface structure characteristic at its trichome [10], as shown in Fig. 1.1 (c). Scanning electron microscope scan reveals that its surface structure has hierarchically structured ribs perfectly aligned along the trichome to form approximately parallel hierarchical microchannels and two neighbouring high ribs to form a large channel. This structure allows water to move unidirectionally along the microchannel driven by capillary action. These ultrafast water transport properties demonstrate the potential of hierarchical design in microfluidic applications.

(a) Lotus plant

(b) Springtail
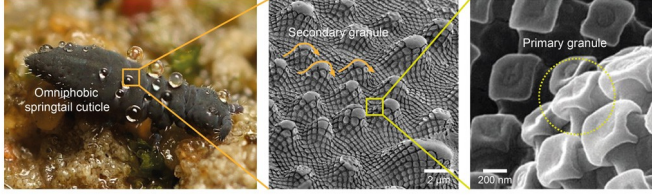
(c) Sarracenia plant
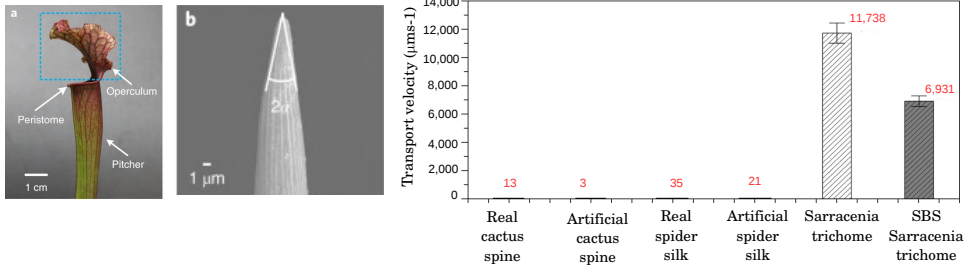
Figure 1.1: Examples of wetting phenomena in nature. (a) Macroscale (left) and microscale (right) views of a water-repellent lotus leaf [1]. (b) Image of the springtail (left) with microscopic (middle) and SEM (right) images of the textured skin [5]. (c) The *Sarracenia* plant (left) with a microscopic image of the trichome surface (middle) and a table of transport velocity for different objects (right) [10].

Besides organisms (plants and animals), wetting phenomena are also important in numerous aspects of human life and the environment. As an example, water vapour is created when we take a shower, with hot water condenses on the window glass in the bathroom. This will

create separate water droplets if the cohesion force of water molecules is stronger than the adhesion force between liquid and glass. In contrast, if the adhesion force is stronger than the cohesive force, a liquid thin film will be formed. Interestingly, the same physics is relevant for phase-change heat transfer mechanisms exploited in a number of engineering applications [11, 12, 13].

Such intriguing and extraordinary surface structures of organisms in nature have inspired scientists and engineers to fabricate synthetic surfaces mimicking similar wetting properties of natural surfaces. These bio-inspired surfaces have become a subject of interest for decades due to the broad spectrum of industrial applications involving wetting phenomena. For example, consider water-repellent surfaces. These superhydrophobic surfaces are attributed to the trapping of air pockets in the rough or porous surface, causing a liquid droplet to be suspended on top of the micron- and nano-scale surface corrugations [14]. This allows superhydrophobic surfaces to have small contact angle hysteresis and large drag reduction (thus, liquid droplets move easily on the surface), and large contact angle (thus, liquid droplets form a spherical shape on the surface). All these make them attractive for a number of applications, such as in textile, architecture, automotive, military and biomedical devices. However, these surfaces suffer multiple weaknesses, such as repellency only towards liquids with high surface tension, low mechanical stability, low transparency, weak pressure stability, and short-term underwater stability [15]. Superoleophobic surfaces have repellency towards low surface tension liquids, but they share all other weaknesses with superhydrophobic surfaces [16].

One alternative for replacing the superhydrophobic surfaces is called bio-inspired liquid infused surfaces or lubricant impregnated surfaces (LIS), which offer better features combining the mechanical stability of a solid substrate with the liquid-like properties and molecular smoothness of the lubricant interface [17, 18, 19]. A typical scenario concerning the study of wetting on LIS involves three fluids: a lubricant (typically an oil) infused in between the surface texture, a droplet of liquid (such as a water droplet), and the gas environment [20]. LIS has been shown to exhibit many superior wetting properties compared to superhydrophobic surfaces, including lower contact angle hysteresis [20], self-cleaning [21], anti-bioadhesion [22], anti-corrosion [23], drag reduction [24], anti-icing [25]. LIS also demonstrate excellent repellency and drop mobility to a broad range of liquids, including low surface tension and complex fluids such as blood or cell medium. This is manifested due to the mobility of the lubricant trapped inside the surface structures. Moreover, LIS are robust against pressure-

induced instabilities and failure, which makes them favourable for applications to a wide range of problems, ranging from marine fouling and product packaging to heat exchanger and medical devices [17, 26, 27]. However, despite its advantageous features, LIS also suffers from certain weaknesses, in particular the loss of lubricant, which may occur due to a variety of reasons, including evaporation, shear instability and droplet-induced depletion [28, 29, 30, 31].

Controlling the mobility of liquids (droplets or thin films) along surfaces is crucial for many applications ranging from microfluidics to liquid hydrocarbon recovery. The surfaces used in such applications are usually fabricated using nano-/micropatterning technologies (such as lithography) to create textures with tunable wettability and transport properties. These textured surfaces affect the wettability of solid, inducing interesting wetting behaviours such as superphilicity, as well as interesting liquid transport mechanisms such as hemiwicking (i.e. spontaneous flow of liquid through an enclosed porous medium driven by capillary action) [32]. The applications involving hemiwicking include thermal management [33], liquid-infused surfaces [34], energy harvesting [35], and lab-on-a-chip devices [36].

These applications require a fundamental understanding of wetting and its properties, as well as the interplay between surface textures and liquids. Many of these applications employ a complex surface geometry. Hence, understanding the role of this complexity is key to further utilization and development.

Since the early studies of wetting dating back to the eighteenth century by Young and Laplace [37, 38], a number of theoretical models have been proposed to describe both static and dynamics wetting properties. Some of the fundamental theories include the contact angle, contact angle hysteresis, contact line dynamics and bulk liquid hydrodynamics. While many of the theoretical predictions can be confirmed by experimental evidence, experimentalists face significant constraints in terms of what can be measured, what time and length scales can be studied, and which parameters can be controlled. Moreover, the experimental study could be limited by resources and tools when the case of the study involves high complexity in geometry and structure.

Computer simulations, on the other hand, are extremely versatile in terms of the degree to which parameters can be controlled and useful information extracted. This is supported by increasingly powerful hardware and algorithms being developed which extend the limits of length and time scales. As a result, this type of simulation can be used in a growing number of applications to bridge the gap between theory and experiment in the pursuit of a deeper

understanding of fundamental wetting physics.

There are many simulation methods available used to study fluid dynamics, commonly referred to as computational fluid dynamics (CFD). In this thesis, we choose the Lattice Boltzmann method (LBM) [39] for its computational efficiency and simplicity in handling complex geometry. The LBM is a particle-based method that tracks the distribution of particles. This contrasts with other popular particle-based methods, such as Molecular Dynamics (MD) [40], which track individual atoms or molecules. Therefore, while capable of providing atomistic details, MD is often deemed too computationally expensive for simulating liquid dynamics at macroscopic scales.

We also adopt a diffuse interface model [41, 42] over the sharp interface model, as we apply it in the LBM and phase field methods. There are several advantages to using the diffuse interface model. While sharp interface models often struggle to capture interface motion when interfaces break up or merge, diffuse interface models handle such phenomena seamlessly due to their continuous interface representation. Moreover, diffuse interface models often exhibit greater numerical stability than sharp interface models, especially in simulations involving dynamic wetting processes. Therefore, diffuse interface models are more suitable for the problems of interest in this thesis.

CHAPTER 2

Literature Review

2.1 Wetting on Flat Surfaces

When a liquid droplet is put in contact with a solid surface, two extreme conditions might happen: 1) the liquid droplet will spread over the surface (complete wetting), or 2) the liquid droplet remains spherical without developing any contact with the surface, leaving the surface dry (complete non-wetting) [43]. What parameters determine which condition is favourable? To answer this question, let us start by looking into wetting on a flat and chemically homogeneous solid surface (an ideal solid). Thomas Young and Pierre-Simon Laplace proposed that surfaces carry a specific energy that reflects the cohesion of the underlying condensed phase (solid or liquid) [37, 38]. This quantity is called surface tension, denoted as γ_{ij} for an interface between phases i and j (indices i and j are s, l, and g for solid, liquid, and gas, respectively). It has the dimension of energy per unit area or, alternatively, a force per unit length. This force applies along the ij surface to minimise the corresponding surface energy. The competition between three surface tensions, γ_{gs}, γ_{ls}, and γ_{lg}, determines the wetting behaviour and is represented by the spreading parameter S, defined as

$$S = \gamma_{\mathrm{gs}} - (\gamma_{\mathrm{ls}} + \gamma_{\mathrm{lg}}), \tag{2.1}$$

which measures the difference between the surface energy (per unit area) of the surface when dry and wet [43, 44]. For complete wetting condition, γ_{gs} is larger than or equal to the sum of liquid-solid and liquid-gas surface tensions, $\gamma_{\mathrm{ls}} + \gamma_{\mathrm{lg}}$, because liquid spreading expands the two corresponding surface areas. Its spreading parameter is larger than or equal to zero ($S \geq 0$).

For partial wetting condition, the spreading parameter is negative ($S < 0$). Since the sum of the liquid-solid and liquid-gas surface tensions is larger than the gas-solid surface tension, it is not advantageous to completely replace the gas-solid interface with the two others. Different surface tensions acting on the contact line provide the equilibrium condition of the drop. The balance can be written as

$$\gamma_{gs} = \gamma_{ls} + \gamma_{lg} \cos \theta, \tag{2.2}$$

which is known as the Young equation [37]. The contact angle θ is called the Young's contact angle. This relation is schematically depicted in Fig. 2.1. The contact angle decreases when a liquid droplet spreads further on a solid surface. Hence, the contact angle provides a measure of the degree of wetting. The contact angle is measured at the three-phase contact line, defined as the point at which the liquid, solid and surrounding gas phases meet.
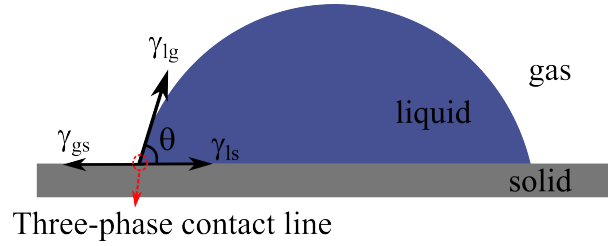
Figure 2.1: Droplet on a flat surface with contact angle θ. Liquid-solid, gas-solid and liquid-gas surface tensions, γ_{ls}, γ_{gs} and γ_{lg}, respectively, are balanced at the three-phase contact line.

When $\gamma_{ls} < \gamma_{gs}$, the tendency of a solid surface to create an interface with the liquid droplet increases. As a result, the contact angle decreases (usually less than 90°, referred to as hydrophilic). On the contrary, when $\gamma_{ls} > \gamma_{gs}$, the liquid droplet tends to avoid making contact with the solid surface, allowing the contact angle to increase (usually larger than 90°, referred to as hydrophobic). These two conditions correspond to the partial wetting regime.

Another important concept related to the surface tension is called the Laplace pressure. The surface tension is at the origin of the overpressure existing in the interior of a liquid droplet [45]. This pressure difference is responsible for the phenomenon of capillary adhesion, for instance, in a capillary tube induced by a capillary bridge. The pressure difference, Δp, that occurs upon traversing the boundary between two fluids (say liquid and gas) is proportional to the surface tension γ_{lg} and the curvature of the interface, C. Mathematically, this theorem can be written as

$$\Delta p = \gamma_{lg} C. \tag{2.3}$$

For a water droplet suspended in a gas, the curvature is given by $C = \left(\frac{1}{R_1} + \frac{1}{R_2} \right)$, where R_1 and R_2 are the principal radii of curvature. Since the droplet adopts a spherical shape in order to minimise its surface energy, the curvature is only determined by the droplet radius R. The Laplace pressure is then given by $\Delta p = \frac{2\gamma_{\mathrm{lg}}}{R}$. In an equilibrium condition, the mean curvature between two fluid phases, hence the Laplace pressure, is constant.

2.2 Wetting on Structured Surfaces

The texture of the solid surface is another important factor in determining the wetting behaviour. In fact, most of the surfaces in nature are rough and chemically inhomogeneous, with scales ranging from nano to micrometres. In the process of fabrication, such as lamination or coating, rough surfaces may result from a defect or undesired materials trapped on the surface. To understand the wetting behaviour on rough surfaces, let us consider a liquid droplet deposited on a periodically textured surface, as shown in Fig. 2.2.

When a droplet is placed on a rough surface, two possible mechanisms can occur at equilibrium. First, the liquid droplet fills the roughness, enlarging the contact area between the liquid and solid phases. This state is called the Wenzel state, as illustrated in Fig. 2.2 (a). The apparent contact angle may be different from the Young's contact angle in Eq. (2.2). It was first demonstrated by Wenzel [46], and using a geometrical argument, the apparent contact angle, θ_W, is given by

$$\cos \theta_W = r \cos \theta, \tag{2.4}$$

where r is the roughness factor defined as the ratio between the actual surface area and the apparent or projected surface area, whose values are always larger than unity. From the Wenzel relation in Eq. (2.4) we can see that roughness enhances wettability. Since $r > 1$, a hydrophilic surface becomes more hydrophilic when rough ($\theta_W < \theta$) and a hydrophobic surface becomes more hydrophobic ($\theta_W > \theta$).

The second possible state is the Cassie-Baxter state [47], as illustrated in Fig. 2.2 (b). Instead of filling the surface roughness, the liquid droplet can sit on top of the surface roughness, leaving the surface a composite of solid and air below the droplet. As a consequence, only a fraction of the solid is in contact with the liquid. If φ_s is defined as the contact area of the droplet divided by the area of solid under the drop projected on the plane of the surface, the

contact angle θ_{CB} is therefore given by

$$\cos \theta_{CB} = \varphi_s \cos \theta - (1 - \varphi_s). \tag{2.5}$$

In the Cassie-Baxter state, surface roughness reduces the effective solid-gas and solid-liquid surface area. Therefore, the apparent contact angle appears to be larger, thus enhancing the surface hydrophobicity. From Eq. (2.5), we can see that the contact angles can be as large as $180°$. Typically, a surface with $\theta_{CB} > 150°$ is termed a superhydrophobic surface.

(a) **(b)**

Wenzel state   Cassier-Baxter state
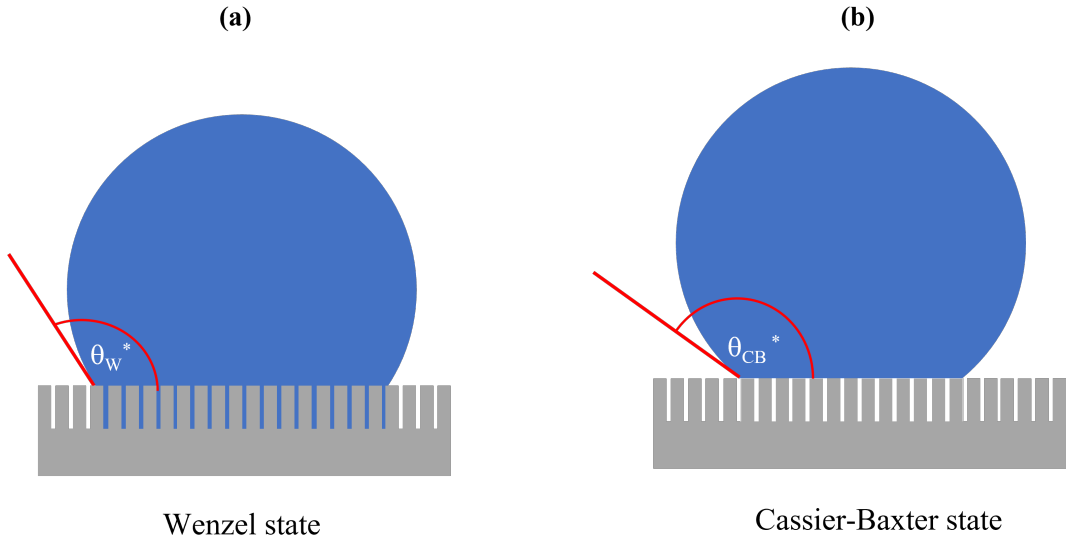
Figure 2.2: Illustration of two possible states due to the surface roughness: (a) Wenzel state and (b) Cassie-Baxter state with their corresponding apparent contact angles.

The roughness of the surface can also cause a contact angle hysteresis (CAH). It is defined as the difference between the advancing, θ_A, and receding, θ_R, angles,

$$CAH = \theta_A - \theta_R. \tag{2.6}$$

The illustration for the CAH is shown in Fig. 2.3. This image shows a practical way of measuring the CAH by means of varying the volume of the droplet. When the droplet volume slowly increases, the contact angle increases until it reaches its maximum value, and then it remains constant. This maximum angle is referred to as the advancing contact angle, θ_A (Fig. 2.3 (a)). Conversely, by slowly reducing the droplet volume, the contact angle will decrease until it reaches a minimum angle. This minimum angle is referred to as the receding contact angle, θ_R (Fig. 2.3 (b)). The CAH occurs because, when increasing or decreasing the droplet volume, the

contact line is pinned to the surface (usually occurs at the corner of the texture). This creates an asymmetry between θ_A and θ_R. For the Wenzel state, the CAH is generally large, caused by a large pinning force due to the high liquid-solid contact area. For the Cassie-Baxter state, on the contrary, the CAH value is low because of the low liquid-solid contact area.

(a)   (b)

Advancing   Receding
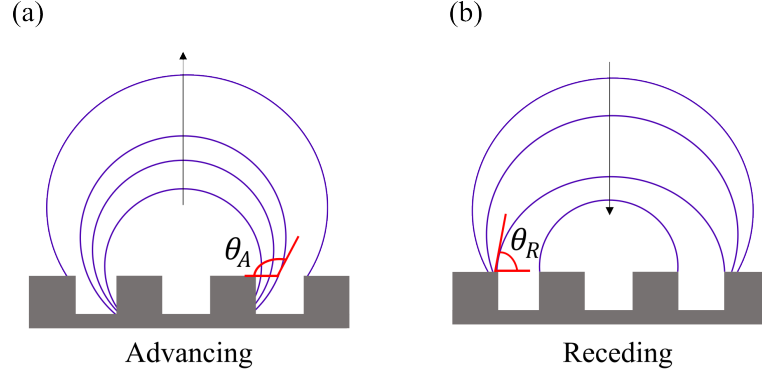
Figure 2.3: Illustration of the contact angle hysteresis on a structured surface showing (a) advancing contact angle θ_A and (b) receding contact angle θ_R [48].

The condition for the liquid-gas interface to be pinned on a solid corner can be described by the Gibbs pinning criterion [49]. For an illustration, let us consider the contact line pinning at a $\varphi = 90°$ corner, as illustrated in Fig. 2.4. Here, the measured contact angle can be between $\beta = \theta$ and $\beta = \theta + \varphi$. The liquid-gas interface will spontaneously depin from the edge and slide to the left when $\beta < \theta$ or downwards when $\beta > \theta + \varphi$ [50].
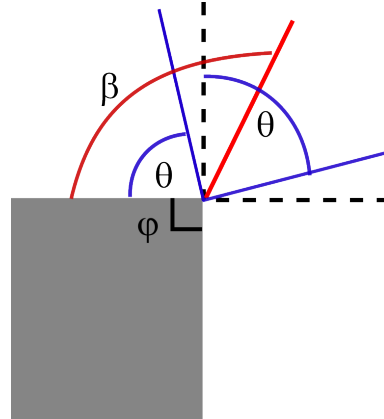
Figure 2.4: Illustration of contact line pinning at the 90° corner of surface roughness. At the corner, the contact angle can take any value between $\beta = \theta$ and $\beta = \theta + \varphi$. The sketch is adapted from [50].

2.3 Superhydrophobicity: Cassie-Baxter to Wenzel States Transition

Increasing the roughness of a hydrophobic surface is one way of achieving superhydrophobicity. The superhydrophobic surfaces are characterised by the high contact angle (typically larger than 150°) and low CAH (typically less than 20°) [51]. These properties can be achieved if the liquid droplet is in the Cassie-Baxter state, in which it will form a near-spherical droplet and roll on the surface when slightly inclined. However, a droplet on the Cassie-Baxter state is susceptible to transition to a Wenzel state, which leads to the loss of the advantageous surface properties.

This Cassie-Baxter to Wenzel transition can occur due to a variety of perturbations sufficient enough to deform the liquid-gas interface. These include pressure, vibration, evaporation-condensation, droplet impact, flow, or changes to electric or magnetic fields. In real-world applications, the wetting transition may be initiated by several perturbations simultaneously instead of a single perturbation.

Numerous studies have been devoted to understanding the theoretical explanation behind this wetting transition [52, 53]. For instance, Lafuma *et al* [52] derived the condition for the transition to occur from the Cassie-Baxter and Wenzel models and proposed that the transition occurs at a critical contact angle, θ_c. If the contact angle θ is larger than θ_c, the droplet will remain in the Cassie-Baxter state. However, for $90° < \theta < \theta_c$, the two states might coexist, showing the metastability of this regime. This metastable region has been validated by experiment and simulation results [54, 55].

The explanation of the mechanism and criteria for the Cassie-Baxter/Wenzel transition can be divided into two groups: thermodynamic analysis and force-based analysis [56]. The thermodynamic analysis associates the wetting transition with minimising the Gibbs energy of the system [57, 58]. When the Cassie-Baxter state has higher energy than the Wenzel state, as the droplet penetrates the gap between pillars, the system reduces the Gibbs energy by replacing the solid-gas interface with the solid-liquid interface and changing the liquid-gas interfacial area. Patankar *et al.* [57] showed that, although the Cassie-Baxter/Wenzel is energetically favourable, there is an energy barrier between the two states, necessitating additional work to induce the transition.

The force-based analysis elucidates the balance of the capillary force in the proximity of

the three-phase contact line [59, 60]. For example, Zheng *et al.* [60] argued that the wetting transition process is driven by a hydraulic pressure, which may be generated by the liquid-gas interfacial tension of the droplet or external forces such as gravity, drop impact, etc. This model also suggests that there is a critical pressure, which is the maximum pressure that the Cassie-Baxter state can sustain.

2.4 Complex Geometry Surfaces

Conventional superhydrophobic surfaces are textured with arrays of micropillars. This simple pillar texture is prone to wetting transition when wetted by liquid droplets like water. Even more, when a liquid with a lower contact angle (such as oil) wets the surface, the Cassie-Baxter state normally breaks down. Therefore, the design of superhydrophobic surfaces has evolved to become more complex. In an attempt to make the superhydrophobic surfaces resistant against many different types of liquid, new textured surfaces emerge: superoleophobic surfaces, describing a surface that is resistant to wetting by oil; superamphiphobic surfaces, describing a surface that is resistant to wetting by both oil and water; and superomniphobic surfaces, describing a surface that is resistance against wetting by all liquids.
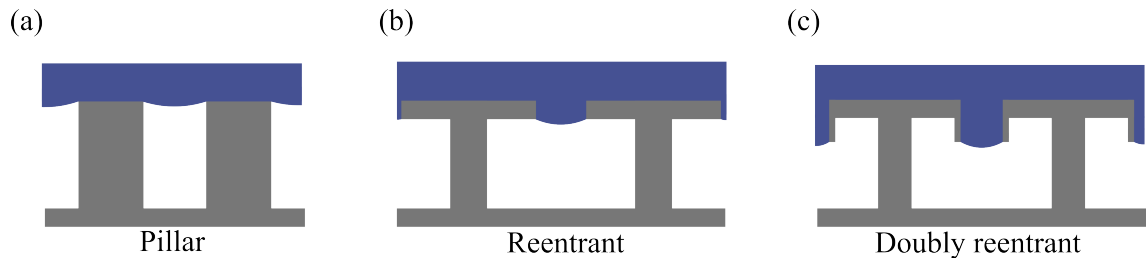
Figure 2.5: Surfaces textured with (a) simple pillar, (b) reentrant and (c) doubly-reentrant geometries.

The reentrant and doubly reentrant geometries are two promising textures that enable these super-repellant properties (Fig. 2.5). The reentrant geometry features an overhanging cap structure, while the doubly reentrant geometry builds upon this by incorporating a lip structure onto the cap. The reentrant geometry can effectively trap air pockets beneath the cap structure, preventing the penetration of low surface tension liquids (e.g. oil). Therefore, this structure is often referred to as a superamphiphobic surface. On the doubly reentrant geometry, the liquid-gas interface may wet the inner cap lip while getting pinned at the bottom of the cap lip. This allows perfectly wetting liquids to be in the Cassie-Baxter state, achieving superomniphobicity

performance. More detail of the geometrical influence of the surface structure on the wetting states and the wetting transition is given in Refs [61, 62].

2.5 Wetting on Micro- to Nanoscale: the Long-range Interactions

When a spreading liquid completely wets a solid surface, a thin layer of liquid film will be formed whose thickness could be in the mesoscopic range (a few angstroms to a micrometer). In such a range of length scale, the wetting behaviour is determined by a competition between the cohesive interactions of the liquid molecules and the adhesive interaction between the liquid and solid [63]. These molecular interactions are often described in terms of the repulsive (short-range) and attractive (long-range) potentials, for which the Lennard-Jones form of potential has been widely used due to its simplicity [64]:

$$V_{LJ}\left(r\right) = 4\epsilon\left[\left(\frac{\sigma}{r}\right)^{12} - \left(\frac{\sigma}{r}\right)^{6}\right]. \tag{2.7}$$

The repulsive term occurs at the very short range (in order of the molecular magnitude or less) and plays a role in determining intrinsic properties of liquid, such as the order of molecular structure and the density. On the other hand, the long-range attraction component is mainly responsible for the wetting properties. This long-range potential could be a result of the van der Waals force toward the solid and other types of interactions, especially when the film thickness is very small, such as dipole-dipole, hydrogen bonds and various effects due to different densities of the liquid near the solid surface [65].

These molecular interactions determining the wetting behavior of liquid thin film are often quantified in terms of the free energy (per unit area) of a film of thickness e. One can consider a liquid thin film of thickness of e on a solid surface. If the liquid-solid interactions are strong, the system can lower its free energy by increasing the distance between the two surfaces. This results in a net repulsive force per unit area between the liquid-solid and liquid-gas interfaces, called the disjoining pressure, $\Pi(e)$ [63]. The excess free energy (per unit area) is then given by [45, 65]

$$F\left(e\right) = \gamma_{\text{ls}} + \gamma_{\text{lg}} + P\left(e\right), \tag{2.8}$$

where $P(e)$ is called the effective interface potential, from which the disjoining pressure is

defined: $\Pi(e) = -dP(e)/de$. When the film is considerably thick (larger than 100 nm), $P(e) \to 0$ and its free energy is contributed by the surface energy at the two interfaces. When the film becomes very thin ($e \to 0$), its free energy must be equal to the energy of the dry solid (γ_{gs}), and hence $P(e)$ acts as the spreading parameter (S), $S \equiv \gamma_{gs} - \gamma_{ls} - \gamma_{lg}$. At the intermediate range, the long-range interaction contributes to the variation of $P(e)$. If the potential is controlled by the long-range van der Waals interaction between the molecules, which varies with the inverse sixth power of the distance ($1/r^6$), the effective interface potential can be modelled as

$$P(e) = \frac{A}{12\pi e^2}, \tag{2.9}$$

where A is the Hamaker constant (whose value can be negative or positive), which describes the molecular characteristics of the solid and liquid molecules.
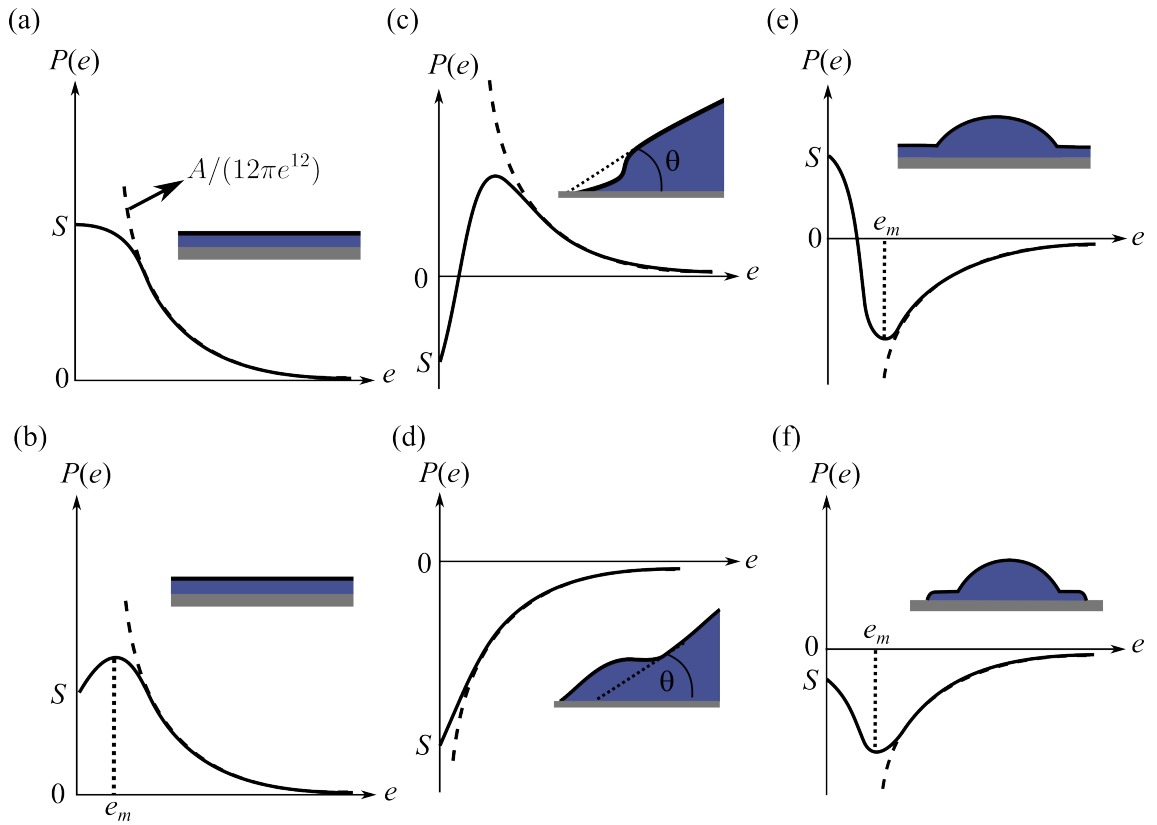
Figure 2.6: Different possible shapes of the effective interface potential, $P(e)$ for different wetting states: complete wetting ($S > 0$, $A > 0$) with (a) $P(e)$ decreases monotonically and (b) $P(e)$ has a maximum, partial wetting with (c) $S < 0$, $A > 0$ and (d) $S < 0$, $A < 0$ and pseudo-partial wetting with (e) $S > 0$, $A < 0$ and (f) $S < 0$, $A < 0$. The dashed lines show $P(e)$ modelled in Eq. (2.9). Sketches are adapted from [65].

Different possible shapes of the effective interface potential $P(e)$ are shown in Fig. 2.6 [45, 65]. For complete wetting situations, $S > 0$ and $A > 0$, and the functional dependency of $P(e)$

can be a decreasing function (Fig. 2.6 (a)) or have a maximum at $e = e_m$ (Fig. 2.6 (b)). For partial wetting situations, $S < 0$, and the Hamaker constant, A, can be positive or negative. For the former, the functional dependency of $P(e)$ has the shape illustrated in Fig. 2.6 (c). The droplet profile near the three-phase contact line would be hyperbolic and curved downward (see inset). For the latter, $P(e)$ increases monotonously and has no minimum (see Fig. 2.6 (d)). The droplet profile near the three-phase contact line would be hyperbolic and curved upward (see inset) [65].

Interestingly, another wetting state can be obtained due to these intermolecular liquid-solid interactions, termed pseudo-partial wetting [65]. In this wetting state, a droplet coexists with a thin film surrounding it. The functional dependency of $P(e)$ has a minimum at $e = e_m$ corresponding to the thin film thickness, as illustrated in Fig. 2.6 (e,f). The Hamaker constant, A, is negative, but the spreading parameter, S, can be positive or negative. For the former, the droplet has a finite contact angle, and the solid is completely coated with a thin film of thickness e_m, while for the latter, the droplet still has a finite contact angle, and the thin film has a finite contact area [65]. Several experiments [66, 67, 68, 69] have observed the existence of the pseudo-partial wetting state on a number of systems, such as brine-AOT/alkane/air, water/PDMS/air and water/alkane/air.

2.6   Capillary Imbibition and Hemiwicking

From the Wenzel state model discussed earlier, we can see that the surface roughness can enhance hydrophilicity. Patterning on a hydrophilic surface at a scale much smaller than the capillary length can induce superhydrophilicity. Another important consequence of surface roughness on a hydrophilic surface is wicking, the spontaneous liquid flow on textured surfaces driven by capillary action. The wicking dynamics depend strongly on the texturing of the surface. A special case of wicking is called hemiwicking, defined as the spreading of a liquid on a textured surface where the wetting of dry regions is accompanied by increased liquid-gas interfacial area.

Let us consider a solid surface textured with micropillars as illustrated in Fig. 2.7. Such a surface can be characterized by its pillar density φ_s (number of the pillars on a projected plane) and roughness factor r. For a liquid to imbibe the textured surface, the solid must lower its energy by being wet, such that $\gamma_{ls} < \gamma_{gs}$. The surface area of the solid that is coated by
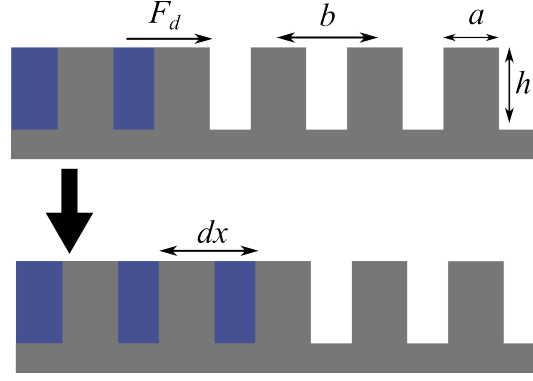
Figure 2.7: Illustration of the hemiwicking process through an array of micropillars with pillar diameter (side) a, spacing b and height h. Liquid driven by a force per unit length, F_d, imbibes the micropillar array by a distance dx.

liquid is proportional to $r - \varphi_s$, whereas the liquid-gas interface area is proportional to $1 - \varphi_s$. As the liquid imbibes the surface by a distance dx, the change of surface energy per unit length can be written as

$$dE = \{(\gamma_{\text{ls}} - \gamma_{\text{gs}})(r - \varphi_s) + \gamma_{\text{lg}}(1 - \varphi_s)\}\, dx. \tag{2.10}$$

The force per unit length that drives the hemiwicking can be derived from Eq. (2.10),

$$F_d = -\frac{dE}{dx} = \gamma_{\text{lg}}(r - \varphi_s)(\cos\theta - \cos\theta_c). \tag{2.11}$$

Hence, imbibition is favourable when the Young contact angle is smaller than the critical value, θ_c, which depends only on the geometry of the surface:

$$\cos\theta_c = \frac{1 - \varphi_s}{r - \varphi_s}, \tag{2.12}$$

which is called the wicking criterion [70]. The force in Eq. (2.11) is typically balanced by the viscous force due to the small scale of the textures. The viscous dissipation force is proportional to the average velocity of the propagation, viscosity, and propagation distance, $F_v \sim \mu\nu x$.

The classical analysis of capillary imbibition was initially done by Lucas [71] and Washburn [72]. Consider a liquid flowing in a cylindrical hydrophilic tube in contact with an infinite liquid reservoir with dynamic viscosity η at one end. The rate of capillary imbibition is then determined by the balance between the driving capillary forces and the resisting viscous forces. Following a simplified scaling law approach by Ishino *et al.* [73], the capillary force can be scaled as $\gamma_{\text{lg}}L$ where L is a length scale that produces the capillary effect (can be assumed as

Table 2.1: Theoretical models of propagation coefficient suggested in previous studies. Here, the geometrical parameters are a = pillar diameter, h = pillar height, and b = pillar spacing.

Reference	Propagation coefficient, D	Condition
Bico *et al.* [70]	$\frac{\gamma_{\mathrm{lg}} h}{\eta} \left(\frac{\frac{\pi a h}{b^2}}{1-\pi(a/b)^2/4} \right)$	-
Ishino *et al.* [73]	$\frac{\gamma_{\mathrm{lg}} b}{\eta} \left(\frac{h}{b} \right)^2$	$b \gg h$
	$\frac{\gamma_{\mathrm{lg}} b}{\eta} \left(\ln \left(\frac{2b}{a} \right) - 1.31 \right)$	$b \ll h$
Srivastava *et al.* [76]	$\frac{\gamma_{\mathrm{lg}}}{\eta} \left(\frac{a^{0.5} h^{0.17} (b-a)^{1.33}}{b(1-\pi(a/b)^2/4)} \right)$	-
Kim *et al.* [77]	$\frac{\gamma_{\mathrm{lg}} h}{\eta} \left(\frac{\frac{\pi a h}{b^2}}{1+\frac{\pi a h}{b^2}} \right)$	-
Kim *et al.* [75]	$\frac{\gamma_{\mathrm{lg}} h}{\eta} \left(\frac{\frac{\pi a h}{b^2}}{1+\frac{h}{b} \left(1+\frac{\pi a h}{b^2} \right)} \right)$	-

the tube radius) and the viscous force is scaled as $\eta x v$ where x is the imbibed length from the reservoir and $v = dx/dt$ is the mean velocity of the liquid. Balancing these forces results in the famous Washburn's law for x, which states that the length of imbibition increases as the square root of time:

$$x = (Dt)^{1/2}, \tag{2.13}$$

where $D \sim 2\gamma_{\mathrm{lg}} L/\eta$ is the propagation coefficient in the capillary imbibition (not to be confused with the spreading parameter, S) [74, 75].

The coefficient D derived above can only be valid for capillary imbibition in a cylindrical tube of smooth surfaces where D is determined by a single geometrical parameter, L. However, for capillary imbibition on structured surfaces, pillar dimensions and arrangements need to be taken into consideration [70, 73, 75, 76, 77]. Several theoretical models have been suggested to obtain a functional form of D by incorporating these geometrical parameters as tabulated in Table. 2.1.

An example of the applications of the hemiwicking is the flow of a fluid in microfluidics [78]. Microscopic flows the likes of in microfluidics usually occur in low Reynolds number (Re = $n\nu R/\eta$, where n, ν, R, and η are the density, typical velocity, length-scale, and viscosity of the system, respectively) and hence inertia can be neglected. In addition, the Bond numbers (Bo = $nh^2 g/\gamma_{\mathrm{lg}}$, where g is the acceleration due to the gravity and h is the pillar height)

are also small so that the gravitational force can be ignored [79]. The effect of the channel geometry is significant as, for a given pressure drop, the flow rate through a capillary changes with the fourth power of the radius in laminar flow [80]. This has been explored previously where the geometrical patterning is used to control the flow in the channels. For example, Zao *et al.* used hydrophilic stripes to confine the fluid flows [81]. Stroock *et al.* used oriented grooves to enhance mixing [82]. Kusumaatmaja *et al.* used a one-sided patterned wall with posts and ridges to show that the fluid flow is not only dependent on the geometry but also the spacing of the posts [74]. Blow *et al.* used triangular post shapes to show the anisotropic spreading occurs due to the pinning-depinning process [83].

CHAPTER 3

Objectives and Thesis Structures

3.1 Objectives

As a computational contribution to the study of wetting, we perform dynamic simulations of liquid on structured surfaces textured with arrays of various pillar geometries using state-of-the-art simulation methodologies developed in-house, namely the Lattice Boltzmann method. In addition, we also exploit the phase-field-based free energy minimisation simulation to study the static equilibrium properties of wetting on textured surfaces in nano- to micrometre scales. Furthermore, we develop a new ternary-based phase-field model, the Frozen Fluid Method, and implement it in the free energy minimisation simulation to enable us to study wetting phenomena on highly complex geometry surfaces.

The purpose of this thesis is to exploit these methods to understand some fundamental concepts of wetting on structured surfaces. In particular, we demonstrate and quantify several important aspects. As discussed in Chapter 2, previous studies have proposed theoretical predictions for the hemiwicking coefficient of liquid propagating on structured surfaces. However, they are only accurate under limited conditions. Furthermore, the breadth of applicability of certain models is restricted by the semianalytical or empirical nature of their approach. Let us take, for example, the models by Ishino *et al.* [73] and Srivastava *et al.* [76]. Ishino *et al.* identified two structural regimes in which dissimilar scaling behaviours were observed owing to different dominant dissipative phenomena. For short and long pillar heights, h, relative to the pitch, p, viscous friction was shown to be dominated by either the bottom surface ($h \ll p$) or the pillars ($h \gg p$) themselves, respectively. However, the boundaries between these regimes were not clarified, and a model describing the behaviour in the broad $h \approx p$ regime was lacking.

Srivastava *et al.* developed a semianalytical scaling model that used dimensional analysis and finite element (FE) simulations to estimate the viscous resistance around a single cylindrical pillar. While this approach is fruitful, the presented model is only valid for a specific pillar geometry and in the design space where multipillar effects are negligible. Therefore, in this thesis, we aim to build a predictive model that is simple and broadly applicable to textured surfaces that contain various pillar geometries, patterns and a relative dimension scale.

Computational study on wetting phenomena at the micro- to nanoscale is mostly done using atomistic simulations such as Molecular Dynamics and Density Functional Theory. Here, to the best of our knowledge, for the first time, the phase-field simulation will be used to study liquid filling and emptying on structured surfaces with the incorporation of short-range and long-range interactions. This is distinct from previous phase-field simulations, which typically treat wetting as a boundary condition at a solid surface and neglect long-range forces. We aim to explore the mechanism and behaviour of liquid filling and emptying on grooved surfaces and contrast them for complete, partial, and pseudo-partial wetting cases.

Finally, our last objective in this thesis is to study the wetting phenomena on highly complex geometries. To achieve this aim, we will develop a new method that enables us to construct highly complex geometry surfaces in the framework of the phase field simulation. This thesis then explores some fundamental aspects of the wetting phenomena, such as the wetting transition in superhydrophobic surfaces.

3.2   Thesis Structure

This thesis is organised as follows. Following the Introduction, Part II is devoted to discussing the hemiwicking on regularly and non-regularly patterned surfaces. It begins with a discussion of the computational method used in this work, the Lattice Boltzmann method, in Chapter 4, followed by presenting simulation results in Chapter 5. Here, theoretical models for predicting the propagation coefficient for both patterned surfaces are presented and validated.

Part III discusses the filling transition of thin liquid films on nano- and micro-structured surfaces. In Chapter 6, the energy minimisation method used to investigate the static equilibrium properties upon the variation in the pressure difference between the liquid and gas phases is discussed. In Chapter 7, the effects of the long-range potential on the liquid-solid interaction will be explored, in addition to the effects of the surface geometry on the filling transition.

Part IV discusses the wetting study of complex geometry surfaces using the frozen fluid method. In Chapter 8, the phase-field model for the frozen fluid method is discussed. This includes the formulation of the free energy functional and the implementation of the confining potentials. In Chapter 9, the parameterisation in the confining potential is verified, and the frozen fluid method is validated using several benchmarking tests. Several applications of the frozen fluid method are presented.

Finally, in Part V, we draw some conclusions in Chapter 10 and highlight avenues for future works in Chapter 11.

Part II

Hemiwicking Propagation on Textured Surfaces

Wicking is the spontaneous flow of liquid through an enclosed porous medium driven by capillary action [84]. It is an important surface science phenomenon critical to applications ranging from inkjet printing [85] to liquid hydrocarbon recovery [86]. While wicking broadly describes liquid propagation through a three-dimensional (3D) porous medium, hemiwicking is the spreading of a liquid on a textured surface where the wetting of dry regions is accompanied by the increase of the liquid air interfacial area [87, 88]. Interest in hemiwicking was kindled by early studies showing that the addition of texture to smooth substrates significantly enhanced the propagation rates of liquids [89, 90].

Recent advancements in nano-/micropatterning technology have enabled the fabrication of textures with tunable wettability and transport properties. These developments have enabled applications exploiting hemiwicking in thermal management [33], liquid-infused surfaces [19, 34], energy harvesting [91], and lab-on-a-chip devices [92, 93]. The patterned textures have also allowed the investigation of interesting flow behaviour such as zipping [94], anisotropic/polygonal spreading [95, 96], and large rise heights [97]. However, further utilization of fast hemiwicking dynamics in commercial applications requires a quantitative understanding of the role of complex liquid-solid interactions that dictate liquid propagation and wetting.

It is now well known that the flow through porous media follows the diffusive scaling law (Washburn's law), $x = (Dt)^{1/2}$, where x is the wicked distance, t is the time, and D is a propagation coefficient [72]. For flow through a cylindrical tube, D is a function of the diameter, a, given by $D = \gamma_{\text{lg}} a \cos\theta / 4\eta$, where γ_{lg} is the liquid-gas surface energy, θ is the equilibrium contact angle of the liquid on a smooth surface made from the same solid, and η is the liquid viscosity. However, for hemiwicking through a texture, D must be described by a more complex function involving at least three geometrical parameters (pitch, cross-sectional size, height).

There have been several efforts (Table. 2.1) to arrive at a functional form of D for hemiwicking by incorporating the geometric parameters of textured surfaces into models for capillary pressure and viscous resistance. Ishino *et al.* identified two structural regimes in which dissimilar scaling behaviours were observed owing to different dominant dissipative phenomena [73]. For short and long pillar heights, h, relative to the pitch, p, viscous friction was shown to be dominated by either the bottom surface ($h \ll p$) or the pillars ($h \gg p$) themselves, respectively. However, the boundaries between these regimes were not clarified, and a model describing the

behaviour in the broad $h \approx p$ regime was lacking. Srivastava *et al.* developed a semianalytical scaling model that used dimensional analysis and finite element (FE) simulations to estimate the viscous resistance around a single cylindrical pillar [76]. While this approach is fruitful, the presented model is only valid for a specific pillar geometry and in the design space where multipillar effects are negligible. Kim *et al.* have demonstrated models that capture the velocity scaling appropriately, but their models are found to require a fitting factor to match the measured D values [75]. While other hemiwicking models have been suggested, Kim *et al.* have demonstrated that these other models do not capture the scaling behaviour correctly [75]. In summary, previously suggested forms of the hemiwicking coefficient are only accurate under limited conditions. Additionally, the breadth of applicability of certain models is restricted by the semianalytical or empirical nature of their approach. A universal analytical model to accurately predict liquid propagation rates on patterned surfaces is thus far absent.

In this work, we seek to build a predictive model that is simple and broadly applicable to textured surfaces that contain various pillar geometries, patterns, and a relative dimension scale. Our model balances the capillary pressure, described previously by Quéré *et al.* [88], with the viscous resistance estimated by solving the Navier-Stokes equation for a rectangular channel. The size of the channel is appropriately selected to capture the frictional contribution of the array geometry. Our model provides an analytical expression that predicts the hemi-wicking coefficient for a wide range of textured geometries generated by micropillars. The final expression is validated using Lattice Boltzmann (LB) simulations to show that the present model is applicable over a much broader range of micropillar geometries compared to previously published models, albeit a completely general model is still absent for highly complex pillar arrangements.

CHAPTER 4

Method

A single-phase Lattice Boltzmann (LB) simulation is used to study the dynamic of hemiwicking of liquid on micropillar arrays. In order to predict the hemiwicking coefficient D, we do not explicitly simulate the hemiwicking dynamics but solve the flow profile for a unit cell of the micropillar arrays while implementing the appropriate boundary conditions. In this approach, we assume a flat meniscus and coplanarity between the meniscus and the tops of the micropillar. Moreover, in the long timescale limit (large liquid column), the wicking front meniscus can be ignored.

4.1 Fluid Hydrodynamics and the Boltzmann Equation

The hemiwicking dynamics can be described by relevant equations of motion, including the continuity equation (Eq. (4.1)), for mass conservation, and Navier-Stokes equation (Eq. (4.2)), for momentum conservation, [39]

$$\partial_t \rho + \partial_\beta \left(\rho u_\beta \right) = 0, \tag{4.1}$$

$$\partial_t \left(\rho u_\alpha \right) + \partial_\beta \left(\rho u_\alpha u_\beta \right) = -\partial_\alpha p + \partial_\beta \left[\eta \left(\partial_\beta u_\alpha + \partial_\alpha u_\beta \right) \right] + F_\alpha. \tag{4.2}$$

In these equations, ρ is the fluid density, u is the fluid velocity, η is the dynamic viscosity, p is the pressure, and F_α is the body force. The subscripts α and β denote the spacial indices, *e.g.* $\{x, y, z\}$ for the cartesian coordinates. The pressure term in the Navier-Stokes equation can be expressed in different forms depending on the choice of the equation of state (EOS) of the system and fluid-fluid interactions. In this work, we choose the equation of state for an

isothermal gas ideal, $p = \rho RT$, which is suitable for a single-phase system. The temperature in our system is assumed to be constant, $T \approx T_0$, and together with the specific gas constant, R, we can relate the pressure to the speed of sound, $c_s^2 = \sqrt{RT_0}$, to obtain $p = c_s^2 \rho$. The force term F_α in the Navier-Stokes equation comes from external forces, which can be in the forms of gravitational force, fluid-solid interaction or pressure difference, among others.

We solve these equations using an approach based on the Boltzmann equation, whereby we attribute the macroscopic fluid quantities to a set of distribution functions of position $\mathbf{x}$, velocity $\mathbf{c}$, and time t: $f(\mathbf{x}, \mathbf{c}, t)$. The distribution function $f(\mathbf{x}, \mathbf{c}, t)$ represents the mass density in both three-dimensional physical and three-dimensional velocity space at time t. Therefore, the fluid density at position $\mathbf{x}$ and time t, as in the continuity equation, can be expressed as the integral of the distribution function over the velocity space

$$\rho(\mathbf{x}, t) = \int f(\mathbf{x}, \mathbf{c}, t) \mathrm{d}^3 c. \tag{4.3}$$

Similarly, we can also express the momentum density in terms of the distribution function as

$$\rho(\mathbf{x}, t)\mathbf{u}(\mathbf{x}, t) = \int \mathbf{c} f(\mathbf{x}, \mathbf{c}, t) \mathrm{d}^3 c. \tag{4.4}$$

Notice that we differentiate the microscopic velocity $\mathbf{c}$ from the macroscopic fluid velocity $\mathbf{u}$.

The evolution of the distribution function $f(\mathbf{x}, \mathbf{c}, t)$ is governed by the Boltzmann equation, which is given by

$$\frac{\mathrm{d}f}{\mathrm{d}t} = \frac{\partial f}{\partial t} + c \cdot \nabla f + \frac{\mathbf{F}}{\rho} \cdot \frac{\partial f}{\partial \mathbf{c}} = \Omega(f). \tag{4.5}$$

The right-hand side of the Boltzmann equation is called the collision operator or the source term $\Omega(f)$, which describes changes to the local distribution of f due to collisions. This operator is a crucial term in the Boltzmann equation, as it informs the rate at which collisions redistribute particles between velocities in the distribution function. The choice of the collision operator must conserve mass and momentum during the collision. We shall discuss in more detail about this operation in the next section.

We can recover the continuity and Navier-Stokes equations from the Boltzmann equation. For instance, if we integrate the Boltzmann equation over the velocity space, we will recover

the continuity equation, as the following

$$\frac{\partial}{\partial t} \int f \mathrm{d}^3 c + \nabla \cdot \int \mathbf{c} f \mathrm{d}^3 c + \frac{\mathbf{F}}{\rho} \cdot \int \frac{\partial f}{\partial \mathbf{c}} \mathrm{d}^3 c = \int \Omega(f) \mathrm{d}^3 c \tag{4.6a}$$

$$\frac{\partial \rho}{\partial t} + \nabla \cdot (\rho \mathbf{u}) = 0. \tag{4.6b}$$

Here, the last term on the left-hand side and the term on the right-hand side in Eq. (4.6a) vanish due to mass conservation. Although the continuum Boltzmann equation can directly describe the continuity equation, solving it analytically coupled with the Navier-Stokes equation is only possible for simple cases. Therefore, we use a numerical method that discretizes the Boltzmann equation into lattice nodes called the Lattice Boltzmann (LB) method.

4.2 Lattice Boltzmann Method

The LB method discretizes the space, time and velocity into a square (or cubic) lattice in 2-dimensional (or 3-dimensional) computational domain. The Boltzmann equation can be written as

$$\frac{\mathrm{d}f}{\mathrm{d}t} = \Omega(f) \rightarrow \frac{f_i(\mathbf{x} + \mathbf{c}_i \Delta t, t + \Delta t) - f_i(\mathbf{x}, t)}{\Delta t} = \Omega(\mathbf{x}, t). \tag{4.7}$$

The time and space steps are usually taken as $\Delta t = 1$ and $\Delta x = 1$ in lattice units, respectively. The velocity vector $\mathbf{c}_i$ consists of discrete velocities whose values depend on the choice of lattice domain. In the LB method, a lattice domain is usually denoted as $\mathbf{DdQq}$, where $\mathbf{d}$ is the number of dimensions and $\mathbf{q}$ is the number of discretised velocities $\mathbf{c}_i$ coupled with the weight w_i. In this work, we use D3Q19 lattice domain. The set of velocities $\mathbf{c}_i$ is illustrated in Fig. 4.1, and their magnitudes are given by

$$\mathbf{c}_0 = 0 \qquad\qquad |\mathbf{c}_{1-6}| = 1 \qquad\qquad |\mathbf{c}_{7-18}| = \sqrt{2}. \tag{4.8}$$

The collision factor $\Omega(\mathbf{x}, t)$ can take different forms. The simplest form is the so-called Bhatnagar-Gross-Krook (BGK) operator, named after its inventors. The BGK operator is written as

$$\Omega_i(f) = -\frac{1}{\tau}(f_i - f_i^{\mathrm{eq}}), \tag{4.9}$$

where τ is the relaxation time and f_i^{eq} is the equilibrium distribution function. The collision
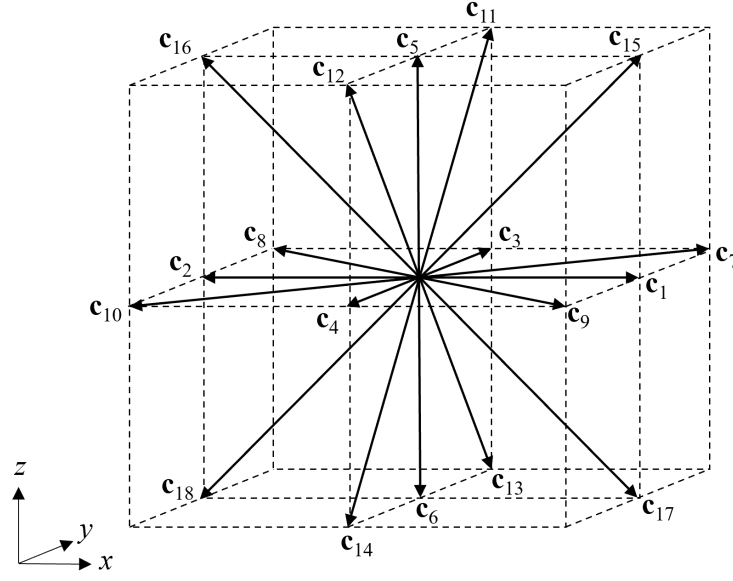
Figure 4.1: Directions of the lattice velocity vectors in D3Q19 model.

factor is essentially used to relax the distribution function f_i to an equilibrium value f_i^{eq} at relaxation time τ. The equilibrium functions f_i^{eq} must be chosen appropriately so that the system's mass and momentum are conserved. In this work, we use an equilibrium function as a power series in the fluid and lattice velocities, written as [39]

$$f_i^{\mathrm{eq}} = w_i \rho \left(1 + \frac{\mathbf{u} \cdot \mathbf{c}_i}{c_s^2} + \frac{(\mathbf{u} \cdot \mathbf{c}_i)^2}{2c_s^4} - \frac{\mathbf{u} \cdot \mathbf{u}}{2c_s^2} \right), \tag{4.10}$$

for $i \neq 0$, and

$$f_0^{\mathrm{eq}} = \rho - \sum_{i \neq 0} f_i^{\mathrm{eq}}, \tag{4.11}$$

for $i = 0$. Here, c_s is the speed of sound, which takes the value of $1/\sqrt{3}$ in lattice units. The weights w_i are associated with the vector velocities. Their values are then dependent on the lattice domain. In the D3Q19 lattice domain, the values of w_i are

$$w_0 = \frac{1}{3} \qquad\qquad w_{1-6} = \frac{1}{18} \qquad\qquad w_{7-18} = \frac{1}{36}, \tag{4.12}$$

where the indices correspond to the vector velocity indices. Using this BGK operator, the Boltzmann equation can be rewritten as

$$f_i(\mathbf{x} + \mathbf{c}_i \Delta t, t + \Delta t) - f_i(\mathbf{x}, t) = -\frac{\Delta t}{\tau}(f_i - f_i^{\mathrm{eq}}). \tag{4.13}$$

Next, we also need to describe the macroscopic quantities, such as density, velocity and force, in terms of the distribution functions. Writing down the density and velocity is rather straightforward as they are directly related to the distribution functions as in Eq. (4.3) and in Eq. (4.4), respectively. They can then be discretised as

$$\rho = \sum_i f_i, \tag{4.14}$$

$$\mathbf{u} = \frac{1}{\rho} \sum_i \mathbf{c}_i f_i. \tag{4.15}$$

The forcing term F_α, however, is treated differently as it does not appear as an isolated term in Eq. (4.5). It has to be discretised as a full term $\frac{\mathbf{F}}{\rho} \cdot \frac{\partial f}{\partial \mathbf{c}}$. There are several methods, usually called forcing schemes, to incorporate the force term F_α in the LB method. We use the so-called Guo forcing scheme, which discretises the force term in velocity and space-time. Using this method, the Boltzmann equation is rewritten as

$$f_i(\mathbf{x} + \mathbf{c}_i \Delta t, t + \Delta t) - f_i(\mathbf{x}, t) = -\frac{\Delta t}{\tau}(f_i - f_i^{\text{eq}}) + (1 - \frac{\Delta t}{2\tau})F_i \Delta t, \tag{4.16}$$

where

$$F_i = w_i \left(\frac{\mathbf{c}_i - \mathbf{u}}{c_s^2} + \frac{(\mathbf{u} \cdot \mathbf{c}_i)\mathbf{c}_i}{c_s^4} \right) \cdot \mathbf{F}. \tag{4.17}$$

It is worth noting that the forcing term should not add the mass density but instead contribute to the momentum. Therefore, the velocity has to be redefined as

$$\mathbf{u} = \frac{1}{\rho} \sum_i \mathbf{c}_i f_i + \frac{\mathbf{F} \Delta t}{2\rho}. \tag{4.18}$$

Another macroscopic quantity that also appears in the Navier-Stokes equation is the dynamic viscosity η. This quantity can be related to the Boltzmann equation through the BGK operator. The dynamic viscosity is given by

$$\eta = \rho c_s^2(\frac{\tau}{\Delta t} - \frac{1}{2}), \tag{4.19}$$

where ρc_s^2 is the gas ideal pressure. It is worth noting that the gradient of the ideal gas pressure also appears in the Navier-Stokes equation in Eq. (4.2). This suggests that the fluid in the LB method is compressible.

4.2.1   Lattice Boltzmann Method Implementation

The LB method calculates the evolution of the distribution function through the Boltzmann equation. At each time step, the evolution is decomposed into two steps: a collision step and a streaming step. This can numerically be expressed as

$$\text{Collision} : f_i^*(\mathbf{x}, t) = f_i(\mathbf{x}, t) - \frac{\Delta t}{\tau}(f_i - f_i^{\text{eq}}) + (1 - \frac{\Delta t}{2\tau})F_i \Delta t, \tag{4.20}$$

$$\text{Streaming} : f_i(\mathbf{x} + \mathbf{c}_i \Delta t, t + \Delta t) = f_i^*(\mathbf{x}, t). \tag{4.21}$$

The collision step evolves the distribution functions f_i into a new distribution function after collision f_i^* using the BGK collision operator and the forcing term. The resulting post-collision distribution function f_i^* is then streamed to the neighbouring lattice point in the streaming step. The illustration of these steps is shown in Fig. 4.2.

| t: Streaming | t: Pre-collision | $t+\Delta t$: Collision | $t+\Delta t$: Streaming |
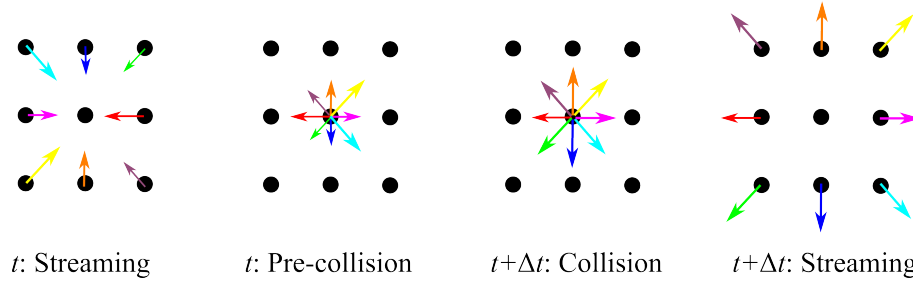
Figure 4.2: An illustration of the collision and streaming steps for a 2-dimensional lattice. Each arrow with different colours indicates f_i. At time t, f_i is streamed to a central node and is used to compute f_i^{eq} and f_i^* at the collision step. The new values of f_i^* are then streamed to the neighbouring nodes at the next streaming step at $t + \Delta t$.

In general, the LB algorithm is as follows.

1. Determine the force density $\mathbf{F}$ for each time step.

2. Compute the fluid density (Eq. (4.14)) and velocity (Eq. (4.18)).

3. Compute the equilibrium distribution function f_i^{eq}.

4. If desired, output the macroscopic quantities such as ρ and $\mathbf{u}$.

5. Compute the forcing term $(1 - \frac{\Delta t}{2\tau})F_i \Delta t$.

6. Apply the collision and forcing term to find the post-collision distribution function f_i^*.

7. Stream f_i^*.

8. Increment the time step and return to step 1.

4.2.2 Boundary Conditions

So far, we have laid down the foundation of the LB simulation. Another ingredient to solving the equations of motion is to apply proper boundary conditions. There are several boundary conditions applied in our simulations. One part is related to the presence of the solid (or wall), and another is related to the treatment at the inlet (one end of the simulation window where the liquid enters the system) and the outlet (another end of the simulation window where the liquid leaves the system).

4.2.2.1 Wall Boundary Conditions: No-Slip and Free-Slip

No-slip boundary condition. It assumes that the fluid velocity at the solid boundary is the same as the velocity at the solid boundary. It means that for a resting wall, the fluid velocity at the solid boundary is zero. We implement this condition using the half-way bounce-back (BB) method. The idea behind this method is that distribution functions streaming toward a solid node meet the solid boundary midway between lattice nodes and are swapped to the original node, as demonstrated in Fig. 4.3. For these distribution functions, the standard streaming step is replaced by

$$f_{\bar{i}}(\mathbf{x}, t + \Delta t) = f_i^*(\mathbf{x}, t), \tag{4.22}$$

where $\bar{i}$ denotes the opposite direction of i.
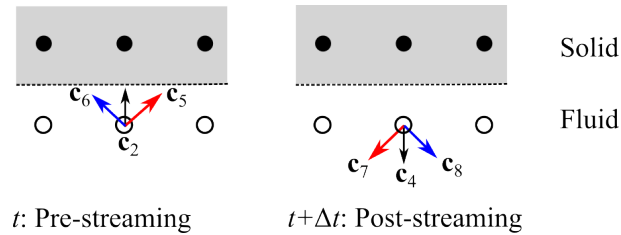
Figure 4.3: An illustration of half-way bounce back method for a 2-dimensional (D2Q9) lattice domain. Solid and boundary nodes are coloured black and white, respectively. The arrows show the directions of the distribution functions.

Free-slip boundary condition. It enforces a zero normal fluid velocity, $u_n = 0$, but does not restrict the tangential fluid velocity. It means that the distribution function pointing toward the normal direction of the wall is reflected as in the bounce-back rule, whereas the others are reflected specularly, resulting in the distribution functions being streamed to their neighbours, as illustrated in Fig. 4.4. For these distribution functions, the standard streaming step is
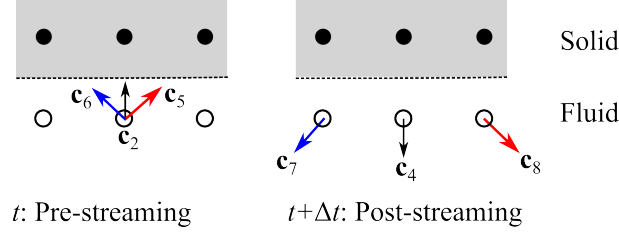
Figure 4.4: An illustration of the free-slip boundary condition for a 2-dimensional (D2Q9) lattice domain. Solid and boundary nodes are coloured black and white, respectively. The arrows show the directions of the distribution functions.

replaced by

$$f_j(\mathbf{x} + \mathbf{c}_{j,\mathrm{t}}\Delta t, t + \Delta t) = f_i^*(\mathbf{x}, t), \qquad (4.23)$$

where the $\mathbf{c}_{j,\mathrm{t}} = \mathbf{c}_{i,\mathrm{t}}$ is the tangential velocity of the distribution functions, equalling $\mathbf{c}_i$ and $\mathbf{c}_j$ with their normal velocity set to zero.

4.2.2.2 Inlet-outlet Boundary Conditions

It is sometimes desirable to simulate just a portion of the system to reduce the size of a simulation. For this purpose, the system's boundary conditions must be chosen carefully to satisfy the original system intended to simulate. The most common boundary condition used in LB simulations is the periodic boundary condition. In this method, the distribution functions leaving the simulation domain during the streaming step will re-enter the simulation domain from the opposite side. This boundary condition is suitable when simulating a repeating flow pattern in the system. In this work, we use the periodic boundary condition when the flow is driven by a body force.

The implementation of periodic boundary conditions in the LB method is straightforward [39]. During the streaming step, the unknown incoming distribution functions, f^* on one side are given by those leaving the domain at the opposite site:

$$f_i^*(\mathbf{x}, t) = f_i^*(\mathbf{x} + \mathbf{L}, t), \qquad (4.24)$$

where the vector $\mathbf{L}$ is the periodicity direction and length of the flow pattern. The illustration of the periodic boundary condition for the 2D flow is shown in Fig. 4.5. At the inlet, the missing distribution functions are f_1^*, f_5^* and f_8^*, whereas at the outlet f_3^*, f_6^* and f_7^*. the
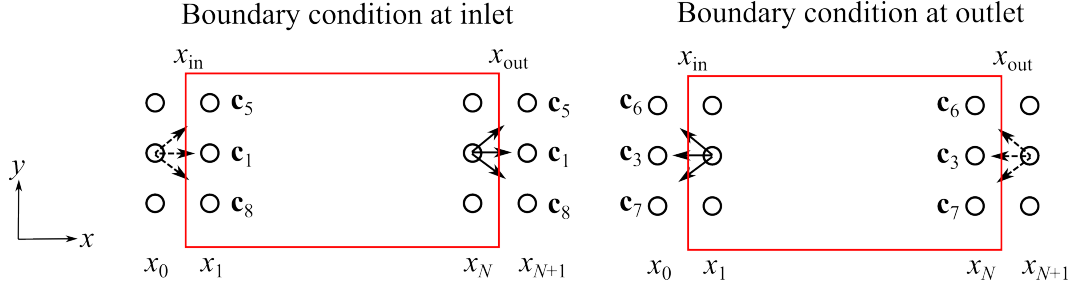
Figure 4.5: Illustration of the periodic boundary condition at the inlet and outlet for a 2-dimensional (D2Q9) lattice domain. Layers of "virtual" nodes are added before and after the periodic boundaries, i.e. at $x_0 = x_1 - \Delta x$ and $x_{N+1} = x_N + \Delta x$, respectively. The dashed arrows show the missing distribution functions after the streaming step.

periodic condition along the x-axis becomes

$$f_i^*(\mathbf{x}, t) = f_i^*(\mathbf{x} + \mathbf{L}, t) \Rightarrow \begin{cases} f_1^*(x_0, t) = f_1^*(x_N, t) \\ \\ f_5^*(x_0, t) = f_5^*(x_N, t) \\ \\ f_8^*(x_0, t) = f_8^*(x_N, t) \end{cases} \tag{4.25}$$

$$f_i^*(\mathbf{x} + \mathbf{L}, t) = f_i^*(\mathbf{x}, t) \Rightarrow \begin{cases} f_3^*(x_{N+1}, t) = f_3^*(x_1, t) \\ \\ f_6^*(x_{N+1}, t) = f_6^*(x_1, t) \\ \\ f_7^*(x_{N+1}, t) = f_7^*(x_1, t) \end{cases} \tag{4.26}$$

It is worth noticing here that we have added an additional layer of "virtual" nodes before and after the periodic boundaries at $x_0 = x_1 - \Delta x$ and $x_{N+1} = x_N + \Delta x$, respectively, for computational convenience rather than being part of the simulated physical system.

Another inlet-outlet boundary condition that we also consider in this work is the pressure boundary condition. This is one type of open boundary condition in which a specific pressure (density) value is imposed at the inlet and outlet to give a pressure difference along the flow. We use this boundary condition for cases where the flow is driven by a constant pressure gradient.

The pressure boundary conditions can be implemented by prescribing the density as a specific value at the inlet and assigning the density using average-velocity convective boundary conditions at the outlet [98, 99]. The schematic of the pressure boundary condition is illustrated in Fig. 4.6. The distribution functions pointing into the fluid will be missing after the streaming
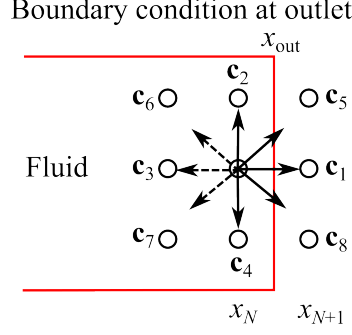
Figure 4.6: Illustration of the boundary condition at the outlet for D2Q9 lattice domain. Dashed arrows denote the missing distribution functions after the streaming step.

step. We follow the method introduced by Zou-He [100] for the computation of the missing distribution functions, f_i and the fluid velocity at the boundary.

Let the pressure (density) and the transverse velocity at the outlet be specified (e.g. $\rho = \rho_{\text{out}}$ and $u_y = 0$). After the streaming, f_1, f_2, f_4, f_5, f_8 are known and f_3, f_6, f_7 are missing. From the expressions of density and velocity in Eq. (4.14) and Eq. (4.15), we can calculate the velocity in terms of the known values:

$$u_x = 1 - \frac{f_0 + f_2 + f_4 + 2(f_1 + f_5 + f_8)}{\rho_{\text{out}}}.$$

(4.27)

We then assume the bounce-back rule applies for the non-equilibrium part of the distribution functions normal to the outlet to find $f_3 - f_3^{\text{eq}} = f_1 - f_1^{\text{eq}}$. We can then find the missing distribution functions:

$$f3 = f_1 - f_1^{\text{eq}} + f_3^{\text{eq}},$$

(4.28)

$$f6 = f_5 - \frac{1}{2}(f_2 - f_4 + f_1^{\text{eq}} - f_3^{\text{eq}} - \rho_{\text{out}} u_x),$$

(4.29)

$$f7 = f_8 - \frac{1}{2}(f_4 - f_2 + f_3^{\text{eq}} - f_1^{\text{eq}} - \rho_{\text{out}} u_x).$$

(4.30)

Having the missing distribution functions found, the usual collision step should then be applied.

4.3   Benchmarking

To validate the Lattice Boltzmann method, we simulate a steady fluid flow (a Poiseuille flow) in a 2-dimensional domain of $N_x \times N_y$, with $N_x = N_y = 102$ in simulation units (s.u.). The fluid propagates in the x-direction between two parallel plates separated by h along the y-axis,

as illustrated in Fig. 4.7 (a). As for the driving force for the fluid flow, we compare two cases: 1) an external body force, F_x, and 2) a constant pressure gradient, $\frac{\partial p}{\partial x}$. Both driving forces are applied in the x-direction.

Assuming the flow only has an x component (i.e. $u_z = 0$), the equation of motion of the Poiseuille flow is described by the Navier-Stokes equation:

$$-\frac{F_x}{\eta} = \frac{\partial^2 u_x}{\partial y^2}, \tag{4.31}$$

for the external body force-driven flow, and

$$-\frac{\partial p}{\partial x}\frac{1}{\eta} = \frac{\partial^2 u_x}{\partial y^2}, \tag{4.32}$$

for the constant pressure gradient-driven flow. Here, η is the fluid dynamic viscosity. Based on the system criteria given in Fig. 4.7 (a), the equation must satisfy two boundary conditions: Dirichlet (no slip velocity) condition at the bottom wall, $u_x(y = 0) = 0$ and a Neumann (free-slip velocity) condition at the top wall, $\frac{\partial u_x}{\partial y}\big|_{y=h} = 0$. Applying these boundary conditions to Eqs. (4.31) and (4.32) leads to

$$u_x(y) = -\frac{F_x}{2\eta}y(y - 2h), \tag{4.33}$$

$$u_x(y) = -\frac{1}{2\eta}\frac{\Delta p}{x_{\text{out}} - x_{\text{in}}}y(y - 2h), \tag{4.34}$$

for the external force and constant pressure gradient-driven flows, respectively. From these expressions, we can relate the body force to pressure difference by the relation: $\Delta p = F_x(x_{\text{out}} - x_{\text{in}})$. Here, $x_{\text{out}} - x_{\text{in}} = N_x - 1$ is the distance between the inlet and outlet.

In the LB simulations, a free-slip boundary condition is applied on the top wall, allowing the fluid to flow at the top wall, whereas a no-slip boundary condition is applied on the bottom wall, making the fluid have zero velocity at the bottom wall. For the case where the flow is driven by an external body force, periodic boundary conditions are applied in the x-direction. Here, we use a gravitational force, $F_x = \rho g$, where ρ is the fluid density and g is the gravitational acceleration. When the flow is driven by a constant pressure gradient, pressure boundary conditions are employed. This is done by setting the fluid densities at the inlet and outlet using $\rho_{\text{in}} = \rho_0 + \frac{\Delta \rho}{2}$ and $\rho_{\text{out}} = \rho_0 - \frac{\Delta \rho}{2}$, respectively. The fluid density difference, $\Delta \rho$, is related to the pressure difference through $\Delta \rho = \Delta p / c_s^2$ and can be calculated from the body
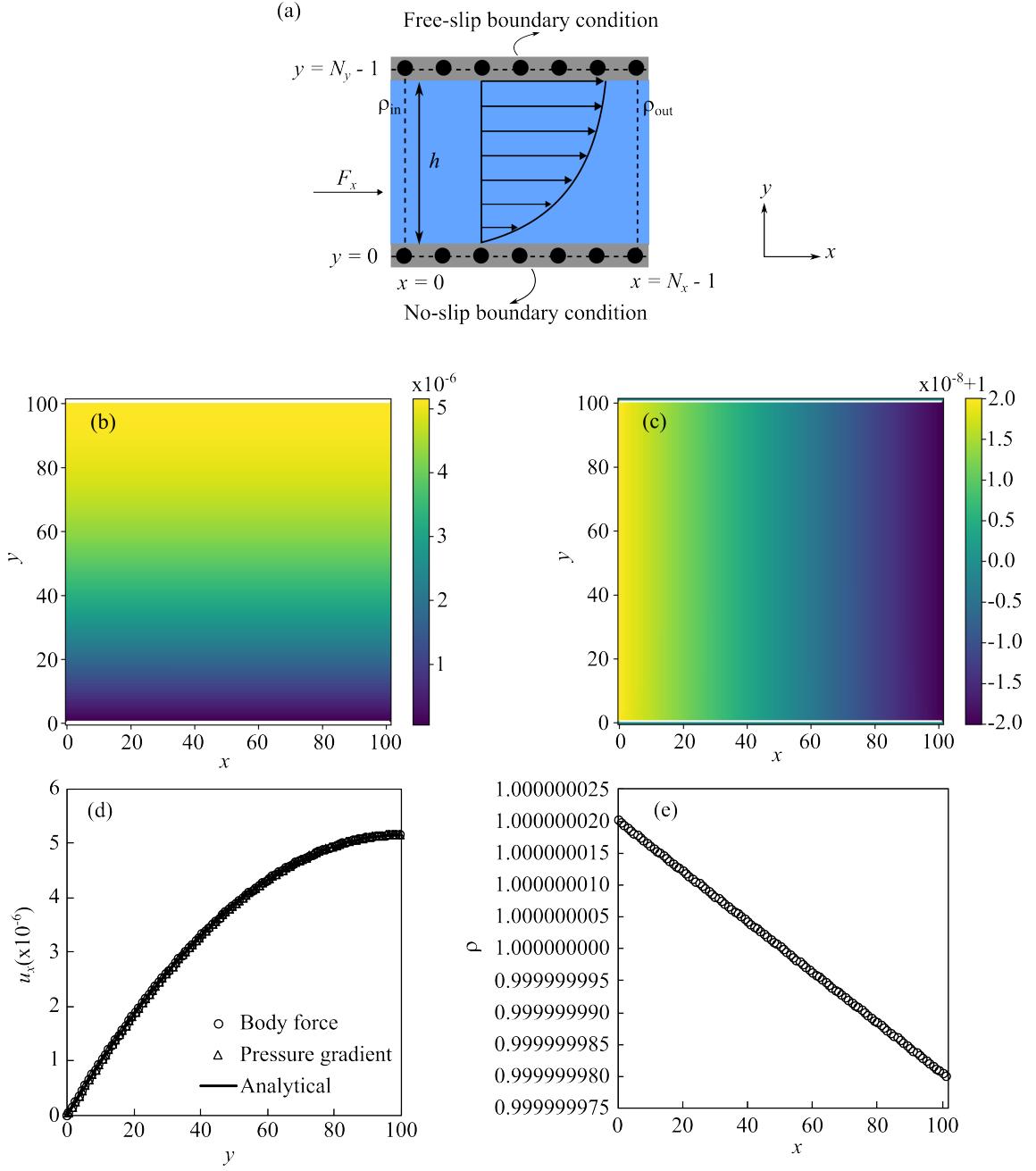
Figure 4.7: (a) Schematic diagram of a 2-dimensional Poiseuille flow between two parallel plates. (b) Contour plot of the simulated liquid velocity profile obtained for both external force and pressure gradient cases. (c) Contour plot of the simulated fluid density profile obtained for the pressure gradient case. (d) Comparison between liquid velocity in the x-direction along the y-axis obtained from simulations using external force and constant pressure gradient and predicted by Eq. (4.33). (e) Plot of the simulated density profile along the x-direction for the simulation using the constant pressure gradient.

force via $\Delta\rho = F_x(x_{\text{out}} - x_{\text{in}})/c_s^2$. We use these parameters in the simulations for both cases (otherwise stated): $c_s^2 = 1/3$, $\tau = 1$, $\eta = 1/6$, $F_x = 1.32 \times 10^{-10}$ (for the external force case and used in the constant pressure gradient case for calculating $\Delta\rho$), $\rho_0 = 1$ (for the constant pressure gradient case). All values are given in simulation units.

It should be noted here that we use a link-wise boundary mode where, at the liquid-solid boundaries, the physical boundary lies between the fluid nodes and the solid nodes. In Fig. 4.7 (a), we illustrate this condition by assigning the first node ($y = 0$) and the last node ($y = N_y - 1$) in the y-direction as solid. Therefore, the physical liquid-solid boundaries are at $y = 0.5$ and $y = N_y - 1.5$ at the bottom and top walls, respectively.

The simulated velocity profile of liquid obtained by using either the external force or the constant pressure gradient is shown in Fig. 4.7 (b). The velocity is constant in the x-direction, but its value increases in the y-direction. The increasing of the velocity as a function of the fluid position in the y-direction is plotted in Fig. 4.7 (d). We show that our simulation results, either using the external force or the constant pressure gradient, are in excellent agreement with the analytical solution giving evidence for the accuracy of our simulation. Furthermore, we plot the density profile of the liquid when using the constant pressure gradient and its variation along the x-direction at $y = 50$, in Fig. 4.7 (c) and (e), respectively. We can clearly see that ρ varies linearly along x-direction, proving that the pressure gradient is constant.

4.4   Simulation Setup

In this work, we simulate fluid flow profiles in 3-dimensional unit cells of square and face-centred/hexagonal micropillar arrays. The geometries of a unit cell of these arrays are illustrated in Fig. 4.8 (a). The micropillars have a diameter a, height h, and pitch length, which is the side length of the unit cell, b. The boundary conditions used in the simulations are shown in Fig. 4.8 (b). In the flow direction, we apply inlet-outlet boundary conditions. Periodic boundary conditions are applied on the sides of the unit cell. A no-slip boundary condition is applied at the liquid-solid interface using a bounce-back boundary condition. A free-slip boundary condition is employed to represent the liquid-gas interface at the upper boundary of the unit cell. We should note here that the geometries used in the simulation are constructed using a staircase approximation. This may affect the accuracy of the simulated area and volume compared to the expected values, particularly for the cylindrical pillars.
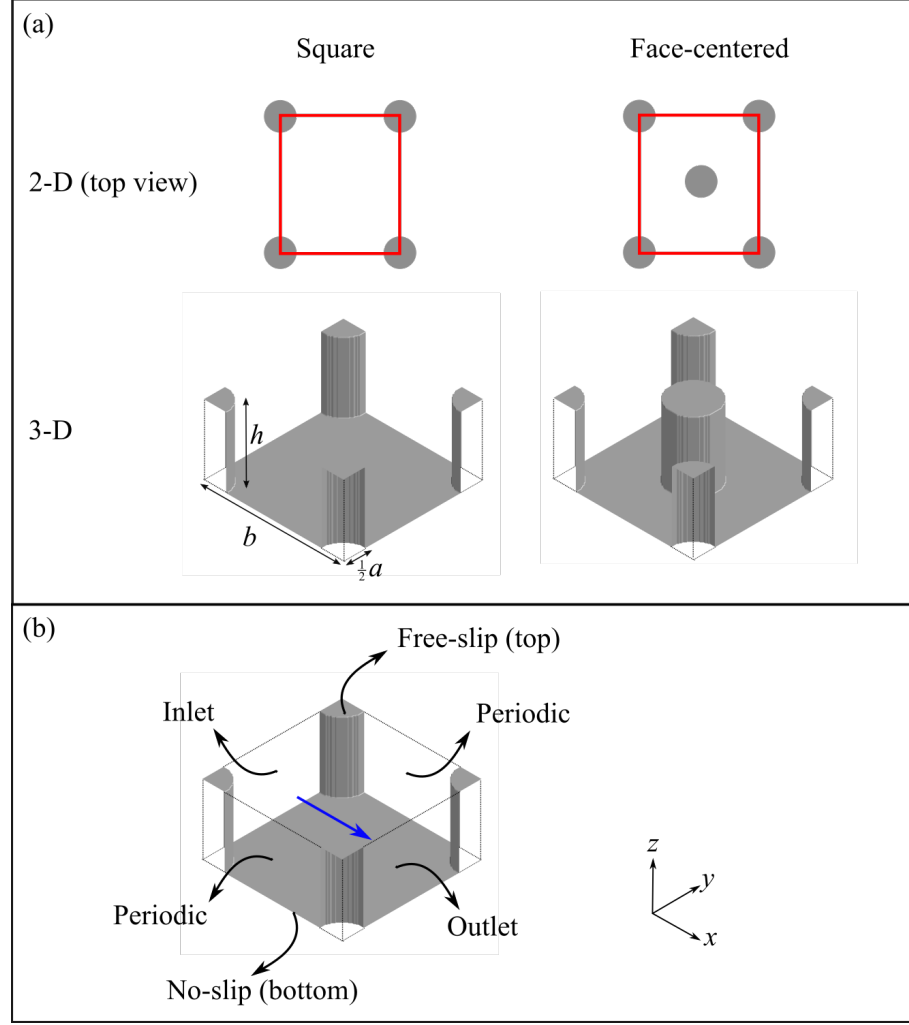
Figure 4.8: (a) Geometrical illustration of a unit cell of square and face-centred micropillar arrays. (b) Boundary conditions of the simulation: inlet-outlet in the x-direction, periodic in the y-direction, no-slip at the bottom and free slip at the top. The blue arrow indicates the flow direction.

The physical value of the parameters used in the simulations is tabulated in Table. 4.1. Here, we use different liquids with a wide range of viscosity and surface tension. For example, in our list of liquids, the least viscous liquid is water ($\gamma = 72$ mN/m and $\eta = 1$ mPa.s), and the most viscous one is silicone oil ($\gamma = 33.99$ mN/m and $\eta = 39.4$ mPa.s). This will ensure that our study applies to a wide range of liquids. We also use different sizes of micropillars and unit cells to see whether our study is valid for a wide range of micropillar dimensions. Note that we also use one square array of square micropillars. In this case, the diameter refers to the side of the square. These physical values are then converted into simulation units.

Table 4.1: Parameter values used in the study for square array cases.

	Pillar Shape	Contact Angle (°)	Height (μm)	Diameter (μm)	Pitch (μm)	Viscosity (mPa s)	Surface Tension (mN/m)
1	Cylinder	18	0.75	0.275	1	39.4	33.99
2	Cylinder	18	2	0.3	1	39.4	33.99
3	Cylinder	0	14	2.6	10	97	20
4	Cylinder	0	10	2.6	10	9.5	20
5	Cylinder	0	6	2.6	10	9.5	20
6	Cylinder	0	10	2.6	10	19	20
7	Cylinder	0	26	2.6	10	19	20
8	Cylinder	0	26	2.6	10	9.5	20
9	Cylinder	0	26	2.6	10	97	20
10	Cylinder	0	14	2.6	10	19	20
11	Cylinder	0	14	2.6	10	4.6	20
12	Cylinder	0	8.3	2.82	8.1	1	72
13	Cylinder	38	8.3	2.9	5.5	1	72
14	Cylinder	10	17	5	20	1	72
15	Cylinder	25.6	26	10	40	18	48
16	Cylinder	0	26	10	40	1.3	72.8
17	Square	5	7	10	20	3	26.6
18	Cylinder	0	26	10	40	18	48

CHAPTER 5

Results

5.1 Hemiwicking Propagation on Square Arrays of Micropillars

5.1.1 Model Development

We begin by developing a theoretical model to predict the dynamics of hemiwicking of liquid into an array of micropillars through the propagation coefficient, D. The model was originally developed by Natarajan, *et al.* in Ref. [32], where the model was used to predict the hemiwicking of liquid in square arrays of micropillar. I contributed to this work by benchmarking the model against the Lattice Boltzmann simulations. We further develop this model to be applied in face-centred/hexagonal arrays.

Let us consider a square array with cylindrical micropillars having diameter a, height h, and pitch length b as illustrated in Fig. 5.1 (a). We can define some textured surface parameters, such as the roughness r, which is the ratio of the actual surface area to the projected 2-dimensional area, and the dry fraction φ_s, defined as the ratio of the top surface of the pillar to the projected area. For a cylindrical micropillar on a square unit cell, these parameters are given as

$$r = \frac{A_r}{A_p} = \frac{(b^2 + \pi a h)}{b^2}, \tag{5.1}$$

$$\varphi_s = \frac{A_t}{A_p} = \frac{\pi a^2}{4b^2}, \tag{5.2}$$

where A_r is the actual surface area, A_p is the projected 2-dimensional area, and A_t is the surface area of the top of the pillar. By definition, the top of the pillars remains dry in the

purely imbibed state. When such an array is brought into contact with a liquid reservoir, the imbibition of liquid is energetically favourable when the wetting energy of the dry part of the array is greater than the wetted part. This can be mathematically formulated in terms of the interfacial energy change of the propagation of liquid by a distance dx

$$\mathrm{d}E = E_\mathrm{wet} - E_\mathrm{dry} \tag{5.3}$$

$$= (\gamma_\mathrm{ls} - \gamma_\mathrm{gs})(r - \varphi_s)\mathrm{d}x + \gamma_\mathrm{lg}(1 - \varphi_s)\mathrm{d}x, \tag{5.4}$$

where γ_ls, γ_gs, and γ_lg are the liquid-solid, gas-solid and liquid-gas interfacial energies, respectively. For the imbibition to occur, $\mathrm{d}E \leq 0$. Using Young's equation, this leads to a criterion which allows the imbibition to occur, known as the wicking criterion [101]

$$\cos\theta \geq \cos\theta_c = \frac{1 - \varphi_s}{r - \varphi_s}, \tag{5.5}$$

where θ is the equilibrium contact angle of the liquid on a smooth surface and θ_c is the critical contact angle, which is defined by the texture geometry. Hemiwicking is favoured for all inherent contact angles smaller than θ_c. It is worth noting that our model assumes a flat liquid meniscus and coplanarity between the meniscus and the top of the pillar. For superhydrophilic substrates ($\theta = 0°$), the liquid will wet the top of the pillars at equilibrium. However, the velocity of the wicking front far exceeds the rate of spreading of a liquid film on the tops of the pillars. Therefore, we can consider the tops of the pillars as being dry in our calculations. For any surface with texture, $r > 1$ and $\varphi_s < 1$. Thus, θ_c is between $0°$ (i.e. the critical contact angle for spreading on a flat plane, $r \rightarrow 1$) and $90°$ (i.e. the critical contact angle for wicking in porous media, $r \rightarrow \infty$).

In hemiwicking, the Reynolds and Bond numbers are small, hence the inertial effects and gravitational forces can be ignored. Therefore, when the wicking criterion in Eq. (5.5) is satisfied, the rate of imbibition of liquid into the array is given by the balance between the driving capillary pressure (Δp_L) and a resisting viscous force per unit area (Δp_V). The capillary pressure is the change of energy per unit volume of liquid imbibed and is given by [70]

$$\Delta p_L = \frac{\gamma_\mathrm{lg}}{h}\left(\frac{\cos\theta - \cos\theta_c}{\cos\theta_c}\right). \tag{5.6}$$

It can be seen here that the capillary pressure is only positive when $\theta \leq \theta_c$, which is in agreement
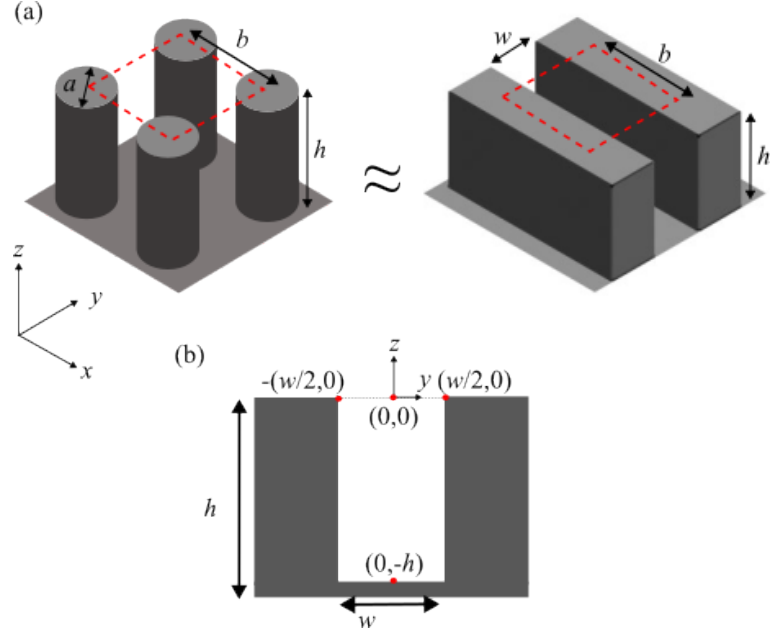
Figure 5.1: (a) Illustration of a square array of cylindrical micropillars with diameter a, pitch b and height h showing a unit cell (indicated by dashed red lines) used in our simulation and its equivalent unit cell of a microchannel. The channel width (w) is modified to ensure that the volume of liquid containing the unit cell areas is identical. (b) Side view of the approximated unit cell showing a schematic of the coordinate system that is used to derive the flow profile.

with the wicking criterion. The viscous dissipation force per unit area can be estimated from a modification to the classical Poiseuille flow for a liquid film of thickness, h, flowing on a flat surface, given by [70]

$$\Delta p_V = \frac{3\eta u x}{h^2}\beta, \tag{5.7}$$

where u is the average velocity of propagation ($\mathrm{d}x/\mathrm{d}t$), η is the viscosity of the liquid, and β is a correction factor due to the surface roughness. Here, h is the same as the pillar height and the top of the liquid volume is pinned to the top edge of the pillar during hemiwicking. It is well known that the displacement of the wicking front with time follows Washburn's law

$$x = (Dt)^{1/2}, \tag{5.8}$$

where x is the displacement of wicking front, t is the time of the wicking process, and D is the hemiwicking coefficient that is independent of x and t. Balancing Eq. (5.6) and Eq. (5.7) leads to

$$u = \frac{\gamma_{\mathrm{lg}}h}{3\eta x}\left(\frac{\cos\theta - \cos\theta_c}{\cos\theta_c}\right)\frac{1}{\beta}. \tag{5.9}$$

Since $u = \mathrm{d}x/\mathrm{d}t$, we can extract the expression of x by integrating Eq. (5.9) and comparing

the result to Eq. (5.8). We get the coefficient D to be

$$D = \frac{2\gamma_{lg}h}{3\eta} \left(\frac{\cos\theta - \cos\theta_c}{\cos\theta_c} \right) \frac{1}{\beta}. \tag{5.10}$$

The values of γ_{lg}, η, and θ may be readily available for a given liquid and substrate, while h and θ_c are the topographical parameters of the micropillar array. Therefore, the only unknown parameter is β. In order to determine the value of β, we approximate the flow of liquid through the micropillar array as flow through an equivalent microchannel, taking inspiration from the works of Hay *et al.* [102] and Mai *et al.* [103].

Figure 5.1 (a) illustrates the approximation of an array of micropillars in a unit cell by an equivalent microchannel of the same height and unit cell size. The width of the channel, w, however, has to be modified for the viscous dissipation between systems to become equivalent. This can be achieved by equating the volume available for the flow between the two systems. We shall explain the rationale behind this approximation below.

We start with Darcy's law, which relates the volume flux in a porous medium to the pressure gradient, given by,

$$Q = \frac{kA}{\eta} \frac{\mathrm{d}p}{\mathrm{d}x}, \tag{5.11}$$

where Q is the volume flow per time, A is the cross-sectional area of the material, k is the permeability and $\frac{\mathrm{d}p}{\mathrm{d}x}$ is the pressure gradient. The term $\frac{kA}{\eta}$ is called hydraulic conductivity or $\frac{1}{kA/\eta}$ being the hydraulic resistance; hence the flux and pressure gradient in Eq. (5.11) are equivalent to current and voltage in Ohm's law: $I = \frac{V}{R}$, respectively. For two systems to be equivalent, they must have the same velocity Q/A. Since the driving force for imbibition is the capillary pressure, the pressure between the systems is set to be identical. Thus, for equivalence, our approximation needs to ensure that the permeability between the systems is also identical.

Now, let's consider a porous medium of a cross-sectional area A, consisting of N parallel pipes of radius r, whose axes are misaligned with the length direction, making the flow path through this medium, L_e, larger than the length L, as shown in Fig. 5.2. The flux through this medium is given by,

$$Q = \frac{N\pi r^4 \Delta p}{8\eta L_e}, \tag{5.12}$$

where Δp is the pressure gradient. We utilize the terms tortuosity, τ, and porosity, Φ, defined
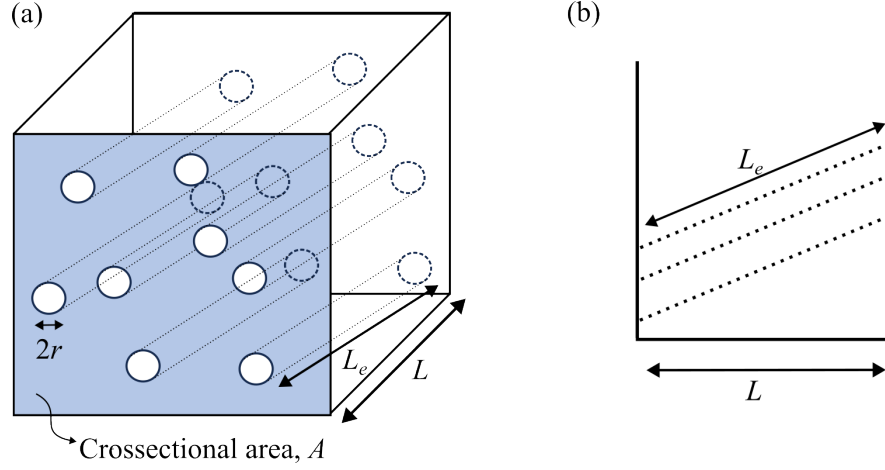
Figure 5.2: (a) Illustration of the porous system employed to derive the relationship between permeability and pore geometry. (b) A cross-section plane showing the difference between the flow path through pipelines, L_e and the medium length, L that is used to define the tortuosity.

as L_e/L and $\frac{N\pi r^2 L_e}{AL}$, respectively, to obtain

$$Q = \frac{Ar^2 \Phi \Delta p}{8\eta\tau^2 L} = \frac{Ar^2 \Phi \mathrm{d}p}{8\eta\tau^2 \mathrm{d}x}. \tag{5.13}$$

Comparing Eqs. (5.11) and (5.14), we find

$$k \propto \frac{r^2 \Phi}{\tau^2}. \tag{5.14}$$

We then introduce a new term called the hydraulic radius, R_h, which is defined as the ratio between the pore volume, V_p and the liquid-solid interaction area during the flow, A_{ls},

$$R_h = \frac{V_p}{A_{ls}} = \frac{\pi r^2 L_e}{2\pi r L_e} = \frac{r}{2}. \tag{5.15}$$

Substituting Eq. (5.15) into Eq. (5.14), we get

$$k \propto \frac{R_h^2 \Phi}{4\tau^2}. \tag{5.16}$$

Therefore, for the two systems to have the same permeability, they need to have identical $\frac{R_h^2 \Phi}{\tau^2}$ values. We can further relate the porosity and tortuosity through Archie's law [104], given as

$$\tau \propto \Phi^{-m}, \tag{5.17}$$

where m is a real number with values usually greater than 1. From Eq. (5.16) and Eq. (5.17), we find

$$k \propto R_h^2 \Phi^{2m+1}. \tag{5.18}$$

Since $R_h = V_p/A_{ls}$ and the porosity is the pore volume over the total volume (V_t), we can re-write Eq. (5.18) as

$$k \propto \frac{V_p^{2m+3}}{A_{ls}^2} \frac{1}{V_t^{2m+1}}. \tag{5.19}$$

In the approximated microchannel (Fig. 5.1 (a)), the total volume of the unit cell is set to be identical by setting the same unit cell size and height between the microchannel and the array. Thus, for equivalence, the necessary condition is

$$\frac{V_{p,\text{ch}}^{2m+3}}{A_{ls,\text{ch}}^2} = \frac{V_{p,\text{array}}^{2m+3}}{A_{ls,\text{array}}^2}, \tag{5.20}$$

where the subscripts ch and array denote for microchannel and array, respectively. In this relation, the equivalence criterion is more strongly reliant on the volume of the channel than the liquid-solid interaction area due to a higher power in the volume term. Hence, it is possible to approximate the equivalent microchannel by forcing the system to have identical volumes. For instance, we approximate a cylindrical micropillar array by an equivalent microchannel patterned with grooves with the same height h and unit cell size of side length b (See Fig. 5.1 (a)) such that the total volume of the fluid in the grooved microchannel is the same as that in the micropillar array. For these two systems, we have

$$V_{p,\text{array}} = (b^2 - \pi a^2/4)h, \tag{5.21}$$

$$V_{p,\text{ch}} = wbh, \tag{5.22}$$

where w is the width of the microchannel. Using the volume equivalence approximation, we can calculate the width of the microchannel w, given by

$$w_{\text{cyl}} = \frac{b^2 - \pi a^2/4}{b}. \tag{5.23}$$

Using the same method, we can also approximate a square array with square pillars of height h, side length a and pitch length b by an equivalent microchannel with grooves with the same

height and pitch length to obtain

$$V_{p,\mathrm{array}} = (b^2 - a^2)h, \tag{5.24}$$

$$V_{p,\mathrm{ch}} = wbh, \tag{5.25}$$

and the width of the microchannel,

$$w_{\mathrm{sq}} = \frac{b^2 - a^2}{b}. \tag{5.26}$$

To demonstrate the approximation quantitatively, we calculate the width of the microchannel, w (Eq. (5.20)) for various values of m, and plot them against w calculated using the identical volume approximation (Eqs. (5.23) and (5.26)) in Fig. 5.3. We find the slope ~ 1, validating the approximation.
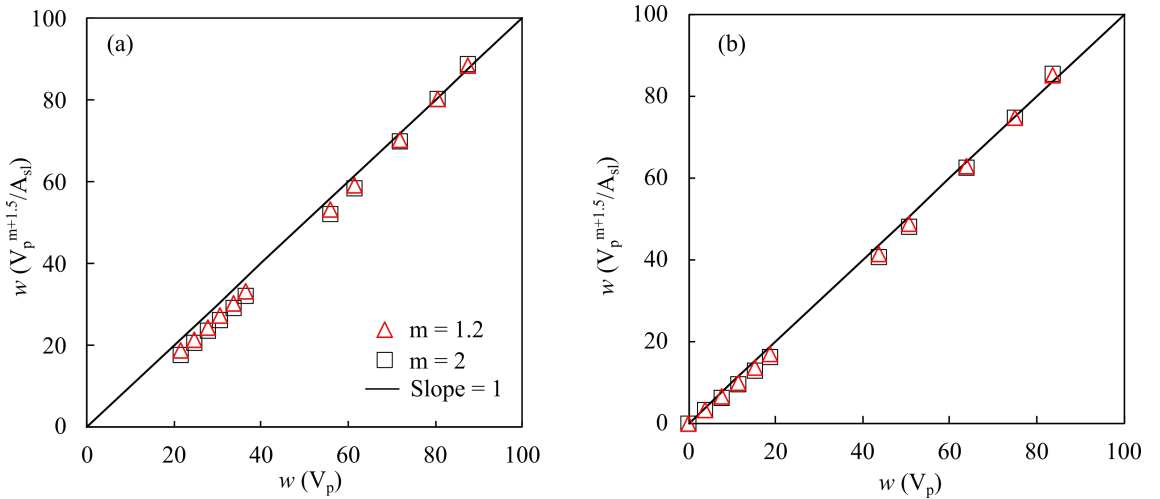
Figure 5.3: Plot of w calculated for $m = 1.2$ and $m = 2$ versus w calculated using the identical volume for (a) cylindrical and (b) square micropillars as in Eqs. (5.23) and (5.26), respectively.

Having the equivalence established, the velocity of the fluid can be calculated by solving the Navier-Stoke equation for a steady-state, incompressible, and parallel flow

$$\frac{\Delta p_L}{\eta x} = \frac{\partial^2 U}{\partial y^2} + \frac{\partial^2 U}{\partial z^2}, \tag{5.27}$$

where $U(y, z)$ is the velocity profile in the microchannel in the x-direction (See Fig. 5.1 (b)). We assume no-slip and free-slip boundary conditions at the bottom and top walls of the microchannel, respectively. This equation can be solved by implementing boundary conditions:

$U(y, -h) = 0, U(-w/2, z) = U(w/2, z) = 0$, and $\frac{\partial U}{\partial z}(y, 0) = 0$, giving us the velocity

$$U(y, z) = \frac{16\Delta p_L h^2}{\eta \pi^3 x} \sum_{n=0}^{\infty} \frac{(-1)^n}{(2n + 1)^3} \left(1 - \frac{\cosh\left[\frac{(2n+1)\pi y}{2h}\right]}{\cosh\left[\frac{(2n+1)\pi w}{4h}\right]} \right) \cos\left[\frac{(2n + 1)\pi z}{2h}\right]. \qquad (5.28)$$

Averaging $U(y, z)$ over the cross-section area in the channel $(w \times h)$ to find the mean velocity U_{mean}, we obtain

$$\begin{aligned}
U_{\mathrm{mean}} &= \frac{1}{wh} \int_{-w/2}^{w/2} \int_{-h}^{0} U(y, z)\, \mathrm{d}y \mathrm{d}z \\
&= \frac{32\Delta p_L h^2}{\eta \pi^4 x} \sum_{n=0}^{\infty} \frac{1}{(2n + 1)^4} \left(1 - \frac{4h}{(2n + 1)\pi w} \tanh\left[\frac{(2n + 1)\pi w}{4h}\right] \right).
\end{aligned} \qquad (5.29)$$

The expression of U_{mean} can be simplified further by evaluating the contribution of each n term in the summation series. Due to the $\frac{1}{(2n+1)^4}$ dependence, the value of the terms in the summation becomes negligibly small for $n \geq 1$. Therefore, the mean velocity can be approximated as

$$U_{\mathrm{mean}} \approx U_{\mathrm{mean}}^{n=0} C = C \frac{32\Delta p_L h^2}{\eta x \pi^4} \left(1 - \frac{4h}{\pi w} \tanh\left[\frac{\pi w}{4h}\right] \right), \qquad (5.30)$$

where C is a correction factor to account for the contributions from $n > 0$ terms. We can obtain the value of C by comparing the mean velocity obtained here for $w \to \infty$ with the Poiseuille flow velocity over a flat plane. We find that the value of C is slightly larger than 1, indicating that the contribution from the $n > 0$ terms is very small. Therefore, the mean velocity U_{mean} is then given by

$$U_{\mathrm{mean}} = \frac{\Delta p_L h^2}{3\eta x} \left(1 - \frac{4h}{\pi w} \tanh\left[\frac{\pi w}{4h}\right] \right). \qquad (5.31)$$

Substituting Δp_L from Eq. (5.6), we find

$$U_{\mathrm{mean}} = \frac{\gamma_{lg} h}{3\eta x} \left(\frac{\cos\theta - \cos\theta_c}{\cos\theta_c} \right) \left(1 - \frac{4h}{\pi w} \tanh\left[\frac{\pi w}{4h}\right] \right). \qquad (5.32)$$

Comparing Eq. (5.32) to Eq. (5.9), we get

$$\beta = \frac{1}{1 - \frac{4h}{\pi w} \tanh\left[\frac{\pi w}{4h}\right]}. \qquad (5.33)$$

Therefore, the hemiwicking coefficient D is given by

$$D = \frac{2\gamma_{lg}h}{3\eta} \left(\frac{\cos\theta - \cos\theta_c}{\cos\theta_c} \right) \left(1 - \frac{4h}{\pi w} \tanh\left[\frac{\pi w}{4h} \right] \right). \tag{5.34}$$

If the coefficient D is expressed in terms of U_{mean}, substituting Eq. (5.32) into Eq. (5.34), we find

$$D = \frac{2\gamma_{lg}}{h} \left(\frac{\cos\theta - \cos\theta_c}{\cos\theta_c} \right) \frac{U_{\mathrm{mean}}}{\Delta p_L/x}. \tag{5.35}$$

5.1.2 Model Validation Using Lattice Boltzmann Simulations

In this section, we show Lattice Boltzmann (LB) simulation results to validate our model. Unless stated otherwise, we simulate a unit cell of a square array of micropillars in the domain of $N_x \times N_y \times N_z$ (all in simulation units, s.u.), with $N_x = N_y = 50$ s.u. and N_z is varied between 8 and 100 s.u.. The pillar diameter b is also varied between 8 and 40 s.u. We apply a body force in the x-direction, $F_x = \rho g = -\Delta p_L/x$, to the fluid to mimic the capillary pressure. A no-slip boundary condition for the liquid-solid interface is implemented using a bounce-back boundary condition. At the upper boundary of the unit cell, a free slip boundary condition is employed to represent the liquid-gas interface. Periodic boundary conditions are applied on the sides of the unit cell and at the inlet and outlet. The simulated D values are computed from the average fluid velocity in the unit cell, U_{mean}, as in Eq. (5.35), or in terms of the body force,

$$D = -\frac{2\gamma_{lg}}{h} \left(\frac{\cos\theta - \cos\theta_c}{\cos\theta_c} \right) \frac{U_{\mathrm{mean}}}{F_x}. \tag{5.36}$$

The simulated U_{mean} is computed by averaging the fluid velocity of all fluid nodes across a yz-plane sliced at a position in the x-direction. Since the applied F_x is constant, the simulated U_{mean} is the same along the x-direction. The physical parameters of the array geometry and the liquids are given in Table. 4.1.

We start by comparing the typical velocity profile through a rectangular channel of dimension $(w \times h)$ to confirm the expression of $U(y, z)$ in Eq. (5.28). The comparison with the LB simulation is shown in Fig. 5.4 A. From this, we can see a close similarity of the velocity profile. Furthermore, we will confirm that Eq. (5.32) represents the appropriate equation for mean velocity through a rectangular channel. We perform LB simulations of flow through rectangular channels of various geometries (varying channel width w and post height h) and compare the simulated D against those predicted by Eq. (5.32). The agreement between the simulated and

predicted values, shown in Fig. 5.4 B, validates the expression in Eq. (5.32). The theoretical prediction is valid for a wide range of D values, exhibiting a broad-range applicability of the formula.

Next, we validate the volume equivalent approximation by performing LB simulations of flow through the array of micropillars of various geometries and the equivalent rectangular channels. We use the liquid and geometrical parameters tabulated in Table. 4.1 for these simulations and compare the results with the experimental data. These geometries span from sparse ($b/a \gg 1$) to dense ($b/a \sim 1$) arrays and also from short ($b/h \gg 1$) to tall ($b/h \ll 1$) pillar heights. We compare the simulated D values between the arrays and channels, as well as those measured experimentally, as shown in Fig. 5.5. The proximity of our simulation data to the slope of 1 in Fig. 5.5 (a,b) demonstrates the accuracy of the volume equivalent approximation and the ability of Eq. (5.34) to accurately determine the experimentally obtained hemiwicking coefficients over a wide range of values. It is worth noticing that in our model development, we do not consider the effect of pinning/depinning phenomena as we are primarily focused on low, equilibrium contact angle systems that favour rapid liquid transport. This is reflected in our simulations, where we only use a single-phase flow without worrying about the front liquid-gas interface dynamics and assume a contact angle of $0°$ in the definition of the capillary pressure.

The volume equivalent approximation relies upon the liquid-solid interaction area and the volume of the array. These two parameters are determined by the geometrical parameters of the pillars. To further understand the effect of the geometrical parameters, we systematically investigate the validity of the model through the D values upon variations of the height (h) and diameter (a) of the pillars as well as the pitch length (b). We performed extensive LB simulations for microarrays with cylindrical pillar geometries with b/h values from 0.5 to 10 and b/a values between 1.25 and 6.25. The D values measured from these simulations were then compared against those predicted by the analytical expression in Eq. (5.34), and the absolute error percentage is plotted as a function of geometry in Fig. 5.6 (a). We note that over a broad range of geometries, the absolute error is within 30%. This represents a reasonable error value, allowing for uncertainties in measuring the viscosity, surface tension, geometry, hemiwicking rate, and inter- and intrasample nonuniformities.

Our model appears to deviate from the predicted values in the region where the pitch is comparable to the diameter, i.e. in very dense arrays. In this regime, the deviation is due to the confinement of the flow primarily within the narrow gap between the pillars. Hence, the effective

A

B
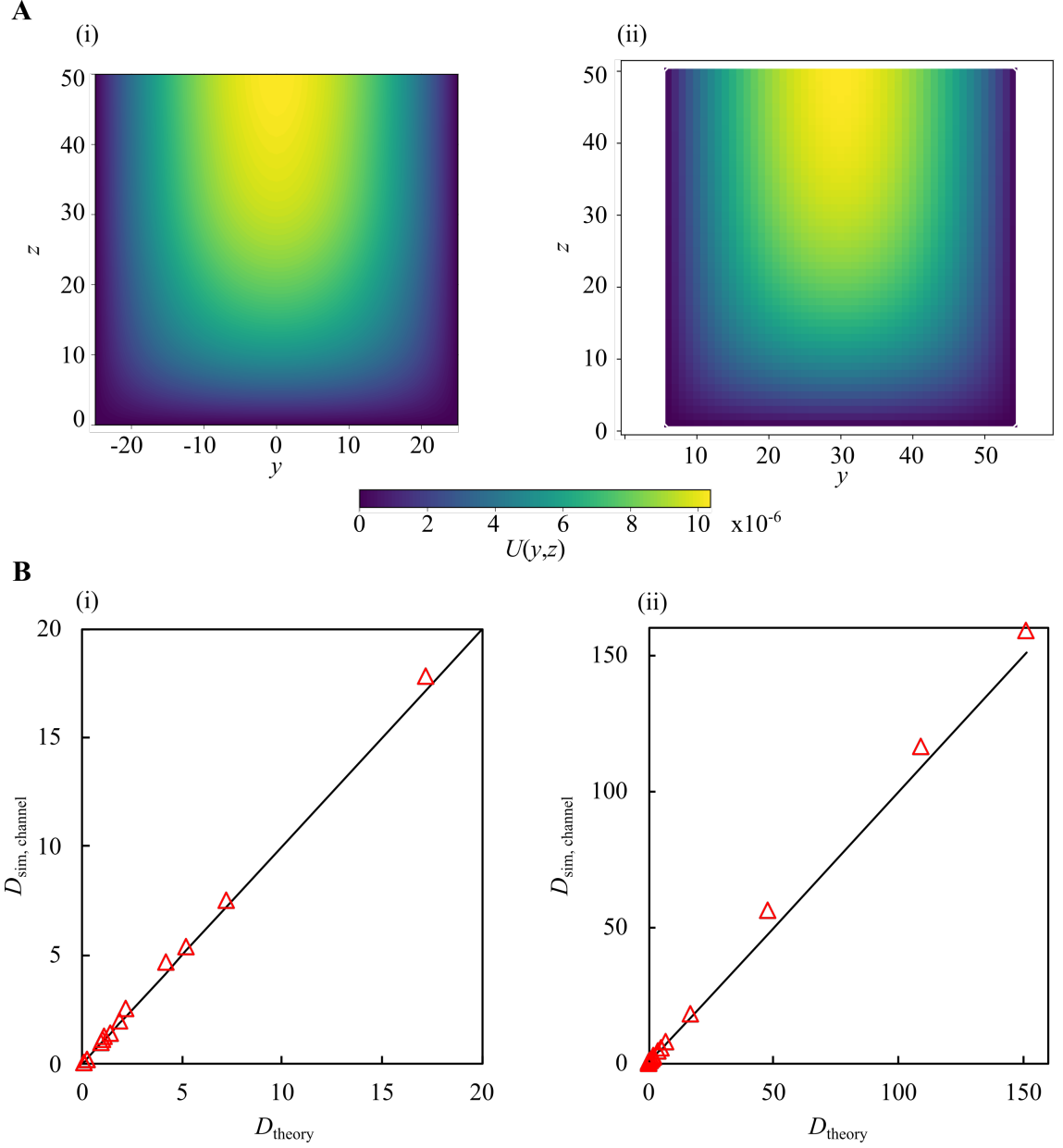
Figure 5.4: **A**. Contour plots of typical velocity profiles in a vertical plane of a rectangular channel obtained from the analytical prediction of $U(y, z)$ as in Eq. (5.28) (i) and an LB simulation (ii). **B.** Plot of the hemiwicking coefficient D for rectangular channels calculated using the analytical expression in Eq. (5.35) versus those calculated from LB simulations for small D values (i) and extended to higher values (ii).
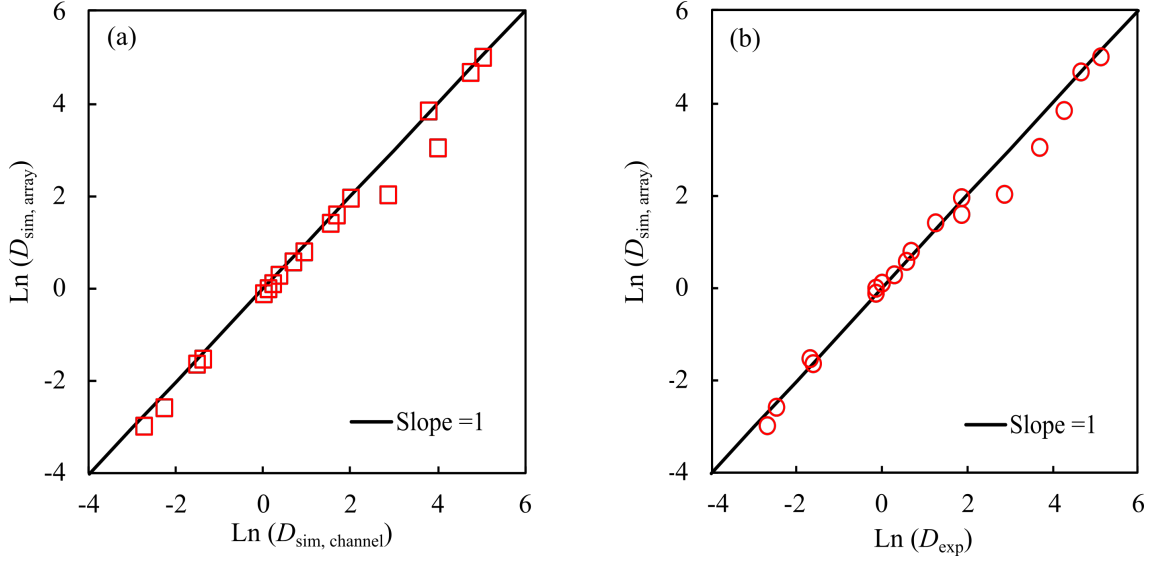
Figure 5.5: Plot of the natural logarithm of the simulated hemiwicking coefficient through the array of micropillars of various geometries, $D_{\text{sim, array}}$, versus (a) the equivalent rectangular channels, $D_{\text{sim, channel}}$, and (b) the experimentally measured D reported in the literature.

width, w, becomes smaller than our current assumption for the equivalent microchannel. That said, the highly dense arrays do not represent practically useful geometries as available flow through the narrow spaces is much reduced.

Having demonstrated the prediction accuracy of D values for a wide range of geometries, we now discuss how the limitation of prior models was addressed. We limit our discussion to models that present an expression for D [73, 75, 76]. Ishino models [73] assume drag to arise from only the pillar sidewalls. This assumption results in the overprediction of D as the viscous losses are underestimated. While such exclusive contributions to viscous dissipation are likely in extreme scenarios where $b \ll h$ or $b \gg h$, in all intermediate situations, combined contributions from the base and pillars need to be accounted for. In our model, by approximating the array to a channel, we explicitly consider frictional contribution for both the walls and the base, resulting in closer predictions. From Fig. 5.6 (b), it can be seen that the Ishino models appear to predict well in a band of intermediate b/h and b/a, which is mainly within our domain of accuracy, as well as when b/h and b/a are very small. These extremes are where the assumptions in the Ishino model are appropriate.

Other models are limited by how they reduce the texture into very simplistic representative elements. Srivastava *et al.* [76] presented a semianalytical model where the viscous dissipation was estimated using finite element (FE) modelling of flow around a single pillar. This results in overestimated values of D and requires a fitting parameter. The mismatch in predicted
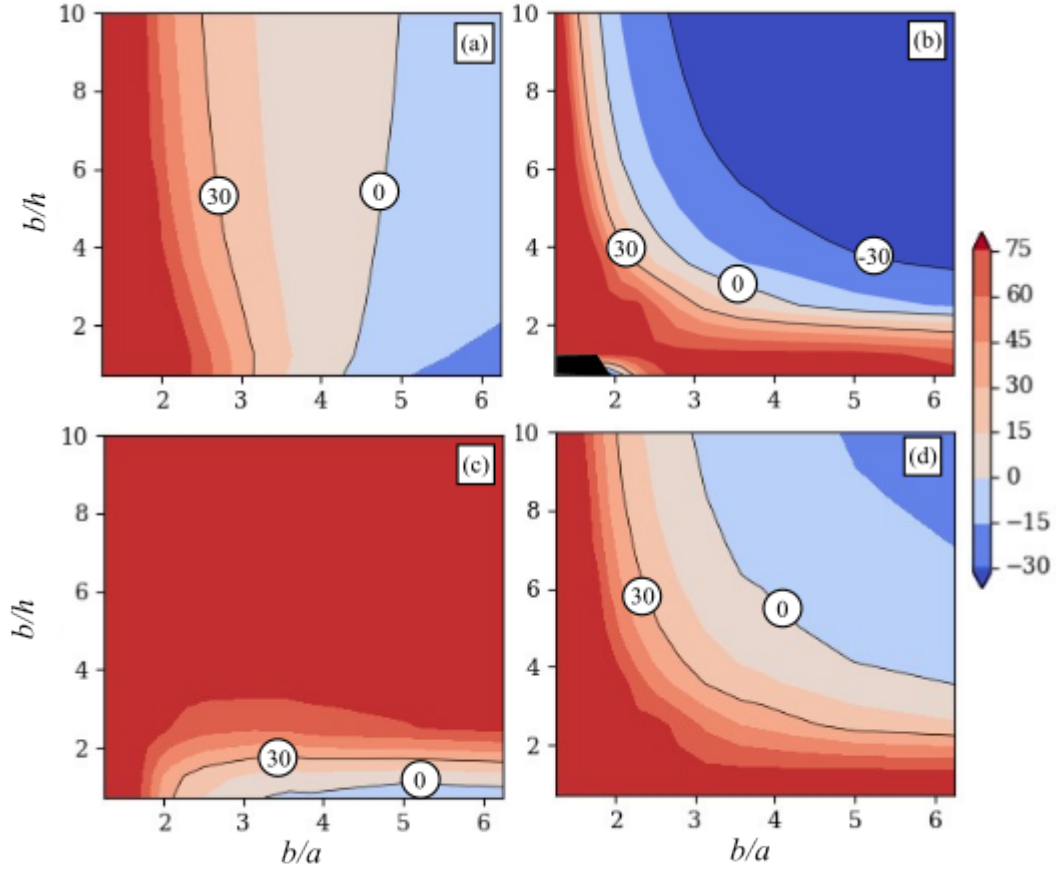
Figure 5.6: Contour plot of error (%) as a function of pitch/diameter and pitch/height for the model developed in this work (a), the Ishino model [73] (b), the Srivastava model [76] (c) and the Kim model [75] (d).

and simulated values of D is likely attributed to the exclusion of multi-pillar effects in their single-pillar FE simulations. From Fig. 5.6 (c), we can see the Srivastava model predicts well for tall pillars with $b/a > 2$, where drag from sidewalls dominates the dissipation and multi-pillar effects are diminished.

More recent models have considered the arrays in their full complexity (Kim *et al.* [75]) and have further argued for the explicit consideration of the extension length of the wicking front (Krishnan *et al.* [105]). These models predict scaling correctly for a broad range of geometries. However, they require empirically determined correction factors to predict the velocity accurately and are applicable only in the superhydrophobic limit ($\theta = 0°$). The empirical nature of these recent models limits their universality. In contrast, our model demonstrates the capability to predict the absolute value of the hemiwicking coefficient in an ab- initio fashion. That said, from Fig. 5.6 (d), we observe that the Kim model can predict well in a good range

of geometries (after applying a fitting factor of ~ 0.24) extending to the regime where b/a is small and b/h is large.

5.2 Hemiwicking Propagation on Face-centred/Hexagonal Arrays of Micropillars
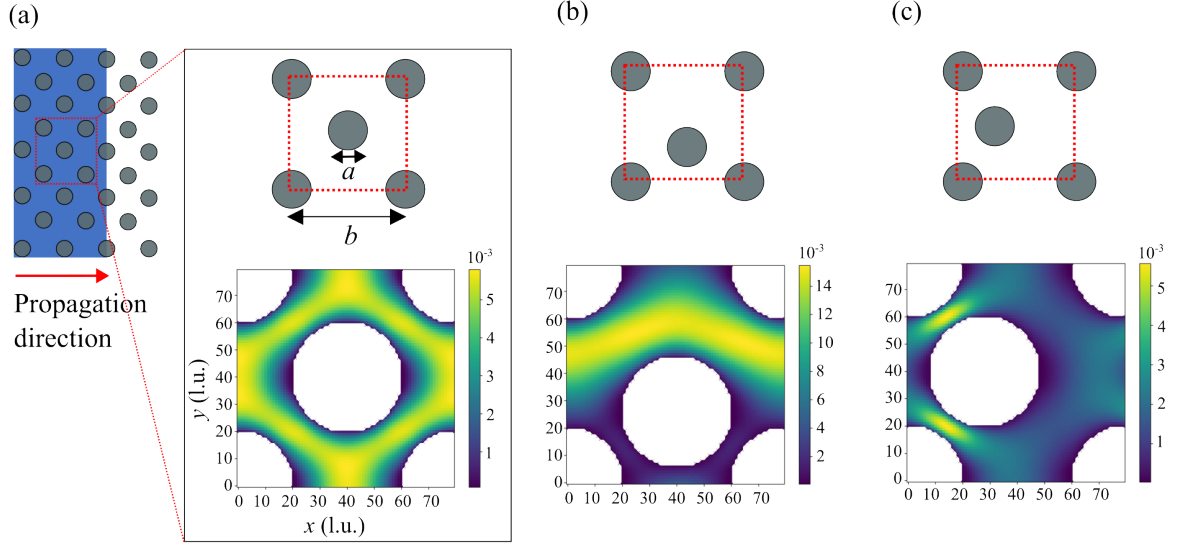
Figure 5.7: (a) Schematic of hemiwicking of liquid into a face-centred/hexagonal array of micropillars. The inset shows a unit cell of the face-centred square array with pillar diameter, a, and pillar separation (pitch length), b, as well as the typical fluid velocity profile across an xy-plane. The square dashed line shows the unit cell used in simulations. (b) and (c) Unit cells and typical fluid velocity profiles of the asymmetric face-centred square arrays where the mid-pillar is moved towards the sides of the unit cell perpendicular to and in line with the fluid propagation direction, respectively.

Having successfully predicted the dynamics of hemiwicking of liquid on square arrays of micropillars using Darcy's law-based volume equivalence model, we will extend our investigation of hemiwicking of liquid to more complex arrangements of micropillars, namely face-centred/hexagonal arrays of micropillars. The schematic of hemiwicking and pillar arrangements is shown in Fig. 5.7. Here, we consider a face-centred square array with cylindrical pillars having pillar diameter of a and pillar spacing (pitch length) of b, as pictured in Fig. 5.7 (a). A unit cell and the typical liquid velocity profile are shown in the inset of Fig. 5.7 (a). A hexagonal array of micropillars would have a similar arrangement of unit cells to the face-centred square array, except that the unit cell will be rectangular rather than square. However, the liquid velocity profile of both arrays will be identical. In order to broaden the field of our

investigation, we also consider asymmetric face-centred arrays where the mid-pillar is moved towards the sides of the unit cell perpendicular to (which we shall call **A1b** array) and in-line with (which we shall call **A1c** array) the fluid propagations creating non-uniform pillar spacings between side pillars and mid-pillar, as illustrated in Fig. 5.7 (b,c), respectively. This allows us to investigate the hemiwicking of liquid through an irregular array.

As shown in Fig. 5.7, putting a pillar in the middle of a unit cell of a square array results in a change in liquid velocity profile compared to the square array. The yellow colour in the contour plot of the velocity profile shows the area where the liquid has high velocities in the unit cell. It suggests the liquid branches out the flow in two directions when passing through the mid-pillar. When the mid-pillar is moved toward the side of the unit cell perpendicular to the fluid propagation direction (A1b array), the velocity profile becomes non-uniform, in which the area with larger pillar spacing between the side pillars and the mid-pillar (top part of Fig. 5.7 (b)) has higher local velocities than the rest of the unit cell (bottom part of Fig. 5.7 (b)). When the mid-pillar is moved toward the side of the unit cell in line with the fluid propagation direction (or toward the inlet) (A1c array), however, the higher local velocity occurs at the narrow region between the side and mid-pillars (left part off Fig. 5.7 (b)). In any case, since the body force driving the liquid is applied at a constant value, the average velocity across a plane perpendicular to the flow along the flow direction is still the same. Our main question is, can we use the volume equivalence method to predict the hemiwicking coefficient?

5.2.1 Model Development

5.2.1.1 Equivalent Microchannel Approximation

Let us consider unit cells of cylindrical pillars with a diameter of a, height of h and pitch length of b as illustrated in Fig. 5.7. The flow of liquid through these face-centred arrays can be approximated as a flow through an equivalent groove microchannel with the same pillar height and unit cell size. The remaining task is determining an appropriate width of the microchannel to satisfy the equivalence criterion. In this model, we consider three approaches in determining the width of the microchannel: (1) Volume Equivalence (VE), (2) Volume-Area Equivalence (VAE) and (3) Pillar Face-Face Spacing (FF). We shall detail these three approaches in the following section.

Volume Equivalence (*VE*) *Approach*

Let us recall the equivalence criterion in Eq. (5.20). In this approach, we assume the array to have an identical volume with the equivalent microchannel due to the higher contribution of the volume term compared to the liquid-solid interaction area, $A_l s$. In a face-centred array, the volume of the array is given by,

$$V_{p,\text{array}} = (b^2 - \pi a^2/2)h. \tag{5.37}$$

Meanwhile, the volume equivalence of the microchannel is identical to that of the square array, $V_{p,\text{ch}} = wbh$. Thus, using the volume equivalence, balancing $V_{p,\text{array}}$ and $V_{p,\text{ch}}$ gives us the width of the channel

$$w_{\text{VE}} = \frac{b^2 - \pi a^2/2}{b}. \tag{5.38}$$

It is worth noticing here that for asymmetric face-centred arrays (A1b and A1c), the position of the mid-pillar does not affect the volume of the array; hence, the width of the channel will always be the same.

Volume-Area Equivalence (VAE) Approach

In this approach, we appreciate the effect of the mid-pillar on the volume and the liquid-solid interaction area in the array. Compared to a square array, it is clear that adding a mid-pillar in the face-centred array reduces the pore volume (V_p) of the array and, at the same time, increases the liquid-solid interface area (A_{ls}). This makes the contribution of A_{ls} in the equivalent criterion in Eq. (5.20) to be more significant in contrast to the square array case. When the array is approximated by the equivalence microchannel, the two systems are forced to have not only an identical volume but also an identical liquid-solid interaction area. Therefore, the width of the equivalence channel, w_{VAE} is determined by solving Eq. (5.20), which, for a face-centred array with cylindrical micropillars, is given by

$$(b^2 - \frac{1}{2}\pi a^2 + 2\pi ah)b^{m+1.5}w_{\text{VAE}}^{m+1.5} - b(b^2 - \frac{1}{2}\pi a^2)^{m+1.5}w_{\text{VAE}} - 2bh(b^2 - \frac{1}{2}\pi a^2)^{m+1.5} = 0. \tag{5.39}$$

It is worth noticing here that w_{VAE} may depend on m whose value is larger than 1. In addition, the effect of pillar height, h, is also not neglected. However, similar to VE approach, the mid-pillar position does not affect the volume of the array and the width of the channel.

Pillar Face-to-Face Spacing (FF) Approach

The last approach we use to determine the width of the channel in approximating a face-centred array to an equivalence microchannel is by taking the pillar spacing between the sides and middle pillars. We base this approach on looking at the velocity profile of liquid in a unit cell of the face-centred array where the majority of the flow occurs in the area between the sides and middle pillars. In addition, the effect of moving the mid-pillar in asymmetric face-centred arrays (A1b and A1c) is considered, unlike the two aforementioned approaches.

Using this approach, we consider the width of the channel, w_{FF}, as the pillar spacing where the majority of flow occurs, given by

$$w_{\text{FF}} = \frac{b\sqrt{2}}{2} - a, \tag{5.40}$$

for a symmetric face-centred array, and

$$w_{\text{FF}} = \frac{b}{2}\sqrt{2\left[1 - 2\frac{\Delta x}{b} + 2\left(\frac{\Delta x}{b}\right)^2\right]} - a, \tag{5.41}$$

for an asymmetric face-centred array, where Δx is the displacement of the mid-pillar from the centre of the array towards the sides (inlet for A1b array and side for A1c array).

Figure 5.8 shows the comparison of w calculated using the three approaches for variation of pillar diameter and height relative to the pitch length in symmetric face-centred arrays. The effect of m in the VAE approach is also shown. It can be seen that the VE approach deviates from the VAE approach for very sparse arrays (low a/b) and very dense arrays (large a/b) (Fig. 5.8 (a)). Moreover, the effect of pillar height is not present in the VE and FF approaches but can be seen in the VAE approach (Fig. 5.8 (b)).

5.2.1.2 Hydraulic-electric Circuit Analogy

It is intuitive to consider the flow of liquid similar to the flow of current in electrical wires: the liquid molecules in a hydraulic circuit behave much like the electrons in an electrical circuit. As we have mentioned earlier, the flux (Q) and pressure gradient ($\frac{dp}{dx}$) in Darcy's law in Eq. (5.11) are equivalent to current (I) and voltage (V) in Ohm's law, respectively, whereas the hydraulic resistance $\frac{\eta}{kA}$ is equivalent to the electrical resistance, R. As the the liquid flows into a face-centred array of micropillars, the flow path passing through a unit cell of the array can be
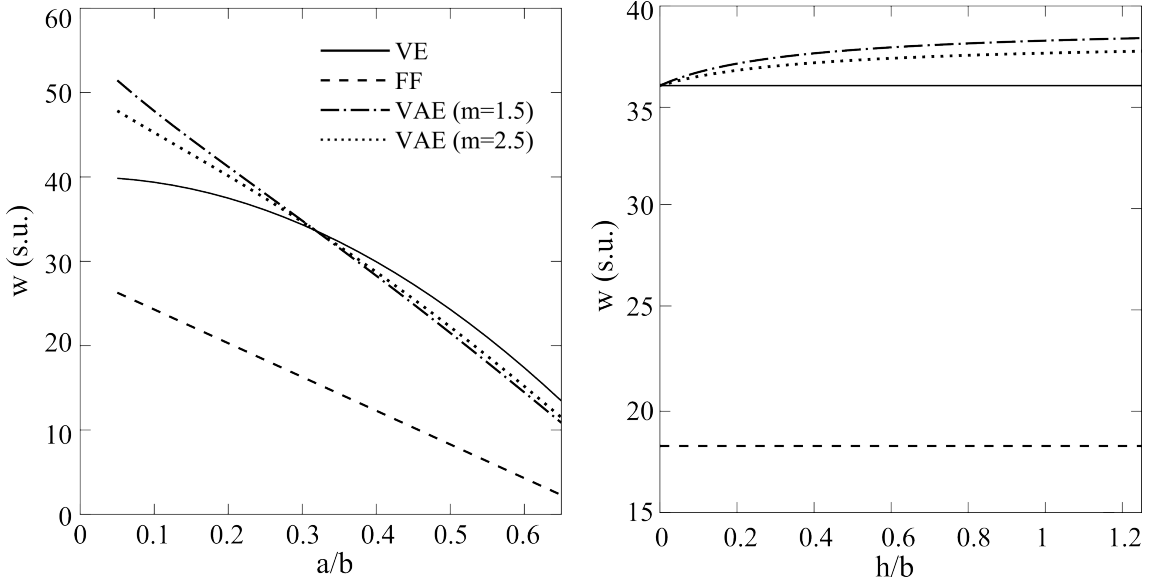
Figure 5.8: Comparison of w calculated using VE, VAE, and FF approaches for variation of pillar diameter to pitch length ratio, a/b (a) and pillar height to pitch length ratio h/b (b) in symmetric face-centred arrays. Here, we use $m = 1.5$ and $m = 2.5$ in the VAE approach.

considered a sub-unit cell representing an electrical circuit. We attempt to employ this analogy to prescribe the permeability of liquid, k of each of the sub-unit cells. In this approach, we will consider parallel and series circuits and use Kirchhoff's rules to find the effective permeability of liquid, k_{eff} of the unit cell. Furthermore, to predict the flow in each of the sub-unit cells, we will approximate the sub-unit cell by the equivalent microchannel and use VE, FF and VAE approximations to estimate the effective width of the channel.

From Darcy's law, the flow velocity, U_{Darcy} can be defined as the flux divided by the cross-sectional area of the system, or $U_{\text{Darcy}} = Q/A = k\frac{\Delta p_c}{\eta L}$, where Δp_c is the pressure difference across the circuit. Recognizing that $U_{\text{Darcy}} = \frac{\mathrm{d}L}{\mathrm{d}t}$, we can calculate the hemiwicking coefficient from U_{Darcy} to get

$$D = 2k_i\frac{\Delta p_c}{\eta}, \tag{5.42}$$

where, k_i is the permeability of liquid in a sub-unit cell. Comparing the hemiwicking coefficient in Eq. (5.42) to Eq. (5.34), we can get k_i for an equivalent rectangular microchannel

$$k_i = \frac{\gamma_{\text{lg}}h}{3}\left(1 - \frac{4h}{\pi w_i}\tanh\left[\frac{\pi w_i}{4h}\right]\right), \tag{5.43}$$

where w_i is the channel width of a sub-unit cell. To obtain the hemiwicking coefficient of a unit cell, we can replace k_i, by the effective permeability of the circuit, k_{eff} which will be determined based on the type of the circuits in the unit cell. In the following sections, we shall discuss how
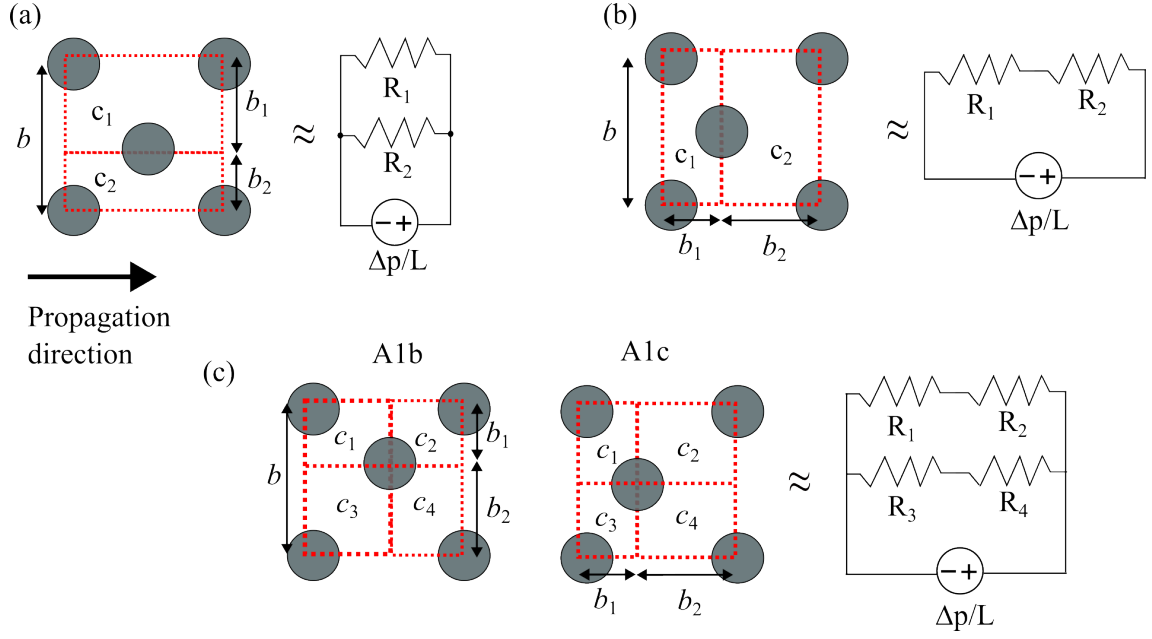
Figure 5.9: Schematics of hydraulic-electric circuit analogy for (a) parallel, (b) series and (c) parallel-series circuits. Black arrow denotes the flow direction.

to calculate k_{eff} for different circuits.

Parallel Cells

A parallel network of a unit cell of face-centred arrays and its parallel circuit analogue is shown in Fig. 5.9 (a). Here, a unit cell with a pillar diameter of a and pitch length of b is divided into two sub-unit cells, c_1 and c_2, with widths of b_1 and b_2 parallel to the fluid flow. The hydraulic resistances of these sub-unit cells are analogous to R_1 and R_2 in the equivalence electrical circuit. The pressure gradient, analogous to the voltage, is the same across the unit cell. Therefore, this circuit is applicable for symmetric and A1b arrays.

Applying Kirchhoff's rule to calculate the effective permeability of the circuit, k_{eff}, we find

$$Q_{\text{total}} = Q_1 + Q_2,$$

$$\frac{k_{\text{eff}}A}{\eta}\frac{\Delta p_c}{L} = \frac{k_1 A_1}{\eta}\frac{\Delta p_c}{L} + \frac{k_2 A_2}{\eta}\frac{\Delta p_c}{L},$$

$$k_{\text{eff}}A = k_1 A_1 + k_2 A_2, \tag{5.44}$$

where A_1 and A_2 are the cross-sectional area of the sub-unit cells c_1 and c_2, respectively. Notice here that the last line in Eq. (5.44) is equivalent to $1/R_{\text{eff}} = 1/R_1 + 1/R_2$ in the analogue electrical circuit given that $R = \eta/kA$. Since $A_1 = b_1 h$, $A_2 = b_2 h$ and $A = (b_1 + b_2)h$,

k_{eff} is then given by

$$k_{\text{eff}} = \frac{k_1 b_1 + k_2 b_2}{b_1 + b_2}, \tag{5.45}$$

where $b = b_1 + b_2$. k_1 and k_2 are given by Eq. (5.43) with w_1 and w_2 the effective channel width of sub-unit cells c_1 and c_2, respectively. For a symmetric array, $b_1 = b_2 = b/2$ and $k_1 = k_2$, hence $k_{\text{eff}} = k_1 = k_2$.

Series Cells

A series network of a unit cell of face-centred arrays and its series circuit analogue is shown in Fig. 5.9 (b). The flux of flow in sub-unit cell c_1 is the same as in sub-unit cell c_2, and the effective hydraulic resistance equals the total hydraulic resistance of both sub-unit cells, $R_{\text{eff}} = R_1 + R_2$. The pressure gradient in each of the unit cells may differ depending on the position of the mid-pillar. Therefore, we apply this approach to symmetric and A1c arrays. Since the cross-sectional area of the unit cell equals the cross-sectional area in sub-unit cells c_1 and c_2, the effective permeability, k_{eff} for a series cell, is given by

$$k_{\text{eff}} = \frac{k_1 k_2}{(k_1 + k_2)}. \tag{5.46}$$

For a symmetric face-centred array of micropillars, both sub-unit cells c_1 and c_2 are identical, giving the same permeability on both sub-unit cells, $k_1 = k_2$. Therefore, the effective permeability of the unit cell equals half of the permeability of a sub-unit cell, $k_{\text{eff}} = k_1/2$.

Parallel-Series Cells

The last hydraulic-electric circuit analogy that we look at is the combination of parallel and series networks, which is shown in Fig. 5.9 (c). Here, a unit cell is divided into four sub-unit cells denoted as c_i with $i = \{1, 2, 3, 4\}$, in which c_1 and c_3 are in series with c_2 and c_4, respectively, and one pair of the series cells is in parallel to the other. The effective hydraulic resistance is then given by

$$R_{\text{eff}} = \frac{(R_1 + R_2)(R_3 + R_4)}{R_1 + R_2 + R_3 + R_4}. \tag{5.47}$$

For the symmetric face-centred array, all sub-unit cells are identical ($c_1 = c_2 = c_3 = c_4$), resulting in the same hydraulic resistances in each of the sub-unit cells ($R_1 = R_2 = R_3 = R_4$). This makes the effective hydraulic resistance of the circuit equal to the hydraulic resistance of

a sub-unit cell,

$$R_{\text{eff}} = R_i. \tag{5.48}$$

Consequently, since the cross-sectional area of the sub-unit cell equals half of the cross-sectional area of the unit cell, $A_i = A/2$, the effective permeability is given by

$$k_{\text{eff}} = \frac{k_i}{2}. \tag{5.49}$$

For asymmetric arrays, we have to divide our calculations for A1b and A1c arrays as the mid-pillar position and the propagation direction give different effective hydraulic resistance and permeability. For the A1b array, as the mid-pillar position is moved towards the side perpendicular to the propagation direction, we have $c_1 = c_2$ and $c_3 = c_4$, hence $R_1 = R_2$ and $R_3 = R_4$. The cross-sectional area of the sub-unit cells is given by $A_1 = A_2 = b_1 h$ and $A_3 = A_4 = b_2 h$. We can calculate R_{eff} and k_{eff}, given by

$$R_{\text{eff}} = \frac{2R_1 R_3}{(R_1 + R_3)}, \tag{5.50}$$

$$k_{\text{eff}} = \frac{k_1 b_1 + k_3 b_2}{2(b_1 + b_2)}. \tag{5.51}$$

For A1c array, on the other hand, as the mid-pillar position is moved towards the side in-line the propagation direction (or towards the inlet) we have $c_1 = c_3$ and $c_2 = c_4$. The cross sectional area of the sub-unit cells are given by $A_1 = A_2 = A_3 = A_4 = A/2 = \frac{1}{2}bh$. Therefore,

$$R_{\text{eff}} = \frac{(R_1 + R_2)}{2}, \tag{5.52}$$

$$k_{\text{eff}} = \frac{k_1 k_2}{(k_1 + k_2)}. \tag{5.53}$$

To determine the effective channel of sub-unit cells in parallel, series and parallel-series cells, we use the three aforementioned approaches: volume equivalence (VE), volume-area equivalence (VAE) and pillar face-to-face spacing (FF). In summary, the expression of k_{eff} and w_{i} for the symmetric and asymmetric face-centred array is tabulated in Table. 5.1.

Table 5.1: The width of the equivalent channel calculated using VE, FF and VAE approaches. Subscript i denotes the sub-unit cells 1 and 2 in the corresponding circuits.

Cell Types	VE	FF	VAE
Symmetry array			
Parallel	$\dfrac{bb_i - \pi a^2/4}{b}$	$\sqrt{(b/2)^2 + b_i^2} - a$	$\dfrac{(bb_i - \pi a^2/4)h^{m+1.5}}{bb_i - \pi a^2/4 + \pi ah} = \dfrac{bw_i h^{m+1.5}}{bw_i + 2bh}$
Series	$\dfrac{bb_i - \pi a^2/4}{b_i}$	$2\left(\sqrt{(b/2)^2 + b_i^2} - a\right)$	$\dfrac{(bb_i - \pi a^2/4)h^{m+1.5}}{bb_i - \pi a^2/4 + \pi ah} = \dfrac{bw_i h^{m+1.5}}{bw_i + 2bh}$
Parallel-Series	$\dfrac{bb_i - \pi a^2/4}{b_i}$	$\sqrt{(b/2)^2 + b_i^2} - a$	$\dfrac{(bb_i/2 - \pi a^2/8)h^{m+1.5}}{bb_i/2 - \pi a^2/8 + \pi ah} = \dfrac{bw_i h^{m+1.5}}{bw_i + 2bh}$
Asymmetry A1b array			
Parallel	$\dfrac{bb_i - \pi a^2/4}{b}$	$\sqrt{(b/2)^2 + b_i^2} - a$	$\dfrac{(bb_i - \pi a^2/4)h^{m+1.5}}{bb_i - \pi a^2/4 + \pi ah} = \dfrac{bw_i h^{m+1.5}}{bw_i + 2bh}$
Parallel-Series	$\dfrac{bb_i - \pi a^2/4}{b}$	$\sqrt{(b/2)^2 + b_i^2} - a$	$\dfrac{(bb_i/2 - \pi a^2/8)h^{m+1.5}}{bb_i/2 - \pi a^2/8 + \pi ah} = \dfrac{bw_i h^{m+1.5}}{bw_i + 2bh}$
Asymmetry A1c array			
Series	$\dfrac{bb_i - \pi a^2/4}{b_i}$	$\sqrt{(b/2)^2 + b_i^2} - a$	$\dfrac{(bb_i - \pi a^2/4)h^{m+1.5}}{bb_i - \pi a^2/4 + \pi ah} = \dfrac{bw_i h^{m+1.5}}{bw_i + 2bh}$
Parallel-Series	$\dfrac{bb_i - \pi a^2/4}{2b_i}$	$\sqrt{(b/2)^2 + b_i^2} - a$	$\dfrac{(bb_i/2 - \pi a^2/8)h^{m+1.5}}{bb_i/2 - \pi a^2/8 + \pi ah} = \dfrac{bw_i h^{m+1.5}}{bw_i + 2bh}$

5.2.2 Model Validation Using Lattice Boltzmann Simulations

In this section, we show LB simulation results of liquid propagating through face-centred arrays of cylindrical micropillars to validate our model. Firstly, we will try to validate the equivalent microchannel approximation of the full arrays, i.e., approximating a unit cell of the face-centred array of cylindrical micropillars by the equivalent microchannel and using VE, VAE, and FF approaches to calculate the width of the channel. Secondly, we will try to validate the hydraulic-electric circuit analogy model.

In the LB simulations, we consider ethylene glycol 99 wt% liquid with properties taken from Ref. [75] including viscosity $\eta = 18$ mPa.s, surface tension $\gamma = 48$ mN/m, density $\rho = 1140$ kg/m^3 and equilibrium contact angle $\theta = 0°$. The unit cell of the face-centred array has a pitch length of $b = 40$ μm and consists of cylindrical pillar geometries with variations of pillar density (via diameter-to-pitch length ratio, a/b) and pillar height (via height-to-pitch length ratio, h/b). All of these parameters are then converted into simulation units (s.u.).

In our simulations, we use pressure boundary conditions along the propagation direction, in which a constant density (or pressure) is applied at the inlet and outlet of the system, and the pressure gradient is set to be constant along the propagation direction. We derive the value of the pressure gradient, $\Delta p_c/L$, from the body force whose values depend on the density and gravitational force, ρg. To obtain the values of the fluid density at the inlet and outlet, we

use the relation $\Delta p_c / L = \rho g$ and $\Delta p_c = c_s^2 \Delta \rho$. Since $c_s^2 = \frac{1}{3}$, we get the density difference $\Delta \rho = 3\rho g L$, where L is the length of the system. We set the density at the inlet $\rho_{in} = \rho_o + \frac{\Delta \rho}{2}$ and at the outlet $\rho_{out} = \rho_o - \frac{\Delta \rho}{2}$, where $\rho_o = 1$ is the density at the center of the system. This scheme is favourable compared to applying a constant body force because it is more useful in the hydraulic-electric circuit analogy.

5.2.2.1   Symmmetric Face-centred Arrays

We begin by investigating the hemiwicking of liquid on symmetric face-centred arrays using microchannel approximation of a full array. In Fig. 5.10 (a), we show a plot of the hemiwicking coefficient versus a/b ratio for a symmetric face-centred array of micropillar with height $h = 52$ s.u. ($h/b = 0.65$), which corresponds to $h = 26$ μm in physical unit. From the simulation results, we can see that the hemiwicking coefficient increases with increasing a/b ratio and reaches a peak value before decreasing for high a/b values. This trend can be explained by analyzing the multiplication of the average velocity, U_{mean}, and the term $\frac{(\cos\theta - \cos\theta_c)}{\cos\theta_c}$ which appears in Eq. (5.35) that is used in computing the hemiwicking coefficient. The average velocity decreases with increasing a/b (Fig. 5.10 (c)), whereas the term $\frac{(\cos\theta - \cos\theta_c)}{\cos\theta_c}$ increases with increasing a/b. The increasing of the hemiwicking coefficient for low a/b values can be attributed to the stronger growth of term $\frac{(\cos\theta - \cos\theta_c)}{\cos\theta_c}$ compared to the decreasing of the average velocity. For high a/b values, the average velocity becomes very small because the pillar spacing becomes very narrow for the liquid flow. In this case, the effect of the decreasing of the average velocity is more dominant. We can also rationalise the reduction of the hemiwicking coefficient after a peak a/b as a result of the viscous resistance that grows more strongly than the capillary driving force due to the addition of more texture in the unit cell.

The trend of the hemiwicking coefficient computed from simulation results is in qualitative agreement with our models using VE, FF and VAE approaches. With VE and VAE approaches, the value of the hemiwicking coefficient overestimates the simulation results, particularly for moderate and high a/b. In addition, the hemiwicking coefficient reaches the peak value at higher a/b than the simulation results. A better agreement is obtained for the FF approach, where the hemiwicking coefficient less deviates from the simulation results and reaches the peak at closely the same a/b.

In Fig. 5.10 (b), we show the dependency of the hemiwicking coefficient on pillar height by plotting D as a function of h/b ratio. Here, we use micropillars with diameter $a = 20$ s.u.
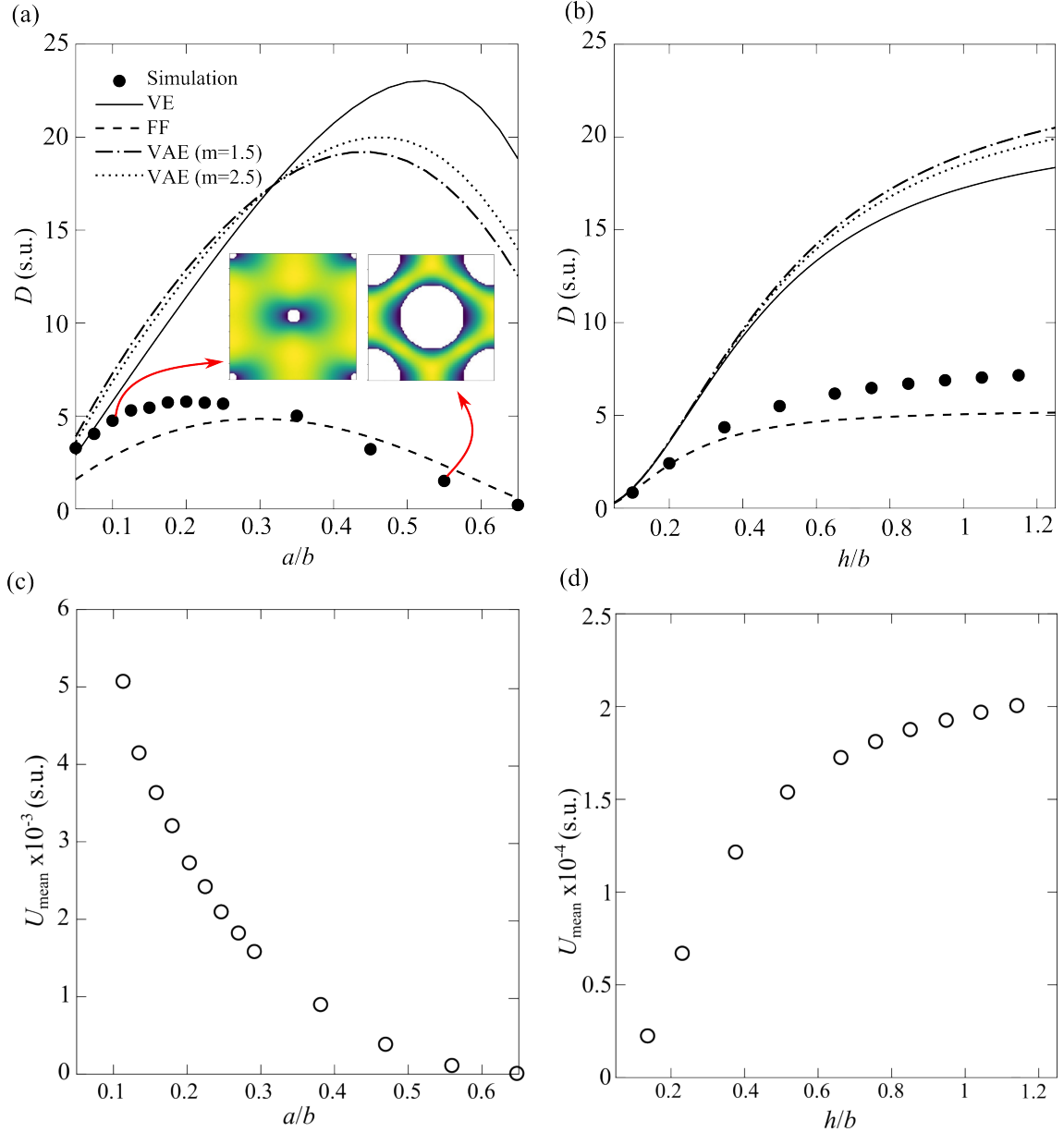
Figure 5.10: Comparison between the hemiwicking coefficient, D, of liquid propagating on symmetric face-centred arrays with cylindrical micropillars calculated from LB simulations and predicted from microchannel approximation model for a full array using volume equivalent (VE), pillar face-to-face spacing (FF) and volume-area equivalent (VAE) models with $m = 1$ and $m = 2$ approaches. (a) D plotted against pillar diameter to pitch length (a/b) ratio for $h/b = 0.65$. (b) D plotted against pillar height to pitch lenght (h/b) ratio for $a/b = 0.25$. The inset shows liquid velocity profiles across the xy-plane of several unit cells with different a/b values as denoted in panel (a). (c) and (d) Average liquid velocity, U_{mean}, plotted against a/b and h/b, respectively. All values are given in simulation units (s.u.).

($a/b = 0.25$), which corresponds to $a = 10$ μm in physical unit. The hemiwicking coefficient calculated from simulation results increases with increasing h/b ratio following the trend of the average velocity, as shown in Fig. 5.10 (d). This is because the term $\frac{(\cos\theta - \cos\theta_c)}{\cos\theta_c}$ increases linearly with increasing h/b. We also notice that the hemiwicking coefficient increases steeply

with height for small h/b values and reaches a saturation value as $h \sim b$. This suggests minimal dependency on height for $h \gg b$.

Comparing the simulation results with our models shows that all approaches in our model are in qualitative agreement with simulation results. However, the VE and VAE approaches seem to overestimate the simulation results, whereas the FF approach agrees better.
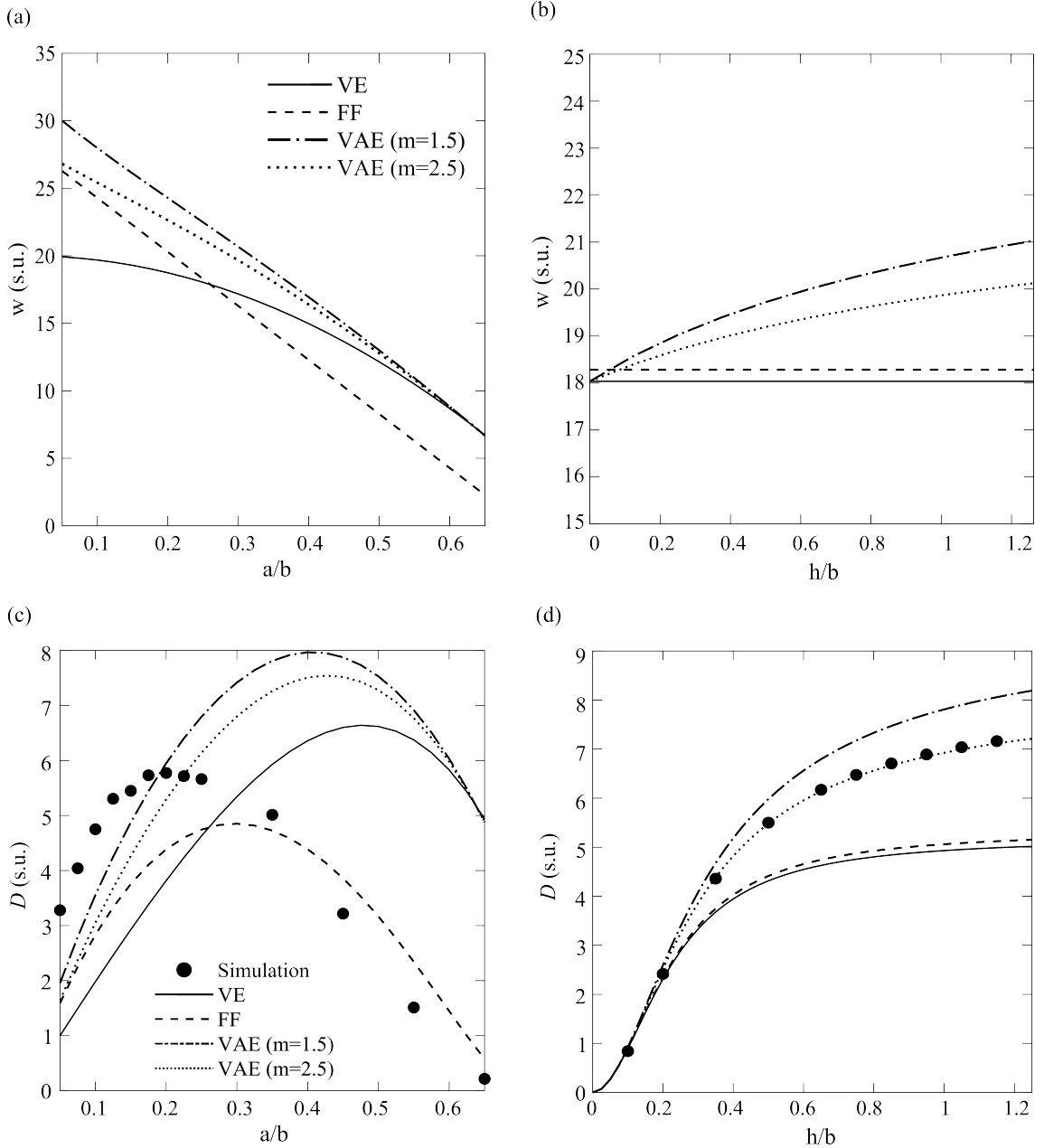
Figure 5.11: The effective channel width and hemiwicking coefficient of symmetric face-centred arrays predicted using a parallel cell analogy with VE, FF and VAE ($m = 1.5$ and $m = 2.5$) approaches. (a) and (b) Effective channel width plotted as a function of a/b and h/b ratios, respectively. (c) and (d) Hemiwicking coefficients plotted as a function of a/b and h/b ratios, respectively, and their comparison with the simulation. The simulation data in (c) and (d) are the same as in Fig. 5.10 (a) and (b), employing $h/b = 0.65$ and $a/b = 0.25$ in (c) and (d), respectively.

Now, we want to investigate the hydraulic-electric circuit analogy approach on the symmetric face-centred array. We compare the analytical prediction with the simulation results in Fig. 5.10. Here, we apply a parallel circuit to the unit cell and predict the effective width, w, of the equivalent microchannel of the sub-unit cells using VE, FF, and VAE with $m = 1.5$ and $m = 2.5$ approaches. The plots of w calculated with these approaches in a parallel circuit of the array against a/b and h/b ratios are shown in Fig. 5.11 (a,b), respectively. We notice in Fig. 5.11 (a) that w predicted using VE and VAE approaches coincide for high a/b values and deviates for low a/b values. Moreover, the parallel circuit analogy brings w values predicted using VE and VAE much closer to w values predicted using FF approaches, which has shown a better agreement to simulation results for a full array approximation. The closer w values calculated using VE and VAE approaches to the FF approach can also be seen with a variation of h/b, as shown in Fig. 5.11 (b). It is worth noticing here that w values predicted using the FF approach in parallel circuit analogy are still the same as those in full array approximation.

The comparison of the hemiwicking coefficient between simulations and prediction for a variation of a/b values is shown in Fig. 5.11 (c). Here, we still use the same parameters as in Fig. 5.10. Compared to the full array approximation, we notice an improved agreement for VE and VAE approaches with the simulation results. In particular, a good agreement with simulations can be seen for low a/b values, although overestimated values are still found for high a/b values. The parallel circuit analogy also brings the peak of D predicted using VE and VAE approaches to occur at a closer value of a/b with the simulation.

The comparison of the hemiwicking coefficient between simulations and prediction for a variation of h/b values is shown in Fig. 5.11 (d). We notice an improved agreement between VE and VAE approaches and simulations compared to results in Fig. 5.11 (b). The VAE approach with $m = 2.5$, which shows a good agreement for $a/b = 0.25$ in Fig. 5.11 (c), is able to capture variation in h/b. All approaches appear to work well for low h/b. This suggests the hydraulic-electric circuit analogy approach is applicable to a certain geometry.

To further probe the breadth of applicability of this model, we expand our investigation to a broader range of geometries varying a/b and h/b. We simulate symmetric face-centred arrays of cylindrical pillar geometries with a/b values from 0.05 to 0.65 and h/b from 0.1 to 3. The D values measured from these simulations are then compared against those predicted by our models. In addition to parallel cells, we also employ series and parallel-series cells to predict the effective permeability of the circuits. We then plot the absolute error percentage
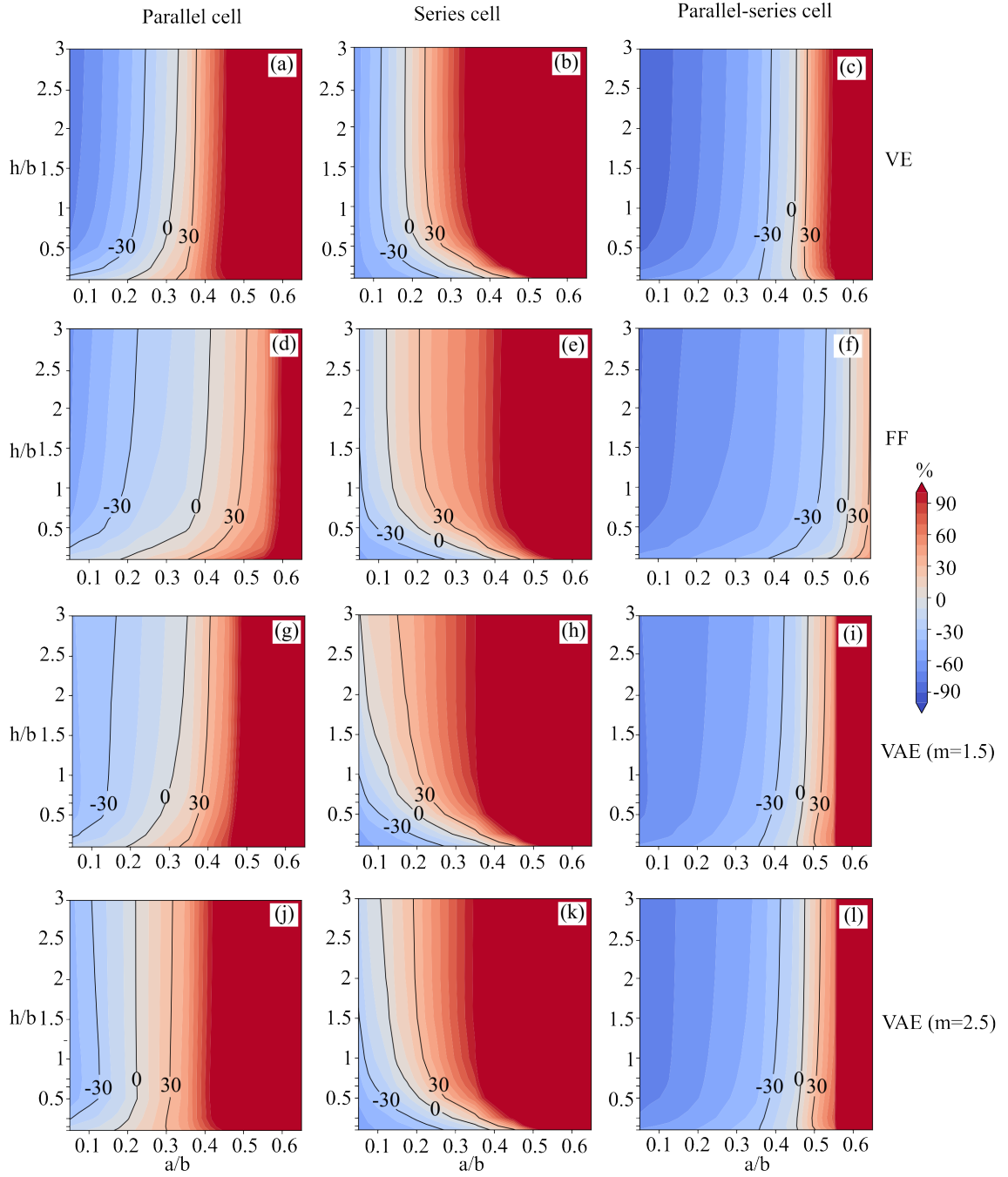
Figure 5.12: Contour plot of error (%) as a function of diameter/pitch and height/pitch for the models developed in this work for parallel (first column), series (second column) and parallel-series cells (third column) of symmetric face-centred unit cells. The equivalent channel width of the sub-unit cells is calculated using VE (panels a,b,c), FF (d,e,f), VAE with $m = 1.5$ (g,h,i) and VAE with $m = 2.5$ (j,k,l). The iso-percentage error lines are indicated in the plots. The error is the difference between the simulated and model-predicted values over the simulated value, expressed in percentages.

as a function of geometry as shown in Fig. 5.12. Here, we show that the model agrees well with simulations when the error is in the range of 30%. From these plots, we observe that the parallel cells predict the hemiwicking coefficient accurately for moderate a/b values, whereas the series and parallel-series cells are in good agreement with the simulations for low and high a/b values, respectively. This trend seems to apply to all channel approximation models (VE, FF and VAE) and the variation of h/b, with the exception of small h/b values ($h/b < 0.5$). Looking at the variation of h/b, we can see that the models will agree if the values of a/b are in the range the models predict well. For instance, for the parallel cell model using the VAE ($m = 2.5$) approach, if $0.1 < a/b < 0.3$, the model will predict well with the variation of h/b. This confirms the results shown in Fig. 5.11 (d), where the parallel cells model with the VAE approach is in good agreement with the simulation with the variation of h/b.

5.2.2.2 Asymmmetric Face-centred Arrays

Now, we want to investigate the hemiwicking of liquid on asymmetric face-centred arrays, A1b and A1c arrays. Similarly to the symmetric face-centred arrays, we will employ a microchannel approximation of full array and hydraulic-electric circuit in computing the hydrodynamic coefficient, D, and use FF, VE, and VAE approaches in determining the width of the equivalent channel.

Figure 5.13 (a) shows the plot of the hemiwicking coefficient as a function of the mid-pillar displacement, Δx, from the centre towards a side perpendicular to the propagation direction for A1b array, or towards the inlet for A1c array. The velocity profiles across xy-plane for A1b and A1c arrays with different Δx are shown in Fig. 5.13 (b,c), respectively. Here, we use a moderately dense array geometry with $a = 10$ μm, $h = 26$ μm and $b = 40$ μm. The displacement of mid-pillar does not alter the geometrical properties of the array, *i.e.* the roughness factor r and the solid fraction φ_s, hence the term $\frac{(\cos\theta - \cos\theta_c)}{\cos\theta_c}$ for all geometries, but does change the average velocity U_{mean} due to the change of the pillar spacing. Therefore, the main contribution of D measured from the simulation is through U_{mean}. In Fig. 5.13 (a), the simulation results show that D increases as the mid-pillar gets closer to the side of the array in A1b array but decreases as the mid-pillar gets closer to the inlet in A1c array. The rise of D in the A1b array is because more and more spacing for the fluid flow is created when the mid-pillar is moved away from the centre, resulting in an increase of the average velocity. On the contrary, the reduction of D in the A1c array is because the closer the mid-pillar is to the
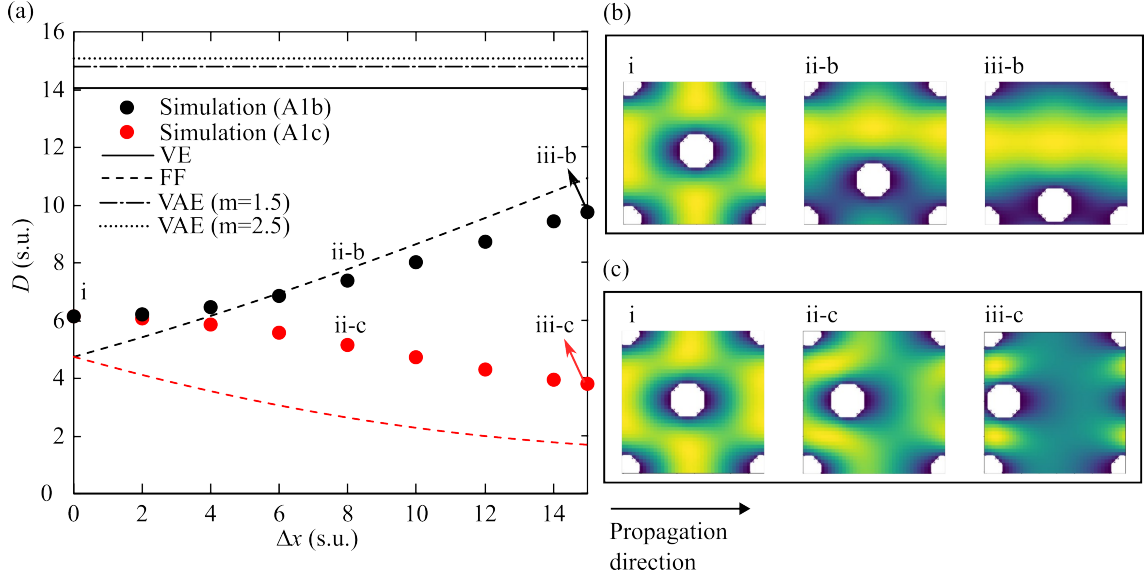
Figure 5.13: Comparison between the hemiwicking coefficient, D, of liquid propagating on asymmetric face-centred arrays with cylindrical micropillars calculated from LB simulations and predicted from microchannel approximation model for a full array using volume equivalent (VE), pillar face-to-face spacing (FF) and volume-area equivalent (VAE) with $m = 1$ and $m = 2$ approaches. (a) D plotted as a function of the mid-pillar displacement, Δx, from the centre of the array ($\Delta x = 0$) towards the sides perpendicular to (black circles) and inline with (red circles) the liquid propagation direction. (b) and (c) Liquid velocity profiles across xy-plane of several unit cells with different Δx values as denoted in panel (a). All values are given in simulation units (s.u.).

inlet, the less spacing is created for the fluid flow.

When we compare the simulation result to our model, it is clear that the FF approach gives a better agreement than others. This is because, in the FF approach, the movement of the mid-pillar is taken into account when calculating the effective width channel, whereas other approaches do not consider this movement, resulting in a constant value of D for all Δx. When we compare the A1b and A1c arrays, it appears that the FF approach works better for the A1b array. It might be related to the pressure distribution across the system. For the A1b array, since the mid-pillar is moved to the side, the pressure gradient at the area on the left-hand side of the mid-pillar (closer to the inlet) and on the right-hand side of the mid-pillar (closer to the outlet) is always the same. For the A1c array, on the other hand, the movement of the mid-pillar creates an unbalanced pressure gradient between the area closer to the inlet and the outlet.

Now, we apply the hydraulic-electric circuit analogy to predict the hemiwicking coefficient in the A1b and A1c arrays. Due to the effect of the mid-pillar displacement, we apply parallel and series cells for A1b and A1c, respectively. In Fig. 5.14 (a), it is shown that the D values
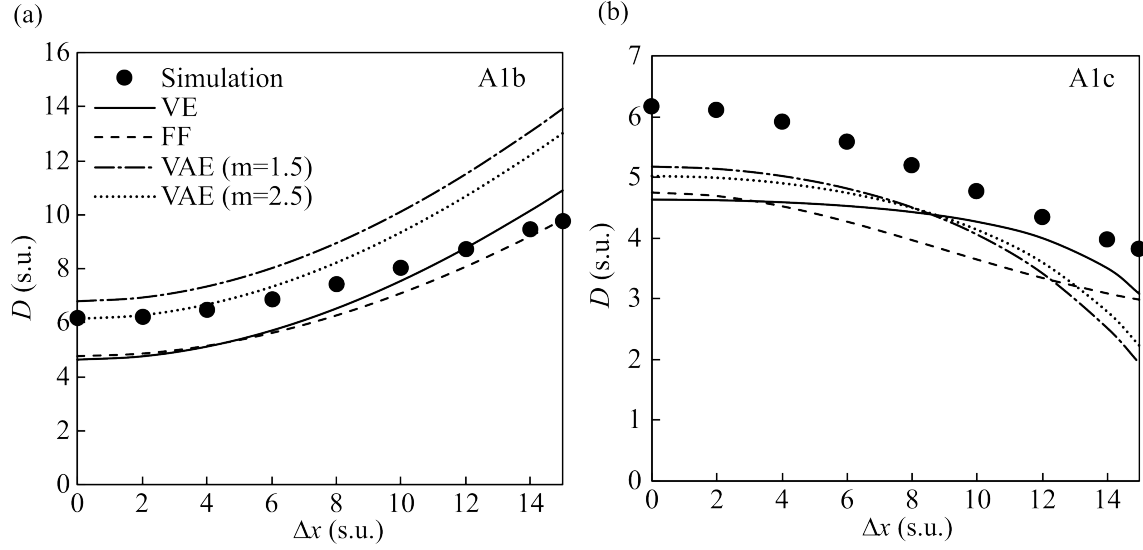
Figure 5.14: Hemiwicking coefficient, D, calculated using a parallel cell analogy for A1b array (a) and using a series cell analogy for A1c array (b) compared to simulation results. In both panels, D is plotted as a function of the mid-pillar displacement, Δx, from the centre of the array ($\Delta x = 0$) towards the sides perpendicular to (a) and in line with (b) the liquid propagation direction. The channel width of the sub-unit cells is calculated using FF, VE and VAE with $m = 1.5$ and $m = 2.5$ approaches.

calculated from a parallel cell in the A1b array are in much better agreement with the simulation results compared to those calculated from the full array approximation shown in Fig. 5.13 (a). Particularly for VE and VAE approaches, since the microchannel approximation is taken for sub-unit cells, the effect of mid-pillar displacement now appears in the calculation, which results in D values being dependent on Δx. The D values predicted by these approaches are also found to be closer to those measured from simulations. A similar result can also be seen for the A1c array (Fig. 5.14 (b)), where the VE and VAE approaches show an improvement in D. The D values are in qualitative agreement with simulations, although they are slightly underestimated.

To probe the breadth of applicability of hydraulic-circuit analogy on asymmetric face-centred A1b and A1c arrays, we extend our simulations over an extensive range of geometries, as illustrated in Fig. 5.15. The geometrical parameters used in these simulations are tabulated in Table. 5.2. The geometries we choose encompass low to high density arrays and short to tall micropillars. In each of the geometries, we vary the position of the mid-pillar from the centre of the array toward the side and inlet for the A1b and A1c arrays, respectively. We also apply parallel-series cells for both A1b and A1c arrays in addition to the parallel and series cells.

Figure 5.16 compares the hemiwicking coefficient predicted by our models and measured
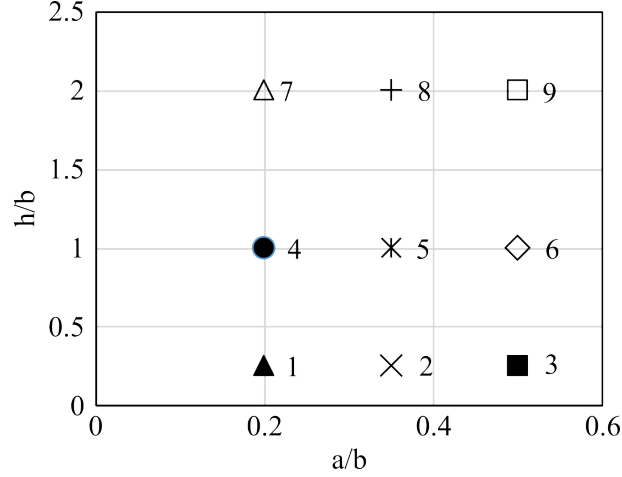
Figure 5.15: Geometries a/b and h/b used for hydraulic-electric circuit analogy for asymmetric face-centred A1b and A1c arrays. The values of a, h and b are given in Table. 5.2.

Table 5.2: Geometrical parameters for hydraulic-electric circuit analogy for asymmetric face-centred A1b and A1c arrays. The data points are denoted in Fig. 5.15.

Data point	Pitch (μm)	Diameter (μm)	Height (μm)
1	40	8	10
2	40	14	10
3	40	20	10
4	40	8	40
5	40	14	40
6	40	20	40
7	40	8	80
8	40	14	80
9	40	20	80

from simulations for A1b arrays. The value of D, in general, increases as the position of the mid-pillar gets closer to the side of the array, as we have seen in Fig. 5.13. Here, we show that our models, either using parallel cells or parallel-series cells, can capture this trend as denoted by a linear slope of each data point. For the parallel cell approximation, we notice that some approaches overestimate the measured values of D from simulation, particularly for parallel cells, when estimating the equivalent channel width using VE and VAE approaches. However, we observe the FF approach is in qualitative agreement with the simulation results. Moreover, all approaches appear to work better for low-density arrays with short pillars. When the pillar density gets higher and the pillar height gets taller, we observe that the implementation of parallel-series cells improves the accuracy of our models, particularly for the VE and VAE
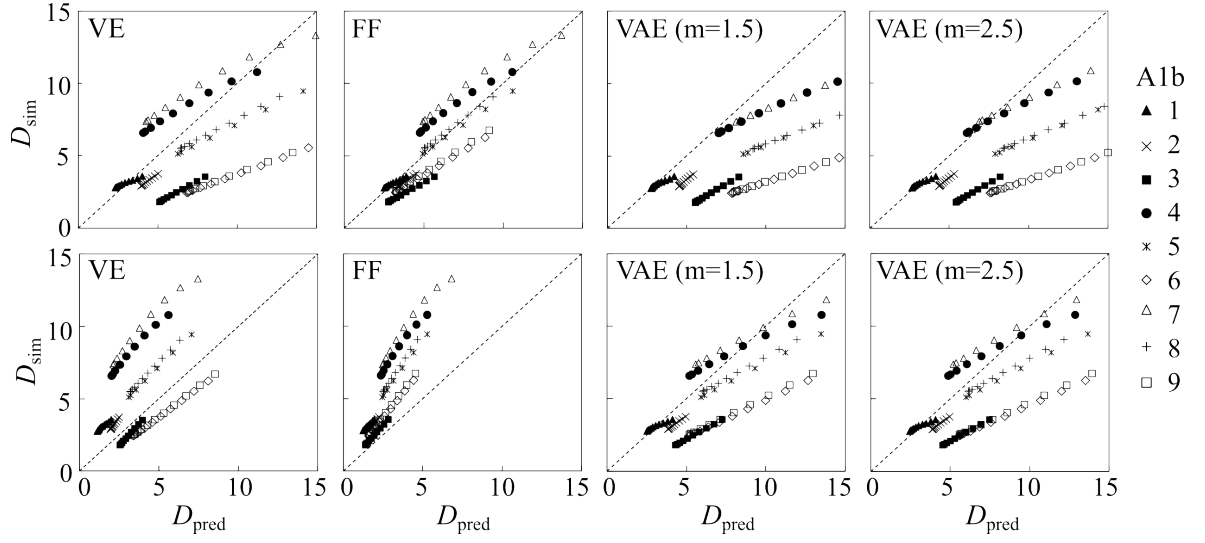
Figure 5.16: Hemiwicking coefficient, D, values measured from simulations plotted against those predicted by parallel cell (top row) and parallel-series cells (bottom row) models using VE (left column) and FF (right column) approaches for the A1b array. Symbols in data points refer to those depicted in Fig. 5.15. The dashed line denotes the slope = 1. All values are given in simulation units (s.u.)
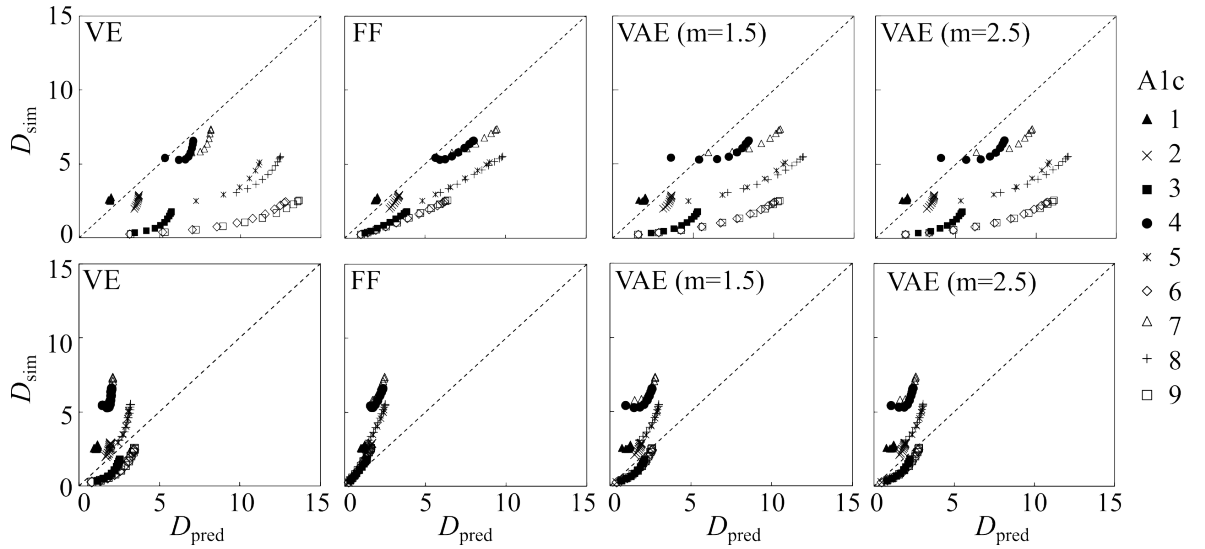
Figure 5.17: Hemiwicking coefficient, D, values measured from simulations plotted against those predicted by series cell (top row) and parallel-series cells (bottom row) models using VE (left column) and FF (right column) approaches for the A1c array. Symbols in data points refer to those depicted in Fig. 5.15. The dashed line denotes the slope = 1. All values are given in simulation units (s.u.)

approaches. However, this does not seem to work for the FF approach, particularly for tall pillar geometries where the predicted D values underestimate the simulated ones.

The comparison between predicted and simulated D values for the A1c arrays is shown in Fig. 5.17. The value of D, in general, decreases as the mid-pillar gets closer to the inlet. Our models capture this trend when the mid-pillar is away from the inlet but fail as the mid-pillar

gets closer to the inlet. We notice that the series cells approximation using any approaches overestimates the simulation results for almost all geometries except for data point 1 geometry ($a/b = 0.2$ and $h/b = 0.25$). For this data point, due to low pillar density and short pillar height, the mid-pillar displacement does not significantly change the fluid flow, resulting in a constant hemiwicking coefficient, which is also captured by our models. Our prediction improves when we approximate the array using parallel-series cells. We observe that our models agree with simulation for high-density arrays (data points 3, 6 and 10). For such arrays, we also observe the VAE approach improves the estimation of the channel width as the liquid-solid interaction area becomes more significant. For low-density arrays, however, our models underestimate the simulation results.

5.3   Discussion

In summary, we have proposed analytical models that are able to predict, in a number of cases, the hemiwicking coefficient for macroscale liquid transport on textured surfaces with regular and irregular pillar arrays. We have performed extensive Lattice Boltzmann simulations to validate the models. Our models do not require explicit consideration of microscale wicking phenomena such as zipping or meniscus extension. This makes our simulations much simpler, as we are only required to simulate the liquid velocity across a unit cell of the pillar arrays. The effects of pinning were also not considered in this work, as the systems studied here are highly wetting (in favour of rapid wicking), and the equilibrium contact angles are well below the lower bound of depinning critical angles.

The derived expression is demonstrated to be flexible as one can adjust it to meet the properties of the geometries. We have shown that our model, originally developed for a square array, can be expanded to other types of geometry, such as face-centred or hexagonal arrays. Furthermore, we have also shown that we can adopt other approaches (e.g. hydraulic-electric circuit analogy) and implement them in our model.

For square arrays, our model has shown its capability to accurately predict the hemiwicking coefficient over a broad range of textural densities for cylindrical and square pillars. However, the model is observed to break down in some cases, particularly in the extreme case, where drag (neglected here) plays an enhanced role, and in the case where the flow is confined in the narrow gap between the pillars.

For face-centred arrays, the original model using the volume equivalent approach appears to deviate from the simulation. However, with the implementation of the hydraulic-electric circuit analogy approach, our models are able to predict the hemiwicking coefficient accurately for symmetric and asymmetric arrays of micropillar for a certain range of textural densities, depending on the type of cells used. For the symmetric face-centred arrays, the parallel cell approach predicts the hemiwicking coefficient for moderately dense arrays (moderate a/b values), whereas the series and the combination of parallel and series cells approaches are applicable for low and high arrays (low and high a/b values), respectively. For the asymmetric face-centred arrays, we show that the parallel cell approach using the face-to-face spacing approximation is applicable for the case where the mid-pillar is moved sideways. When the mid-pillar is moved towards the direction of the propagation, the model presented here can capture the qualitative trend, but the quantitative agreement is generally poor.

We acknowledge that the models presented here are not able to accurately predict all geometries universally. However, with the flexibility to adjust the expression of the hemiwicking coefficient in our model in many cases, one can choose the best expression, which results in the best agreement with simulations. We believe that our model can be extended further to other pillar shapes as long as the contact angles remain low, and it will be interesting to verify this in the future. Hopefully, this work sheds light on complex interfacial interactions that dictate the spreading behaviour in practically useful textured surfaces.

Part III

Liquid Filling on Grooved Surfaces

Wetting of solid surfaces by liquids is ubiquitous in nature and critically important for many technological and industrial applications ranging from printing, coating, microfluidics to oil recovery and carbon capture [63, 106, 107, 108]. Given the importance of surface wettability, along with rapid advances in surface engineering techniques, such as lithography, 3D printing, and surface self-assembly [109, 110, 111], understanding the roles of surface topography on the wetting behaviour of liquids has emerged as a prominent area of research.

Numerous works to date have investigated how surface structures can give rise to advantageous surface wettability [112, 113, 114, 115], including superhydrophobicity, self-cleaning, drag reduction, and directional spreading. However, the majority of these studies take a macroscopic view of wetting phenomena where the liquid-solid-gas interactions are represented by a single parameter describing the contact angle. At the same time, it is well established in the literature that the intermolecular interactions between the liquid and solid molecules can be highly complex [63, 64, 116].

Such intermolecular interactions include hydrogen bonds, van der Waals, dipole-dipole interactions, and others [65]. However, their effect on wetting can be understood by looking at a thin liquid film of thickness e on a solid substrate, from which all intermolecular interactions can be incorporated in terms of an effective interface potential. This is defined as the cost of energy per unit area to maintain the thin film at a given thickness [116]. From this effective interface potential, one can derive the effective repulsive force per unit area between the solid-liquid and liquid-gas interfaces, known as the disjoining pressure [63].

When considering phenomena at length scales smaller or comparable to the range of the effective interface potential (typically, of the order of hundreds of nanometres [116, 117]), a contact angle description of the three-phase interaction in itself is not adequate. It is important to consider the distance-dependent interactions from the solid surface. Indeed, depending on the disjoining pressure profiles (which capture the aforementioned distance-dependent interactions), different wetting states can arise [65, 118]: complete wetting, where liquid fully spreads on the solid surface; partial wetting, where a finite contact angle is formed at the three-phase solid-liquid-gas contact line; and pseudo-partial wetting, where the macroscopic liquid domain (*i.e.* droplet) is surrounded by a thin liquid film.

Previous approaches to computationally study nanoscale fluid phenomena incorporate atomistic details, such as using Molecular Dynamics (MD) [119] and Density Functional Theory (DFT) [120, 121, 122, 123, 124]. Here, we show how a mesoscale model, the phase field model,

can be augmented to enable a wide variety of short and long-range solid-fluid interactions described above. This is distinct from previous phase field wetting simulations, which typically treat wetting as a boundary condition at a solid surface [125, 126], and neglect long-range forces. Since we are interested in static and quasi-static phenomena in this paper, we will directly minimize the free energy of the phase field models.

As phase-field models are computationally less demanding than traditional nanoscale methods, the incorporation of long-range interactions should allow highly complicated structures to be studied. This is relevant not only because smaller and more complex features can be reliably manufactured [127]; but also because they are key for the emergence of interfacial phase transitions, such as liquid adsorption and liquid filling [122, 128, 129, 130], which start at the smallest surface features. Such phase transitions are important for many applications, such as thin film condensation and evaporation [131, 132], and heat transfer [133].

To demonstrate the versatility of the phase field method, we apply it to study liquid filling and emptying on grooved surfaces as the liquid pressure is varied [120, 134, 135]. We will compare the results for short-range and long-range liquid-solid interactions. We will also contrast them for complete, partial, and pseudo-partial wetting scenarios. To the best of our knowledge, this is the first systematic liquid filling transition study for the pseudo-partial wetting case. Due to the competition between short-range attraction and long-range repulsion, it leads to several possible pathways and critical pressure dependence on geometry that are distinct from the complete and partial wetting cases.

CHAPTER 6

Method

6.1 Free Energy Functional

In this chapter, we employ the phase field (PF) method to capture the equilibrium properties of wetting by minimizing the free energy functional using the limited-memory Broyden-Fletcher-Goldfarb-Shanno (L-BFGS) algorithm. The free energy function describes the coexistence of the fluid phases in the system, the interfacial tension between the fluids, and the fluid-solid interactions which determine the wetting state. Our system of interest consists of two immiscible different fluids and solid surfaces. The interface between the two fluids is modelled using a diffuse interface model, which describes a multi-phase system through an order parameter which varies continuously across an interface.

The free energy of a binary fluid system in contact with solid surfaces is given by [61, 136]

$$\Psi = \Psi_b + \Psi_s + \Psi_c. \tag{6.1}$$

Here, the free energy is contributed by the sum of fluid bulk and interface term Ψ_b, fluid-solid interaction Ψ_s, and constraining potential Ψ_c. We shall discuss each of the terms separately. The scalar order parameter $\phi(\mathbf{r})$ is used to represent the local composition of the fluid.

6.1.1 Bulk and Interfacial Energies

Ψ_{b} is the free energy contribution arising from a binary fluid system describing the homogeneous bulk and fluid-fluid interface, given by [39]

$$\Psi_{\mathrm{b}} = \int_V \left[\frac{A}{4} \left(\phi^2 - 1 \right)^2 + \frac{\kappa}{2} |\nabla \phi|^2 \right] \mathrm{d}V, \tag{6.2}$$

where the coefficient A, with the dimension of energy per unit volume, determines the property of the bulk phase, and the coefficient κ, with the dimension of energy per unit length, controls the surface tension between the two fluids. The free energy densities are integrated over the volume of the system V. The first term of the integrand is the Landau-type energy density which describes the free energy contribution due to the local composition of the two fluids. The function forms a quartic double-well potential with two minima occurring at $\phi = 1$ and $\phi = -1$. Throughout this thesis, we shall refer to $\phi = 1$ as the pure liquid phase and $\phi = -1$ as the pure gas phase. The square gradient term is associated with the interfacial energy contribution. This term is responsible for penalizing the formation of fluid-fluid interfaces and is essential for ensuring the interface between the two fluids has a diffuse rather than a step-like transition. The variation of the order parameter across the interface can be determined by analysing the chemical potential, defined as the change of bulk and interfacial energy densities over the order parameter. In equilibrium, the chemical potential is given by

$$\mu \equiv \frac{\mathrm{d}\Psi_{\mathrm{b}}(\phi)}{\mathrm{d}\phi} = A(\phi^3 - \phi) - \kappa \frac{\mathrm{d}^2 \phi}{\mathrm{d}\phi^2} = 0. \tag{6.3}$$

Assuming the interface between the two fluids is flat and located at $x = 0$ and we have the bulk fluid behaviour at $x = \pm\infty$, the solution of this equation leads to the interfacial profile,

$$\phi(x) = \tanh \frac{x}{\sqrt{2}\epsilon}, \tag{6.4}$$

where $\epsilon = \sqrt{\kappa/A}$ defines the width of the diffuse interface. Here, we take $\kappa = 1/A$, which leads to $\epsilon = \kappa$. Higher values of ϵ correspond to stronger interface penalties, resulting in narrower diffuse interfaces, while lower values lead to wider interfaces. Using the tanh profile of the order parameter in Eq. (6.4), we can calculate the surface tension between fluids 1 (liquid) and

2 (gas) by integrating the free energy densities across the interface leading to

$$\gamma_{\text{lg}} = \sqrt{\frac{8}{9}}. \tag{6.5}$$

6.1.2 Fluid-solid Interaction Energies

The second contribution in the free energy function comes from the surface energy, Ψ_{s}, as a result of interactions between fluid and solid. Here, we explore describing the fluid-solid interactions in two ways: via (1) long-range interactions and (2) short-range interactions, which shall soon be discussed separately.

6.1.2.1 Long-range Interactions

When considering wetting phenomena at microscales, the surface energy is determined by complex intermolecular interactions between liquid and solid. We employ distance-dependent long-range solid-liquid interactions to mimic such complexity of intermolecular interactions. The energy contribution can be written as

$$\Psi_{\text{s}} = \int_V \mathcal{F}_{\text{s}}(\mathbf{r}) f(\phi) \mathrm{d}V. \tag{6.6}$$

$\mathcal{F}_{\text{s}}(\mathbf{r})$ is the long-range interaction potential between liquid and solid separated by a distance $\mathbf{r}$. We are free to choose any $\mathcal{F}_{\text{s}}(\mathbf{r})$ we desire, but for this work we choose

$$\mathcal{F}_{\text{s}}(\mathbf{r}) = \int_{V_{\text{s}}} u_{\text{lr}}(\mathbf{r}) \mathrm{d}V_{\text{s}}, \tag{6.7}$$

where $u_{\text{lr}}(\mathbf{r})$, namely the effective interaction, is integrated over the volume of solid, V_s. The effective interactions $u_{\text{lr}}(\mathbf{r})$ can take one of the following forms

$$u_{\text{lr}}^1(\mathbf{r}) = \frac{\alpha}{(\beta + |\mathbf{r} - \mathbf{r}_{\text{s}}|)^6}, \tag{6.8}$$

or

$$u_{\text{lr}}^2(\mathbf{r}) = \begin{cases} -u_{\text{o}} & , |\mathbf{r} - \mathbf{r}_{\text{s}}| < \sigma, \\ u_{\text{p}} \left(\frac{\sigma}{|\mathbf{r} - \mathbf{r}_{\text{s}}|} \right)^6 & , |\mathbf{r} - \mathbf{r}_{\text{s}}| \geq \sigma, \end{cases} \tag{6.9}$$

in which α, β, σ, u_{o} and u_{p} are parameters in the models and $\mathbf{r}_{\mathrm{s}}$ is the coordinate position in the solid. The effective interaction u_{lr}^1 can be either attractive or repulsive depending on the sign of α. The parameter β, which is taken to be positive, is used to avoid u_{lr}^1 going to infinity for $|\mathbf{r} - \mathbf{r}_{\mathrm{s}}| = 0$ and to control the width of the decaying interaction u_{lr}^1. The form of u_{lr}^2 is designed to have an attractive interaction near the surface with a finite value of $-u_{\mathrm{o}}$ and a repulsive interaction far from the surface with a maximum value of u_{p} at $|\mathbf{r} - \mathbf{r}_{\mathrm{s}}| = \sigma$. The effective interaction u_{lr}^2 is chosen so that, when integrated, the long-range liquid-solid interaction is repulsive close to the solid surface and attractive far from the surface.

To ensure this interaction energy density is only contributed by the interaction between liquid and solid, it must be modulated by the local fluid composition, such that the liquid phase should experience the full $\mathcal{F}_{\mathrm{s}}(\mathbf{r})$, and the gas phase should not experience $\mathcal{F}_{\mathrm{s}}(\mathbf{r})$. For this purpose, we use $f(\phi)$, which is a fourth order polynomial that switches $\mathcal{F}_{\mathrm{s}}(\mathbf{r})$ between the liquid and gas phases, given by

$$f(\phi) = \frac{3}{4}\phi - \frac{1}{3}t(\mathbf{r})\phi^2 - \frac{1}{4}\phi^3 + \frac{1}{6}t(\mathbf{r})\phi^4 + \frac{1}{6}(t(\mathbf{r}) + 3), \tag{6.10}$$

with $t(\mathbf{r}) = -\mathrm{sign}(\mathcal{F}_{\mathrm{s}}(\mathbf{r}))$. We choose the form in Eq. (6.10) because it prevents the enrichment of one of the phases at the surface owing to the following features: (i) $\frac{\mathrm{d}\Psi_{\mathrm{s}}}{\mathrm{d}\phi} = 0$ at the bulk equilibrium values of $\phi = \pm 1$, (ii) Ψ_{s} increases monotonically with $|\phi|$ for $|\phi| > 1$ which gives an energy penalty to the total free energy, and (iii) Ψ_{s} is globally minimized at $\phi = +1$ (*i.e.* the liquid phase) for $\mathcal{F}_{\mathrm{s}}(\mathbf{r}) < 0$ and at $\phi = -1$ (*i.e.* the gas phase) for $\mathcal{F}_{\mathrm{s}}(\mathbf{r}) > 0$. Without the enrichment at the surface, we are able to maintain the simulation stability as well as approximate the fluid incompressibility.

6.1.2.2 Short-range Interactions

The second way to introduce the liquid-solid interaction, following Cahn [125], is to use a short-range interaction between liquid and solid at the surface, which can be approximated by an integral over the solid surface area A,

$$\Psi_{\mathrm{s}} = \int_A \mathcal{F}_{\mathrm{s}}(\mathbf{r}_{\mathrm{s}}) f(\phi_{\mathrm{s}}) \mathrm{d}A, \tag{6.11}$$

where we recall that $f(\phi_s)$ is the polynomial form in Eq. (6.10) for $\phi = \phi_s$, where ϕ_s is the value of ϕ at the solid surface. To calculate the liquid-solid energy density at the surface, $\mathcal{F}_s(\mathbf{r}_s)$, we relate its value to the gas-solid, liquid-solid, and liquid-gas surface tensions, γ_{gs}, γ_{ls} and γ_{lg} respectively, via the spreading parameter S, where $S = \gamma_{gs} - \gamma_{ls} - \gamma_{lg}$. The surface energy density must be equal to the gas-solid surface tension when the surface is completely dry $(\mathcal{F}_s(\mathbf{r}_s)f(\phi_s = -1) = \gamma_{gs})$, and be equal to the liquid-solid surface tension when the surface is completely wet $(\mathcal{F}_s(\mathbf{r}_s)f(\phi_s = +1) = \gamma_{ls})$. Therefore, from Eq. (6.10) we can have the relation $\gamma_{gs} - \gamma_{ls} = -\mathcal{F}_s(\mathbf{r}_s)$, independent of the value of $t(\mathbf{r})$ leading to

$$\mathcal{F}_s(\mathbf{r}_s) = -S - \gamma_{lg}. \tag{6.12}$$

For partial wetting $(S < 0)$, we can also relate $\mathcal{F}_s(\mathbf{r}_s)$ to the contact angle θ via Young equation, $\gamma_{lg} \cos\theta = \gamma_{gs} - \gamma_{ls}$, yielding

$$\mathcal{F}_s(\mathbf{r}_s) = -\sqrt{8/9} \cos\theta, \tag{6.13}$$

where we have substituted $\gamma_{lg} = \sqrt{8/9}$ from Eq. (6.5).

6.1.3 Constraining Potential

The last term in the free energy in Eq. (6.1), Ψ_{ext}, reflects the constraint applied to the system, which can be chosen to either define the pressure difference between the liquid and gas, or constrain the volume of the liquid phase. In the first case, the pressure difference across the liquid-gas interface, Δp, can be imposed through the term

$$\Psi_c = -\Delta p V_l, \tag{6.14}$$

where $\Delta p = p_l - p_g$, with p_l and p_g as the liquid and gas pressures, respectively [61]. In this approach, the liquid volume can vary until the system reaches equilibrium in the grand canonical ensemble. In the second case, we can instead constrain the liquid volume through the soft constraint

$$\Psi_c = \frac{1}{2}k\left(V_l - V_0\right)^2, \tag{6.15}$$

where $k > 0$ is a constant and V_0 is the target volume [136]. Here, the liquid volume is maintained as approximately the same amount as the target volume, *i.e.*, we are in the canonical

ensemble. In either approach, V_l is the actual liquid volume present in the simulation, given by

$$V_l = \int_V \frac{\phi + 1}{2} dV, \tag{6.16}$$

where V is the volume of the simulation domain.

6.2 Simulation Implementation

6.2.1 Discretization

To implement the energy minimization of the free energy functional for a general fluid configuration and solid boundary conditions, the computational domain is discretized into $N_x \times N_y \times N_z$ cubic lattice of points, which we call nodes. Each node is associated with a value of ϕ_{ijk}, where $i, j, k \in \{1, \ldots, N\}$ indicate the spatial dimension in the x-, y-, and z-directions, respectively. The spatial dimension between adjacent points is labelled as G. Each of the nodes is labelled according to whether it is within the bulk of the system (bulk nodes), within the solid (solid nodes), or at the surface of the solid boundary (surface nodes). At initialization, each node in the computational domain is assigned to an initial ϕ. However, the solid nodes do not contribute to the total free energy and the free energy gradients of the system, hence are not updated in the energy minimization. The illustration of node arrangement and assignment is shown in Fig. 6.1.
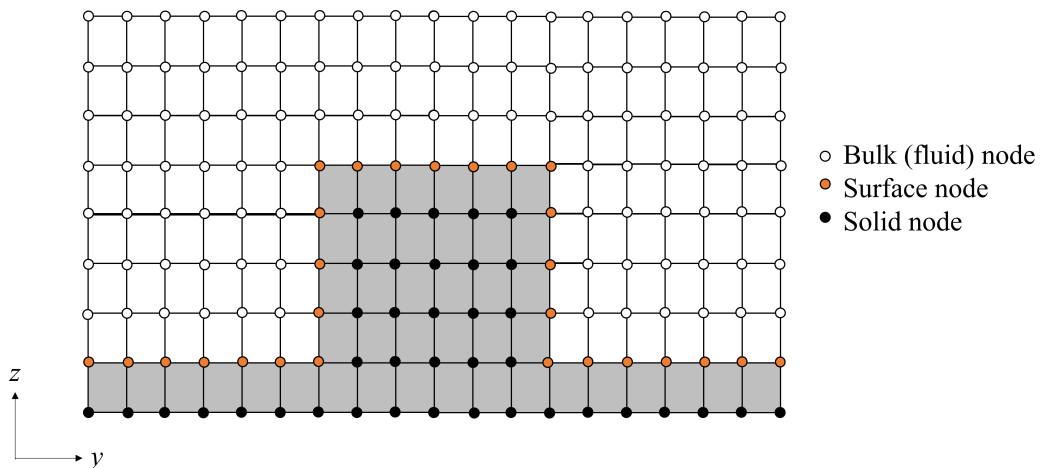

Figure 6.1: Illustration of the arrangement and assignment of the nodes in a 2D slice through 3D simulation domain. The shaded gray box shows a post on a flat solid surface.

The total free energy in Eq. (6.1) is discretized as follows. The bulk and interfacial energies

in Eq. (6.2) can be written as

$$\Psi_b = \sum_{ijk}^{N} \left[\frac{A}{4} \left(\phi_{ijk}^4 - 2\phi_{ijk}^2 + 1 \right) \right.$$
$$\left. + \frac{\kappa}{2} \left(\left(\frac{\partial \phi_{ijk}}{\partial x} \right)^2 + \left(\frac{\partial \phi_{ijk}}{\partial y} \right)^2 + \left(\frac{\partial \phi_{ijk}}{\partial z} \right)^2 \right) \right] W_{ijk} G^3. \tag{6.17}$$

The volume weights W_{ijk} denote the volume fraction associated with each node that lies outside the solid surface. For bulk nodes, $W_{ijk} = 1$, but for surface nodes, $W_{ijk} < 1$, depending on the local surface structure. The spatial derivatives are approximated using the Taylor series expansion to a second-order accuracy in G to avoid the checkerboard instability [136]. This is given by

$$\left(\frac{\partial \phi_{ijk}}{\partial x} \right)^2 = \frac{1}{2G^2} \left[\left(\phi_{(i+1)jk} - \phi_{ijk} \right)^2 + \left(\phi_{(i-1)jk} - \phi_{ijk} \right)^2 \right], \tag{6.18}$$

and similarly for the derivatives in y and z directions.

The long-range fluid-solid interaction energy contribution in Eq. (6.6) is written as

$$\Psi_s = \sum_{ijk}^{N} \left[\mathcal{F}_s(\mathbf{r}) \left(\frac{3}{4}\phi_{ijk} + \frac{1}{3}t(\mathbf{r})\phi_{ijk}^2 - \frac{1}{4}\phi_{ijk}^3 + \frac{1}{6}t(\mathbf{r})\phi_{ijk}^4 + \frac{1}{6}(t(\mathbf{r}) + 3) \right) \right] W_{ijk} G^3, \tag{6.19}$$

whereas the short-range interaction energy in Eq. (6.11) is written as

$$\Psi_s = \sum_{ijk}^{\text{Surface}} \left[\mathcal{F}_s(\mathbf{r_s}) \left(\frac{3}{4}\phi_{ijk} + \frac{1}{3}t(\mathbf{r})\phi_{ijk}^2 - \frac{1}{4}\phi_{ijk}^3 + \frac{1}{6}t(\mathbf{r})\phi_{ijk}^4 + \frac{1}{6}(t(\mathbf{r}) + 3) \right) \right] S_{ijk} G^2, \tag{6.20}$$

where the surface weights S_{ijk}, in unit of G, describe the surface area associated with each node. Similar to W_{ijk}, the values of S_{ijk} also depend on the local surface structure. The liquid-solid interaction potentials $\mathcal{F}_s(\mathbf{r_s})$, as given in Eq. (6.12) and Eq. (6.13), are independent of ϕ, hence, do not require to be discretized. However, the long-range interaction potentials, $\mathcal{F}_s(\mathbf{r})$, depend on ϕ due to distance-dependent interaction between liquid and solid nodes. The discretization of $\mathcal{F}_s(\mathbf{r})$ shall be discussed in the next section.

The constraining energy contribution is discretized as

$$\Psi_c = -\Delta p \sum_{ijk}^{N} \left(\frac{\phi_{ijk} + 1}{2} \right) W_{ijk} G^3, \tag{6.21}$$

for the pressure constraint, and

$$\Psi_c = \frac{1}{2}k\sum_{ijk}^{N}\left(\frac{\phi_{ijk}+1}{2}-V_0\right)^2 W_{ijk}G^3,\qquad(6.22)$$

for the volume constraint.

Periodic boundary conditions are employed in the x and y directions if solid surfaces do not cap the simulation boundaries. In the z-direction, perpendicular to the texture plane, the z-gradient at $k = N_z$ is fixed at zero in order to enforce bulk fluid behaviour at the top of the system.

In the minimization routine, the value of ϕ_{ijk} of each node needs to be updated in order to achieve the minimum total energy configuration. To do this, the gradient of the total free energy with respect to ϕ_{ijk} has to be computed to determine the direction of the update, either to increase or decrease the value of ϕ_{ijk}. In general, the gradient can be calculated as

$$\frac{\partial\Psi}{\partial\phi_{ijk}} = \frac{\partial\Psi_b}{\partial\phi_{ijk}} + \frac{\partial\Psi_c}{\partial\phi_{ijk}} + \frac{\partial\Psi_s}{\partial\phi_{ijk}},\qquad(6.23)$$

where the derivative in each term can be obtained by differentiating the discretized equations in Eq.(6.17 - 6.22).

6.2.2 Grid Refinement and Surface Images

When we compute the numerical integration of interaction energy density $\mathcal{F}_s(\mathbf{r})$ as in Eq. (6.24), all effective liquid-solid interactions are taken into account. These include contributions from bulk fluid-solid, bulk fluid-surface, surface-solid, and surface-surface nodes interactions. A schematic of these interactions is illustrated in Fig. 6.2 (a). Here, three types of nodes are shown: bulk fluid nodes, solid nodes, and surface nodes at the fluid-solid interface containing part fluid and part solid. Each node is represented by a cube with a side length of G (which also corresponds to a lattice spacing) for the fluid nodes. Typically, we use $G = 0.02$ in simulation units. The interface width is set such that $\epsilon = 2G$. For the solid and surface nodes, we may use grid refinement, see Fig. 6.2 (b). This leads to a smaller cube of side length is $G/(2g_{\mathrm{res}}-1)$ for the solid nodes, with $g_{\mathrm{res}} = 1, 2, 3, ..., n$. For the surface nodes, we only refine the solid fraction.

In addition to grid refinement, we also employ several periodic images of the solid domain
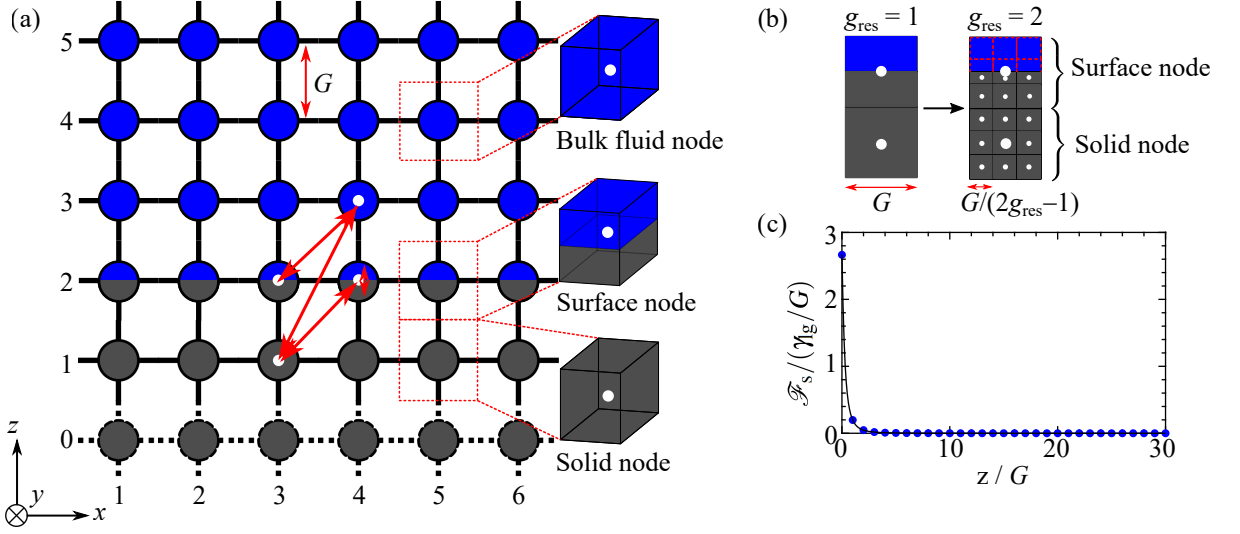
Figure 6.2: (a) Schematic of lattice nodes configuration with a flat solid surface showing fluid-solid interactions, including between bulk fluid-solid, bulk fluid-surface, surface-solid and surface-surface nodes. (b) Lattice nodes containing solid can be refined with a grid resolution of g_{res}. Here we illustrate the grid refinement on a 2D xz plane of the surface and solid nodes with $g_{\text{res}} = 2$. For the surface nodes, only the solid fraction is refined. (c) Reduced interaction energy density $\mathcal{F}_{\text{s}}/(\gamma_{\text{lg}}/G)$ as a function of fluid node position in the z-direction ($z = 0$ is taken at the surface node). Here, we use $u_{\text{lr}}^1(\mathbf{r})$ with $a = 6.0 \times 10^{-4}$ and $b = 0.5$. We compare the results from the numerical calculation (blue dot) and the analytical solution (black solid line).

to ensure the long-range interactions are sufficiently accounted. To determine the number of images needed, we calculate a cutoff point of $\mathcal{F}_{\text{s}}(\mathbf{r})$ such that beyond which its contribution to the integration is considerably small. The solid images are added outside the simulation domain in the x- and y-directions, as well as below the bottom surface (see Fig. 6.2 (a)).

As discussed above, the calculation of $\mathcal{F}_{\text{s}}(\mathbf{r})$ takes into account fluid-solid interactions that are contributed by bulk fluid-solid, bulk fluid-surface, surface-solid, and surface-surface nodes interactions. For a bulk fluid-solid nodes interaction, a fluid node is considered to interact with a unit volume of a cubic solid node that has a distance of $|\mathbf{r} - \mathbf{r}_{\text{s}}|$ from the fluid node. The same scheme applies to the interaction of the surface-solid nodes, although we must account that only a fraction of the surface node is fluid. For bulk fluid-surface interactions, the interaction only occurs with the solid fraction. We use a solid weight W_{s} which describes the volume fraction of solid associated with each node that lies inside the solid surface. For solid nodes, $W_{\text{s}} = 1$, but for surface nodes $W_{\text{s}} < 1$, depending on the local surface structure. Finally, for the interactions between two surface nodes, we must carefully account for the fractions of fluid and solid in respective nodes. Note that the solid parts are centered at their center of mass, while the fluid part is centered at the original node position at the fluid-solid interface.

The numerical computation of $\mathcal{F}_{\mathrm{s}}(\mathbf{r})$ is done using the middle Riemann sum approach, taking the nodes as the midpoints of the sub-interval of the integration, given by

$$\mathcal{F}_{\mathrm{s}}(\mathbf{r}) = \int_{V_{\mathrm{s}}} u_{\mathrm{lr}}(\mathbf{r})\mathrm{d}V_{\mathrm{s}} \rightarrow \sum_{s=1}^{N_s} u_{\mathrm{lr}}(|\mathbf{r} - \mathbf{r}_{\mathrm{s}}|)W_{\mathrm{s}}(G/(2g_{\mathrm{res}} - 1))^3, \tag{6.24}$$

where $|\mathbf{r} - \mathbf{r}_{\mathrm{s}}| = \sqrt{|\mathbf{x} - \mathbf{x}_s|^2 + |\mathbf{y} - \mathbf{y}_s|^2 + |\mathbf{z} - \mathbf{z}_s|^2}$, with $\{\mathbf{x,y,z}\}$ as the fluid position and $\{\mathbf{x}_{\mathrm{s}}, \mathbf{y}_{\mathrm{s}}, \mathbf{z}_{\mathrm{s}}\}$ as the solid position. N_s is the total of solid and surface nodes. The comparison with the analytical solution for a flat solid surface is shown in Fig. 6.2 (c). A good agreement is obtained between the simulation and analytical solution. Since effective interaction $u_{\mathrm{lr}}(\mathbf{r})$ decays quickly, the nodes far away from the surface have minimal contributions to the total liquid-solid interaction energy. Although the interaction energy density calculation is computationally expensive, particularly for a large domain and a high solid node resolution, it is only calculated once at the start of the simulation.

Upon the energy minimization routine, the discretized order parameter in the bulk fluid and surface nodes will evolve towards the minimum energy configurations. We employ the L-BFGS algorithm due to its efficiency for problems with a large number of degrees of freedom. For details on the energy minimization routine, see Refs. [61, 136].

CHAPTER 7

Results

7.1 Wetting on a Flat Surface

7.1.1 Long-range Interactions
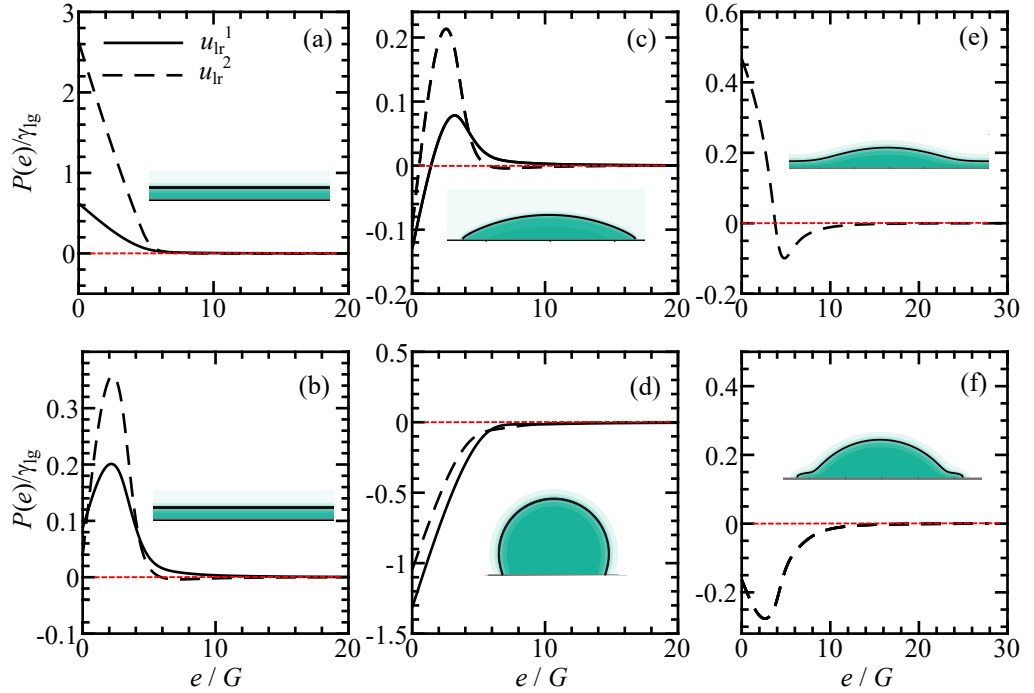
Figure 7.1: Plots of the reduced effective interface potential $P(e)/\gamma_{\mathrm{lg}}$ of a thin liquid film versus thickness e (in lattice unit G) for different wetting states: (a,b) complete wetting, (c,d) partial wetting, and (e,f) pseudo-partial wetting. Insets show the equilibrium state of a droplet on a flat surface. Here, for u_{lr}^1 we use (in simulation unit) $\beta = 0.5$ and α of $-8 \times 10^{-4}, -4 \times 10^{-4}, -3.2 \times 10^{-4}$ and 1×10^4 for (a-d), respectively. For u_{lr}^2, we choose $\sigma = 3$ and $(u_{\mathrm{o}}, u_{\mathrm{p}})$ of $(2.4 \times 10^{-6}, 1 \times 10^{-8})$, $(1.12 \times 10^{-7}, 1 \times 10^{-8})$, $(1 \times 10^{-7}, 1 \times 10^{-8})$, $(1.0 \times 10^{-6}, 1.0 \times 10^{-6})$, $(2 \times 10^{-6}, 1 \times 10^{-6})$ and $(2 \times 10^{-6}, 1.4 \times 10^{-6})$ for (a-f), respectively.

To evaluate the effect of the long-range liquid-solid interactions, it is convenient to look at
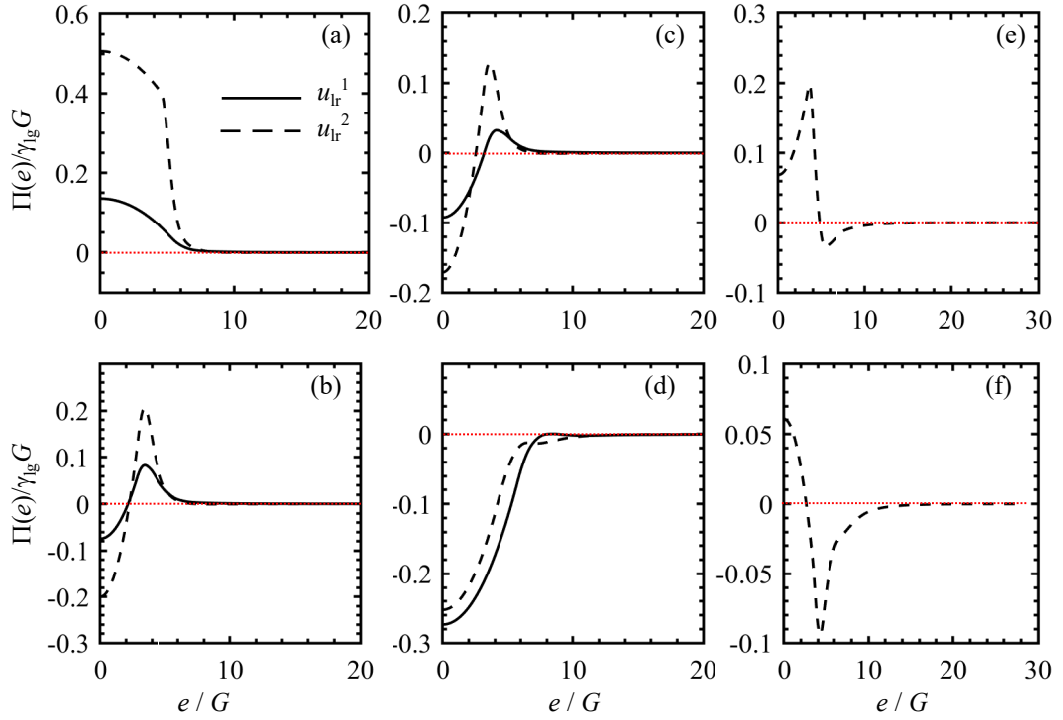
Figure 7.2: Disjoining pressure $\Pi(e)$ (scaled by $\gamma_{\mathrm{lg}}G$) plotted as a function of film thickness e (in lattice unit G) for complete (a,b), partial (c,d) and pseudo-partial (e,f) cases. $\Pi(e)$ is obtained from the first derivative of $P(e)/\gamma_{\mathrm{lg}}$ curve with respect to e in the corresponding panels of Fig. 7.1

the free energy per unit area of a thin film with a given thickness of e, given by [45, 65]

$$F\left(e\right) = \gamma_{\mathrm{lg}} + \gamma_{\mathrm{ls}} + P\left(e\right). \tag{7.1}$$

Here, $P(e)$, called the effective interface potential [63], is related to the disjoining pressure $\Pi(e)$ in the thin film due to liquid-solid interactions, which vanishes when the thin film is sufficiently thick $(e \to \infty)$ and acts as the spreading parameter, $S = P(0)$, as the film becomes infinitesimally thin $(e \to 0)$. The disjoining pressure is defined as $\Pi(e) = -\frac{\mathrm{d}P(e)}{\mathrm{d}e}$.

In our model, $\gamma_{\mathrm{lg}} = \sqrt{8/9}$, and γ_{ls} can be calculated when the film thickness is sufficiently thick such that $\gamma_{\mathrm{ls}} = F(e \to \infty) - \gamma_{\mathrm{lg}}$. $P(e)$ can then be determined by evaluating $F(e)$ at varying film thickness. To get the variation of $P(e)$, we simulate a liquid film with small interfacial area on a flat surface to avoid the coexistence between a liquid film and a dry solid. For convenience, here we employ the volume constraint as given in Eq. (6.15), and vary the film thickness by adjusting the target volume V_0 in the simulation. Different variations of $P(e)$ representative of different wetting states are shown in Fig. 7.1. These capture the profiles previously proposed in the literature, such as by Brochard, *et al.* [65]. In the insets, we show

an equilibrium state of a sessile droplet placed on a flat surface under the respective wetting states. We can also show the corresponding disjoining pressure $\Pi(e)$ profiles of these wetting states, as shown in Fig. 7.2.

Figure 7.1 (a,b) show the complete wetting case indicated by the positive value of $P(0)$ ($S > 0$) and the formation of a liquid thin film (insets). In panel (a), we use a large negative α in the effective interaction u_{lr}^1. Here, the functional $P(e)$ decreases as the film thickness increases, which results in positive $\Pi(e)$ and S. In panel (b), the value of α is less negative than that in panel (a). This makes $P(e)$ non-monotonic leading to negative $\Pi(e)$ at small e. The resulting value of S is also smaller but remains positive. A similar profile of $P(e)$ can be seen when using the effective interaction u_{lr}^2. Here, $|-u_{\mathrm{o}}| \gg |u_{\mathrm{p}}|$ is used to give a strong attractive interaction near the solid surface to allow the droplet to spread across the surface.

Figure 7.1 (c,d) show the partial wetting case indicated by the negative value of $P(0)$ ($S < 0$) and droplets with finite contact angles ($\theta < 90°$ for panel (c) and $\theta > 90°$ for panel (d)), as depicted in the inset of the figures. In panel (c), we still use a negative α in effective interaction u_{lr}^1 but the value is smaller than that in the complete wetting case. As a result, the liquid-solid interaction is weaker. Similar to Fig. 7.1 (b), $P(e)$ is increasing at small e but decreasing at large e. However, the resulting spreading parameter S is negative. If we now switch to positive α, $P(e)$ is monotonically increasing with a larger negative S, as shown in panel (d). For $\alpha = 0$, $\theta = 90°$ and $S < 0$. We can also show the partial wetting case using effective interaction u_{lr}^2, as depicted in Fig. 7.1 (c,d), where u_{p} is increased to make a stronger repulsive interaction preventing the droplet from completely spreading.

If we tune the variable parameters in u_{lr}^2 such that the short-range attractive interaction is strong enough to allow the liquid spreading and the long-range repulsive interaction is sufficient to stabilize a droplet, we will obtain a pseudo-partial wetting case, where a droplet is surrounded by a thin liquid film wetting the solid surface, as shown in the insets of Fig. 7.1 (e,f). The spreading parameter S can be negative or positive [65, 137], and the $P(e)$ profile is characterized by a minimum at a certain e. In panel (e), the attractive term is quite strong at short ranges (due to large $|-u_{\mathrm{o}}|$) that $P(e)$ is decreasing. Since $S > 0$, the thin film extends indefinitely. At long ranges, the repulsive term becomes more dominant (due to moderate value of $|u_{\mathrm{p}}|$) to change the direction of $P(e)$ to be increasing. The droplet formed in this condition has a lower contact angle, as seen in the inset. When the strength of repulsive terms is increased, but the attractive term is kept unchanged, the decreasing trend of $P(e)$ at short ranges reduces, and

the increasing trend of $P(e)$ at long ranges increases, as shown in panel (f). As can be seen, the contact angle of the droplet is larger (see inset). Moreover, since $S < 0$, the thin film does not extend indefinitely, as illustrated in the inset. The pseudo-partial wetting case cannot be obtained with effective interaction u_{lr}^1.

7.1.2   Short-range Interactions
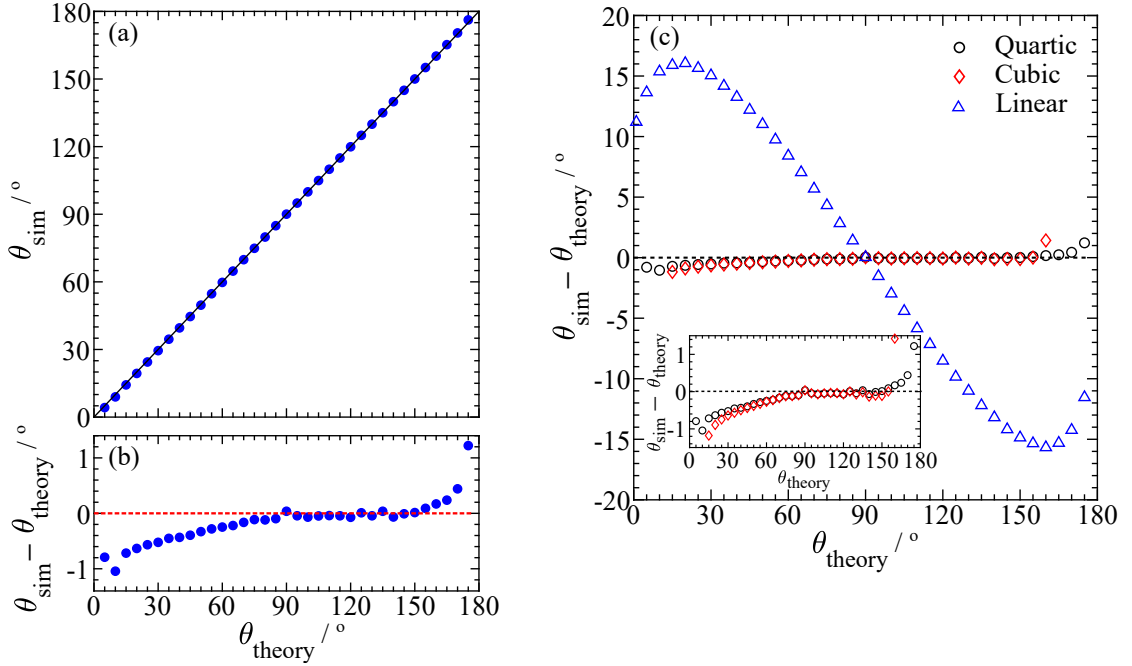
Figure 7.3: (a) Comparison of the input (θ_{theory}) and the measured (θ_{sim}) contact angles when the short-range interaction is used in the surface energy density. (b) Absolute error of the measured contact angle. Excellent agreement is obtained with an error of $< 1°$. (c) Absolute error of the measured contact angle for different forms of $f(\phi_{\mathrm{s}})$: linear, cubic and quartic functions. Inset shows the comparison of absolute error in the measured contact angle between cubic and quartic functions.

When considering large-scale wetting phenomena, the long-range liquid-solid interactions discussed in the preceding sub-section are often not directly relevant, as they occur at much smaller length scales. The short-range surface energy density implemented in the free energy is directly related to the contact angle at the surface via Eq. (6.13). Similar short-range energy densities have previously been demonstrated in the literature [62]. Here, the main difference is the quartic form of $f(\phi_{\mathrm{s}})$. In Fig. 7.3 (a), we compare the measured contact angle of a sessile 2D drop from the simulation, labelled θ_{sim}, with the input contact angle, θ_{theory}. To measure the contact angle, we fit a circular arc to the drop profile. We found an excellent accuracy of the contact angle with the error of $< 1°$ (Fig. 7.3 (b)). Such accuracy is superior

Table 7.1: Forms of $f(\phi_{\rm s})$ for linear, cubic and quartic functions.

Function name	$f(\phi_{\rm s})$	Remark
Linear [138]	$h\phi_{\rm s}$	$h = {\rm sign}(\pi/2 - \theta)\sqrt{2\cos(\alpha/3)(1 - \cos(\alpha/3))}$
		and $\alpha = \arccos(\sin\theta)$
Cubic [138]	$-\sqrt{2}\cos(\theta)(-\phi_{\rm s}^3/6 + \phi_{\rm s}/2 + 1/3)$	-
Quartic	$\frac{3}{4}\phi_{\rm s} - \frac{1}{3}t(\mathbf{r})\phi_{\rm s}^2 - \frac{1}{4}\phi_{\rm s}^3 + \frac{1}{6}t(\mathbf{r})\phi_{\rm s}^4 + \frac{1}{6}(t(\mathbf{r}) + 3)$	Used in this chapter

compared to a range of frequently used forms of $f(\phi_{\rm s})$ [138] including linear and cubic models. The comparisons between the different forms of $f(\phi_{\rm s})$ are shown in Fig. 7.3 (c), which shows a comparison of the absolute error of the measured contact angle ($\theta_{\rm sim} - \theta_{\rm theory}$) obtained for different forms of $f(\phi_{\rm s})$, as tabulated in Table. 7.1.

7.2 Wetting on Grooved Surfaces

Our next investigation is the wetting behaviour of liquid on a structured surface. In this context, we consider a long periodic grooved surface with a groove width of d, depth h, and wall barrier width w, as shown in Fig. 7.4 (a). To reduce the simulation cost, it is only necessary to simulate a single groove unit cell with periodic boundary conditions being applied in the x and y directions to capture the periodicity of the grooves. In this work, the simulation domain size is chosen to be $N_x = w + d$, $N_y = 6G$ and $N_z = h + 50G$. The groove dimension is taken as $w = h = 50G$ and $d = 20G$, unless stated otherwise. The typical liquid-solid interaction energy densities due to long-range interactions across the system are shown in Fig. 7.4 (b) for the effective interactions $u_{\rm lr}^1$ and $u_{\rm lr}^2$. Here, the energy density is scaled by $\gamma_{\rm lg}/G$. For $u_{\rm lr}^1$, the parameter α is taken as a negative value; hence, liquid and solid experience an attractive interaction which is higher at the surface and decays towards zero farther from the surface. This is depicted in Fig. 7.4 (c) for complete and partial wetting cases at $x = 0$ and varying z. The decay rate of $u_{\rm lr}^1$ depends on the parameter β. The higher β, the slower the decay and the longer the interaction tail. For $u_{\rm lr}^2$, the attractive interaction only occurs near the surface, and the interaction becomes repulsive in the bulk of the liquid, as depicted in Fig. 7.4 (c) for the pseudo-partial wetting case. It is also worth noting that for both effective interactions, the liquid-solid interaction is stronger at the bottom corners and weaker at the top corners of the barrier wall, consistent with observations from MD [139] and DFT [121, 122] simulations.
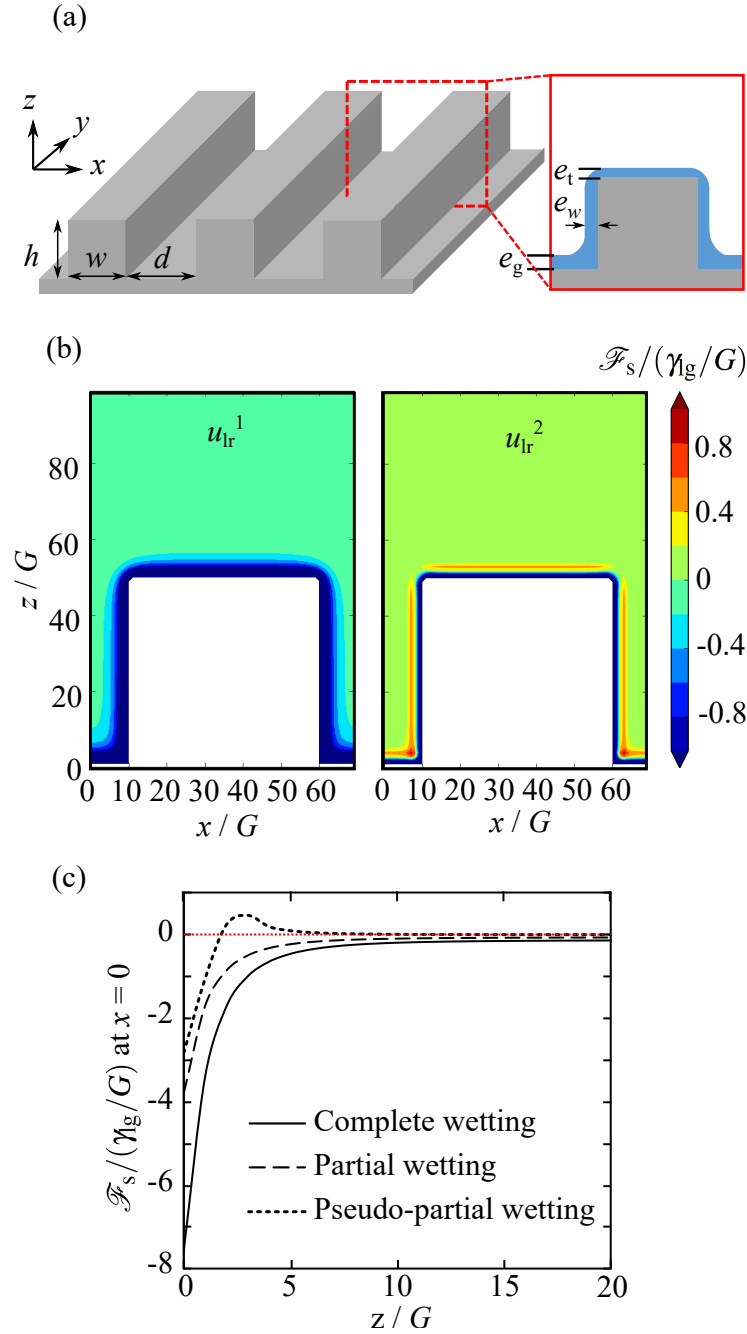
Figure 7.4: (a) (left) 3D sketch of the groove patterned surface and (right) a 2D slice of a unit cell of the surface. (b) Contour plots of the typical profile of reduced interaction energy density $\mathcal{F}_s/(\gamma_{lg}/G)$ due to effective interactions u_{lr}^1 (left) and u_{lr}^2 (right) for a 2D slice of the system. Color bars show the value of the energy density. (c) Reduced interaction energy density $\mathcal{F}_s/(\gamma_{lg}/G)$ plotted as a function of position in the z direction taken at $x = 0$ for the complete and partial wetting cases using u_{lr}^1 and the pseudo-partial wetting case using u_{lr}^2.

7.2.1 Complete Wetting

Figure 7.5 (a,b,c) shows the filling and emptying transition as the pressure Δp is varied, for the case of complete wetting. Here, we use u_{lr}^1 for the long-range interaction with $\alpha = -8 \times 10^{-4}$
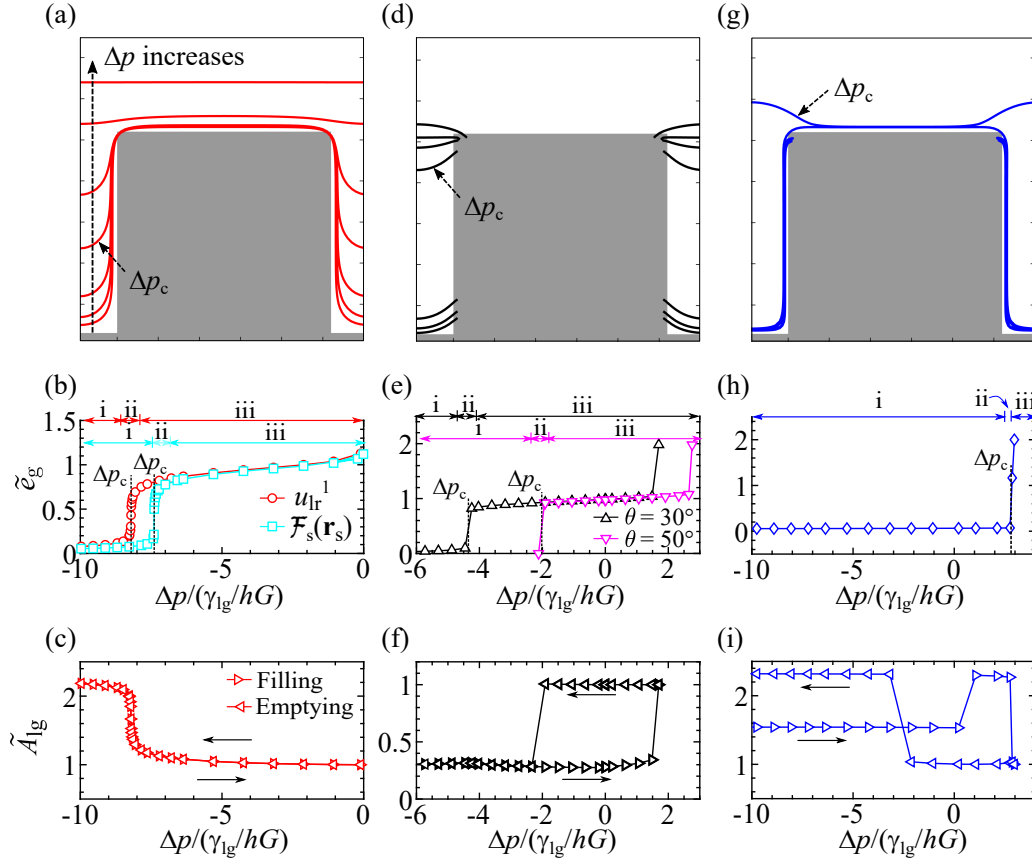
Figure 7.5: Liquid filling processes on the grooved surface for complete (a, b, c), partial (d, e, f) and pseudo-partial wetting (g, h, i) cases. Here, $d/h = 0.4$. Each contour line in panels (a, d, g) corresponds to the liquid-gas interface ($\phi = 0$) at an increasing Δp. Panels (b, e, h) show the plot of reduced liquid film thickness measured at the middle of the gap $\widetilde{e}_g$ against reduced pressure difference $\Delta p/(\gamma_{lg}/hG)$. In panel (b) we show the complete wetting case when using $\mathcal{F}_s(\mathbf{r})$ with u_{lr}^1 and $\mathcal{F}_s(\mathbf{r}_s)$. In panel (e) we show the partial wetting case for two contact angles, $\theta = 30°$ and $\theta = 50°$. (i-iii) denote the liquid filling stages with increasing Δp: (i) pre-filling, (ii) capillary filling and (iii) post-filling. The filling transition occuring at Δp_c is indicated in the figures. Panels (c, f, i) are the plots of reduced liquid-gas interface area $\widetilde{A}_{lg}$ against $\Delta p/(\gamma_{lg}/hG)$. Right and left arrows indicate the liquid filling path and liquid emptying path for increasing and decreasing $\Delta p/(\gamma_{lg}/hG)$, respectively. The solid line is to guide the eyes.

and $\beta = 0.5$. Similar results are obtained when u_{lr}^2 is used. Upon increasing the liquid pressure, the liquid begins to fill the grooved surface, as shown in Fig. 7.5 (a). We can categorize the liquid filling process into three stages [140], namely (i) pre-filling, (ii) capillary filling, and (iii) post-filling, which occur after one and the other with increasing liquid pressure.

The pre-filling stage occurs at large negative Δp, which means the pressure in the liquid is much lower than in the gas phase. Here, the liquid forms a thin film that follows the shape of the groove structure. The thickness of the film depends on the strength of the interaction (parameter α in u_{lr}^1) and increases as the liquid pressure is increased. The dependency is well

approximated by $e \propto (2\alpha/\Delta p)^{-1/3}$ at the bottom, top and sides of the barrier wall, where α can be associated with the Hamaker constant [141, 142]. Assuming the grooves have the dimension of the order of hundreds nm, the values of α in our simulation translate 10^{-20} to 10^{-19} J, which are the typical values of the Hamaker constant [64].

The key to understanding the capillary filling stage lies in changes to the film thickness in the bottom corners of the groove. As the menisci in the corners grow and approach $d/2$ in size, liquid from either side merges and rapidly fills the gap. The liquid interface then rises up from the bottom of the groove. This can be seen from the sudden increase in liquid film thickness as calculated at the middle gap, $\widetilde{e}_{\mathrm{g}}$ (Fig. 7.5 (b)) and from the sudden decrease of the liquid-gas interfacial area, $\widetilde{A}_{\mathrm{g}}$ (Fig. 7.5 (c)). We define the critical pressure Δp_{c} as the pressure value with the largest gradient in the $\widetilde{e}_{\mathrm{g}}$ and $\widetilde{A}_{\mathrm{g}}$ plots. At this capillary filling stage, the growth of thin film at the side walls and top of the barrier wall still follows $e \propto (1/\Delta p)^{-1/3}$.

The liquid, however, does not immediately fill the whole gap of the groove. In the post-filling stage, with increasing pressure, the liquid-gas interface between the barrier walls starts to smooth out until it becomes flat. The thin film thickness at the top of the barrier wall also increases more rapidly compared to the pre-filling and capillary filling stages. This occurs when Δp has small negative values, which means $p_{\mathrm{l}} \to p_{\mathrm{g}}$. As $p_{\mathrm{l}} > p_{\mathrm{g}}$, the film thickness increases to infinity as liquid fills up the whole domain.

If Δp is reversed from positive to large negative values, the liquid will be emptied from the grooved surface. Upon decreasing Δp, the liquid-gas interface follows the reverse path as the liquid fills the groove surface (Fig. 7.5 (c)). Therefore, the liquid filling does not exhibit hysteresis behaviour for the complete wetting case. Recently, filling transitions have been investigated via DFT [122]. It was also observed that the filling transition is mediated by the growth of the menisci in the bottom corners of the groove. However here, we are also able to show the contribution of the films on the sidewalls and top of the barrier wall.

Next, we want to compare the effect of long-range and short-range liquid-solid interactions on the liquid filling transition. In this case, we use the effective interaction u_{lr}^{1} in the interaction energy density $\mathcal{F}_{\mathrm{s}}(\mathbf{r})$ for the former and $\mathcal{F}_{\mathrm{s}}(\mathbf{r}_{\mathrm{s}})$ as in Eq. (6.12) for the latter. Although the filling behaviour for both interactions is qualitatively the same, the filling transition occurs at different critical pressures (Fig. 7.5 (b)). This is because the liquid film thickness at the wall is different, which changes the effective separation between the walls. The critical pressure dependency can be inferred from the Kelvin equation, in which Δp_c is expected to be inversely

proportional to the effective wall separation.

The liquid film formed due to long-range interactions is thicker than that due to short-range interactions. For the former, the contribution of the liquid-solid interaction is determined by how long the tail of the decaying interaction is until it becomes essentially zero. This is controlled by the parameter β. The higher β, the longer the tail. As a result, the interaction with higher β forms a thicker liquid film at the wall. For the short-range interaction, the liquid-solid interaction is assumed to occur only at the surface of the solid. Therefore, there is no liquid-solid interaction contribution farther from the surface. Hence, the liquid film is thinner, and the filling transition occurs for larger Δp.

7.2.2 Partial Wetting

We now turn our attention to the partial wetting case ($\theta > 0°$). The results presented here employ the short-range interaction. Equivalent results are obtained for the long-range interactions once the contact angles are mapped. The liquid filling behaviour for the partial wetting case is illustrated in Fig. 7.5 (d,e,f). In the same manner as the complete wetting case, we can also group the filling process into (i) pre-filling, (ii) capillary filling and (iii) post-filling stages. The capillary filling stage is also marked by a critical pressure at Δp_c. Here, we have to divide our discussion into two scenarios [120], which are for $\theta < 45°$ and for $\theta > 45°$.

For $\theta < 45°$, in the pre-filling stage, liquid condensation could be nucleated at the corner of the groove forming menisci at a large negative Δp (Fig. 7.5 (d)). In this case, the corner menisci grow as the liquid pressure increases until they merge as a single meniscus. Once this has happened, we enter the capillary filling stage, in which the liquid starts filling the gap while maintaining the shape of the meniscus. In sharp interface models, at a certain Δp_c, the filling transition occurs as signified by an abrupt increase in $\widetilde{e}_g$. Δp_c can be predicted using the Kelvin equation, as will be discussed in Section 7.2.4. Using the diffuse interface model in the present study results in a rounding of this first-order phase transition. However, this effect is marginal if there is a suitable separation of length scales (at least a factor of 10) between the diffuse interface width and the wall height. Thus, as is shown in Fig. 7.5 (e), the partial wetting filling transition is still sharp compared to the complete wetting case. After the filling transition occurs, the liquid again does not completely fill the gap, as in the complete wetting case, but both ends of the liquid-gas interface are pinned in the top edge of the wall. In the post-filling stage, the meniscus starts to flatten as $p_l \rightarrow p_g$. When Δp turns positive, the

curvature of the meniscus also turns sign from negative to positive. As the liquid manages to overcome the contact line pinning, it fills up all the gas phase.

For $\theta > 45°$, the pre-filling stage is marked by a gas-like phase with a completely dry solid (Fig. 7.5 (e)). The corner menisci do not form, and the filling transition immediately occurs when the pressure has reached Δp_c. The liquid will then be pinned at the top edge of the groove with smaller curvature due to higher θ. The post-filling stage is then similar to that for $\theta < 45°$ except that the positive curvature at positive Δp could grow larger in size before it overcomes the contact line pinning and fills all of the gas phase. This means that Δp at which the liquid fills the gas phase occurs at a larger value than that for $\theta < 45°$.

Figure 7.5 (f) shows liquid filling and emptying paths for increasing and decreasing Δp. The hysteresis behaviour is clearly pronounced. Due to contact line pinning at the top corner of the walls, during the filling process, the meniscus curvature changes from negative to positive as Δp increases. During the emptying process, however, upon decreasing Δp the liquid continues to wet all of the surface and maintains a flat liquid-gas interface until a significantly lower pressure difference. Once the top of the wall is fully dewetted, the liquid gets pinned at the top corners with negative curvature. The liquid emptying path then follows along the same path as the liquid filling. This can be seen in the snapshots of configuration during the filling and emptying processes, as shown in Fig. 7.6 (top row). This hysteresis behaviour in partial wetting case has also been reported elsewhere [134, 143].

7.2.3   Pseudo-partial Wetting

Figure 7.5 (g,h,i) show the liquid filling behaviour on a grooved surface for the pseudo-partial wetting case. The effective interaction u_lr^2 is used in the interaction energy density $\mathcal{F}_\mathrm{s}(\mathbf{r})$. The magnitude of parameter $-u_\mathrm{o}$ controls the strength of the attractive interaction. To obtain a pseudo-partial wetting state, a large enough $-u_\mathrm{o}$ is employed to get a liquid film near the surface. The parameter σ controls the thickness of the liquid film. Here, we use $\sigma = 3$ and $u_\mathrm{o} = -5 \times 10^{-7}$ and $u_\mathrm{p} = 2 \times 10^{-7}$.

In the pre-filling stage (at large negative Δp), in contrast to the partial wetting case at the same Δp, the liquid wets the bottom surface of the groove and the side walls forming a liquid film but leaves the top of the barrier wall dry as the liquid film is pinned at the top edges of the wall. At the bottom corners of the groove, the meniscus of liquid condensation is not as pronounced as it is for the full and partial wetting case. This is because the interaction at the
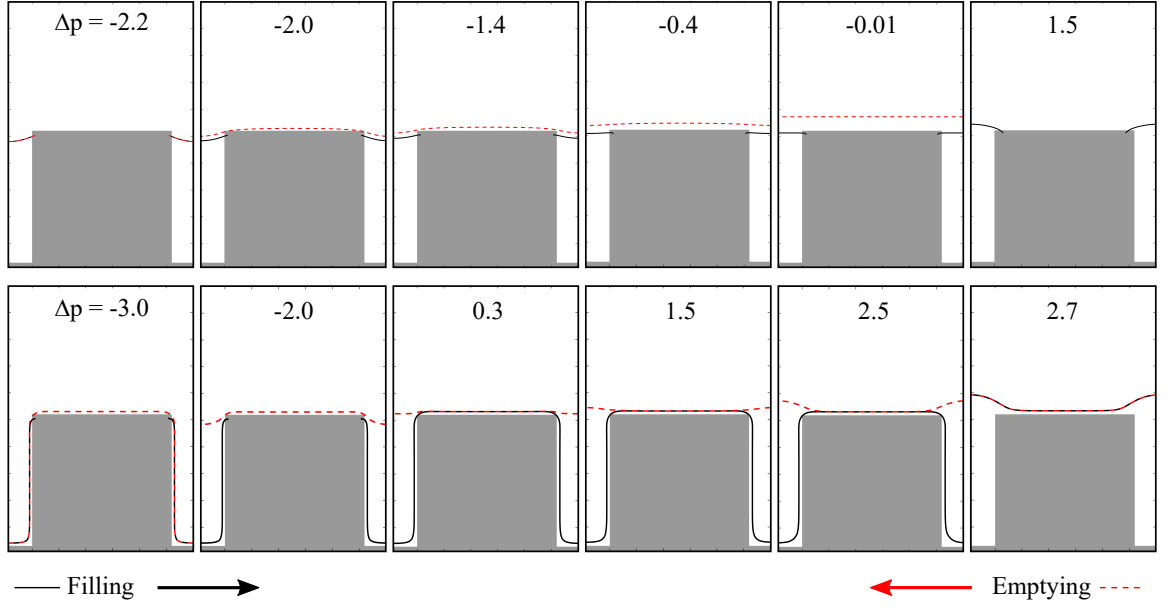
Figure 7.6: Snapshots of liquid-gas interface configurations during filling (black solid line) and emptying (red dashed line) processes at different Δp for partial (top row) and pseudo-partial (bottom row) wetting showing hysteresis behaviours. For the partial wetting at $\Delta p = 1.5$, the liquid fills up the whole simulation domain during the emptying process; hence, the liquid-gas interface does not appear in the image. At $\Delta p = -2.2$, the filling and emptying processes have the same liquid-gas interface configuration. Similarly, for the pseudo-partial wetting at $\Delta p = 2.7$, the liquid-gas interfaces of the filling and emptying processes are on top of each other.

surface near the corner slightly reduces due to the effect of the repulsive term in the effective interaction u_{lr}^2. As the liquid pressure increases the liquid overcomes the contact line pinning at the top edges and covers the top of the wall. This is shown in Fig. 7.5 (i) (right-pointing triangle), in which the liquid-gas interface area increases abruptly at $\Delta p/(\gamma_{\mathrm{lg}}/hG) \approx 0.3$. The bottom corner menisci only slightly grow with increasing pressure, unlike for the complete and partial wetting cases where they grow and merge as their size approaches $d/2$.

In the capillary filling stage, the critical pressure for the filling transition occurs sharply at positive Δp_{c} (indicated in Fig. 7.5 (h)). The sharp transition applies for narrow and wide groove widths. Compared to the negative Δp_{c} observed for complete and partial wetting cases, this suggests the filling transition is more energetically expensive for the pseudo-partial wetting case. At the critical pressure Δp_{c}, liquid fills the gap, and it forms a droplet in the middle of the gap coexisting with the liquid film on top of the barrier wall (Fig. 7.5 (g)). Such coexistence is reminiscent of the morphology observed on a flat surface. However, the range of stability of the droplet is limited. With increasing pressure in the post-filling stage (with positive Δp),

the droplet becomes unstable and the liquid fills the simulation domain.

The hysteresis behaviour is also clearly observed in the pseudo-partial wetting case, as shown in Fig. 7.5 (i) (See Fig. 7.6 (bottom row) for snapshots of configuration during the filling and emptying processes). During the filling process, the contact line pinning at the top corners of the walls allows the liquid to form a droplet bulge in the middle of the gap as Δp increases. Upon decreasing Δp, however, the droplet bulge slowly flattens until the liquid filling the gap abruptly drains, leaving a liquid film that follows the shape of the groove structure. The top of the wall remains covered by a liquid film; hence, we find higher $\widetilde{A}_{\mathrm{lg}}$ than in the liquid filling path.

7.2.4   Critical Pressure Scaling with Groove Width

In this section, we will now consider how the critical pressure for the filling transition depends on the groove width, d. We will begin by considering the partial wetting case. To describe the critical pressure quantitatively, we can use the following argument. During the transition, the groove will experience a change of liquid volume ΔV, accompanied by a change of liquid height in the groove by h. As such, the change in the total free energy is given by

$$\Delta E = -\Delta p \Delta V + \gamma_{\mathrm{lg}} \Delta A_{\mathrm{lg}} + \gamma_{\mathrm{ls}} \Delta A_{\mathrm{ls}} + \gamma_{\mathrm{gs}} \Delta A_{\mathrm{gs}}, \tag{7.2}$$

where ΔA_{lg}, ΔA_{ls} and ΔA_{gs} are the changes in liquid-gas, liquid-solid and gas-solid interface areas, respectively. During the filling transition, the liquid-gas interface remains nearly constant, hence $\Delta A_{\mathrm{lg}} \approx 0$. ΔV, ΔA_{ls} and ΔA_{gs} can be approximated by $d^2 h$, $2dh$ and $-2dh$, respectively. Using Young's equation, we can rearrange Eq. (7.2) to obtain

$$\Delta E = -\Delta p d^2 h - 2\gamma_{\mathrm{lg}} \cos\theta dh. \tag{7.3}$$

The critical pressure corresponds to the case where $\Delta E = 0$, leading to a relation

$$\Delta p_{\mathrm{c}} = -\frac{2\gamma_{\mathrm{lg}} \cos\theta}{d}. \tag{7.4}$$

This equation has the same form as the Kelvin equation and, as shown in Fig. 7.7, it captures the critical pressure obtained in the simulation accurately.

A similar argument can be applied for the complete wetting case with $\theta = 0$. However, to
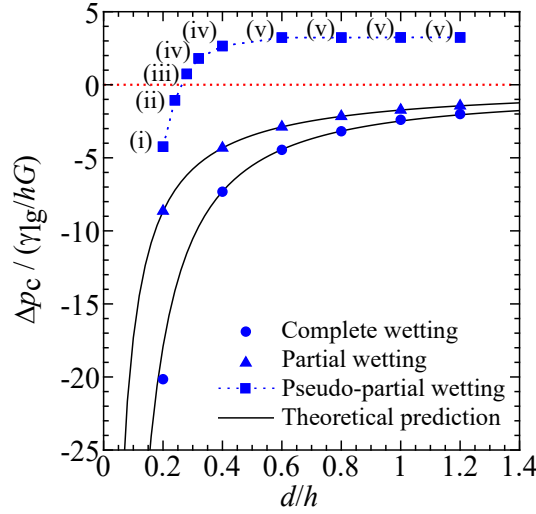
Figure 7.7: Reduced critical pressure $\Delta p_{\mathrm{c}}/(\gamma_{\mathrm{lg}}/hG)$ as a function of separation-to-post height ratio d/h for complete, partial, and pseudo-partial wetting cases. The error bars for the data points are not visible as they are comparable to the marker size. The solid curve is the theoretical prediction for partial and complete wetting cases given by Eq. (7.4) with $\theta = 30°$ and Eq. (7.5), respectively. (i-v) denote specific d/h at which different scenarios of the filling transition occur for the pseudo-partial wetting case (see text and Fig. 7.8).

account for the effect of the liquid film at the wall, a correction term of $3e_{\mathrm{w}}$, where e_{w} is the film thickness at the wall, needs to be added because the effective wall separation is not equal to d, as proposed by Derjaguin [129]. Therefore, the critical pressure becomes [144]

$$\Delta p_{\mathrm{c}} = -\frac{2\gamma_{\mathrm{lg}}}{d - 3e_{\mathrm{w}}}, \tag{7.5}$$

where e_{w} depends on Δp through the relation $e_{\mathrm{w}} \propto (1/\Delta p)^{-1/3}$. The comparison of the critical pressure between simulation and theoretical predictions for complete wetting case is also shown in Fig. 7.7. It shows a good agreement to a very narrow gap although there is a slight deviation for $d/h = 0.2$ because the interface width of our diffuse liquid-gas interface becomes comparable to d.

The pseudo-partial wetting case, however, cannot be captured by a relation akin to Eq. (7.4) or Eq. (7.5). We argue that this is because the corner menisci are not so apparent during the capillary filling stage and do not merge into a single meniscus before the filling transition occurs. Therefore, d does not affect Δp_{c}. This can be observed for $d/h > 0.6$ in Fig. 7.7. In this scenario, the liquid fills up the simulation when the filling transition occurs, as illustrated in Fig. 7.8 (v). When d is very small ($d/h < 0.6$), however, Δp_{c} starts to be dependent on d, but
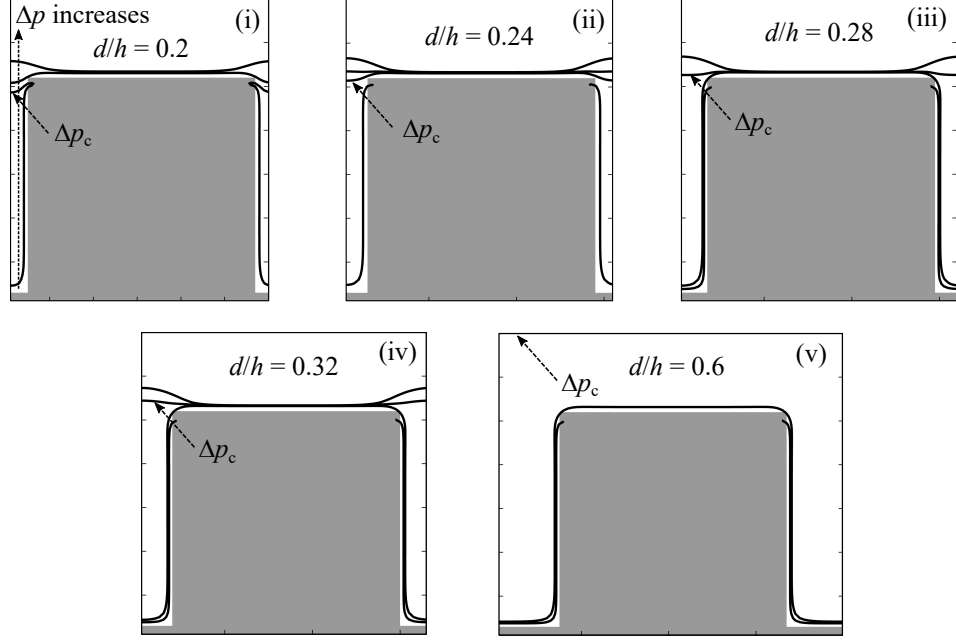
Figure 7.8: Liquid filling states at different groove widths for the pseudo-partial wetting case. Panels (i-v) correspond to different scenarios as indicated in Fig. 7.7 and explained in the main text. In panel (v), the liquid fills up the whole simulation domain when the liquid filling transition occurs; hence the liquid-gas interface at Δp_c lies at the top of the domain.

it still does not obey Eq. (7.4). Instead, we find this variation is accompanied by non-trivial changes in the morphological pathway during the filling transition. With increasing groove width, five distinct pathways are identified, illustrated in Fig. 7.8, and indicated in Fig. 7.7: (i) liquid fills the gap forming a liquid-gas interface with a negative curvature while keeping the top of the wall dry, (ii) the same as scenario (i) except that top of the wall is covered by a liquid film, (iii) the same as scenario (ii) but the liquid film at the top of the wall is formed before the capillary filling stage, (iv) the same as scenario (iii) but the liquid-gas interface curvature is positive, and (v) liquid fills the system at the critical pressure.

7.3 Discussion

In this part of the thesis, we have presented systematic numerical studies of liquid filling on grooved surfaces using a phase field method. We consider both short-range and long-range liquid-solid interactions. The latter include purely repulsive and attractive interactions, and more complex interactions with short-range attraction and long-range repulsion. To the best of our knowledge, such versatility allows us to capture complex disjoining pressure profiles for the first time in a phase field approach, in agreement with previous works using atomistic

modelling [119, 124] and analytical theory [65, 137], which in turn give rise to complete, partial, and pseudo-partial wetting states. In this work, we have also introduced a quartic polynomial to switch the interaction energy density between the liquid and gas phases ($f(\phi)$ in Eq. (6.10)). This polynomial prevents enrichment of the liquid and/or gas phases on the solid surface, and it leads to more accurate contact angle calculations compared to the linear and cubic forms previously used in the literature.

We rationalize the liquid filling process on grooved surfaces into three stages: (i) pre-filling, corresponding to the growth of the thin film around the structure (for complete or pseudo-partial wetting), or liquid menisci in the bottom corners of the groove (for partial wetting); (ii) capillary filling, where there is a rapid increase of liquid volume in the groove marked by a critical pressure; and (iii) post-filling, typically signified by the flattening of the liquid-gas interface before liquid completely fills the whole domain. Comparing the results for complete, partial, and pseudo-partial wetting, we find there is no contact line pinning for the complete wetting case and the liquid filling and emptying trajectories are reversible. In contrast, we observe clear hysteretic behaviour for partial and pseudo-partial wetting, caused by the coexistence of two metastable states over a pressure range. In the partial wetting case, late in the filling transition, pinning of the interface on the top corner of the wall leads to a state that remains metastable over a range of positive pressures. Coexisting with this is the unpinned state, which, at positive pressures, sees liquid completely fill the system. In the pseudo-partial wetting case, the origin of metastability is different. Here, repulsive interactions in the centre of the groove energetically penalise partial filling of the groove. Instead, either the groove remains almost empty, or the groove is full.

Considering the critical pressure, although the diffuse interface marginally rounds the first-order transitions, both the complete and partial wetting cases follow a Kelvin-like equation for its dependence on the groove width: large and negative at small widths, and plateaus to zero for large widths. The pseudo-partial wetting case, however, is different. At large widths, the critical pressure is positive and constant. We find the critical pressure does depend on groove width for smaller widths, and interestingly, this is accompanied by morphological changes in the trajectories of the liquid filling process.

There are a number of exciting avenues for future work. Here, we have considered grooved surfaces. It is straightforward to extend the study to other, more complex surface geometries such as re-entrant geometries, seesaws, hierarchical posts, or even non-symmetric structures

which have extensively been harnessed in wetting applications. Another possible direction is to consider the liquid dynamics, beyond the quasi-static results presented here. There are some limitations, however, of the phase field method used in this study. The present method does not include the interfacial fluctuation effects, which have been shown to occur at nanoscale [145] and captured by atomistic simulations [146]. To capture these phenomena, one possible route is to couple the phase field model here with fluctuating hydrodynamics methods [147, 148]. Finally, we hope the simulation results will inspire experimental studies to verify our theoretical predictions.

Part IV

Wetting on Complex Geometries: Frozen Fluid Method

CHAPTER 8

Method

8.1 Phase Field Model for the Frozen Fluid Method

The frozen fluid method is based on a phase field model for three-component immiscible fluids in which the local composition of each component is represented by an order parameter C_n, where $n = \{1, 2, 3\}$. In general, the order parameter C_n describes fluid phases within the ternary system. However, in this context, we designate one component, C_1, as a solid phase and the rest, C_2 and C_3, as liquid and gas phases, respectively.

The ternary model used in this work is based on Ref. [149], in which the thermodynamics of the system are described by a free-energy functional of the fluids that captures the immiscibility of the fluid components and the surface tensions between different fluids. The phase interface is modelled using a diffuse interface with a finite thickness model, which yields a smooth transition region between two different phases. Since we are interested in the equilibrium state of the system, the total free energy is minimized using the L-BFGS algorithm.

The total free energy of the system is given by

$$\Psi(C_n) = \int_V (\Psi_{\text{b}} + \Psi_{\text{i}} + \Psi_{\text{c}} + \Psi_{\text{cf}}) \mathrm{d}V, \tag{8.1}$$

where all of the energy densities are integrated over the system's volume, V. The bulk energy density of the phases, Ψ_{b}, is modelled using a double well potential

$$\Psi_{\text{b}} = \sum_{n=1}^{3} \frac{\kappa_n}{2} C_n^2 (1 - C_n)^2. \tag{8.2}$$

Here, the κ_n's are tunable parameters related to the interfacial tension between different fluids.

The form of potentials chosen in this model has two minima at $C_n = 0$ and 1. We then relate $C_n = 0$ to indicate the absence of component n and $C_n = 1$ to indicate pure component n. We also normalise the total composition to unity so that $C_1 + C_2 + C_3 = 1$ to obtain $C_3 = 1 - C_1 - C_2$, which reduces the number of the order parameter in the system that needs to be optimised. It is worth noting that this constraint allows C_1 and C_2, in principle, to have any value.

Ψ_i is referred to as the gradient energy density, which accounts for the energy penalty for having interfaces. The gradient term takes the form

$$\Psi_b = \sum_{n=1}^{3} \frac{\kappa'_n}{2} (\nabla C_n)^2, \tag{8.3}$$

where κ'_n's are also tunable parameters whose values determine the contribution of the gradient terms to the total free energy. By relating the bulk and gradient energy densities to the chemical potential, we can calculate the interfacial profile of C_n and the interfacial tension between phases n and m, given by

$$C_n(x) = \frac{1}{2} + \frac{1}{2} \tanh \frac{x/2}{\sqrt{(\kappa'_n + \kappa'_m)/(\kappa_n + \kappa_m)}}, \tag{8.4}$$

and

$$\gamma_{nm} = \frac{\alpha}{6} (\kappa_n + \kappa_m), \tag{8.5}$$

where $\alpha = \sqrt{(\kappa'_n + \kappa'_m)/(\kappa_n + \kappa_m)}$ denotes the interface width. Here, the value of C_n varies between 0 and 1 at an interface, and we take the value of $C_n = 0.5$ as the interfacial boundary between the two phases. We can further use the definition of α to simplify the simulation variables by relating $\kappa'_{\{n,m\}}$ and $\kappa_{\{n,m\}}$ via $(\kappa'_n + \kappa'_m) = \alpha^2 (\kappa_n + \kappa_m)$. In this work, we take $\kappa'_n = \alpha^2 \kappa_n$ and use $\alpha = 1$. While we will call α as the interface width, for $\alpha = 1$, the transition between $C_n = 0$ and $C_n = 1$ occurs over 4-5 the units of α (see Fig. 8.1). From Eq. (8.5), we can calculate the values of κ_n as input parameters given that the surface tensions are known,

$$\begin{aligned}
\kappa_1 &= \frac{3}{\alpha} (\gamma_{12} + \gamma_{13} - \gamma_{23}), \\
\kappa_2 &= \frac{3}{\alpha} (\gamma_{12} - \gamma_{13} + \gamma_{23}), \\
\kappa_3 &= \frac{3}{\alpha} (-\gamma_{12} + \gamma_{13} + \gamma_{23}).
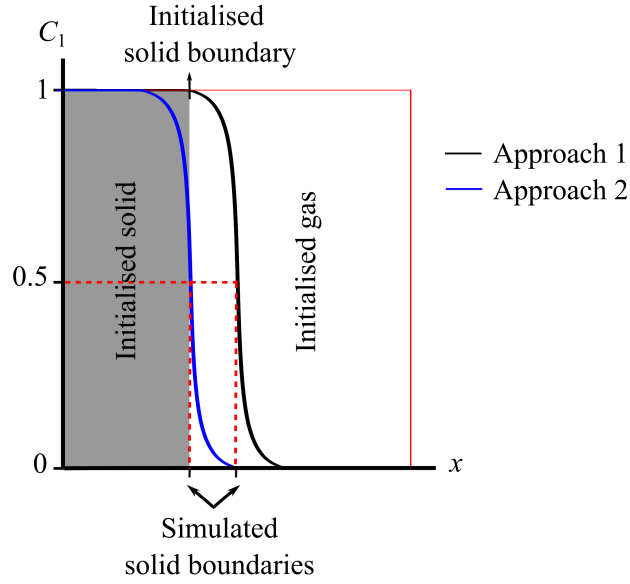\end{aligned} \tag{8.6}$$

Figure 8.1: Illustration of the solid boundaries and interface width. Black and blue solid lines are the solid component C_1 profiles in the x-direction across the gas-solid boundary obtained after applying the confining potentials using Approaches 1 and 2, respectively (see Section 8.2.2 for details of these approaches). Dash lines show the simulated solid boundaries for both approaches.

In the ternary fluid system, the balance of forces of the three fluids must satisfy Neumann's angles at equilibrium. These angles are influenced by the interfacial tensions of the three fluids which satisfy this relation: $\gamma_{23}/\sin\theta_1 = \gamma_{13}/\sin\theta_2 = \gamma_{23}/\sin\theta_3$. Depending on the magnitude of the interfacial tensions, a liquid droplet will form a liquid lens, as illustrated in Fig. 8.2. In the frozen fluid method, however, since one of the fluids is treated as a solid, the interfacial tension-contact angle relation is simplified to the Young's equation: $\gamma_{23}\cos\theta = \gamma_{13} - \gamma_{12}$.
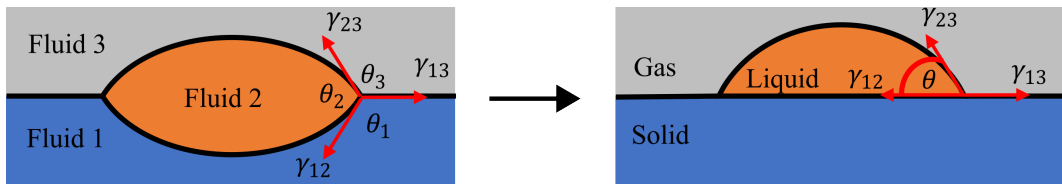
Figure 8.2: Illustration of the interfacial tensions in the ternary fluid system (left) and in the frozen fluid method (right).

Ψ_c is the constraining energy density that allows the system to preserve either the pressure difference between liquid and gas phases, Δp, or the volume of the liquid phase, V_l, during the minimisation. When the former is desired, the constraining potential takes the form,

$$\Psi_\mathrm{c} = -\Delta p V_\mathrm{l}, \tag{8.7}$$

whereas for the latter,

$$\Psi_c = \frac{1}{2}k(V_l - V_0)^2. \tag{8.8}$$

Here, $k > 0$ is a constant, and V_0 is the target volume. The volume of the liquid phase, V_l can be calculated as

$$V_l = \int_V C_2 dV. \tag{8.9}$$

The last component in the total energy is the confining energy density, Ψ_{cf}, for the frozen fluid given by

$$\Psi_{cf} = \int_V \psi_{cf} dV, \tag{8.10}$$

where ψ_{cf} is the confining potential. This energy term is solely used to relax the solid component to create a smooth and diffuse interface. We shall discuss this term in more detail in the next section.

8.2 Simulation Implementation

8.2.1 Discretisation and Energy Minimisation

In the simulation, we employ a similar procedure outlined in Chapter 6 (see Section 6.2.1) to minimise the total free energy numerically. In summary, we discretize Ψ in Eq. (8.1) into $N_x \times N_y \times N_z$ cubic lattice points (called nodes), in which each node is associated with a value of ϕ_{ijk}, where $i, j, k \in \{1, \dots, N\}$ indicate the spacial dimension in the x-, y-, and z-directions. The grid spacing, G, is set to be equal to the interface width α, which is taken to be 1. Depending on the case being investigated, we employ two types of boundary conditions: the periodic and mirror boundary conditions. The energy minimisation is then carried out using the computationally efficient L-BFGS algorithm, optimized for both memory usage and processing speed. During the minimisation routine, the value of ϕ_{ijk} of each node is updated in order to achieve the minimum total energy configuration.

The implementation of the frozen fluid method during the energy minimisation process in the simulation is carried out in two stages. In the first stage, energy minimisation is performed to create a solid geometry with a smooth and diffuse solid interface [150]. The solid is initialised as component 1 (C_1) within the desired geometry. The remaining system is filled with pure gas (C_3), and the liquid phase (C_2) is fixed at 0. The total free energy is subsequently minimised

using the L-BFGS algorithm. During this stage, the energy minimisation process is truncated at a specific number of iterations to allow the 1-3 diffuse interface to form without strongly perturbing the intended solid geometry's shape.

Once this stage is complete, the liquid phase (C_2) is initialised in the system according to a predefined configuration. The solid phase (C_1) is now fixed, while the liquid (C_2) and gas (C_3) phases are allowed to vary. The total free energy is now minimised under these constraints. Convergence of the minimization process is determined based on an *rms* gradient condition: convergence is achieved when $|\nabla \Psi| < 10^{-5}$.

8.2.2 Confining Potentials

In the first stage of energy minimization, we initialise the solid component in a specific shape of geometry by assigning $C_1 = 1$ and fill the rest of the system with a gas phase. The liquid component is set to be fixed at $C_2 = 0$. During the minimization, we allow the solid component to relax to form a smooth and diffuse interface but truncate it when the desired solid geometry is achieved. To accommodate this process, a confining energy term in Eq. (8.10) is applied to the system to ensure that the resulting solid shape remains close to the intended one.

The confining potential ψ_{cf} should meet two main criteria: (i) the potential does not artificially alter the interfacial profile or interfacial tensions with the solid phase, and (ii) the interfacial tension must be uniform at every point in the solid surface regardless of the feature of the solid interface. The truncation of the number of iterations should also be properly considered in order to ensure the confining potential meets those criteria in addition to getting the desired solid geometry.

There are multiple ways of carrying this out. Here, we consider two approaches, namely Approach 1 and Approach 2, with different potential forms and implementations. For illustration, the comparison between solid interface boundaries obtained from applying Approach 1 and Approach 2 for a rectangular solid shape is shown in Fig. 8.1.

8.2.2.1 Approach 1

In the first approach (Approach 1), we employ a fourth-order polynomial of C_1 in the confining energy term,

$$\psi_{\mathrm{cf}} = \beta(3C_1^4 - 4C_1^3), \tag{8.11}$$

where $\beta > 0$ controls the strength of the potential. This potential is globally minimized at $C_1 = 1$ and monotonically increases with $|C_1|$ for $|C_1| > 1$, which gives an energy penalty to the total free energy. In addition, its gradient is zero at the bulk equilibrium values of $C_1 = 0, 1$. These features ensure that the initialised solid component values remain equal to 1 in the bulk.

At the diffuse interface, the solid component with values $0.5 < C_1 < 1$ will be taken as part of the solid phase, whereas $0 < C_1 < 0.5$ as the gas phase. As a result, the simulated solid interface boundary is shifted from the intended one, making the solid size larger than it should be (see Fig. 8.1).

This effect can be controlled by tuning the potential strength variable β. We can think of β as the parameter to control an artificially-applied pressure between the solid and gas phases. When β is small, the potential is weak, and the pressure given by the gas phase to the solid interface is also weak, resulting in a larger shifting of the gas-solid interface boundary. On the contrary, a larger β (i.e. stronger confining potential) gives a higher pressure to the solid phase, making the extra solid component at the interface smaller.

8.2.2.2 Approach 2

In the second approach (Approach 2), we apply a polynomial function of C_1 with a minimum at $C_1 = 0.5$ when the value of $C_1 < 0.5$ within the solid nodes, or when $C_1 > 0.5$ within the fluid (gas) nodes. This ensures the solid components that enter the gas phase are minimised at $C_1 = 0.5$, centring the interface at the boundary between the solid and fluid nodes. Using this approach, the size of the solid will be similar to the initialised one, with some fraction of the solid taken up as the diffuse interface. This prevents the solid size from becoming larger than the intended one. Since we use the interface width $\epsilon = 1$, the diffuse interface will take up about 4-5 lattice units in the simulation (see Fig. 8.1).

We can choose any polynomial function if it is globally minimized at $C_1 = 0.5$. Here, we compare three different polynomial functions, namely Quadratic, Quartic 1 and Quartic 2, given by

$$\psi_{\text{quadratic}} = \beta(C_1 - 0.5)^2, \tag{8.12}$$

$$\psi_{\text{quartic1}} = \beta(C_1 - 0.5)^4, \tag{8.13}$$

$$\psi_{\text{quartic2}} = \beta(3C_1^4 - 2C_1^3), \tag{8.14}$$

where β is a positive value.

The caveat of this approach is, however, that the initialised solid shape is limited to a specific size to ensure the bulk solid is still maintained as part of the solid phase. Below such a limit, the solid component will only consist of the diffuse interface and is prone to annihilation during the minimization.

It is worth noting that the choice of β and the number of iterations during minimization are critical, as they will control the smoothness of the solid interface and maintain the solid shape and size. A large value of β will generally result in a less smooth interface, particularly for a curved interface, and maintain the solid shape and size, whereas a small value of β, on the other hand, will create a smoother interface but is prone to altering the intended solid shape and size. Depending on the shape of the solid, a high number of iterations in the minimization process will easily alter the shape and size as the shape gets closer to an equilibrium state, particularly for weaker potentials (small β). In contrast, a low number of iterations tends to be able to maintain the shape and size of the solid from its initialised state.

8.2.2.3 Objective Function

To determine the effective value of β and the number of iterations, we perform an optimisation algorithm based on several criteria: the size of the solid, the closeness of the shape to the intended one, the smoothness of the interface, and the fitness of the tanh profile of the solid component across a gas-solid interface to the analytical solution. These criteria are chosen to ensure the resulting solid geometry has a smooth interface and maintains the intended shape and size. These criteria are then translated into an objective function that measures the square of the relative error of each criterion, given by

$$O = w_1(\Delta V)^2 + w_2(\Delta R_C)^2 + w_3(\Delta R_S)^2 + w_4(\Delta C_1)^2. \tag{8.15}$$

The variable ΔV (or ΔA in 2D), which determines the solid size criterion, is the difference in the volume (or area) between the simulated and expected solid shape in 3D (or 2D). ΔR_C, defined as the difference between the radius of the simulated and expected points at the interface of the solid, and ΔR_S, defined as the difference between the radius of the simulated and fitted points at the solid interface, are used to determine the closeness and smoothness criteria, respectively. Finally, ΔC_1 is used to determine the tanh profile fitness of the solid interface, which is defined

as the difference between the simulated and analytical tanh profile of the solid component across a gas-solid interface. The coefficients w_1, w_2, w_3 and w_4 weigh the corresponding variables to ensure that each criterion is equally favourable. This objective function is then minimised against several solid geometries for all confining potentials as in Eq. (8.11) and Eqs. (8.12 - 8.14).

CHAPTER 9

Results

9.1   Determining the Confining Potential Parameters

In the Method section, we have elucidated two approaches in applying the confining poten-
tials to obtain the desired solid shape, referred to as Approach 1 and Approach 2. In both
approaches, two parameters need to be assigned correctly: the potential strength β and the
number of iterations. To determine the appropriate values for each approach, we will perform
simulations against several solid geometries that account for different surface features, includ-
ing flat, curved, and corner features. We will then decide the optimised parameters based on
the criteria of an objective function that we have discussed in the Method section.

Firstly, we consider Approach 1. We perform simulations against a simple 2D flat solid
surface with a simulation domain of $N_x \times N_y = 60 \times 60$. The solid component $C_1 = 1$
is set at $0 \le y \le 10$, and the rest of the system is filled by the gas component C_3. The
liquid component C_2 is fixed at zero during the minimisation. We use three different values
of β, $\beta = 1, 10, 50$. We allow the minimisation steps up to 100 iterations and truncated the
iteration when the desired solid shape is obtained. The typical solid surface obtained after the
minimisation is shown in Fig. 9.1 (a), in which the solid phase (blue region) and the gas phase
(grey region) are separated by a smooth diffuse interface. The diffuse interface of the solid can
be demonstrated by plotting the tanh profile of C_1 across a gas-solid interface cross-section, as
shown in Fig. 9.1 (b). Here, the minimisation steps are truncated at 30, 30, and 80 iterations
for $\beta = 1, 10$ and 50, respectively. It can be noticed that the simulated interface boundary is
shifted from the initialised one towards the gas phase. However, the tanh profile of the solid
component across the interface boundary for each value of β is in agreement with the analytical

Figure 9.1: (a) Typical solid geometry obtained after the energy minimisation simulation using Approach 1. Solid and gas phases are denoted by blue and grey regions, respectively, whereas the black solid line indicates the gas-solid interface boundary. (b) Tanh profiles of C_1 for $\beta = 1, 10, 50$ after number of iterations = $30, 30, 80$, respectively, across the A-A' cross-section as indicated in (a). The solid line is the analytical solution from Eq. (8.4). The red vertical dashed line indicates the initialised interface boundary. (c) and (d) Root Mean Square Error (RMSE) of the tanh profile of C_1 and gas-solid interface boundary are plotted against the number of iterations, respectively, for $\beta = 1, 10, 50$.

prediction (solid line) in Eq. (8.4), indicating that the confining potential does not alter the interfacial tension at the gas-solid interface.

To evaluate further the effect of β and the number of iterations, we employ an optimisation algorithm based on an objective function. Since the solid interface is flat, the smoothness and closeness criteria are not critical in the objective function. The determining criteria are the fitness of the tanh profile (ΔC_1) and the size of the solid (ΔA). The effect of β and the number of iterations on the fitness of the tanh profile can be demonstrated in terms of the root mean square error (RMSE) against the analytical solution of C_1, as shown in Fig. 9.1 (c). For all values of β, the deviation is large for a small number of iterations and gets smaller as the number of iterations increases until it saturates at RMSE = 0.03. This is achieved at the
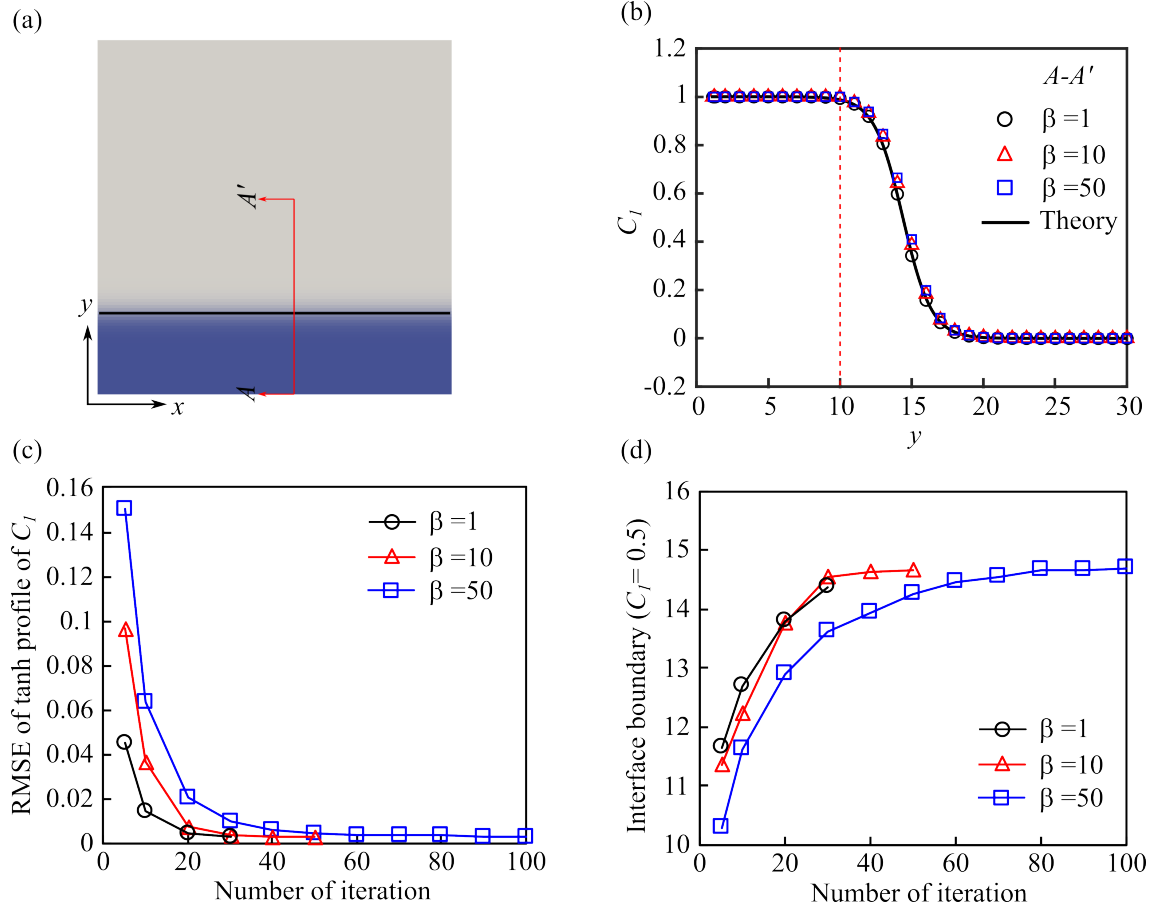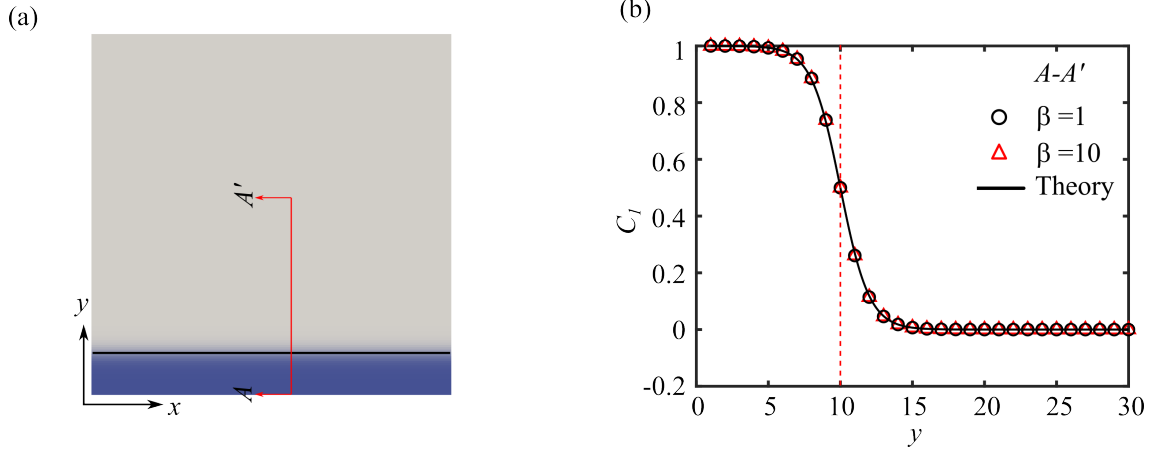
(a)

(b)

Figure 9.2: (a) Typical solid geometry obtained after the energy minimisation simulation using Approach 2. Solid and gas phases are denoted by blue and grey regions, respectively, whereas the black solid line indicates the gas-solid interface boundary. (b) Tanh profiles of C_1 for $\beta = 1$ and 10 after number of iterations $= 10$ across the A-A' cross-section as indicated in (a). The solid line is the analytical solution from Eq. (8.4). Red vertical dashed line indicates the initialised interface boundary.

number of iterations $= 30$, 30 and 80 for $\beta = 1, 10$ and 50, respectively. The effects of varying the number of iterations can also be seen in the size criterion, as shown in Fig. 9.1 (d). Here, instead of measuring the area of the solid, we measure the position of the interface boundary. It can be seen that the interface boundary shifts from the initialised boundary position ($y = 10$) and reaches an effective interface boundary at $y = 15$. From these results, we can conclude that small values of β allow the solid to create a smooth, flat interface and desired shape faster than higher β. The implementation of Approach 1 to other solid shapes, such as the curve and corner features, results in a similar fashion compared to the flat surface. A sphere geometry (or circular in 2D), for instance, will become effectively larger.

Now we will consider Approach 2 with three different polynomial functions as given in Eqs. (8.12 - 8.14). We begin by performing simulations against a 2D flat solid interface with a similar setup as in Approach 1 in order to compare the results between these two approaches. Here, we use a Quadratic polynomial as the confining potential with $\beta = 1$ and 10. The simulated solid interface and its tanh profile after 10 iterations are shown in Fig. 9.2. From Fig. 9.2 (b), it can be seen that the simulated solid boundary is not shifted from the initialised position. In addition, the tanh profile of the solid component is in good agreement with the analytical prediction, indicating that the interfacial tension is not altered.

Next, we apply Approach 2 on solid shapes with curve and corner features. For the curve feature, we use a sphere geometry with a radius of 30 s.u.. The sphere is initialised using a

Figure 9.3: 2D cross-section of the gas-solid interface of a sphere obtained after different numbers of iterations using Approach 2 with $\beta = 1$ (top row) and $\beta = 10$ (bottom row). Panels (a-b), (c-d) and (e-f) show the results when using the Quadratic, Quartic 1 and Quartic 2 polynomial functions, respectively.
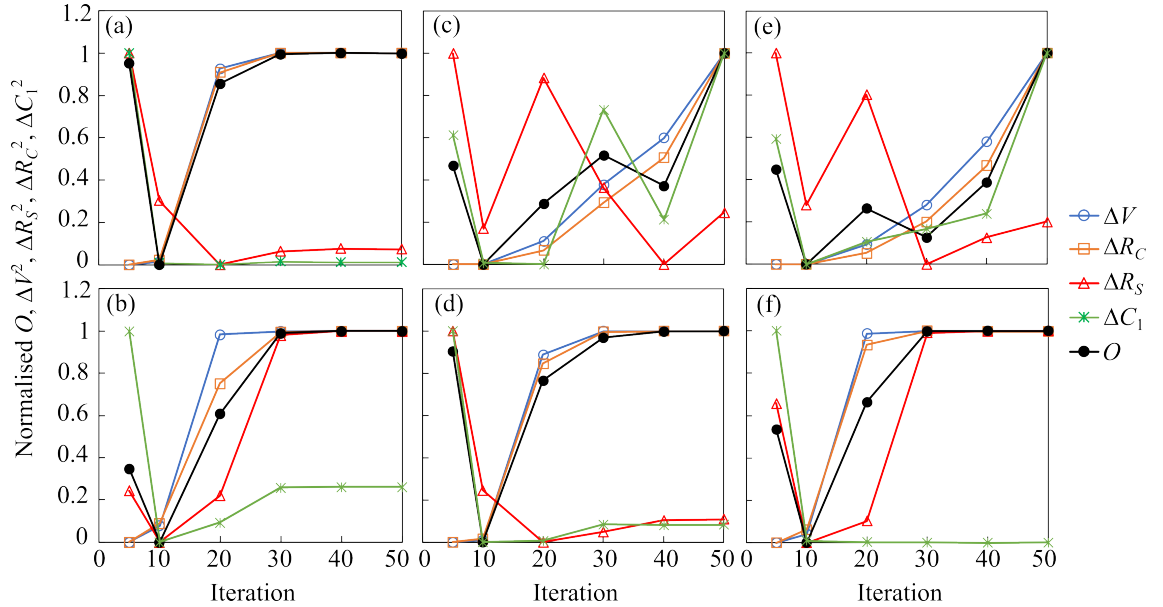
Figure 9.4: The objective function (O) and its components (ΔV, ΔR_C, ΔR_S, and ΔC_1) squared plotted against the number of iterations for $\beta = 1$ (top row) and $\beta = 10$ (bottom row) for a sphere geometry. All values have been normalised such that they range from 0 to 1. Panels (a,b), (c,d) and (e,f) show the results when using the Quadratic, Quartic 1 and Quartic 2 polynomial functions, respectively.

staircase approximation due to the square lattice used in the simulation. We use two values of β, $\beta = 1$ and 10, to account for weak and strong confining potentials. The effect of confining potential with these values of β for the Quadratic, Quartic 1 and Quartic 2 polynomial functions on the gas-solid interface of the sphere is shown in Fig. 9.3. Here, we show 2D cross-sections of the gas-solid interface across the middle of the sphere when the energy minimisation process has been iterated after 5, 10, 20, 30, 40 and 50 steps. For the Quadratic potential, we notice insignificant changes in the sphere volume for both $\beta = 1$ and 10. In addition, the solid size and the gas-solid interface boundary are identical to the initialised ones. For the Quartic 1 and Quartic 2 potentials, on the other hand, the solid size shrinks by a significant amount when the number of iterations is increased for $\beta = 1$. In contrast, for $\beta = 10$, the system is able to maintain the solid size. When we look at the smoothness of the gas-solid interface, in general, it gets smoother as the number of iterations increases for $\beta = 1$, but remains jagged for $\beta = 10$ although the staircase approximation from the initialisation has vanished.

These effects can be evaluated further in more detail from the objective function analysis, as shown in Fig. 9.4. Here, all variables in the objective function have been normalised such that the values range from 0 to 1 to ensure that each variable contributes similarly to the overall objective function. For the Quadratic potential, as shown in Fig. 9.4 (a,b), the deviation of the volume ΔV and radius ΔR_C of the sphere from its initialised values increases with the number of iterations and they reach saturated values after 20 iterations. These changes are caused by a small shrinking of the sphere size. The R_S variable, which measures the smoothness of the interface, decreases with the number of iterations for $\beta = 1$, indicating a smoother interface, but increases for $\beta = 10$. If we look at the tanh profile variable ΔC_1, the deviation drops drastically after 10 iterations for $\beta = 1$ but slightly increases for $\beta = 10$. However, both tanh profiles are still in good agreement with the prediction. If we combine all variables into the total objective function, O, we can see that the minimum deviation of all variables is obtained at 10 iterations for both values of β, which indicates the optimum solid geometry. This also applies to the Quartic 1 and Quartic 2 potentials (see Fig. 9.4 (c-f)), although the trend of each variable may be different.

The effect of implementing Approach 2 on solid geometries with a corner feature is shown in Fig. 9.5 and Fig. 9.6 for the cone and cube geometries, respectively. For both geometries, we notice similar effects for all confining potentials: for $\beta = 1$, the corner experiences widening/rounding as the number of iterations increases and shrinks in size, deviating from the
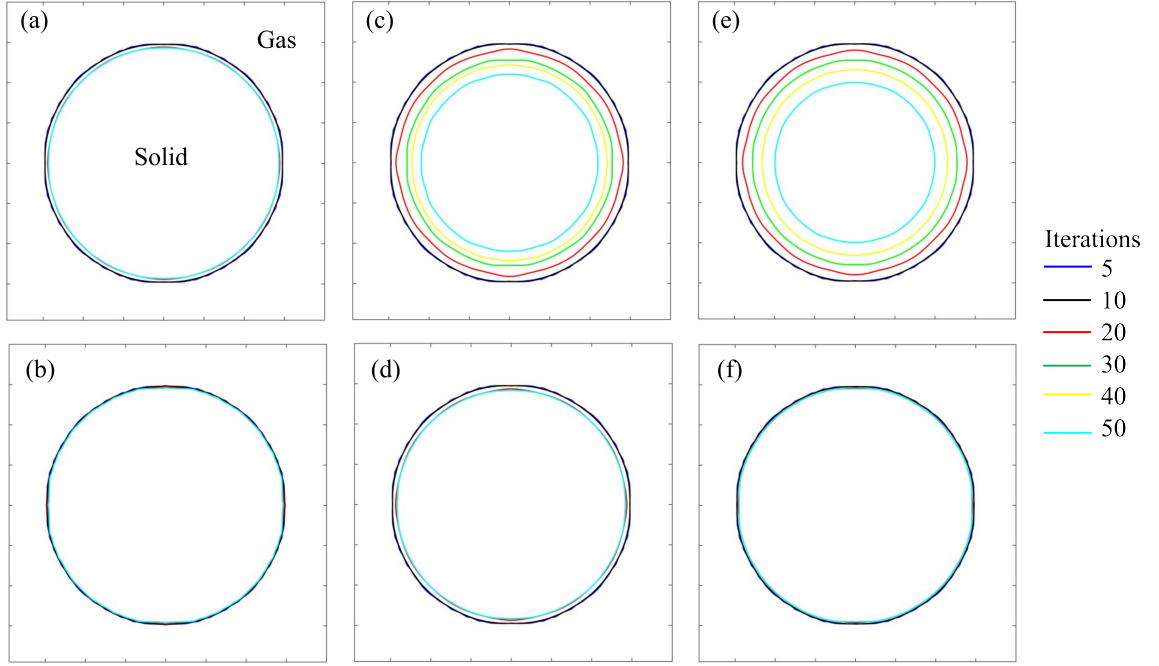
Figure 9.5: 2D cross-section of the gas-solid interface of a cone obtained after different numbers of iterations using Approach 2 with $\beta = 1$ (top row) and $\beta = 10$ (bottom row). Panels (a,b), (c,d) and (e,f) show the results when using the Quadratic, Quartic 1 and Quartic 2 polynomial functions, respectively.
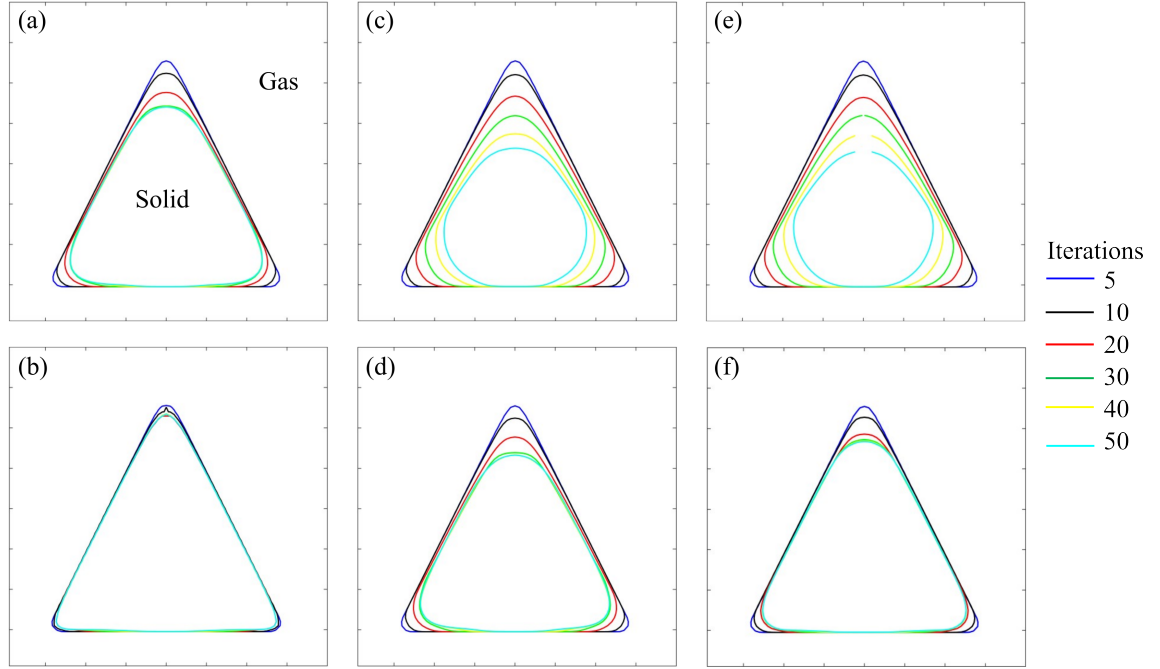
initialised geometry, while for $\beta = 10$, the distortion from the initialised geometry is not significant except for Quartic 1 and Quartic 2 potentials. These effects are also reflected in the objective function, similar to what we see for the spherical geometry. Therefore, to minimise the shrinking in size and widening of the corner, a large β and a small number of iterations are preferable; in this case, we found the optimum values at $\beta = 10$ and a number of iterations = 10.

Based on these results, we find that the Quadratic potential with $\beta = 10$ and the number of iterations = 10 will result in an optimum solid geometry, particularly for the geometry with a curve or corner feature. For a flat solid surface, both $\beta = 1$ and 10 would give a similar result.

9.2   Model Benchmarkings

So far, we have shown how our model is able to produce solid shapes as desired, thanks to the confining potential that is incorporated in the free energy function and implemented in the first stage of the energy minimisation procedures. During this stage, we have not yet introduced the liquid phase in the system. As explained in the Method section, the liquid phase is put in the system after the solid shape is formed. At this stage, the liquid phase is initialised as
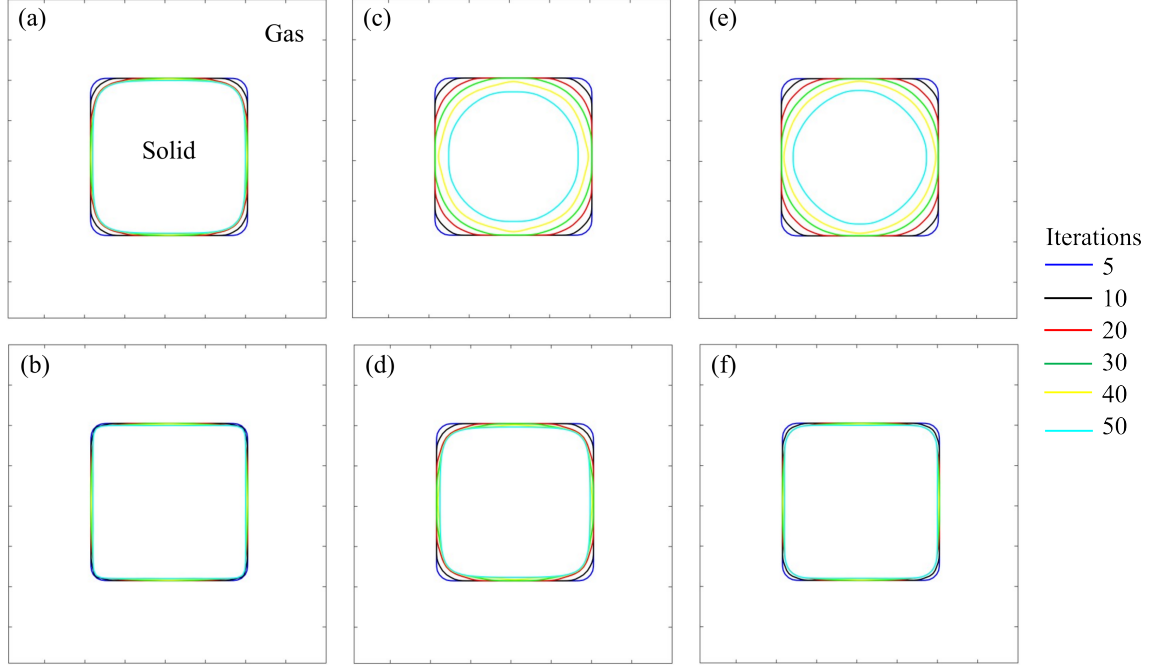
Figure 9.6: 2D cross-section of the gas-solid interface of a cube obtained after different numbers of iterations using Approach 2 with $\beta = 1$ (top row) and $\beta = 10$ (bottom row). Panels (a,b), (c,d) and (e,f) show the results when using the Quadratic, Quartic 1 and Quartic 2 polynomial functions, respectively.

desired, and during the minimisation routine, the solid phase is fixed, and only the liquid and gas components are allowed to evolve until the equilibrium is reached. In this section, we will present several benchmarking tests to validate our model of simulating wetting phenomena using the frozen fluid method.

9.2.1 Contact Angle Test

In this benchmarking test, we perform simulations of a liquid droplet wetting on solid surfaces and measure the contact angle. We start with a simple case where a droplet of radius 30 s.u. is placed on an ideal flat surface in the 2D domain of $N_x \times N_y = 300 \times 100$ s.u.. The periodic boundary condition is applied at the left and right boundaries, while the mirror boundary condition is imposed at the top and bottom boundaries. We set $\gamma_{23} = \sqrt{8/9}$, $\gamma_{12} = 1$ and γ_{13} following the Young equation. To form the flat solid, we use both Approach 1 and Approach 2 during the first stage of the minimisation. In Approach 1, we set the values of $\beta = 1$ and the number of iterations to 30 steps. In Approach 2, we use the Quadratic polynomial function as the confining potential and set $\beta = 10$ and the number of iterations 10 steps. The droplet is initialised on top of the solid surface using a staircase approximation of a half circle with

Table 9.1: Measured contact angles from simulations of a droplet on an ideal flat surface. The absolute error percentage of the measurement is shown in parentheses.

Input contact angle	10°	30°	60°	90°	120°	150°
Approach 1	9.4612 (5.38)	29.4780 (1.73)	59.7615 (0.39)	90.0709 (0.07)	119.9254 (0.06)	148.0855 (1.27)
Approach 2 (Quadratic)	9.9874 (0.12)	29.7678 (0.77)	60.2928 (0.48)	90.7793 (0.86)	120.3557 (0.29)	149.1951 (0.53)

a sharp interface. The typical equilibrium shape of the droplet on an ideal flat surface for contact angles $\theta < 90°$ is shown in Fig. 9.7 (a). The solid lines in the figure show the interface boundary between two fluids, $C_i = C_j = 0.5$, with i and j the two fluid components on either side of the interface. It should be noted that the distortion of the interface boundary at the three-phase contact line is due to the diffuse interface used in this method and will be avoided when measuring the contact angle. We also show the spatial profile of each fluid component, C_1, C_2 and C_3, in the direction perpendicular to the solid surface in Fig. 9.7 (b). We note here that the liquid phase, C_2, also follows the tanh profile as expected.
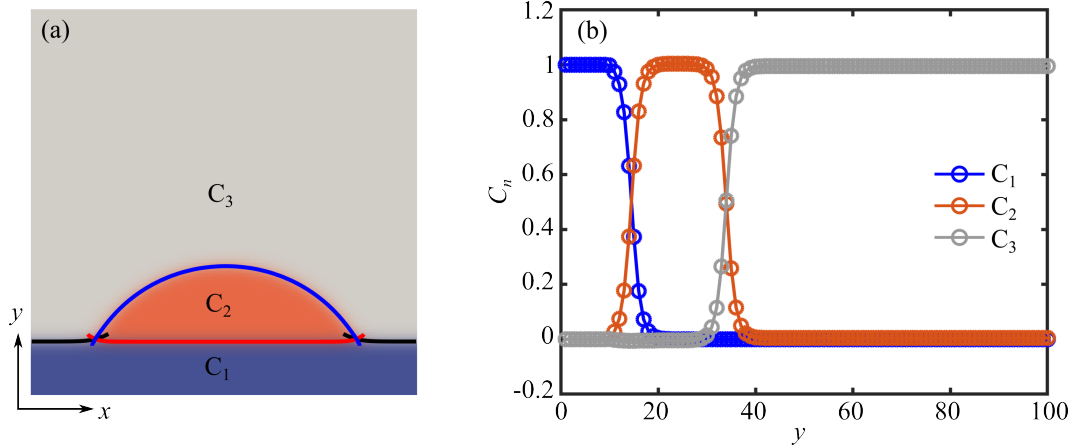
Figure 9.7: (a) Equilibrium shape of the droplet on an ideal flat surface with a contact angle of $\theta = 60°$. (b) Plots of fluid components C_1, C_2 and C_3 along y position of a cross-section of the system in panel (a) at $x = N_x/2$.

The measurement of the contact angle is done by fitting the liquid-gas interface line to a circle. The comparison between the measured and the input contact angles for Approach 1 and Approach 2 is listed in Table. 9.1. We note that both approaches result in a good agreement with the analytical prediction for a wide range of contact angles with an absolute error less than 2% except for the contact angle of $\theta = 10°$ using Approach 1. We suspect this is because of the shifting of the solid interface boundary towards the gas phase, which affects the accuracy of the contact angle measurement.

Next, we will investigate the wetting of a liquid droplet on a curved solid surface. Here, we

Table 9.2: Measured contact angles from simulations of a flat liquid-gas interface on a circle (2D) and a sphere (3D). The absolute error percentage of the measurement is shown in parentheses.

Input contact angle	10°	30°	60°	90°	120°	150°
Circle (2D)	10.6188 (6.18)	29.8890 (0.37)	60.1791 (0.37)	90.0434 (0.048)	119.8375 (0.13)	150.1364 (0.09)
Sphere (3D)	13.1874 (31.8)	31.5318 (5.10)	60.9134 (1.52)	89.5949 (0.45)	119.1576 (0.70)	147.0104 (1.99)

place 2D and 3D spherical particles with a radius of 30 s.u. at the liquid-gas interface in the computational domain of $N_x \times N_y = 100 \times 100$ s.u. and $N_x \times N_y \times N_z = 60 \times 60 \times 100$ s.u. for the 2D and 3D cases, respectively. For the 3D spherical particle, we only simulate a quarter of the sphere to reduce the computational cost and apply mirror boundary conditions on the left and right boundaries and periodic boundary conditions at the bottom and top boundaries. For the 2D case, we apply periodic boundary conditions at all simulation boundaries. We employ Approach 2 with the quadratic polynomial function as the confining potential to create the solid particle. We set the parameters $\beta = 10$ and the number of iterations to 10 steps. The solid particle is initialised using a staircase approximation of a sphere with a sharp interface, and the liquid phase is initialised after forming the solid particle.
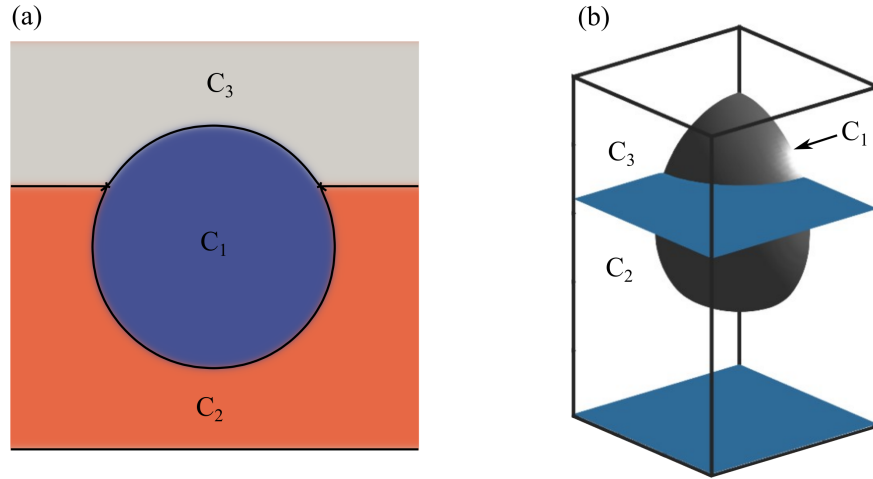
Figure 9.8: Equilibrium shape of liquid wetting a circle (a) and sphere (b) solid particle with a contact angle of $\theta = 60°$. In panel (b), only a quarter of the sphere is simulated with mirror boundary conditions applied on the x and y directions.

The typical equilibrium shape of the liquid-gas interface for the 2D and 3D cases is shown in Fig. 9.8, and the measured contact angles are tabulated in Table 9.2. The position of the three-phase contact line at the solid particle depends on the contact angle. It is in the northern hemisphere for $\theta < 90°$ and in the southern hemisphere for $\theta > 90°$. For $\theta = 10°$, the three-phase contact line meets at nearly the pole of the sphere, and due to the diffuse interface, the

Table 9.3: Comparison between the measured and the theory of the liquid-gas interfacial energy. All values are given in the simulation unit.

N_x	N_y	N_z	γ_{lg}	E_{sim}	E_{theory}	Error (%)
60	60	60	0.9428	3364.7700	3394.1125	0.86
40	60	40	0.9428	1495.4533	1508.4944	0.86
30	60	30	0.9428	841.1925	848.5281	0.86
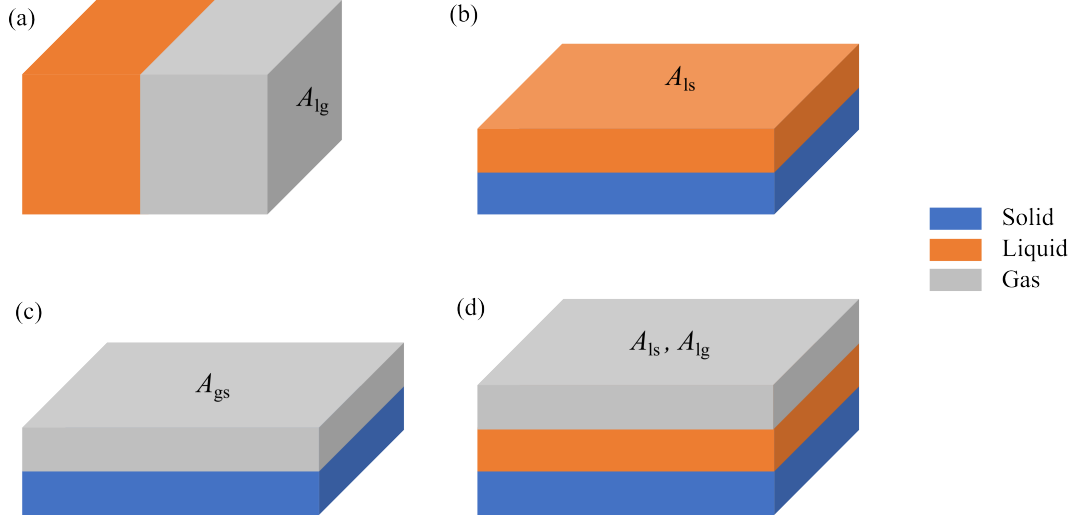
Figure 9.9: Simulation setups for (a) liquid-gas, (b) liquid-solid, (c) gas-solid and (d) liquid-solid liquid-gas interfacial energy tests.

accuracy of the contact angle measurement reduces, yielding a relatively large error, as can be seen in the table.

9.2.2 Interfacial Energy Test

In this test, we will evaluate the interfacial energy of liquid-gas, liquid-solid, and gas-solid interfaces. Theoretically, the interfacial energy between two fluids per unit length is given by the surface tension (γ_{mn}) multiplied by the interfacial area (A_{mn}), $E_{\text{mn}} = \gamma_{\text{mn}} A_{\text{mn}}$, where subscripts m, n denote for fluid 1 and 2. Remember that we represent the solid as a fluid that is 'frozen' and unable to evolve. The simulation setup for each test is shown in Fig. 9.9. All simulations in this test use mirror boundary conditions at all simulation boundaries. For the liquid-gas interfacial energy test, one-half of the simulation domain is filled with liquid and the other half is filled with gas (Fig. 9.9 (a)). No solid is used in the simulation. We use $\gamma_{\text{lg}} = \sqrt{8/9}$ and vary the area of the liquid-gas interface by varying the simulation domain. The interfacial energy measured at the equilibrium is given by the energy of the bulk and squared gradient

terms as in the free energy functional in Eq. (8.1). The results for different simulation domains are listed in Table. 9.3. The measured liquid-gas interfacial energies are in good agreement with the theoretical prediction.

For the liquid-solid and gas-solid interfacial energies, the simulation is set by initialising the solid slab with a flat interface at the bottom wall (see Fig. 9.9 (b,c)). We then apply Approach 2 using quadratic confining potential with $\beta = 10$ and the number of iterations $=$ 10 steps in the first stage of the minimisation to create the solid wall with a diffuse interface. For the liquid-solid interfacial energy test, the rest of the simulation domain is then filled with liquid phase after the desired solid surface is created, and the system is then minimised until equilibrium. For the gas-solid interfacial energy test, the equilibrium is reached after the first stage of the minimisation because the simulation domain has already been filled with the gas phase. Here, we vary the interfacial area, interfacial tension and contact angle. The results are tabulated in Table. 9.4 and Table. 9.5 for the liquid-solid and gas-solid interfacial energy tests, respectively.

Table 9.4: Comparison between the measured and theoretical values of the liquid-solid interfacial energy. All values are given in the simulation unit.

N_x	N_y	N_z	θ	γ_{lg}	γ_{ls}	γ_{gs}	E_{sim}	E_{theory}	Error (%)
60	60	60	90°	0.9428	1.0000	1.0000	3620.3827	3600.0000	0.56
60	60	60	60°	0.9428	1.0000	1.4714	3620.3827	3600.0000	0.56
60	60	60	30°	0.9428	1.0000	1.8164	3620.6089	3600.0000	0.57
60	60	60	30°	0.9428	0.5000	1.3164	1838.15805	1800.0000	2.11
100	100	60	90°	0.9428	1.0000	1.0000	10056.5417	10000.0000	0.56

Table 9.5: Comparison between the measured and theoretical values of the gas-solid interfacial energy. All values are given in the simulation unit.

N_x	N_y	N_z	θ	γ_{lg}	γ_{ls}	γ_{gs}	E_{sim}	E_{theory}	Error (%)
60	60	60	90°	0.9428	0.5000	0.5000	1834.3022	1800.0000	1.90
60	60	60	150°	0.9428	1.5000	0.6835	2490.0572	2460.6123	1.19
60	60	60	60°	0.9428	0.5000	0.9714	3517.3286	3497.0562	0.57
60	60	60	30°	0.9428	0.5000	1.3164	4752.4404	4739.3876	0.27
60	60	60	30°	0.9428	1.0000	1.8164	6534.2116	6539.3876	0.07

We also test the combination of liquid-solid and liquid-gas interfacial energies. The simula-

tion procedure in this test follows a similar manner as in the liquid-solid interfacial energy test, except that only a part of the simulation domain is filled with the liquid phase, whereas the rest is filled with the gas phase (see Fig. 9.9 (d)). The interfacial area of the liquid-solid and liquid-gas interfaces is equal. We also vary the interfacial area, interfacial tension and contact angle. The measured interfacial energies are tabulated in Table. 9.6. We also notice a good agreement with the theoretical prediction confirming the validity of our model.

Table 9.6: Comparison between the measured and theoretical values of the gas-solid and liquid gas interfacial energies. All values are given in the simulation unit.

N_x	N_y	N_z	θ	γ_{lg}	γ_{ls}	γ_{gs}	E_{sim}	E_{theory}	Error (%)
60	60	60	90°	0.9428	1.0000	1.0000	6985.1511	6994.1125	0.12
60	60	60	60°	0.9428	1.0000	1.4714	6985.2004	6994.1125	0.12
60	60	60	30°	0.9428	1.0000	1.8164	6985.3788	6994.1125	0.12
60	60	60	30°	0.9428	0.5000	1.3164	5202.9277	5194.1125	0.17
60	60	60	30°	0.9428	1.5000	2.3164	8770.1817	8794.1125	0.27

9.2.3 Capillary Rise

We next study the problem of capillary rise of a liquid in an ideal smooth cylindrical tube. Capillary rise is a fundamental wetting phenomenon and has been studied for decades [37, 43, 45]. The rise of liquid in a capillary tube is a result of the change in the total energy due to interfacial tension and gravity,

$$\Delta E = \Delta A_{\mathrm{lg}}\gamma_{\mathrm{lg}} + \Delta A_{\mathrm{ls}}\gamma_{\mathrm{ls}} + \Delta A_{\mathrm{gs}}\gamma_{\mathrm{gs}} + \Delta E_{\mathrm{g}}. \tag{9.1}$$

Here, ΔA_{lg}, ΔA_{ls} and ΔA_{gs} are the changes in the liquid-gas, liquid-solid and gas-solid interfacial area between the initial and final states, respectively. ΔE_{g} is the change in gravitational potential energy associated with the difference in liquid centre of mass height between the two states. If we assume a dry capillary tube as an initial state, then we have $\Delta A_{\mathrm{gs}} = -\Delta A_{\mathrm{ls}}$. According the geometry given in Fig. 9.10 (a), the changes of the interfacial area are given by $\Delta A_{\mathrm{lg}} = \pi(r_c^2 + h_m^2)$, $\Delta A_{\mathrm{ls}} = 2\pi r_c h_c$ and $\Delta A_{\mathrm{gs}} = -2\pi r_c h_c$. The change in gravitational potential energy is given by $\Delta E_{\mathrm{g}} = \frac{1}{2}\rho\pi r_c^2 h_c^2 g$. Using Young's equation to relate the interfacial tensions with the wetting contact angle, the change in total energy in Eq. (9.1) can be
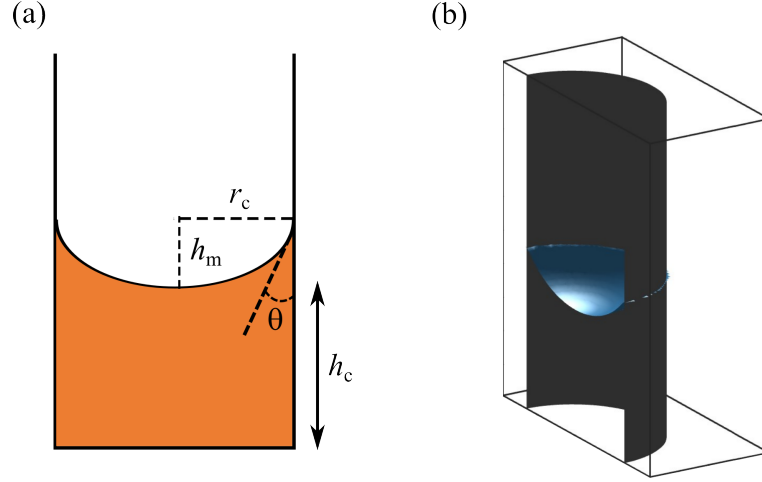
Figure 9.10: (a) Capillary rise configuration to derive the rise height. (b) Typical simulated rise height in a smooth cylindrical tube.

rewritten,

$$\Delta E = (\pi(r_c^2 + h_m^2) - 2\pi r_c h_c \cos\theta)\gamma_{\text{lg}} + \frac{1}{2}\rho\pi r_c^2 h_c^2 g. \tag{9.2}$$

Here, r_c, h_m, h_c, ρ, and g are the tube radius, meniscus height, rise height, liquid density, and gravitational acceleration, respectively. We will refer to the first term in Eq. (9.2) as the change in the surface energy, $\Delta E_{\text{surface}}$. The meniscus height, h_m, can be calculated using the circular arc approximation, yielding $h_m = r_c(1 - \sin\theta)/\cos\theta$ [150]. When the equilibrium is reached, the liquid stops rising, and the change in the total energy goes to zero. The rise height, h_c, can be derived by minimising the change of the total energy with respect to h_c, to obtain the well-known Jurin's Law,

$$h_c = \frac{2\gamma_{\text{lg}}\cos\theta}{\rho g r_c}. \tag{9.3}$$

In our simulations, we initialise a cylindrical tube with an inner radius of r_c using a staircase approximation of a hollow cylinder with a sharp interface. We then apply Approach 2 with the Quadratic confining potential in the first stage of minimisation to obtain a smooth and diffuse solid interface. We use $\beta = 10$ and set the number of iterations $= 10$ steps. After the desired cylindrical tube is formed, we measure the interfacial energy of the systems to be used as the interfacial energy of the initial state. We then initialise the liquid and allow the second stage of minimisation to run until the equilibrium is reached. The interfacial energy of the system is then measured again as the interfacial energy of the final state. In this simulation, the gravitational force is given as a body force, $F_b = \rho g$, and applied in the vertical direction
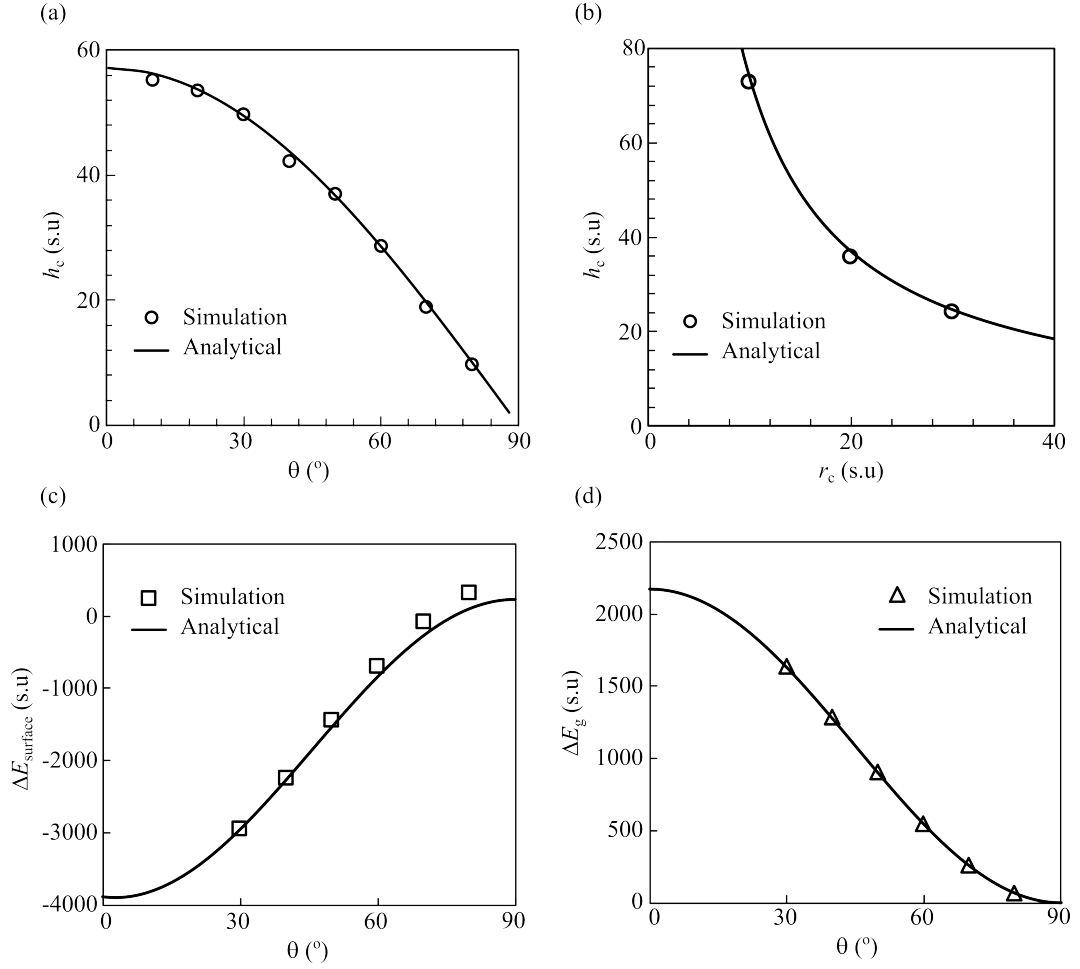
Figure 9.11: (a) and (b) Comparison between simulated and analytical rise heights plotted against contact angle and inner tube radius, respectively. The analytical prediction is taken from Eq. (9.3). (c) and (d) The changes in the surface energy $\Delta E_{\text{surface}}$ and gravitational potential energy ΔE_{g} obtained from simulation and calculated from Eq. (9.2) plotted against contact angle, respectively.

after the liquid phase is initialised in the system. This gravitational force enters the total free energy functional as an additional external energy term

$$\Psi_{\text{g}} = \int_V \left(f_{\text{g}} C_2 z \right) \mathrm{d}V, \tag{9.4}$$

where f_{g} is the gravitational force density. We use water as the rising liquid with properties: $\rho = 1000$ kg m^{-3} and $\gamma_{\text{lg}} = 0.0728$ N m^{-1}. The gravitational acceleration is $g = 9.81$ m s^{-2}. All of these physical parameters are then converted into simulation units via the gravitational force density: $f_{\text{g}} = \rho g \gamma'_{\text{lg}} P^2 / (\gamma_{\text{lg}} P'^2)$, where P and P' are the length scale of the capillary tube in physical and simulation units, respectively, and γ_{lg} and γ'_{lg} are the liquid-gas interfacial tensions in physical and simulation units, respectively. We use these values in simulations:

$\gamma'_{\mathrm{lg}} = \sqrt{8/9}$ s.u., $P' = 100$ s.u. and $P = 10$ mm. To reduce the computational cost, we only simulate half of the cylinder and apply mirror boundary conditions. The typical simulated capillary rise in a smooth cylinder tube is shown in Fig. 9.10 (b).

Figure 9.11 (a,b) show the measured rise height of liquid in a smooth cylinder tube for different wetting contact angles and tube radii. The dependency of the rise height on θ and r_c is captured well by simulations, as shown by a good agreement with the analytical prediction in Eq. (9.3). Furthermore, we also show the change in the surface energy, $\Delta E_{\mathrm{surface}}$, and gravitational potential energy, ΔE_{g}, obtained from simulations for different contact angles and compare them with the analytical prediction in Eq. (9.2), as shown in Fig. 9.11 (c,d). Our energy calculations are in good agreement with the predictions. It should be noted here that the simulated surface energies change are measured from the bulk and squared gradient terms as in the free energy model, while the simulated gravitational potential energy change is obtained from the gravitational force term in Eq. (9.4).

9.3 Applications

In this section, we will apply the frozen fluid method to more challenging cases, particularly cases involving complex surface geometries. We will study the wetting of a liquid droplet on superhydrophobic surfaces with different surface geometries.

Superhydrophobic surfaces are ubiquitous in nature and critical for many applications, as reviewed in the Introduction part. The main feature of superhydrophobic surfaces is the roughness of the surface, which can be in the form of nanostructure, microstructure or hierarchical structures. These structured surfaces allow the liquid droplet to minimise contact with the surface, resulting in the liquid droplet hanging on top of the surface roughness with air pockets trapped underneath the droplet (see Fig. 9.12). This wetting condition is also known as the suspended or Cassie-Baxter state. These structure surfaces lead to advantageous surface properties, including high contact angle [151], low contact angle hysteresis [152] and low rolling angle [153]. In some other cases, the liquid drop can penetrate the gap between the structures resulting in a complete wetting, which is known as the Wenzel state. However, a large energy barrier may prevent the liquid drop from penetrating and allow the droplet to stay in the Cassie-Baxter state. The transition from the Cassie-Baxter to Wenzel states is a key factor for some applications, such as coating and spraying processes, microfluidic devices and for protect-
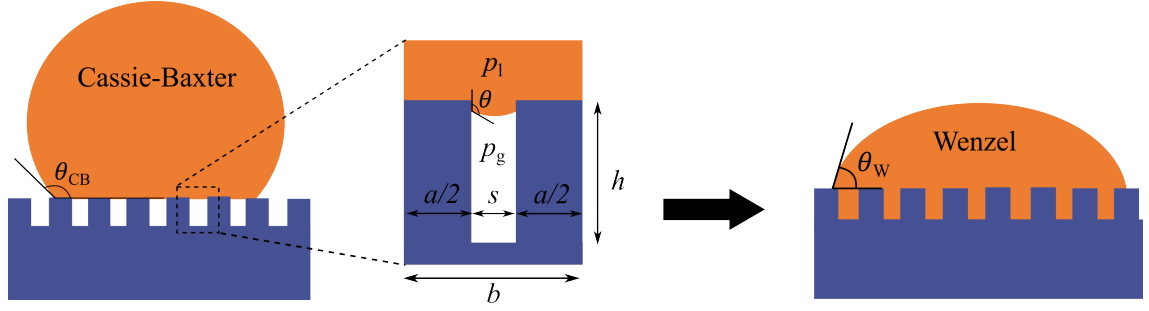
Figure 9.12: Schematic of a droplet undergoing a transition from a Cassie-Baxter state (left) to Wenzel (right) on a 2-dimensional periodically patterned surface with a rectangular micropillar geometry having width a, pillar spacing s, pillar height h and periodicity b. θ_{CB} and θ_{W} are the apparent contact angle of the droplet on the structured structured surface at Cassie-Baxter and Wenzel states, respectively, while and θ is the equilibrium contact angle on the corresponding a flat surface. p_l and p_g are the pressure in the liquid and gas (surrounding air), respectively. The enlarged view shows the liquid-gas interface underneath the droplet hanging between two adjacent pillars in a Cassie-Baxter state and is used as the system setup in simulations.

ing electronic devices underwater, in which the design of the superhydrophobic surfaces should be able to maintain the stability of the suspended state from transitioning to the Wenzel state under an external force such as the liquid pressure [154, 155]. This will be our focus in this study.

9.3.1 Droplet on 2-dimensional Micropillar-structured Surfaces

We start by studying a simple case of liquid drop deposited on a structured surface patterned periodically with 2-dimensional cylindrical micropillars having pillar's width (diameter) a, wall-to-wall spacing s, height h and distance (pitch length) b (see Fig. 9.12). In this case, the wetting transition can occur if the pressure difference is larger than the critical pressure that exists across the liquid-air interface in the gap between any two adjacent pillars [154]. Mathematically, the transition conditions in terms of the liquid pressure can be expressed as [58, 53]

$$\Delta p > \Delta p_c = -\frac{2\gamma_{lg}\cos\theta}{s}, \tag{9.5}$$

where $\Delta p = p_l - p_g$ is the pressure difference between the liquid pressure p_l and the gas (surrounding air) pressure p_g; γ_{lg} is the liquid-gas surface tension; θ is the equilibrium contact angle of the droplet on the corresponding flat surface, and $s = b - a$ is the wall-to-wall spacing between two adjacent pillars. When this condition is satisfied, the droplet will transition to a Wenzel state, otherwise, it will be in a Cassie-Baxter state. We define the critical pressure, Δp_c, as the pressure above which the wetting transition occurs.
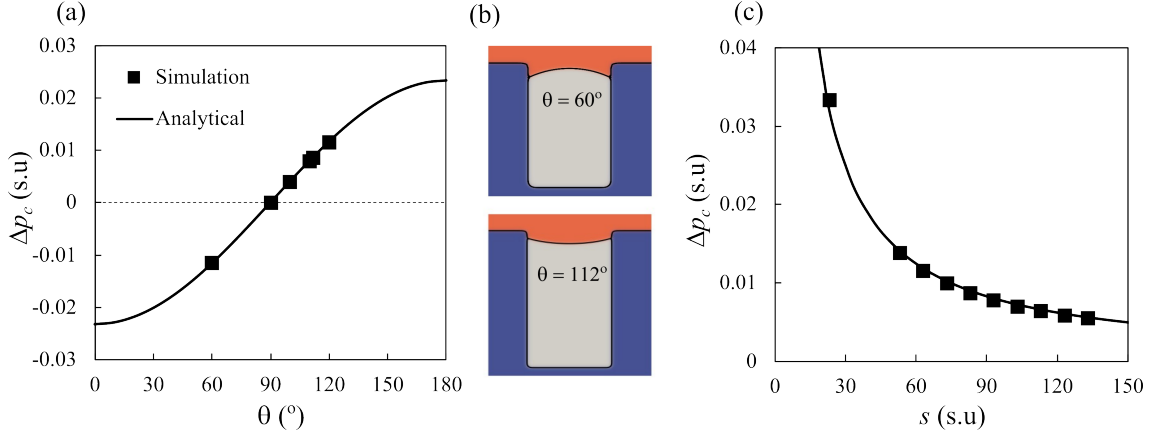
Figure 9.13: (a) and (c) Plots of critical pressure of a liquid deposited on top of 2-dimensional cylindrical pillars as a function of contact angle and pillar's wall-to-wall spacing, s, respectively. The solid line is the analytical prediction in Eq. (9.5). (b) The snapshots of the equilibrium shape of liquid-gas interface hanging in the gap between two cylindrical pillars at the critical pressure Δp_c for $\theta = 60°$ (top) and $\theta = 112°$ (bottom).

We simulate a liquid layer deposited on top of two pillars separated by a gap s instead of simulating a whole droplet on a patterned surface (see inset in Fig. 9.12). We make this approximation assuming that the droplet size is much larger than the pillar size and spacing. In our simulations, we apply Approach 2 using Quadratic confining potential with $\beta = 10$ and the number of iteration $= 10$ steps to create the solid geometry as in the inset in Fig. 9.12. The pillar width is set to be 40 s.u. and the pillar height is set to be tall enough so that the hanging liquid-gas interface does not touch the bottom wall at the critical pressure. A liquid with a flat liquid-gas interface is initialised on top of the pillars with a thickness of 20 s.u.. The system is fitted into a simulation box of $N_x \times N_y = 160 \times 200$ s.u..

We incorporate pressure in the system by applying a pressure difference between the liquid and gas phase, Δp, in the free energy functional in Eq. (8.7). Δp is varied with a small increment for every simulation until it exceeds a critical pressure. In order to obtain an accurate critical pressure, we apply a binary algorithm around the critical pressure value with a tolerance level of 10^{-4}.

Figure 9.13 (a) shows the critical pressure dependency on the equilibrium contact angle θ. As predicted by Eq. (9.5), the critical pressure is linearly dependent on $\cos\theta$. For $\theta < 90°$, the critical pressure is negative, indicating that the energy barrier is low and the transition to the Wenzel state is energetically favourable. On the contrary, the positive critical pressures for $\theta > 90°$ suggest the system has a higher energy barrier, making the transition not energetically favourable to occur unless some external perturbations from the liquid pressure are added to the

system. The latter condition is more suitable for the design of superhydrophobic surfaces. The equilibrium shapes of the liquid-gas interface for $\theta = 60°$ and $\theta = 112°$ at the critical pressure are shown in Fig. 9.13 (b), in which concave and convex meniscii occur due to the liquid-solid surface tension, respectively. At the transition ($\Delta p > \Delta p_c$), the hanging liquid-gas interface drops immediately to the bottom of the surface, filling the whole gap between the pillars. We notice that this Wenzel state applies for all simulated θ. We also show the dependency of the critical pressure on the pillar spacing in Fig. 9.13 (c). As the separation increases, the critical pressure reduces making it more favorable for the liquid to transition to a Wenzel state. The simulated critical pressure is in good agreement with the prediction.

We now look at the case of a droplet deposited on a structured surface patterned periodically with 2-dimensional truncated cone micropillars with pillar's top diameter and height, a and h, respectively, periodicity b and tilt angle α (see Fig. 9.14 (a)). Here, unlike the 2-dimensional cylindrical pillar, the vertical solid walls are tilted by an angle of α with $\alpha < 90°$ making the pillar wall-to-wall spacing s depends on the height of the hanging liquid-gas interface, h_i. Geometrically, the pillar wall-to-wall spacing is given by $s = b - a - \frac{2(h-h_i)}{\tan \alpha}$. Since s varies with h_i, this suggests that the transition from a Cassie-Baxter to a Wenzel state does not occur abruptly as in the 2-dimensional cylindrical pillar case. At the top of the gap between the pillars, the required pressure for the interface to slide is the smallest due to the largest wall-to-wall spacing. As it is closer to the bottom, the wall-to-wall spacing decreases and the required overpressure increases. It means that the pressure needs to be increased in order for the transition to occur. The pressure difference in the gap between 2-dimensional truncated cone micropillars can be expressed mathematically as

$$\Delta p = -\frac{\gamma_{\text{lg}} \sin (\theta + \alpha)}{s}. \tag{9.6}$$

From Eq. (9.6), one can observe that, for the tilt angle $\alpha < 90°$, Δp is negative for $\theta < 90°$ and positive for $\theta > 90°$. However, when the truncated cone is inverted ($\alpha > 90°$) resembling a reentrant geometry, Δp is positive for not only $\theta < 180°$ but also for $\theta < 90°$. This allows such geometry to maintain a Cassie-Baxter state for lower contact angles.

We perform the simulations in this case in a similar manner to that in the 2-dimensional cylindrical pillar case. We show the evolution of the liquid-gas interface at the gap between the pillars at an increasing Δp for $\alpha = 80°$ and $\theta = 112°$ in Fig. 9.14 (b). Here, we observe
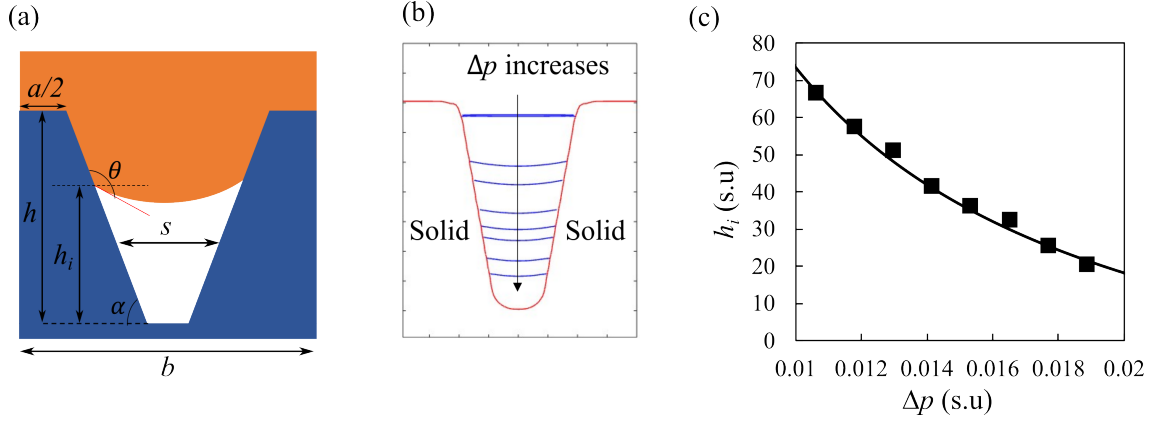
Figure 9.14: (a) Illustration of the liquid interface in between two truncated triangular pillars. (b) Snapshots of the liquid-gas interface at increasing pressure difference Δp. (b) Plot of the hanging liquid-gas interface height, h_i, as a function of Δp. The solid line is the analytical prediction.

the pinning of the liquid-gas interface at the top edge of the pillars at small Δp. As Δp is increased, the liquid-gas interface starts depinning and drops gradually. The transition to a Wenzel state occurs very close to the bottom of the gap. We then measure the heights of the hanging liquid-gas interface for every increment of Δp and plot them in Fig. 9.14 (c). We find a good agreement with the theoretical prediction in Eq. (9.6). It should be noted here that, because of the pinning, the heights of the hanging liquid-gas interface at small Δp are omitted from the plot.

9.3.2 Droplet on 3-dimensional Micropillar-structured Surfaces

Having the simulation and theoretical prediction in 2D established, we now extend our investigation to 3-dimensional cases. We consider 3D structured surfaces patterned with a hexagonal array of cylindrical or truncated cone micropillars with pillar's top diameter a, height h and distance (pitch length) b, as shown in Fig. 9.15 (a). Due to its periodicity, we can consider a unit cell of the hexagonal array that can be taken as a rectangular array with a central pillar having the same adjacent pillar spacing. In our simulation, we reduce this unit cell further by considering half of the unit cell and applying mirror boundary conditions at all simulation boundaries to reduce the simulation cost. We follow similar procedures to create the solid structure and use the same simulation parameters as in the 2-dimensional cases.

Figure 9.15 (b,c) show the snapshots of the equilibrium shape of the liquid-gas interface at the critical pressure for $\theta = 110°$ in a 3D unit cell of cylindrical and truncated pillars, respectively. For the truncated cone pillar, we set the tilt angle of the pillar's side wall to
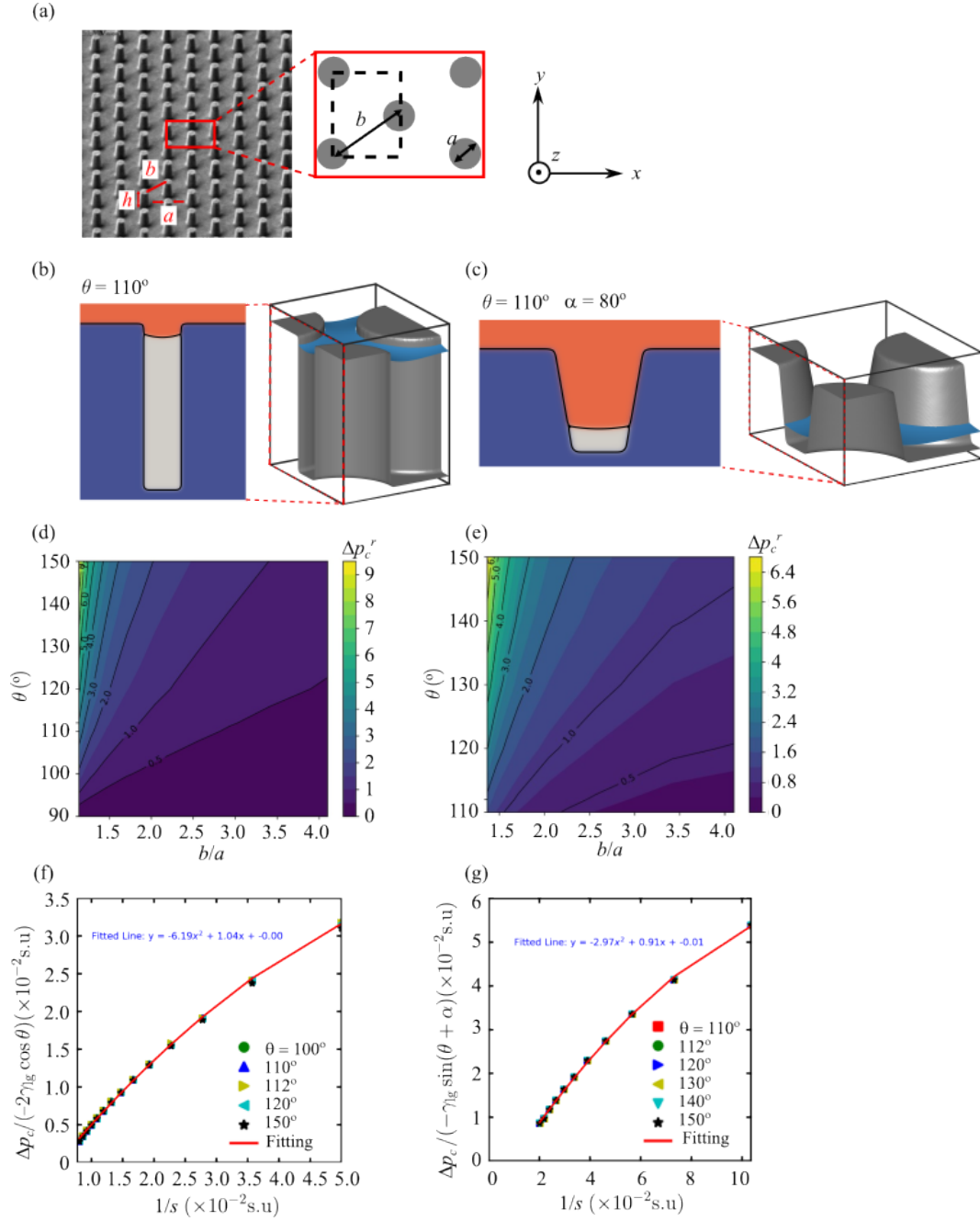
Figure 9.15: (a) SEM image of a 3-dimensional structured surface patterned with a hexagonal array of cylindrical or truncated cone micropillars with pillar's top diameter a, height h and distance (pitch length) b. The enlarged view shows a unit cell of the array viewed from the top and a portion of the array used in the simulation (dashed line). (b) and (c) Snapshots of the equilibrium shape of the liquid-gas interface at the critical pressure for $\theta = 110°$ in a 3D unit cell of cylindrical and truncated pillars, respectively. The enlarged views show the 2D cross-sections of the liquid-gas interface of the corresponding unit cells. (d) and (e) Contour plots of the reduced critical pressure measured from simulations, Δp_c^r, against variations of contact angle θ and pitch/diameter ratio b/a for cylindrical and truncated pillars, respectively. (f) and (g) Measured critical pressure in a 3D unit cell compared with the critical pressure predicted using a 2D model plotted as a function of $1/s$, where s is the pillar spacing for cylindrical and truncated pillars, respectively.

be $\alpha = 80°$. Similar to the 2-dimensional case, we observe an abrupt transition of the liquid from the suspended (Cassie-Baxter) to the Wenzel state for the cylindrical pillar structure when the pressure difference Δp surpasses the critical pressure. For the truncated cone pillar structure, a gradual transition is observed in which the liquid-gas interface gradually descends as Δp increases until it collapses to let the liquid fill the whole gap between the pillars when $\Delta p > \Delta p_c$. As we define the critical pressure before which the liquid-gas interface collapses, the diffuse interface width may influence the exact value of the critical pressure. In Fig. 9.15 (b,c), we also show 2D cross sections of the liquid-gas interface of the corresponding unit cells between two adjacent pillars. It can be seen that for the truncated cone pillar structure, the liquid-gas interface at the critical pressure is very close to the bottom of the gap.

The effect of the contact angle θ and pitch length to diameter (b/a) ratio on the critical pressure of the liquid on these structures is shown in Fig. 9.15 (d,e). Here, the critical pressure Δp_c is divided by (γ_{lg}/b) to make Δp_c^r dimensionless. We choose the b/a ratio to describe the effect of the pillar wall-to-wall spacing on the critical pressure. Low b/a means small pillar wall-to-wall spacing, and *vice versa*. In our simulations, we keep the value of the pitch length constant and vary the pillar's top diameter. From the figures, we observe the similarity in the trend of the critical pressure for both geometries: high critical pressures are obtained for high θ and low b/a, while low critical pressures for low θ and high b/a. For a given θ, the critical pressure decreases as b/a increases. For a given b/a value, the critical pressure increases as θ increases.

The dependency of the critical pressure on the contact angle and pillar's wall-to-wall spacing (via b/a) can be inferred from the 2-dimensional prediction. While the contact angle in the 3D case is the same as in the 2D case, determining the effective pillar wall-to-wall spacing in 3D is not as straightforward as in 2D. Since the unit cell of the hexagonal array is composed of a rectangular array, two adjacent pillars along the width side have different spacing from those along the length side. These two spacing length scales contribute equally to the effective wall-to-wall spacing. To obtain the effect of the wall-to-wall spacing quantitatively, we compare the measured critical pressure from simulations in the 3D unit cell with the analytical prediction using 2D models as in Eq. (9.5) and Eq. (9.6) for cylindrical and truncated cone pillar geometries, respectively. We then plot $\Delta p_c/(-2\gamma_{\text{lg}}\cos\theta)$ and $\Delta p_c/(-\gamma_{\text{lg}}\sin(\theta + \alpha))$ as a function of $1/s$ for different contact angles in Fig. 9.15 (f,g), respectively. Here, s is the pillar wall-to-wall spacing along the width side of the rectangular unit cell, or $s = b - a$. We observe
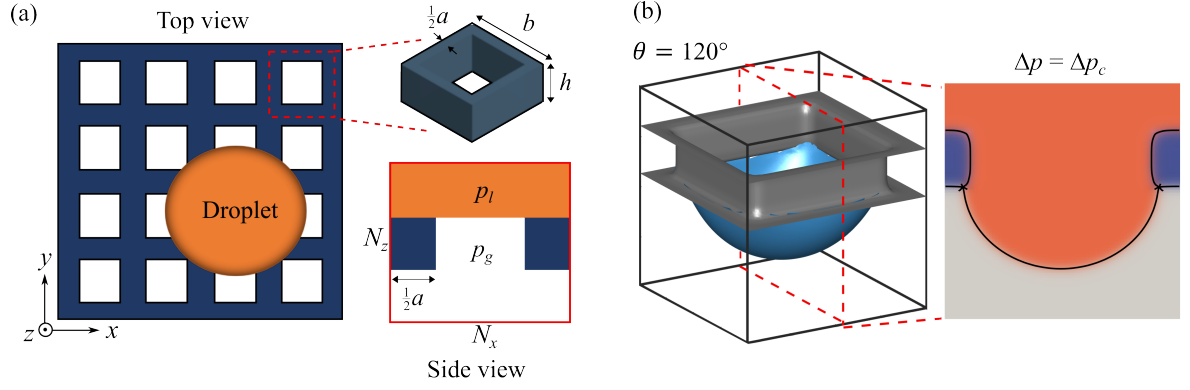
Figure 9.16: (a) Schematic of a liquid drop on top of mesh structure viewed from the top. The enlarged view shows a unit cell of the mesh with a grid size (pitch length) b, width a and thickness h. The bottom right figure shows a 2-dimensional cross-section of the unit cell used as a simulation setup with a layer of liquid placed on top of the grid. N_x and N_z are the simulation domain sizes in the x- and z-directions, respectively. p_l and p_g are the pressures in the liquid and gas phases, respectively. (b) A snapshot of the typical equilibrium shape of the liquid-gas interface in a mesh structure under the critical pressure, Δp_c (here, we show for $\theta = 120°$).

that, for both geometries, all y-axis values for all θ collapse into a single curve. A polynomial fitting of these data shows that the critical pressure in 3D case deviates slightly from the 2D case. For the cylindrical pillar structure, we find $\Delta p_c^{3D}/\Delta p_c^{2D} \approx 1.04 - 6.19/s$, while for the truncated cone pillar structure, we find $\Delta p_c^{3D}/\Delta p_c^{2D} \approx 0.91 - 2.97/s$. These relations allow us to predict the critical pressure on such geometries for any b/a ratio.

9.3.3 Droplet on Mesh Structures

The final case we consider for the frozen fluid application is a liquid droplet on a mesh structure. Here, the mesh structure is formed by a 3-dimensional flat surface patterned with an array of square holes, as shown in Fig. 9.16 (a). The array is characterised by the grid size (pitch length) b, width d and thickness h. In the computational domain, a unit cell of the mesh is used in the simulation and a layer of liquid is placed on top of the mesh rather than a droplet. The periodic boundary condition is applied in the x- and y-directions, whereas the mirror boundary condition is imposed in the top and bottom boundaries. We follow a similar method and use the same simulation parameters in applying the confining potential to create the solid structure as in the previous section.

A typical equilibrium shape of the liquid-gas interface on a unit cell of the mesh under a critical pressure is shown in Fig. 9.16 (b), for $\theta = 120°$. Here, the critical pressure is defined as the pressure above which the liquid penetrates the hole of the mesh completely. From the
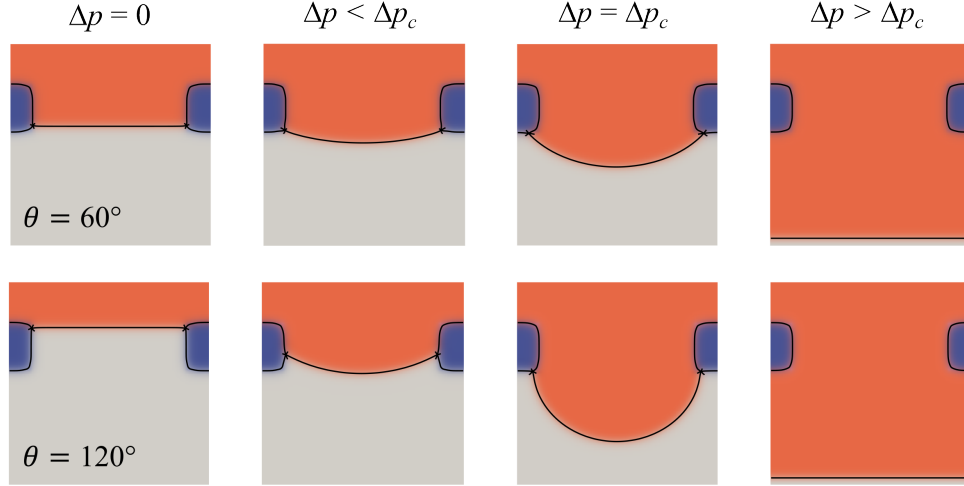
Figure 9.17: Snapshots of the equilibrium shape of the liquid-gas R at a 2-dimensional cross-section of the mesh under different pressures Δp showing a Cassie-Baxter to Wenzel state transition. The top row is for $\theta = 60°$, while the bottom row is for $\theta = 120°$.

figure, it can be seen that the liquid-gas interface slightly slides to the bottom side of the grid and forms a large bulge before the transition to a collapsed state. A more detailed transition mechanism can be seen in Fig. 9.17, where we compare the evolution of the liquid-gas interface at an increasing Δp for $\theta = 60°$ (top row) and $\theta = 120°$ (bottom row).

Let us focus on a low contact angle, $\theta = 60°$. For a micropillar-structured surface, the critical pressure for $\theta = 60°$ will be a negative value as predicted by Eq. (9.5). At this critical pressure, the liquid-gas interface will have a negative curvature (see Fig. 9.13 (b)). When the pressure is greater than the critical pressure, the liquid will overcome the energy barrier in the gap between the pillars to make the transition to a collapsed state, filling the whole gap between the pillars. Similarly, in the mesh structure, the liquid fills the gap between the grid of the mesh at $\Delta p < 0$. However, a large gas phase underneath the mesh creates another energy barrier for the liquid, causing the liquid-gas interface to be pinned at the bottom edge of the grid. At $\Delta p = 0$, due to the pressure balance between the liquid and gas phases, the interface curvature becomes zero. As Δp increases, the liquid-gas interface sags at the bottom sides of the grid. This is accompanied by an increase in the liquid-gas interface curvature until Δp reaches a critical value at Δp_c. Above Δp_c, the energy barrier is overcome, and the liquid makes the transition to a completely collapsed state, allowing the sagging liquid-gas interface to collapse. At this point, the liquid penetrates the hole of the mesh completely.

For a large contact angle, in this case $\theta = 120°$, the liquid-gas interface is pinned at the top edge of the grid with a zero curvature at $\Delta p = 0$. As seen for the micropillar-structured surface,
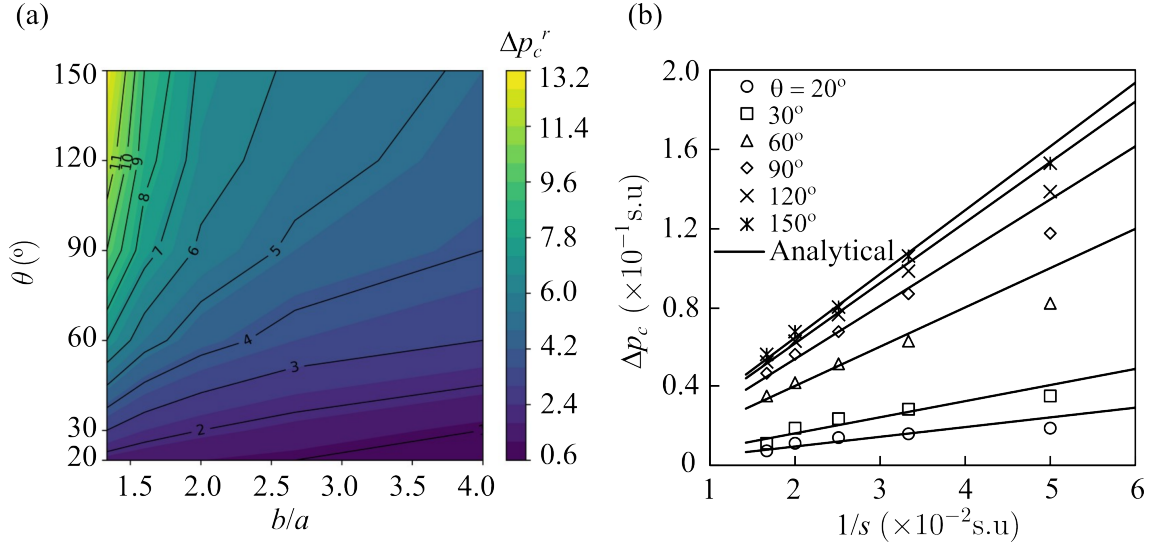
Figure 9.18: (a) Contour plot of the dimensionless critical pressure, Δp_c^r as a function of the grid size-to-width ratio, b/a, and the contact angle θ. (b) The critical pressure is plotted against $1/s$ for different θ and compared with the analytical model in Eq. (9.7).

the critical pressure for $\theta = 120°$ would be at a positive value, and, at this point, the liquid-gas interface would be around the top of the pillar. As Δp increases, the first depinning mechanism starts to occur, in which the liquid-gas interface depins from the top edge of the grid, slides to the bottom of the grid, and gets pinned again at the bottom edge of the grid. At this point, the liquid has overcome the energy barrier in the gap between the grid but cannot pass through due to the energy barrier created by the gas underneath the structure. As Δp keeps increasing, the three-phase contact line eventually slides around the edge because the liquid-gas interface curvature starts to increase. Once the pressure difference exceeds the critical pressure, the liquid penetrates through the mesh completely, and the liquid-gas interface collapses.

Finally, we investigate the effect of the grid geometrical parameters through the grid size-to-width ratio, b/a, on the critical pressure for different contact angles, as shown in Fig. 9.18. To vary b/a, we vary the width a and keep the grid size p constant. In Fig. 9.18 (a), the critical pressure is presented as a dimensionless reduced critical pressure Δp_c^r ($\Delta p_c^r = \Delta p_c/(\gamma_{\text{lg}}/p)$). From the contour plot, it can be seen that the critical pressure reduces as b/a increases (the hole size increases) and increases with the contact angle. To predict the dependency of the critical pressure on the hole size (via the gap distance $s = b - a$) and the contact angle, we use the Laplace pressure equation, $\Delta p = \gamma_{\text{lg}}/R$, where R is the radius of the liquid-gas interface curvature. By relating R to the gap distance s, the critical pressure for the droplet to penetrate

the mesh can be approximated by

$$\Delta p_c = \frac{2\gamma_{lg} \cos{(90° - \theta)}}{s}.$$

(9.7)

where the contact angle θ is measured against the horizontal plane of the bottom grid. The comparison between the simulation and the analytical prediction using this model is shown in Fig. 9.18 (b). We note here that the analytical predictions plotted in this figure use some fitting parameters due to the square geometry of the hole. It can be seen that the critical pressure is linearly dependent on $1/s$.

9.4 Discussion

In this part of the thesis, we proposed a new method to study wetting phenomena on complex geometry surfaces using a reduced ternary phase-field-based model called the frozen fluid method. In this model, one of the fluid components is treated as a solid phase and the rest as liquid and gas phases. The main advantage of using this model is that it allows us to construct highly complex surface structures with a smooth and diffuse interface.

We began by elaborating on the free energy function for the ternary fluids and elucidating the confining potentials applied to create a desired solid geometry. In order to obtain a smooth solid interface with a desired interface profile, we carefully tuned the coefficient β in the confining potential term and truncated the number of iterations during the energy minimisation routine. These two parameter criteria were carefully examined through an objective function against geometries with different features to find their optimum values.

In order to validate the present method, we considered several benchmark problems, including the contact angle test for a flat and curved solid interface, the interfacial energy test and the capillary rise problem. The numerical results are in good agreement with the analytical solutions. We finally applied the frozen fluid method to more challenging complex geometries where we studied wetting transition in different superhydrophobic surfaces.

In addition to enabling us to construct highly complex surface structures, the frozen fluid method also has some other advantages. It is easy to implement in the phase-field model and eliminates the complexity of the wetting condition on the solid surface because one only needs to assign a proper surface tension between the fluid phases. Moreover, the diffuse interface of the solid has its own advantage − enabling facile interactions between fluids and complex

surface topographies [150]. Although not discussed in the applications, the frozen fluid method also allows us to adjust the chemical properties of the solid easily. This is useful if we want to study the effect of chemical patterning on the wetting of complex geometry surfaces.

There are some limitations of this method. As we have seen earlier in this chapter, the effect of the confining potential on the corner feature of the solid makes the sharp corner to be widening/rounding. In addition, due to the diffuse interface used in this model, a solid geometry has to be large enough to accommodate the bulk and interface regions of the solid, which, in turn, makes the simulation domain necessarily large. Furthermore, the model developed in this chapter is limited to the study of quasi-static problems.

In the future, it is interesting to extend the application of this frozen method to investigate the wetting phenomena in many more complex geometry surfaces, such as porous media [156, 157], bio-inspired structured surfacecs [158, 159], etc. In addition, the extension of this model to quarternary fluids will allow us to study the wetting phenomena of ternary fluid on complex geometry surfaces. Furthermore, it will be interesting to couple this model with a dynamic method such as the Lattice Boltzmann method to enable the study of liquid dynamics on complex geometry surfaces.

Part V

Conclusions and Outlook

CHAPTER 10

Conclusions

In this thesis, we studied different wetting phenomena in structured surfaces using Lattice Boltzmann and phase-field-based energy minimization methods. For the latter, we extended the method by incorporating effective long-range interactions, which allowed us to model pseudo-partial wetting scenarios; and by developing the frozen fluid method, which allowed us to simulate wetting phenomena on highly complex geometry surfaces.

In Part II, we studied the dynamics of hemiwicking of liquid into structured surfaces patterned with square and face-centred/hexagonal arrays of micropillars using the Lattice Boltzmann method. A detailed presentation of the single-phase Lattice Boltzmann method was done in Chapter 4. We have validated our method by performing a simple Poiseuille flow test of liquid flowing between two parallel horizontal flat walls under a constant body force and pressure gradient. In Chapter 5, we developed an analytical model to predict the hemiwicking coefficient by balancing the capillary driving force and a viscous force and solving the Navier-Stokes equation for representative channels. We discussed different ways of approximating the representative channel for square and face-centre/hexagonal arrays, from which the equivalent channel width is derived, including volume equivalent, volume-area equivalent and pillar face-to-face spacing approximations. In addition, we proposed a hydraulic-electric circuit analogy to approximate the representative channel for face-center/hexagonal arrays. We have demonstrated that the theoretical predictions for square arrays of micropillars using the volume equivalence approximation showed an excellent agreement with the simulation results and improved accuracy compared to previously proposed models. However, the model was observed to break down for extreme cases where the array is too dense or sparse. Moving on, we have also shown the applicability of the hydraulic-electric circuit analogy approach in approximating the

equivalent channel for symmetric and asymmetric face-centre/hexagonal array cases. For the former, implementing this approach using a parallel cell was found to show a good agreement with simulation results for moderately dense arrays, whereas using series and a combination of parallel and series cells showed a good agreement for low- and high-dense arrays, respectively. For the latter, the parallel cell approach was found to be applicable for the case where the mid-pillar is moved sideways if the unit cell is approximated by the face-to-face approach. When the mid-pillar is displaced towards the propagation direction, we found a good agreement for the parallel-series approximation, particularly for high-density arrays.

In Part III, we presented systematic numerical studies of liquid filling in grooved surfaces using a phase-field-based energy minimization method. We detailed the formulation of the method and its implementation in Chapter 6. In particular, our model includes short-range and long-range (attractive and repulsive) interactions. We have also introduced a new polynomial function in the interaction energy density, which improved the accuracy of the simulation. In Chapter 7, we first showed the effect of long-range interactions on a liquid thin film on a flat surface, which leads to three different wetting conditions: complete, partial and pseudo-partial wetting conditions. We then showed how the liquid filling occurs on groove surfaces for those wetting conditions over a pressure range. We have demonstrated that, while for all cases, the liquid filling process occurs over three stages, namely pre-filling, capillary filling, and post-filling, the liquid filling behaviour of each wetting condition is different. The complete wetting case is characterised by the absence of contact line pinning and hysteresis, whereas in the partial and pseudo-partial wetting cases, the hysteresis behaviour is prominent due to the coexistence of two metastable states over a pressure range. Furthermore, we have also demonstrated that the critical pressure of liquid filling depends on the groove width, in agreement with the theoretical predictions for both partial and complete wetting cases. For the pseudo-partial wetting case, we found that the filling transition can display a number of distinct morphological pathways.

We then turned our interest to the study of the wetting of liquid on complex geometry surfaces in Part IV. To begin with, we introduced a new ternary-fluid-based phase-field model in the energy minimization method, namely the frozen fluid method, in Chapter 8. Unlike the traditional phase field model, the frozen fluid method treats one of the fluid phases as a solid phase, while maintaining the thermodynamics of the three fluid phases. We also proposed two approaches to construct any solid geometry as desired with a smooth and diffuse interface, any of which, if implemented with the suitable parameters, would result in the expected solid

interface. To validate this new method, we performed several benchmarking tests and compared the results with analytical predictions, as detailed in Chapter 9. Our results showed that the frozen fluid method is applicable to different types of solid geometry, including surfaces textured with cylindrical and truncated cone pillars and mesh geometry. We then applied this new methodology to more challenging complex geometries, where we investigated the wetting transition in different superhydrophobic surfaces.

CHAPTER 11

Future Outlook

In this chapter, I will highlight some potential directions for future works building on from this thesis.

11.1 Dynamics of Liquid Filling on Structured Surfaces

In Part III, we have demonstrated the numerical study of liquid filling on a structured surface by taking into account the solid-liquid intermolecular interactions. The method used in this study only captures the quasi-static morphology of the liquid-gas interface on such surfaces upon a variation of pressure difference. While it gives an insightful understanding of the liquid filling behaviour, the dynamics of liquid under non-equilibrium conditions are still lacking. The understanding of how liquid dynamics on structured surfaces is important for various applications, such as self-assembly, coating and microfluidic devices [160]. In addition, it could also give insights into understanding the hydrodynamics in microscopic scales, such as the hydrodynamic slip [161]. Therefore, it is interesting to extend the phase-field model presented in this work into a dynamics method, such as the Lattice Boltzmann method.

The Lattice Boltzmann method is proposed because it can accommodate the free energy functional model used in the phase-field energy minimisation method. This makes it easy to incorporate the contribution of the solid-liquid interactions (either short-range or long-range interactions) in the method. One way to do this is by employing the so-called Guo forcing method [162], in which the solid-liquid interaction contributions enter the dynamic equation (via the lattice Boltzmann equation) through an external force. Once the solid-liquid interaction potential is formulated, it will be used to derive the chemical potential, which will
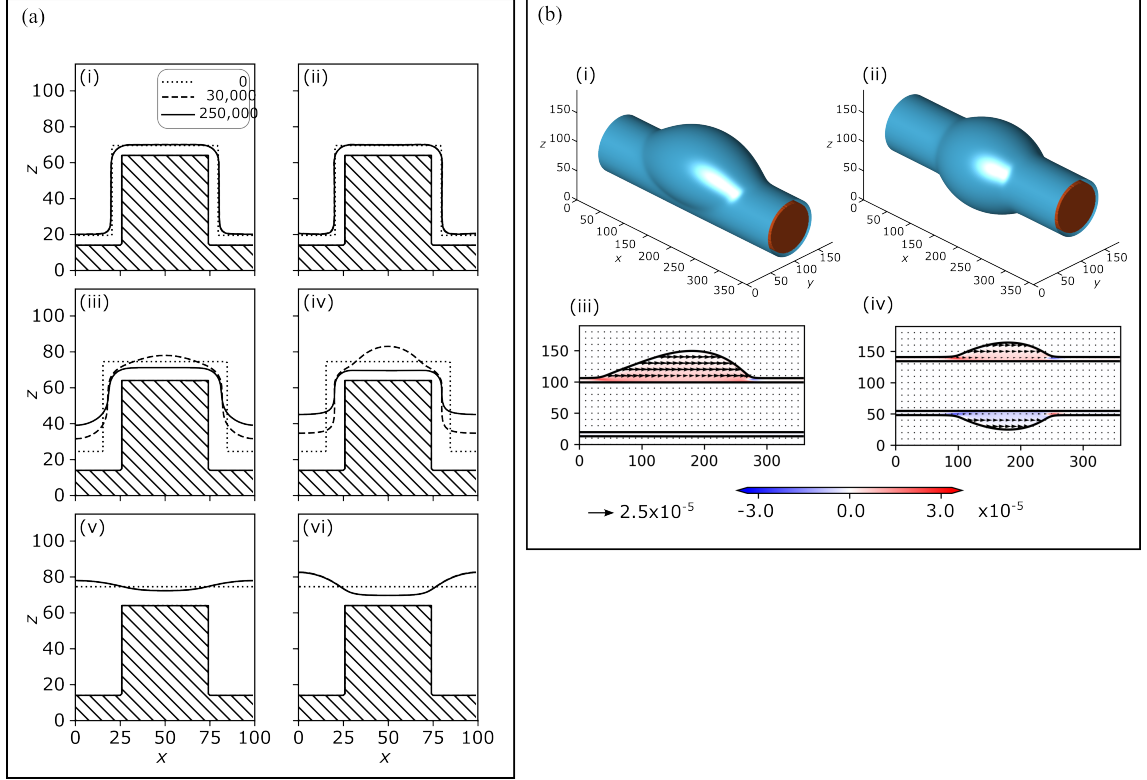
Figure 11.1: Lattice Boltzmann simulation results with the long-range solid-liquid interactions. (a) Liquid filling states on a grooved surface for pseudo-partial wetting case. (b) Droplet in clamshell (left column) and barrel (right column) morphologies. Adapted from [163].

enter the Guo forcing term.

An example is done by Ref [163], in which the long-range potential is implemented in the Lattice Boltzmann method to study the dynamics of a pseudo-partial wetting droplet on a fibre. In this work, the author first shows the morphology of liquid filling on a grooved surface in the pseudo-partial wetting state, as shown in Fig. 11.1 (a). This figure demonstrates the similarity with the one captured by our method in Chapter 7. The author then shows a droplet in clamshell and barrel morphologies sitting on a fibre in pseudo-partial wetting (Fig. 11.1 (b)).

11.2 Liquid Wetting and Dynamics on Bio-inspired Structures

In Part IV, we have applied the frozen fluid method to explore superhydrophobic surfaces with different pillar geometries and patterns and investigated the wetting transition across these geometries. Such surfaces hold significant promise for various applications due to their relatively simple fabrication process. However, natural superhydrophobic surfaces exhibit far more complexity, offering intriguing properties as a result. Take, for example, a *Salvinia* plant whose leaf surfaces have eggbeater-like hydrophobic microhairs topped with hydrophilic
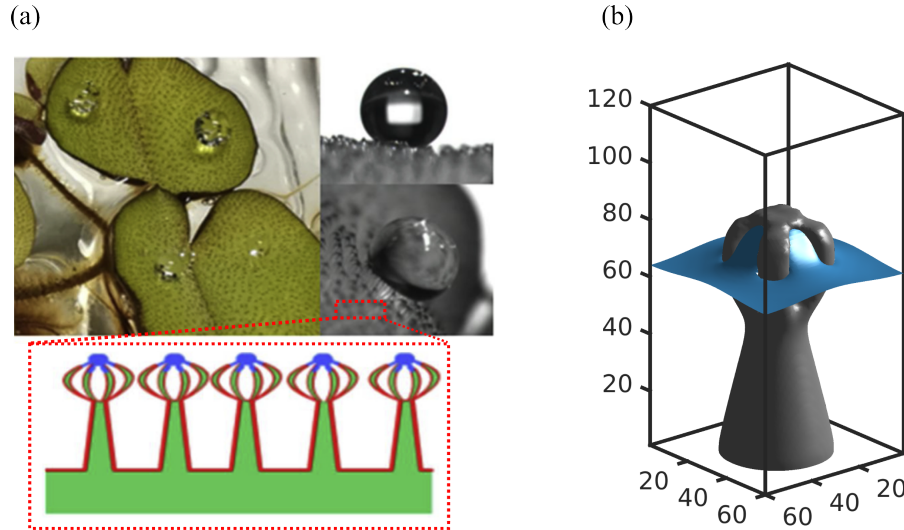
Figure 11.2: (a). *Salvinia* plant and its eggbreaker-like structured surfaces. Adapted from [164]. (b) Frozen fluid method simulation on a *Salvinia*-inspired structure.

tips (Fig. 11.2 (a)) [164]. This combination of hydrophobic and hydrophilic surfaces offers superhydrophobicity alongside strong adhesion to water [165], presenting great potential for applications such as water collection in the desert, lossless micro-liquid manipulation, and ship drag-reduction, among others [158, 166, 167].

The frozen fluid method could be a great tool for this application. Not only does it allow us to create such complex geometry in simulations, but it also enables precise control over the chemical properties of the surface, allowing for the coexistence of superhydrophobic and hydrophilic properties (Fig. 11.2 (b)). Using this method, we can study the behaviour of liquids (or droplets) deposited on this structure and the chemical durability of the structure underwater.

Furthermore, another interesting application of the frozen fluid method is the study of directional liquid transport on leaf-like structured surfaces, inspired by the leaf structure of *Araucaria* plant. The *Araucaria* leaf consists of 3-dimensional ratchets with transverse and longitudinal reentrant curvatures (Fig. 11.3 (a) (top)). Recently in [159], it was reported that this structure allows low-surface-tension liquids to spread in a pathway along the ratchet-tilting direction (forwards spreading), whereas high-surface-tension liquids flow in the opposite direction (backwards spreading) (Fig. 11.3 (a) (bottom right)). This unique behaviour has inspired researchers to create the so-called Araucaria leaf-inspired surface (ALIS) to understand the mechanisms behind these liquid transport properties and their applications. By varying the tilting angle of the leaf structure α and the liquid contact angle θ, it was shown that the
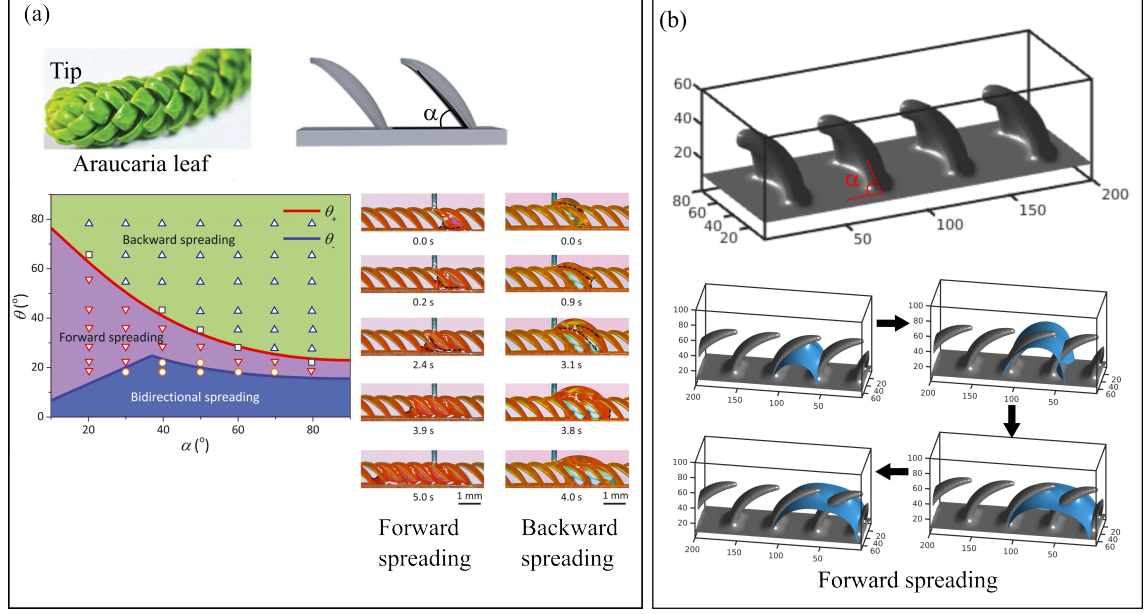
Figure 11.3: (a). Top: *Araucaria* leaf and its structural characteristic of the ratchet arrays. Bottom right: Forward (left) and backward (right) spreadings of liquids with different contact angles. Bottom left: Phase diagram for the directional steering of liquid transport. Adapted from [159]. (b) Frozen fluid method simulations for the liquid spreading on leaf-structured surfaces.

liquid can exhibit forward, backward and bidirectional spreadings depending on α and θ, as shown in the phase diagram in Fig. 11.3 (a) (bottom left).

We have carried out some preliminary investigation on this study by performing simulations on liquid propagation in similar leaf-structured surfaces (Fig. 11.3 (b) (top)). While the frozen fluid method only captures the quasi-static behaviour of the liquid, we can also get an insightful understanding of the mechanisms of the liquid propagation by slowly increasing the liquid volume. This enables us to reproduce the forward, backward and bidirectional spreadings of liquid with variations of α and θ. In Fig. 11.3 (b) (bottom), we show snapshots of the forward spreading of liquid in leaf-structured surfaces at a variation of liquid volumes for $\alpha = 45°$ and $\theta = 60°$. For future work, it is interesting to study the effect of structure geometrical parameters on liquid transport in order to get a full understanding of the liquid transport mechanisms and also to optimise the ALIS design.

In order to get full dynamics of liquid spreading on leaf-like structured surfaces, it is also interesting to combine the frozen fluid method into a dynamic method like the Lattice Boltzmann method. Of course, the Lattice Boltzmann suitable for this purpose is a ternary fluid Lattice Boltzmann method. While the main ingredient in the frozen fluid method is the same as in the Boltzmann method (which is the free energy functional), we still need to consider how

to "freeze" one of the phases as a solid and solve the appropriate equations of motion (such as Cahn-Hilliard and Navier-Stokes equations). A similar method has been recently reported in literature [168].

References

[1] A. Otten and S. Herminghaus, "How plants keep dry: a physicist's point of view", *Langmuir* **20**, 2405–2408 (2004).

[2] L. Feng, S. Li, Y. Li, H. Li, L. Zhang, J. Zhai, Y. Song, B. Liu, L. Jiang, and D. Zhu, "Super-hydrophobic surfaces: from natural to artificial", *Advanced Materials* **14**, 1857–1860 (2002).

[3] M. Li, C. Li, B. R. Blackman, and S. Eduardo, "Mimicking nature to control bio-material surface wetting and adhesion", *International Materials Reviews* **67**, 658–681 (2022).

[4] R. Hensel, R. Helbig, S. Aland, A. Voigt, C. Neinhuis, and C. Werner, "Tunable nano-replication to explore the omniphobic characteristics of springtail skin", *NPG Asia Materials* **5**, e37–e37 (2013).

[5] G.-T. Yun, W.-B. Jung, M. S. Oh, G. M. Jang, J. Baek, N. I. Kim, S. G. Im, and H.-T. Jung, "Springtail-inspired superomniphobic surface with extreme pressure resistance", *Science Advances* **4**, eaat4978 (2018).

[6] Y. Zheng, H. Bai, Z. Huang, X. Tian, F.-Q. Nie, Y. Zhao, J. Zhai, and L. Jiang, "Directional water collection on wetted spider silk", *Nature* **463**, 640–643 (2010).

[7] J. Ju, H. Bai, Y. Zheng, T. Zhao, R. Fang, and L. Jiang, "A multi-structural and multi-functional integrated fog collection system in cactus", *Nature Communications* **3**, 1–6 (2012).

[8] C. Liu, Y. Xue, Y. Chen, and Y. Zheng, "Effective directional self-gathering of drops on spine of cactus with splayed capillary arrays", *Scientific Reports* **5**, 1–8 (2015).

[9] L. Guo and G. Tang, "Experimental study on directional motion of a single droplet on cactus spines", *International Journal of Heat and Mass Transfer* **84**, 198–202 (2015).

[10] H. Chen, T. Ran, Y. Gan, J. Zhou, Y. Zhang, L. Zhang, D. Zhang, and L. Jiang, "Ultrafast water harvesting and transport in hierarchical microchannels", *Nature Materials* **17**, 935–942 (2018).

[11] P. Cheng and H. Y. Wu. "Phase-change heat transfer in microsystems". In *International Heat Transfer Conference 13*. Begel House Inc., (2006).

[12] C. Liu and D. Groulx, "Experimental study of the phase change heat transfer inside a horizontal cylindrical latent heat energy storage system", *International Journal of Thermal Sciences* **82**, 100–110 (2014).

[13] H. J. Cho, D. J. Preston, Y. Zhu, and E. N. Wang, "Nanoengineered materials for liquid–vapour phase-change heat transfer", *Nature Reviews Materials* **2**, 1–17 (2016).

[14] H.-J. Butt, K. Graf, and M. Kappl. *Physics and Chemistry of Interfaces*. John Wiley & Sons, (2023).

[15] X. Li, L. Mao, and X. Ma, "Dynamic behavior of water droplet impact on microtextured surfaces: the effect of geometrical parameters on anisotropic wetting and the maximum spreading diameter", *Langmuir* **29**, 1129–1138 (2013).

[16] A. Tuteja, W. Choi, M. Ma, J. M. Mabry, S. A. Mazzella, G. C. Rutledge, G. H. McKinley, and R. E. Cohen, "Designing superoleophobic surfaces", *Science* **318**, 1618–1622 (2007).

[17] A. K. Epstein, T.-S. Wong, R. A. Belisle, E. M. Boggs, and J. Aizenberg, "Liquid-infused structured surfaces with exceptional anti-biofouling performance", *Proceedings of the National Academy of Sciences* **109**, 13182–13187 (2012).

[18] J. D. Smith, R. Dhiman, S. Anand, E. Reza-Garduno, R. E. Cohen, G. H. McKinley, and K. K. Varanasi, "Droplet mobility on lubricant-impregnated surfaces", *Soft Matter* **9**, 1772–1780 (2013).

[19] T.-S. Wong, S. H. Kang, S. K. Tang, E. J. Smythe, B. D. Hatton, A. Grinthal, and J. Aizenberg, "Bioinspired self-repairing slippery surfaces with pressure-stable omniphobicity", *Nature* **477**, 443–447 (2011).

[20] C. Semprebon, G. McHale, and H. Kusumaatmaja, "Apparent contact angle and contact angle hysteresis on liquid infused surfaces", *Soft Matter* **13**, 101–110 (2017).

[21] K. Liu and L. Jiang, "Bio-inspired self-cleaning surfaces", *Annual Review of Materials Research* **42**, 231–263 (2012).

[22] J. Zhao, L. Song, J. Yin, and W. Ming, "Anti-bioadhesion on hierarchically structured, superhydrophobic surfaces", *Chemical Communications* **49**, 9191–9193 (2013).

[23] Z. Qian, S. Wang, X. Ye, Z. Liu, and Z. Wu, "Corrosion resistance and wetting properties of silica-based superhydrophobic coatings on AZ31B Mg alloy surfaces", *Applied Surface Science* **453**, 1–10 (2018).

[24] R. Truesdell, A. Mammoli, P. Vorobieff, F. van Swol, and C. J. Brinker, "Drag reduction on a patterned superhydrophobic surface", *Physical Review Letters* **97**, 044504 (2006).

[25] L. Cao, A. K. Jones, V. K. Sikka, J. Wu, and D. Gao, "Anti-icing superhydrophobic coatings", *Langmuir* **25**, 12444–12448 (2009).

[26] S. Amini, S. Kolle, L. Petrone, O. Ahanotu, S. Sunny, C. N. Sutanto, S. Hoon, L. Cohen, J. C. Weaver, J. Aizenberg, *et al.*, "Preventing mussel adhesion using lubricant-infused materials", *Science* **357**, 668–673 (2017).

[27] D. C. Leslie, A. Waterhouse, J. B. Berthet, T. M. Valentin, A. L. Watters, A. Jain, P. Kim, B. D. Hatton, A. Nedder, K. Donovan, *et al.*, "A bioinspired omniphobic surface coating on medical devices prevents thrombosis and biofouling", *Nature Biotechnology* **32**, 1134–1140 (2014).

[28] J. H. Guan, G. G. Wells, B. Xu, G. McHale, D. Wood, J. Martin, and S. Stuart-Cole, "Evaporation of sessile droplets on slippery liquid-infused porous surfaces (SLIPS)", *Langmuir* **31**, 11781–11789 (2015).

[29] J. S. Wexler, I. Jacobi, and H. A. Stone, "Shear-driven failure of liquid-infused surfaces", *Physical Review Letters* **114**, 168301 (2015).

[30] S. Armstrong, G. McHale, R. Ledesma-Aguilar, and G. Wells, "Evaporation and electrowetting of sessile droplets on slippery liquid-like surfaces and slippery liquid-infused porous surfaces (SLIPS)", *Langmuir* **36**, 11332–11340 (2020).

[31] M. Villegas, Y. Zhang, N. Abu Jarad, L. Soleymani, and T. F. Didar, "Liquid-infused surfaces: a review of theory, design, and applications", *ACS Nano* **13**, 8517–8536 (2019).

[32] B. Natarajan, A. Jaishankar, M. King, F. Oktasendra, S. J. Avis, A. R. Konicek, G. Wadsworth, A. Jusufi, H. Kusumaatmaja, and M. S. Yeganeh, "Predicting Hemi-wicking Dynamics on Textured Substrates", *Langmuir* **37**, 188–195 (2021).

[33] B. S. Kim, H. Lee, S. Shin, G. Choi, and H. H. Cho, "Interfacial wicking dynamics and its impact on critical heat flux of boiling heat transfer", *Applied Physics Letters* **105**, 191601 (2014).

[34] G. McHale, B. V. Orme, G. G. Wells, and R. Ledesma-Aguilar, "Apparent contact angles on lubricant-impregnated surfaces/SLIPS: from superhydrophobicity to electrowetting", *Langmuir* **35**, 4197–4204 (2019).

[35] M. J. Alshukri, A. K. Hussein, A. A. Eidan, and A. I. Alsabery, "A review on applications and techniques of improving the performance of heat pipe-solar collector systems", *Solar Energy* **236**, 417–433 (2022).

[36] S. Nagrath, L. V. Sequist, S. Maheswaran, D. W. Bell, D. Irimia, L. Ulkus, M. R. Smith, E. L. Kwak, S. Digumarthy, A. Muzikansky, *et al.*, "Isolation of rare circulating tumour cells in cancer patients by microchip technology", *Nature* **450**, 1235–1239 (2007).

[37] T. Young, "III. An essay on the cohesion of fluids", *Philosophical Transactions of the Royal Society of London* **95**, 65–87 (1805).

[38] P. S. Laplace. *Traité de Mécanique Céleste*, volume 1. de l'Imprimerie de Crapelet, (1799).

[39] T. Krüger, H. Kusumaatmaja, A. Kuzmin, O. Shardt, G. Silva, and E. M. Viggen. *The Lattice Boltzmann Method.* Springer, (2017).

[40] D. Frenkel and B. Smit. *Understanding Molecular Simulation: From Algorithms to Applications.* Elsevier, (2023).

[41] D. M. Anderson, G. B. McFadden, and A. A. Wheeler, "Diffuse-interface methods in fluid mechanics", *Annual Review of Fluid Mechanics* **30**, 139–165 (1998).

[42] D. Jacqmin, "Calculation of two-phase Navier–Stokes flows using phase-field modeling", *Journal of Computational Physics* **155**, 96–127 (1999).

[43] P.-G. De Gennes, "Wetting: statics and dynamics", *Reviews of Modern Physics* **57**, 827 (1985).

[44] D. Quéré, "Wetting and roughness", *Annual Review of Materials Research* **38**, 71–99 (2008).

[45] P.-G. de Gennes, F. Brochard-Wyart, and D. Quéré. *Capillarity and Wetting Phenomena: Drops, Bubbles, Pearls, Waves.* Springer (2004).

[46] R. N. Wenzel, "Resistance of solid surfaces to wetting by water", *Industrial & Engineering Chemistry* **28**, 988–994 (1936).

[47] A. Cassie and S. Baxter, "Wettability of porous surfaces", *Transactions of the Faraday Society* **40**, 546–551 (1944).

[48] L. Gao and T. J. McCarthy, "Contact angle hysteresis explained", *Langmuir* **22**, 6234–6237 (2006).

[49] J. W. Gibbs. *The Scientific Papers of J. Willard Gibbs*, volume 1. Longmans, Green and Company, (1906).

[50] J. R. Panter. *Exploring Stability Landscapes for Optimal Material Design: Application to Wetting of Structured Surfaces.* University of Durham (United Kingdom), (2019).

[51] E. Celia, T. Darmanin, E. T. de Givenchy, S. Amigoni, and F. Guittard, "Recent advances in designing superhydrophobic surfaces", *Journal of Colloid and Interface Science* **402**, 1–18 (2013).

[52] A. Lafuma and D. Quéré, "Superhydrophobic states", *Nature Materials* **2**, 457–460 (2003).

[53] A. Giacomello, M. Chinappi, S. Meloni, and C. M. Casciola, "Metastable wetting on superhydrophobic surfaces: continuum and atomistic views of the Cassie-Baxter–Wenzel transition", *Physical Review Letters* **109**, 226102 (2012).

[54] R. Poetes, K. Holtzmann, K. Franze, and U. Steiner, "Metastable underwater superhydrophobicity", *Physical Review Letters* **105**, 166104 (2010).

[55] P. Lv, Y. Xue, Y. Shi, H. Lin, and H. Duan, "Metastable states and wetting transition of submerged superhydrophobic structures", *Physical Review Letters* **112**, 196101 (2014).

[56] X. Wang, C. Fu, C. Zhang, Z. Qiu, and B. Wang, "A comprehensive review of wetting transition mechanism on the surfaces of microstructures from theory and testing methods", *Materials* **15**, 4747 (2022).

[57] N. A. Patankar, "Transition between superhydrophobic states on rough surfaces", *Langmuir* **20**, 7097–7102 (2004).

[58] N. A. Patankar, "Consolidation of hydrophobic transition criteria by using an approximate energy minimization approach", *Langmuir* **26**, 8941–8945 (2010).

[59] C. Extrand, "Contact angles and their hysteresis as a measure of liquid- solid adhesion", *Langmuir* **20**, 4017–4021 (2004).

[60] Q.-S. Zheng, Y. Yu, and Z.-H. Zhao, "Effects of hydraulic pressure on the stability and transition of wetting modes of superhydrophobic surfaces", *Langmuir* **21**, 12207–12212 (2005).

[61] J. R. Panter and H. Kusumaatmaja, "The impact of surface geometry, cavitation, and condensation on wetting transitions: posts and reentrant structures", *Journal of Physics: Condensed Matter* **29**, 084001 (2017).

[62] J. R. Panter, Y. Gizaw, and H. Kusumaatmaja, "Multifaceted design optimization for superomniphobic surfaces", *Science Advances* **5**, eaav7328 (2019).

[63] D. Bonn, J. Eggers, J. Indekeu, J. Meunier, and E. Rolley, "Wetting and spreading", *Reviews of Modern Physics* **81**, 739–805 (2009).

[64] J. N. Israelachvili. *Intermolecular and Surface Forces.* Academic Press, (2011).

[65] F. Brochard-Wyart, J. M. di Meglio, D. Quéré, and P.-G. de Gennes, "Spreading of Nonvolatile Liquids in a Continuum Picture", *Langmuir* **7**, 335–338 (1991).

[66] H. Kellay, J. Meunier, and B. Binks, "Wetting properties of n-alkanes on AOT monolayers at the brine-air interface", *Physical Review Letters* **69**, 1220 (1992).

[67] V. Bergeron and D. Langevin, "Monolayer spreading of polydimethylsiloxane oil on surfactant solutions", *Physical Review Letters* **76**, 3152 (1996).

[68] H. Matsubara, T. Shigeta, Y. Takata, N. Ikeda, H. Sakamoto, T. Takiue, and M. Aratono, "Effect of molecular structure of oil on wetting transition on surfactant solutions", *Colloids and Surfaces A: Physicochemical and Engineering Aspects* **301**, 141–146 (2007).

[69] L. Esibov, D. Sarkisov, U.-S. Jeng, M. Crow, and A. Steyerl, "Dynamics of pseudo-partial wetting studied by neutron reflectometry", *Physica B: Condensed Matter* **241**, 1077–1079 (1997).

[70] J. Bico, C. Tordeux, and D. Quéré, "Rough wetting", *Europhysics Letters* **55**, 214 (2001).

[71] R. Lucas, "Ueber das Zeitgesetz des kapillaren Aufstiegs von Flüssigkeiten", *Kolloid-Zeitschrift* **23**, 15–22 (1918).

[72] E. W. Washburn, "The dynamics of capillary flow", *Physical Review* **17**, 273 (1921).

[73] C. Ishino, M. Reyssat, E. Reyssat, K. Okumura, and D. Quere, "Wicking within forests of micropillars", *Europhysics Letters* **79**, 56005 (2007).

[74] H. Kusumaatmaja, C. Pooley, S. Girardo, D. Pisignano, and J. Yeomans, "Capillary filling in patterned channels", *Physical Review E* **77**, 067301 (2008).

[75] D. Kim, N. M. Pugno, and S. Ryu, "Wetting theory for small droplets on textured solid surfaces", *Scientific Reports* **6**, 37813 (2016).

[76] N. Srivastava, C. Din, A. Judson, N. C. MacDonald, and C. D. Meinhart, "A unified scaling model for flow through a lattice of microfabricated posts", *Lab on a Chip* **10**, 1148–1152 (2010).

[77] J. Kim, M.-W. Moon, K.-R. Lee, L. Mahadevan, and H.-Y. Kim, "Hydrodynamics of writing with ink", *Physical Review Letters* **107**, 264501 (2011).

[78] M. Wörner, "Numerical modeling of multiphase flows in microfluidics and micro process engineering: a review of methods and applications", *Microfluidics and Nanofluidics* **12**, 841–886 (2012).

[79] D. Di Carlo, "Inertial microfluidics", *Lab on a Chip* **9**, 3038–3046 (2009).

[80] H. A. Stone and S. Kim, "Microfluidics: basic issues, applications, and challenges", *AIChE Journal* **47**, 1250–1254 (2001).

[81] B. Zhao, J. S. Moore, and D. J. Beebe, "Surface-directed liquid flow inside microchannels", *Science* **291**, 1023–1026 (2001).

[82] A. D. Stroock, S. K. Dertinger, A. Ajdari, I. Mezić, H. A. Stone, and G. M. Whitesides, "Chaotic mixer for microchannels", *Science* **295**, 647–651 (2002).

[83] M. Blow, H. Kusumaatmaja, and J. Yeomans, "Imbibition through an array of triangular posts", *Journal of Physics: Condensed Matter* **21**, 464125 (2009).

[84] P. S. Raux, H. Cockenpot, M. Ramaioli, D. Quéré, and C. Clanet, "Wicking in a powder", *Langmuir* **29**, 3636–3644 (2013).

[85] H. Shahariar, I. Kim, H. Soewardiman, and J. S. Jur, "Inkjet printing of reactive silver ink on textiles", *ACS Applied Materials & Interfaces* **11**, 6208–6216 (2019).

[86] T. Babadagli, "Dynamics of capillary imbibition when surfactant, polymer, and hot water are used as aqueous phase for oil recovery", *Journal of Colloid and Interface Science* **246**, 203–213 (2002).

[87] J. Bico, U. Thiele, and D. Quéré, "Wetting of textured surfaces", *Colloids and Surfaces A: Physicochemical and Engineering Aspects* **206**, 41–46 (2002).

[88] D. Quéré, "Rough ideas on wetting", *Physica A: Statistical Mechanics and its Applications* **313**, 32–46 (2002).

[89] G. McHale, N. Shirtcliffe, S. Aqil, C. Perry, and M. Newton, "Topography driven spreading", *Physical Review Letters* **93**, 036102 (2004).

[90] R. S. Hale, R. Ranjan, and C. H. Hidrovo, "Capillary flow through rectangular micropillar arrays", *International Journal of Heat and Mass Transfer* **75**, 710–717 (2014).

[91] K. A. Ismail and M. M. Abogderah, "Performance of a heat pipe solar collector", *Journal of Solar Energy Engineering, Transactions of the ASME* **120**, 51–59 (1998).

[92] H. H. Cui and K. M. Lim, "Pillar array microtraps with negative dielectrophoresis", *Langmuir* **25**, 3336–3339 (2009).

[93] S. Nagrath, L. V. Sequist, S. Maheswaran, D. W. Bell, D. Irimia, L. Ulkus, M. R. Smith, E. L. Kwak, S. Digumarthy, A. Muzikansky, P. Ryan, U. J. Balis, R. G. Tompkins, D. A. Haber, and M. Toner, "Isolation of rare circulating tumour cells in cancer patients by microchip technology", *Nature* **450**, 1235–1239 (2007).

[94] M. Sbragaglia, A. M. Peters, C. Pirat, B. M. Borkent, R. G. Lammertink, M. Wessling, and D. Lohse, "Spontaneous breakdown of superhydrophobicity", *Physical Review Letters* **99**, 156001 (2007).

[95] L. Courbin, E. Denieul, E. Dressaire, M. Roper, A. Ajdari, and H. A. Stone, "Imbibition by polygonal spreading on microdecorated surfaces", *Nature Materials* **6**, 661–664 (2007).

[96] R. J. Vrancken, M. L. Blow, H. Kusumaatmaja, K. Hermans, A. M. Prenen, C. W. Bastiaansen, D. J. Broer, and J. M. Yeomans, "Anisotropic wetting and de-wetting of drops on substrates patterned with polygonal posts", *Soft Matter* **9**, 674–683 (2013).

[97] K. H. Chu, R. Xiao, and E. N. Wang, "Uni-directional liquid spreading on asymmetric nanostructured surfaces", *Nature Materials* **9**, 413–417 (2010).

[98] Z. Yang, "Lattice Boltzmann outflow treatments: Convective conditions and others", *Computers & Mathematics with Applications* **65**, 160–171 (2013).

[99] S. Avis. "Massively parallel lattice Boltzmann fluid simulations". Level 4 project report at Department of Physics, Durham University, (2019).

[100] Q. Zou and X. He, "On pressure and velocity boundary conditions for the lattice Boltzmann BGK model", *Physics of Fluids* **9**, 1591–1598 (1997).

[101] J. Bico and D. Quéré, "Rise of liquids and bubbles in angular capillary tubes", *Journal of Colloid and Interface Science* **247**, 162–166 (2002).

[102] K. M. Hay, M. I. Dragila, and J. Liburdy, "Theoretical model for the wetting of a rough surface", *Journal of Colloid and Interface Science* **325**, 472–477 (2008).

[103] T. T. Mai, C. Q. Lai, H. Zheng, K. Balasubramanian, K. Leong, P. Lee, C. Lee, and W. Choi, "Dynamics of wicking in silicon nanopillars fabricated with interference lithography and metal-assisted chemical etching", *Langmuir* **28**, 11465–11471 (2012).

[104] B. Ghanbarian, A. G. Hunt, R. P. Ewing, and M. Sahimi, "Tortuosity in porous media: a critical review", *Soil Science Society of America Journal* **77**, 1461–1477 (2013).

[105] S. R. Krishnan, J. Bal, and S. A. Putnam, "A simple analytic model for predicting the wicking velocity in micropillar arrays", *Scientific Reports* **9**, 20074 (2019).

[106] L. Wen, Y. Tian, and L. Jiang, "Bioinspired super-wettability from fundamental research to practical applications", *Angewandte Chemie International Edition* **54**, 3387–3399 (2015).

[107] Z. Wang, M. Elimelech, and S. Lin, "Environmental applications of interfacial materials with special wettability", *Environmental Science & Technology* **50**, 2132–2150 (2016).

[108] M. S. Yeganeh, A. Jusufi, S. P. Deighton, M. S. Ide, M. Siskin, A. Jaishankar, C. Maldarelli, P. Bertolini, B. Natarajan, J. L. Vreeland, M. A. King, and A. R. Konicek, "Solid with infused reactive liquid (SWIRL): A novel liquid-based separation approach for effective CO_2 capture", *Science Advances* **8**, eabm0144 (2022).

[109] C. Yan, P. Jiang, X. Jia, and X. Wang, "3D printing of bioinspired textured surfaces with superamphiphobicity", *Nanoscale* **12**, 2924–2938 (2020).

[110] K. Brassat and J. K. N. Lindner, "Nanoscale Block Copolymer Self-Assembly and Microscale Polymer Film Dewetting: Progress in Understanding the Role of Interfacial Energies in the Formation of Hierarchical Nanostructures", *Advanced Materials Interfaces* **7**, 1901565 (2020).

[111] T. Kong, G. Luo, Y. Zhao, and Z. Liu, "Bioinspired superwettability micro/nanoarchitectures: fabrications and applications", *Advanced Functional Materials* **29**, 1808012 (2019).

[112] M. Liu, S. Wang, and L. Jiang, "Nature-inspired superwettability systems", *Nature Review Materials* **2**, 17036 (2017).

[113] Y. Zhu, F. Yang, and Z. Guo, "Bioinspired surfaces with special micro-structures and wettability for drag reduction: Which surface design will be a better choice?", *Nanoscale* **13**, 3463–3482 (2021).

[114] P. Lv, Y.-L. Zhang, D.-D. Han, and H.-B. Sun, "Directional Droplet Transport on Functional Surfaces with Superwettabilities", *Advanced Materials Interfaces* **8**, 2100043 (2021).

[115] J. Song, R. Shi, X. Bai, H. Algadi, and D. Sridhar, "An overview of surface with controllable wettability for microfluidic system, intelligent cleaning, water harvesting, and surface protection", *Advanced Composites and Hybrid Materials* **6**, 22 (2023).

[116] M. Rauscher and S. Dietrich, "Wetting Phenomena in Nanofluidics", *Annual Review of Materials Research* **38**, 143–172 (2008).

[117] E. M. Grzelak and J. R. Errington, "Nanoscale limit to the applicability of Wenzel's equation", *Langmuir* **26**, 13297–13304 (2010).

[118] P. Silberzan and L. Léger, "Evidence for a new spreading regime between partial and total wetting", *Physical Review Letters* **66**, 185–188 (1991).

[119] S. K. Sethi, S. Kadian, and G. Manik, "A Review of Recent Progress in Molecular Dynamics and Coarse-Grain Simulations Assisted Understanding of Wettability", *Archives of Computational Methods in Engineering* **29**, 3059–3085 (2022).

[120] A. Malijevský and A. O. Parry, "Modified Kelvin equations for capillary condensation in narrow and wide grooves", *Physical Review Letters* **120**, 135701 (2018).

[121] A. Giacomello, L. Schimmele, S. Dietrich, and M. Tasinkevych, "Perpetual superhydrophobicity", *Soft Matter* **12**, 8927–8934 (2016).

[122] S. L. Singh, L. Schimmele, and S. Dietrich, "Intrusion of liquids into liquid-infused surfaces with nanoscale roughness", *Physical Review E* **105**, 044803 (2022).

[123] A. P. Hughes, U. Thiele, and A. J. Archer, "Liquid drops on a surface: Using density functional theory to calculate the binding potential and drop profiles and comparing with results from mesoscopic modelling", *Journal of Chemical Physics* **142**, 074702 (2015).

[124] A. Malijevský, "Filling and wetting transitions at grooved substrates", *Journal of Physics: Condensed Matter* **25**, 445006 (2013).

[125] J. W. Cahn, "Critical point wetting", *Journal of Chemical Physics* **66**, 3667–3672 (1977).

[126] D. Jacqmin, "Calculation of two-phase Navier–Stokes flows using phase-field modeling", *Journal of Computational Physics* **155**, 96–127 (1999).

[127] M. N. MacGregor-Ramiasa and K. Vasilev, "Questions and Answers on the Wettability of Nano-Engineered Surfaces", *Advanced Materials Interfaces* **4**, 1700381 (2017).

[128] E. Bormashenko and V. Starov, "Impact of surface forces on wetting of hierarchical surfaces and contact angle hysteresis", *Colloid and Polymer Sciences* **291**, 343–346 (2013).

[129] B. Derjaguin, "A theory of capillary condensation in the pores of sorbents and of other capillary phenomena taking into account the disjoining action of polymolecular liquid films", *Progress in Surface Science* **40**, 46–61 (1992).

[130] A. Giacomello, L. Schimmele, and S. Dietrich, "Wetting hysteresis induced by nanodefects", *Proceedings of the National Academy of Sciences* **113**, E262–E271 (2016).

[131] R. Enright, N. Miljkovic, N. Dou, Y. Nam, and E. N. Wang, "Condensation on superhydrophobic copper oxide nanostructures", *Journal of Heat Transfer* **135**, 091304 (2013).

[132] Y. Lu, D. Fan, Y. Wang, H. Xu, C. Lu, and X. Yang, "Surface patterning of two-dimensional nanostructure-embedded photothermal hydrogels for high-yield solar steam generation", *ACS Nano* **15**, 10366–10376 (2021).

[133] Q. Cao, Z. Cui, and W. Shao, "Optimization method for grooved surface structures regarding the evaporation heat transfer of ultrathin liquid films at the nanoscale", *Langmuir* **36**, 2802–2815 (2020).

[134] A. Malijevský, "Does adsorption in a single nanogroove exhibit hysteresis?", *Journal of Chemical Physics* **137**, 214704 (2012).

[135] A. O. Parry, A. Malijevský, and C. Rascón, "Capillary contact angle in a completely wet groove", *Physical Review Letters* **113**, 146101 (2014).

[136] H. Kusumaatmaja, "Surveying the free energy landscapes of continuum models: Application to soft matter systems", *Journal of Chemical Physics* **142**, 124112 (2015).

[137] E. Yeh, J. Newman, and C. Radke, "Equilibrium configurations of liquid droplets on solid surfaces under the influence of thin-film forces: Part II. Shape calculations", *Colloids and Surfaces A: Physicochemical and Engineering Aspects* **156**, 525–546 (1999).

[138] J.-J. Huang, H. Huang, and X. Wang, "Wetting boundary conditions in numerical simulation of binary fluids by using phase-field method: Some comparative studies and new development", *International Journal for Numerical Methods in Fluids* **77**, 123–158 (2015).

[139] X. Liu, H. Zhang, H. Jiang, Y. Yang, S. Feng, C. Liang, and Y. Jia, "A study on the mechanism of water vapour condensation inhibition by nanostructures on the copper surface", *Journal of Materials Science* **57**, 20615–20630 (2022).

[140] T. Hofmann, M. Tasinkevych, A. Checco, E. Dobisz, S. Dietrich, and B. M. Ocko, "Wetting of Nanopatterned Grooved Surfaces", *Physical Review Letters* **104**, 106102 (2010).

[141] R. Lipowsky, "Critical effects at complete wetting", *Physical Review B* **32**, 1731–1750 (1985).

[142] M. Láska, A. O. Parry, and A. Malijevský, "Breaking Cassie's law for condensation in a nanopatterned slit", *Physical Review Letters* **126**, 125701 (2021).

[143] C. Rascón, A. O. Parry, R. Nürnberg, A. Pozzato, M. Tormen, L. Bruschi, and G. Mistura, "The order of condensation in capillary grooves", *Journal of Physics: Condensed Matter* **25**, 192101 (2013).

[144] R. Evans, U. M. B. Marconi, and P. Tarazona, "Capillary condensation and adsorption in cylindrical and slit-like pores", *Journal of the Chemical Society, Faraday Transactions 2* **82**, 1763–1787 (1986).

[145] D. G. A. L. Aarts, M. Schmidt, and H. N. W. Lekkerkerker, "Direct Visual Observation of Thermal Capillary Waves", *Science* **304**, 847–850 (2004).

[146] A. O. Parry, A. J. Wood, and C. Rascón, "Wedge filling, cone filling and the strong-fluctuation regime", *Journal of Physics: Condensed Matter* **13**, 4591 (2001).

[147] A. Chaudhri, J. B. Bell, A. L. Garcia, and A. Donev, "Modeling multiphase flow using fluctuating hydrodynamics", *Physical Review E* **90**, 033014 (2014).

[148] M. Gallo, F. Magaletti, and C. M. Casciola, "Thermally activated vapor bubble nucleation: The Landau-Lifshitz–Van der Waals approach", *Physical Review Fluids* **3**, 053604 (2018).

[149] C. Semprebon, T. Krüger, and H. Kusumaatmaja, "Ternary free-energy lattice Boltzmann model with tunable surface tensions and contact angles", *Physical Review E* **93**, 1–11 (2016).

[150] J. R. Panter, A. R. Konicek, M. A. King, A. Jusufi, M. S. Yeganeh, and H. Kusumaatmaja, "Rough capillary rise", *Communications Physics* **6**, 44 (2023).

[151] M. Jin, X. Feng, L. Feng, T. Sun, J. Zhai, T. Li, and L. Jiang, "Superhydrophobic aligned polystyrene nanotube films with high adhesive force", *Advanced Materials* **17**, 1977–1981 (2005).

[152] G. McHale, N. Shirtcliffe, and M. Newton, "Contact-angle hysteresis on superhydrophobic surfaces", *Langmuir* **20**, 10146–10149 (2004).

[153] D. Wang, Q. Sun, M. J. Hokkanen, C. Zhang, F.-Y. Lin, Q. Liu, S.-P. Zhu, T. Zhou, Q. Chang, B. He, *et al.*, "Design of robust superhydrophobic surfaces", *Nature* **582**, 55–59 (2020).

[154] S. Mitra, N. S. K. Gunda, and S. K. Mitra, "Wetting characteristics of underwater micropatterned surfaces", *RSC Advances* **7**, 9064–9072 (2017).

[155] B.-X. Zhang, S.-L. Wang, and X.-D. Wang, "Wetting transition from the Cassie–Baxter state to the Wenzel state on regularly nanostructured surfaces induced by an electric field", *Langmuir* **35**, 662–670 (2019).

[156] M. Hilpert and C. T. Miller, "Pore-morphology-based simulation of drainage in totally wetting porous media", *Advances in Water Resources* **24**, 243–255 (2001).

[157] S. Bakhshian, S. A. Hosseini, and N. Shokri, "Pore-scale characteristics of multiphase flow in heterogeneous porous media using the lattice Boltzmann method", *Scientific Reports* **9**, 3377 (2019).

[158] W. Barthlott, T. Schimmel, S. Wiersch, K. Koch, M. Brede, M. Barczewski, S. Walheim, A. Weis, A. Kaltenmaier, A. Leder, *et al.*, "The Salvinia paradox: superhydrophobic surfaces with hydrophilic pins for air retention under water", *Advanced Materials* **22**, 2325–2328 (2010).

[159] S. Feng, P. Zhu, H. Zheng, H. Zhan, C. Chen, J. Li, L. Wang, X. Yao, Y. Liu, and Z. Wang, "Three-dimensional capillary ratchet-induced liquid directional steering", *Science* **373**, 1344–1348 (2021).

[160] C. E. Colosqui, M. E. Kavousanakis, A. G. Papathanasiou, and I. G. Kevrekidis, "Mesoscopic model for microscale hydrodynamics and interfacial phenomena: slip, films, and contact-angle hysteresis", *Physical Review E* **87**, 013302 (2013).

[161] M. Rauscher and S. Dietrich, "Wetting phenomena in nanofluidics", *Annual Review of Materials Research* **38**, 143–172 (2008).

[162] Z. Guo, C. Zheng, and B. Shi, "Discrete lattice effects on the forcing term in the lattice Boltzmann method", *Physical Review E* **65**, 046308 (2002).

[163] R. Christianto. *Lattice Boltzmann Modelling of Droplet Dynamics on Fibres and Meshed Surfaces.* PhD thesis, Durham University, (2024).

[164] K. Zhou, D. Li, P. Xue, P. Wang, Y. Zhao, and M. Jin, "One-step fabrication of Salvinia-inspired superhydrophobic surfaces with High adhesion", *Colloids and Surfaces A: Physicochemical and Engineering Aspects* **590**, 124517 (2020).

[165] Y. Wu, Y. Xue, X. Pei, M. Cai, H. Duan, W. T. Huck, F. Zhou, and Q. Xue, "Adhesion-regulated switchable fluid slippage on superhydrophobic surfaces", *Journal of Physical Chemistry C* **118**, 2564–2569 (2014).

[166] H. Bai, X. Tian, Y. Zheng, J. Ju, Y. Zhao, and L. Jiang, "Direction controlled driving of tiny water drops on bioinspired artificial spider silks", *Advanced Materials* **48**, 5521–5525 (2010).

[167] J. Busch, W. Barthlott, M. Brede, W. Terlau, and M. Mail, "Bionics and green technology in maritime shipping: an assessment of the effect of Salvinia air-layer hull coatings for drag and fuel reduction", *Philosophical Transactions of the Royal Society A* **377**, 20180263 (2019).

[168] C. Zhan, Z. Chai, and B. Shi, "A ternary phase-field model for two-phase flows in complex geometries", *Physica D: Nonlinear Phenomena* **460**, 134087 (2024).